Grazing incidence X-Ray scattering from the interfaces of thin film magnetic device materials

Pym, Alexander Thomas Gafswood

How to cite:

Pym, Alexander Thomas Gafswood (2008) *Grazing incidence X-Ray scattering from the interfaces of thin film magnetic device materials*, Durham theses, Durham University. Available at Durham E-Theses Online: http://etheses.dur.ac.uk/2317/

Grazing Incidence X-Ray Scattering from the Interfaces of Thin Film Magnetic Device Materials

by

Alexander Thomas Garswood Pym

A thesis submitted in partial fulfilment of the requirements for
the degree of Doctor of Philosophy

The University of Durham
2008

Table of Contents

Abstract

Thin film devices have found many applications in recently developed technology. With the need to increase data storage capacity and performance there are ever more demanding requirements of these devices. Gaining an understanding at the atomic scale of the growth and subsequent manufacturing treatments is fundamental to improving the device design. Grazing incidence x-ray scattering techniques have been used to study the interfaces in a sequence of samples, starting with repeated bi-layers of single element materials and sequentially working up to a realistic Magnetic Tunnel Junction (MTJ) structure.

The width of the diffuse Bragg sheet from repeated bi-layers of Co/Pd and Co/Ru shows that the correlation length of the out-of-plane roughness is shorter for higher frequency roughness components than longer wavelength features. Scaling behaviour in the intensity profile demonstrates that the interfaces become more two-dimensional as more layers are deposited. Reflectivity measurements with *in-situ* annealing reveal that the interfaces in CoFe/Ru repeated bi-layers are stable with temperature. The interfaces of amorphous CoFeB with ruthenium are also stable until the CoFeB crystallises. Similar measurements on repeated bi-layers of CoFeB/AlO_x show sharpening of the interface during annealing. The diffuse scatter shows this to be a reduction in the interdiffusion of the interface and not a change in topological roughness. The scatter from a single CoFeB/AlO_x interface on a realistic MTJ sub-structure also shows changes with annealing which are consistent with interface sharpening. This sharpening is matched to enhancements in the tunnel magneto-resistance of the MTJ. The changes occurring cannot be explained solely by sharpening of this particular interface and more sophisticated modelling has been attempted to identify the changes. Simulations show that changes in the manganese profile from an IrMn pinning layer in the MTJ should result in a significant change in the variable energy reflectivity recorded at a constant scattering vector.

Acknowledgements

The work presented here would not have been possible without the supervision and guidance of Brian Tanner. I am extremely grateful to him for accepting me as a student of his, and for allowing me to work closely with him and within his research group.

The samples examined were kindly supplied by Chris Marrows of the University of Leeds, Susana Cardoso of INESC in Portugal, and Theo Dimpoulos of Siemens in Germany, all of whom were collaborating within the EU funded Marie Curie Research Training Network, Ultrasmooth. Without them the following work could not have been done.

For the work at the synchrotron sources, where experiments are run continuously, the efforts, support and patience of my colleagues has been invaluable; Brian Tanner, Thomas Hase, James Buchannan, David Eastwood, Amir Rozatian, Veronika Semencová and Alessio Lamperti. I also gratefully acknowledge the local staff of the synchrotrons for their assistance in operating the beamlines; Tony Bell and Steve Thompson of the SRS, and Danny Mannix, Laurence Bouchenoire, and David Paul of BM28 at the ESRF.

I acknowledge my other colleagues who have participated in many discussions of a wide and varied nature; Del Atkinson, Michael Hunt, Sean Giblin, Kathryn Kelly, Rachael Houchin, Lara Bogart and Alexis Ridler.

The support of the group's technician, John Dobson, as well as the administrative support offered by the Physics Department, has been much appreciated.

The EPSRC are thanked for providing three years of funding.

My family have provided a great deal of support, and to them I am indebted. Finally, I must thank the many bell ringers who have provided ample distractions over the course of this research.

Declaration

I hereby declare that the work contained in this thesis is my own and has not been previously submitted for a degree in this or any other university. The work of collaborators is acknowledged as appropriate throughout the thesis.

In particular, the fitting of the specular scatter and transverse diffuse scatter from the Co/Pd layers in chapter 4 was performed by Amir Rozation, at the University of Durham. The magneto-transport measurements presented in Figure 6-9 on page 151, and repeated in Figure 6-26 on page 169, were made by T. Dimopoulos, of Siemens AG, Erlangen, Germany.

The Samples used in chapter 4 were grown by Chris Marrows at the University of Leeds, the samples used in chapter 5 were grown by Susana Cardoso at INESC MN, Portugal, and Theo Dimopoulos at Siemens AG, Erlangen, Germany, and the sample examined in chapter 7 was also grown by Theo Dimopoulos in Siemens AG, Erlangen, Germany.

The experimental data recorded at synchrotrons was done collaboratively with Brian Tanner, Thomas Hase, James Buchannan, David Eastwood, Amir Rozatian, Veronika Semencová and Alessio Lamperti.

List of publications

This thesis includes work that has appeared in the following publications:

"Interface sharpening in CoFeB magnetic tunnel junctions"
A. T. G. Pym, A. Lamperti, B. K. Tanner,
T. Dimopoulos, M. Rührig and J. Wecker
Applied Physics Letters, **88** (2006) 162505

"The out-of-plane correlation length of the conformal roughness in Co-Pd multilayers"
A. T. G. Pym, A. S. H. Rozatian, C. H. Marrows,
B. J. Hickey, T. P. A. Hase and B. K. Tanner
Physica B, **357** (2005) 170-174

"Interface stability in CoFe and CoFeB based multilayers"
A. T. G. Pym, A. Lamperti, S. Cardoso, P.P. Freitas and B. K. Tanner
Superlattices and Microstructures, **41** (2007) 122-126

"Interface Stability of Magnetic Tunnel Barriers and Electrodes"
A. Lamperti, A. T. G. Pym, D. S. Eastwood, S. Cardoso, P. Wisniowski,
P. P. Freitas, G. Anderson, C. H. Marrows and B. K. Tanner
Physica Status Soldi (a), **204** (2007) 2778-2784

"The in-plane length scale of the conformal interface roughness as a function of bilayer repeat number in Co/Pd multilayers"
A. T. G. Pym, A. S. H. Rozatian, C. H. Marrows,
S.D.Brown, L. Bouchenoire, T. P. A. Hase and B. K. Tanner
Journal of Physics D: Applied Physics, **38** (2005) A190-A194

1 Introduction

1.1 Motivation

Components engineered on the nanometre and sub-nanometre scale have become common in many examples of modern technology, from hard-disk drives through to music players and to sensors. With the drive to miniaturise and increase data storage capacity the performance of these devices on smaller and smaller scales becomes extremely important. Many of these devices are based on stacks of very thin films of materials, with thicknesses often of the order of a few nanometres, which are grown layer by layer by various means. Many different materials, such as conducting or insulating layers, or magnetic or non-magnetic layers, must be deposited depending on what characteristics are required of the device.

Understanding what happens during the growth of these layers, and what happens when one material is deposited on another material, is key to being in control of the process. Understanding how their structure is related to performance is fundamental to engineering higher performance devices. Both of these aspects must be considered, along with the associated costs and demands of the device users, when making a commercially viable product.

Magnetic Tunnel Junctions (MTJs) are a particular class of thin film device and have become an area of considerable interest recently because of their applications to the magnetic recording industry, where they are used both as sensors in hard-disk read heads and as memory storage elements in their own right in Magnetic Random Access Memory (MRAM). With novel architectures many MTJs can be combined in one chip to provide memory storage, an idea initially discussed in the late 1990's [1,2]. The first commercial MRAM came into volume production in July 2006 [3]. Critical to the operation of such devices is the interface topology of buried magnetic layers, which affects the electric current passed through the MTJ.

An MTJ is a complex device, with many layers on top of one another. Structurally, understanding how interfaces from sub-layers influence other layers through a stack is an area of importance for achieving the desired quality of a particular interface. Annealing is a common step in the fabrication process of MTJs and the structural changes induced are not obvious. This annealing is done both for its performance enhancing effects and also because it is necessary when integrating MTJs with existing CMOS semiconductor technology [4].

At very small distances the properties exhibited by thin films of materials can often be quite different to those of the bulk. To study architecture at these nanometre and sub-nanometre length scales, hard x-rays, with wavelengths in the region of 1Å (0.1nm), are frequently used and they are able to characterise much larger areas at a time than is possible with electron microscopy techniques. The x-rays are able to penetrate into the device and interact with the interfaces and atomic structure buried below the surface. By measuring the scattered x-rays the nature of the structure which has caused the scattering can be inferred. An excellent review article on the field of nanomagnetism studied by x-ray techniques was published by Srajer *et al.* in 2006 [5].

In this work different layer structures are examined using x-ray reflectivity, gradually building up to the more complex layer structure of an MTJ. X-ray reflectivity, where glancing angles to the surface are used, is a standard technique for the structural determination of layered films and has been used for the MTJ predecessors of spin-valves and GMR structures.

1.2 Samples

This work has been completed with the collaboration of Chris Marrows of the University of Leeds who kindly grew the Co/Pd and Co/Ru samples used. The remaining samples were obtained through EU Marie Curie research training network, Ultrasmooth, which was set up between industrial partners and academic laboratories across Europe to perform "experiments designed to improve the growth, crystallinity and surface quality" of thin magnetic film devices. In particular the samples were grown by Theo Dimopoulos, of Siemens AG in Germany and Susanna Cardoso at INESC MN in Portugal.

1.3 Outline

In Chapter 2 a brief theoretical overview is presented to give an understanding of the basics of x-ray scattering, sample growth, and the details of Magnetic Tunnel Junctions. Each individual chapter contains more specific theory where it is required.

Chapter 3 looks at the experimental equipment used to make measurements that have been included in this thesis, with consideration given to the associated instrument precision and the effect it has on the measured scatter.

Chapter 4 investigates the changes in the interfaces as successive layers are grown. This is investigated using a CCD detector to record the diffuse scatter at a fixed angle of incidence and analysed to investigate the correlations in the roughness. The samples investigated are repeated bi-layers of Co/Pd and Co/Ru which demonstrate the magnetic phenomena of perpendicular magnetic anisotropy and oscillatory exchange coupling.

Chapter 5 presents an analysis of interfaces found in MTJs, but in a multilayer so that individual interfaces can be isolated and studied in detail. The structures are repeated bi-layers of CoFe/Ru, CoFeB/Ru and CoFeB/AlO_x. The deposition of repeated layers on top of one-another is unrealistic for a MTJ and so the interpretation of these results is performed in the light of the conclusions from chapter 4. The effect of annealing these samples is examined, and the interfaces which are particularly susceptible to modification with annealing are identified.

Chapter 6 looks at realistic MTJ structures and the effects of annealing on the interfaces. The structural changes are compared to the changes in the magneto-transport properties on annealing. The sensitivity of the x-ray scattering techniques when the x-ray energy is changed to exploit the differences in response from different elements is then considered. Predictions are made for the identification of diffusion of elements within the structure using energy scans at a constant scattering vector.

Chapter 7 concludes by bringing together the results from all the chapters and suggests further work that could usefully be performed to further the ideas contained within this thesis.

References for Chapter 1:

[1] Daughton, J. M., J. App. Phys., **81** (1997) 3758

[2] Parkin, S. S. P., *et al.*, J. App. Phys., **85** (1999) 5823

[3] Freescale Semiconductor Inc., News Release, 10th July 2006.

[4] Cardoso, S., *et al.*, App. Phys. Lett., **76** (2000) 610

[5] G. Srajer, *et al.*, J. Magn. Magn. Mat., **307** (2006) 1

2 Theory

2.1 Introduction

In a completely darkened room, in 1895, W. C. Röntgen discovered x-rays with barium platinocyanide coated paper, whilst trying to observe the path of cathode rays through the glass of a vacuum cathode ray tube covered with black card [1]. Initially x-rays were a curiosity, allowing previously hidden objects, such as internal bones, to be viewed. Medical radiographers quickly established themselves, applying the obvious benefits of x-ray imaging to medicine.

The first crystal diffraction experiments were performed by W. Friedrich (at the time Sommerfeld's assistant) and P. Knipping (at the time Röntgen's assistant) following an idea by M. von Laue and the results were presented at the Bavarian Academy of Sciences in 1912 [2,3]. A year later W. L. Bragg explained the diffraction pattern by the interference effects in reflections off planes of atoms, and formed the law that now bears his name [4]:

$$n\lambda = 2d\sin\theta \qquad \textbf{(2-1)}$$

where λ is the wavelength of the incident x-ray, θ is the angle of incidence of the x-rays on the sample, d is the spacing of the atomic planes reflecting the x-rays, and n is the order of the reflection. These experiments confirmed the x-ray wavelength as being close to the atomic spacing in materials and the science of using x-rays to probe matter at this length scale began.

2.2 X-ray scattering

Fundamental to the scattering of x-rays is their interaction with matter, or more precisely, for x-rays with wavelength around 1Å, their interaction with the electrons in the atom. In this interaction of photon and electron it is easy to disappear under a veil of quantum mechanics of ever increasing degrees of complexity. However, to aid understanding an easier to visualise semi-classical approach will here be used.

2.2.1 Scattering from a free electron

Looking at the interaction from a classical viewpoint, the electron, being charged, is forced to vibrate by the electromagnetic field of an incident photon. This vibrating charge then radiates electromagnetic waves as a dipole, which can be described using Maxwell's equations. Through this mechanism scattering of the incident photon is observed, and the dipole radiation has a particular intensity pattern in different directions. The differential cross-section (from which the probability of being scattered, σ, in a particular solid angle, Ω, can be calculated) for this Thomson scattering is [5]:

$$\left(\frac{d\sigma}{d\Omega}\right) = r_e^2 P \tag{2-2}$$

$$\text{Where:} \quad P = \begin{cases} 1 \\ \cos^2\psi \\ \frac{1}{2}\left(1+\cos^2\psi\right) \end{cases} \tag{2-3}$$

$$\text{and} \quad r_e = \left(\frac{e^2}{4\pi\varepsilon_0 m_e c^2}\right) \tag{2-4}$$

Where ψ is the scattering angle and r_e is the Thomson scattering length of the electrons, or the classical electron radius. P is the polarisation factor which equals 1 where the x-ray is polarised in the scattering plane, $\cos^2\psi$ when polarised perpendicularly to the scattering plane, and $\frac{1}{2}\left(1+\cos^2\psi\right)$ for an unpolarised source. In this scattering event the x-ray is elastically scattered; its energy is not changed and the electron after scattering has not gained any momentum. In this work it is assumed that all scattering is elastic, and inelastic Compton scattering, where the electron gains energy, is ignored. At synchrotron x-ray sources, scattering is usually performed in the vertical plane and so, from equation (2-3), there is no additional angular dependence introduced from the polarisation.

2.2.2 Scattering from an atom

In an atom the electrons are bound in their respective quantum mechanical orbitals. For 3d transition metals the most tightly bound electrons are the K shell, which have energies comparable to hard x-rays (approximately 10keV). Classically, the distribution of the electrons in the atom can be described by a density distribution function, $\rho(\mathbf{r})$, and the total scattered intensity calculated by summing the contribution from each charge element over the spatial extent of the atom whilst keeping track of the phases from each element. The atomic scattering factor, f, is defined as the Fourier transform of the electron density;

$$f^0 \equiv \int_V \rho(\mathbf{r}) e^{i\mathbf{k}.\mathbf{r}} dV \qquad \text{(2-5)}$$

However, to consider the response of the electrons to the incident x-rays this scattering factor needs to be modified to take into account the binding of the electrons, which can lead to resonant behaviour occurring. This modification is the so called 'anomalous dispersion corrections' $f'(E)$ and $f''(E)$:

$$f = f^0 + f'(E) + if''(E) \qquad \text{(2-6)}$$

where $f'(E)$ takes into account the change in scattering factor, and $f''(E)$ describes the change in the phase lag from the driving field as a result of different electron bindings.

2.2.3 Propagation in a medium

Once the scattering from an individual atom is calculated, a crystalline solid can be constructed by summing the contribution from each atom, and taking into account the positions of the atoms within the unit cell. However, there is an easier approach to take, which assumes homogenous media and uses a refractive index to describe the propagation of an x-ray in the material. This is valid at grazing angles where the x-ray is not sensitive to individual atoms because the scattering vector is small compared with the reciprocal lattice vector.

X-rays are electromagnetic waves, and the electric field vector is given by:

$$\mathbf{E}(\mathbf{r}, t) = \hat{\varepsilon} E_0 e^{i(\mathbf{k}\cdot\mathbf{r} - \omega t)} \qquad \text{(2-7)}$$

where $\mathbf{r}$ is the position, $\hat{\varepsilon}$ is the polarisation unit vector defining the plane of polarisation, **k** is the wavevector in the direction of propagation of the wave and has magnitude 2π/λ, and λ is the wavelength. The refractive index, n, can be thought of as a modification to the wavevector as a result of propagating in a medium compared to that of a vacuum, $k' = nk$. For x-rays the refractive index of the medium can be described as:

$$n(\mathbf{r}) = 1 - \delta(\mathbf{r}) + i\beta(\mathbf{r}) \tag{2-8}$$

Here complex numbers are used to take into account the dispersion, δ(*r*), and absorption, β(*r*) within the medium. The iβ(r) term in the refractive index, being complex, gives rise to an exponentially decaying intensity when the modified wavevector in the medium, *nk*, is substituted into (2-7) and hence it is related to the linear absorption coefficient $\mu(r)$, equation (2-9).

$$\beta(\mathbf{r}) = \frac{\lambda}{4\pi}\mu(\mathbf{r}) \tag{2-9}$$

where, μ(r) is the linear absorption coefficient of the medium. The depth at which the intensity of the x-rays falls to 1/e of the incident beam, Λ, is given by:

$$\Lambda = \frac{1}{2k\beta} \tag{2-10}$$

The values for δ and β are given by equations (2-11) and (2-12) and include the anomalous dispersion corrections referred to above that model the response of the bound electrons to different energies of incident radiation:

$$\delta(\mathbf{r}) = \frac{\lambda^2}{2\pi} r_e \sum_{j=1}^{N} \frac{\rho_j(\mathbf{r})}{Z_j}\left(f_j^0(\mathbf{q}) + f_j'(E)\right) \tag{2-11}$$

$$\beta(\mathbf{r}) = \frac{\lambda^2}{2\pi} r_e \sum_{j=1}^{N} \frac{\rho_j(\mathbf{r}) f_j''(E)}{Z_j} \tag{2-12}$$

Here the subscript j indexes the element in a compound or mixture, and ρ_j(r) is the electron density associated with each element in the material. In the limit of low angles, all elements within the electron cloud scatter in phase, so from equation (2-6) f^0 is the total charge of the atom, which is equal to the number of protons, Z, in that atom, and equation (2-11) becomes:

$$\delta(\mathbf{r}) \approx \frac{\lambda^2}{2\pi} r_e \sum_{j=1}^{N} \frac{\rho_j(\mathbf{r})}{Z_j}\left(Z_j + f_j'(E)\right) \tag{2-13}$$

It should be noted that *δ(r)* is always a small positive value and so the refractive index for x-rays is always slightly less than unity. This arises because the frequency of an x-ray is higher than the resonance frequencies of the atoms of the medium and has the consequence that materials exhibit total external reflection below a critical angle (measured with respect to the sample surface), and above this angle the x-rays penetrate into the sample. The other implication is that the phase velocity of the x-ray in the medium is greater than the speed of light in a vacuum.

2.2.4 Scattering at interfaces

Where two different materials form an interface, any waves propagating in those media will be influenced by the change in refractive index at the interface, with possibilities for both reflection and refraction on transmission occurring. By matching the tangential components of the electric and magnetic field at the interfaces between two media Fresnel calculated coefficients for the relative amounts of reflection (r_s) and transmission (t_s) at an interface as a function of the z-component (directed along the surface normal) of the wave-vectors.

Assume an incident wave at an interface has wavevector $\mathbf{k_I}$, with amplitude a_I, and the transmitted and reflected wavevectors $\mathbf{k_T}$ and $\mathbf{k_R}$, with amplitudes a_T and a_R, as shown in Figure 2-1 below:

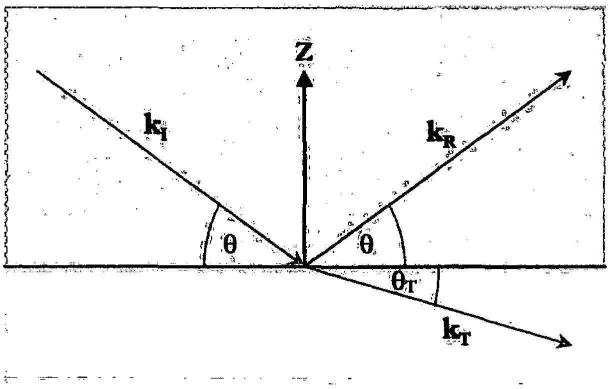

Figure 2-1: Reflection and transmission of an incident beam at an interface

At the interface the wave and its derivative must be continuous, so the total amplitude on both side of the interface must be the same:

$$a_T = a_I + a_R \tag{2-14}$$

And the pre-factors after the derivative is taken of the equation describing the wave, equation (2-7), must be the same on both sides of the interface:

$$a_T \mathbf{k_T} = a_I \mathbf{k_I} + a_R \mathbf{k_R} \tag{2-15}$$

Resolving the wavevectors into components gives, parallel to the interface:

$$a_I k \cos\theta + a_R k \cos\theta = a_T (nk) \cos\theta_T \tag{2-16}$$

and perpendicular to interface:

$$(a_R - a_I) k \sin\theta = -a_T (nk) \sin\theta_T \tag{2-17}$$

Combining (2-14) and (2-16) leads to Snell's law:

$$\cos\theta = n\cos\theta_T \tag{2-18}$$

By including the complex refractive index, (2-8), the angles become complex numbers. Expanding (2-18) in a small angles approximation gives:

$$1 - \frac{\theta^2}{2} \approx n - \frac{n\theta_T^2}{2} \tag{2-19}$$

Using (2-8) to express the refractive index in terms of δ and β, and neglecting the smallest terms, gives:

$$\theta^2 \approx 2\delta + 2i\beta + \theta_T^2 \tag{2-20}$$

Therefore the internal angle is complex and has real and imaginary parts.

The critical angle, α_c, for a material, assuming for simplicity that β is zero and absorption in the medium can be ignored, is then given by:

$$\alpha_c \approx \sqrt{2\delta} \tag{2-21}$$

From Equations (2-14) and (2-17):

$$\frac{a_I - a_R}{a_I + a_R} = n\frac{\sin\theta_T}{\sin\theta} \approx \frac{\theta_T}{\theta} \tag{2-22}$$

From this the Fresnel equations relating the transmitted and reflected amplitudes are derived:

$$r_s = \frac{\theta - n\theta_T}{\theta + n\theta_T} \tag{2-23}$$

$$t_s = \frac{2\theta}{\theta + n\theta_T} \tag{2-24}$$

These are the amplitude reflectivity and transmission coefficients; the intensities are found from the modulus squared values of these quantities.

The description so far has assumed a perfectly flat and sharp interface. The effect of including interface roughness is to introduce a range of angles though which the x-rays are reflected and refracted. The ideal 'mirror' reflection is known as the specular reflection, and the remaining scatter is called diffuse scatter, as illustrated in Figure 2-2 below. This diffuse scatter is described more fully in section 2.5.

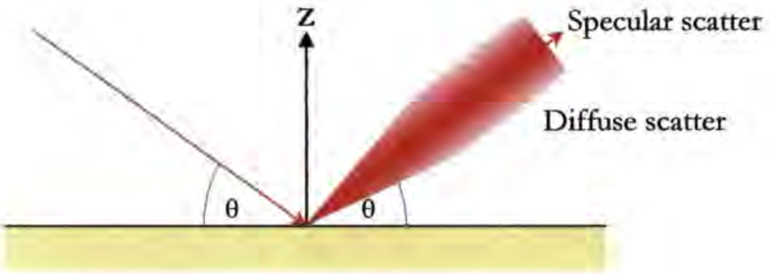

Figure 2-2: Specular and diffuse scatter from an interface

2.3 Scattering geometries and reciprocal space

In making measurements of the scatter from a sample there are three basic parameters that can be altered: the angle of incidence, the angular position of the detector, and the wavelength, or energy, of the incident photons. Often, because x-ray tubes and synchrotrons are hard to move, the angles of the sample and the detector are altered in making the measurements. The sample angle, θ, is the angle of incidence measured to the sample surface. The detector angle, ψ, is measured relative to incident beam, and is the scattering angle of the x-rays. When looking at the specular scatter ψ is twice the sample angle, 2θ. When looking at diffuse scatter this is not the case. The scattering vector, **q**, which is the reciprocal direction of the scattering, is related to the wavevectors of the incident and exit beams, and is given by:

$$\mathbf{q} = \mathbf{k}_f - \mathbf{k}_i \qquad \textbf{(2-25)}$$

This is illustrated in Figure 2-3 below.

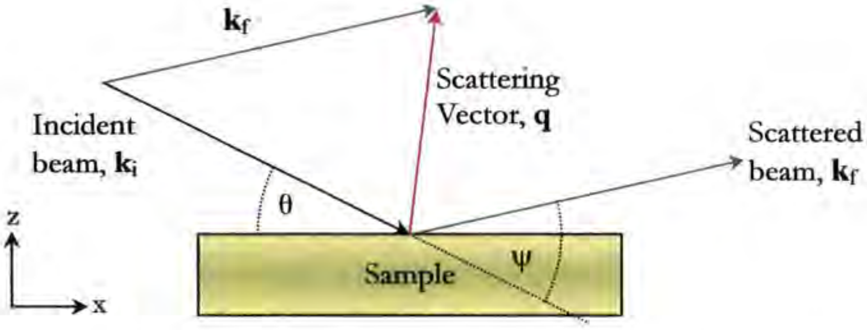

Figure 2-3: Definition of reciprocal space in two dimensions

In this work it is assumed that all the scattering is elastic, and therefore that the energy of the photons are not changed on scattering. In this two dimensional case, the components of the scattering vector, **q**, are given by:

$$q_z = \frac{2\pi}{\lambda}\left[\sin(\psi - \theta) + \sin(\theta)\right] \qquad (2\text{-}26)$$

$$q_x = \frac{2\pi}{\lambda}\left[\cos(\psi - \theta) - \cos(\theta)\right] \qquad (2\text{-}27)$$

For a specular scan, where the mirror reflection is examined, **q** is always directed along the surface normal, and varies in length as the angle of incidence is changed. The detector angle is changed at twice the angular rate to the sample angle to stay on this condition, and q_z is given by:

$$q_z = \frac{4\pi}{\lambda}\sin(\theta) \qquad (2\text{-}28)$$

Alternatively, the diffuse scatter, caused by roughness in the sample, can be examined. The longitudinal diffuse or off-specular scan is similar to a specular scan except that a constant offset is maintained (typically 0.1°) between the detector position and the position of the specular reflection as the detector and sample angles are scanned. The diffuse scatter close to the specular scatter can be measured in this way. In a transverse diffuse scan the detector is kept at a fixed angle and the sample is rocked from its surface initially being parallel to the incident beam until the angle of incidence equals the detector angle, at which point the sample obscures the detector. These geometric restrictions cause a cut-off in the region of reciprocal space accessible. A lesser used scan is the radial scan where the sample angle is kept fixed and only the detector is scanned in a vertical direction to record the scatter. The variation of the **q** vector for these scans is illustrated in reciprocal space in Figure 2-4 below.

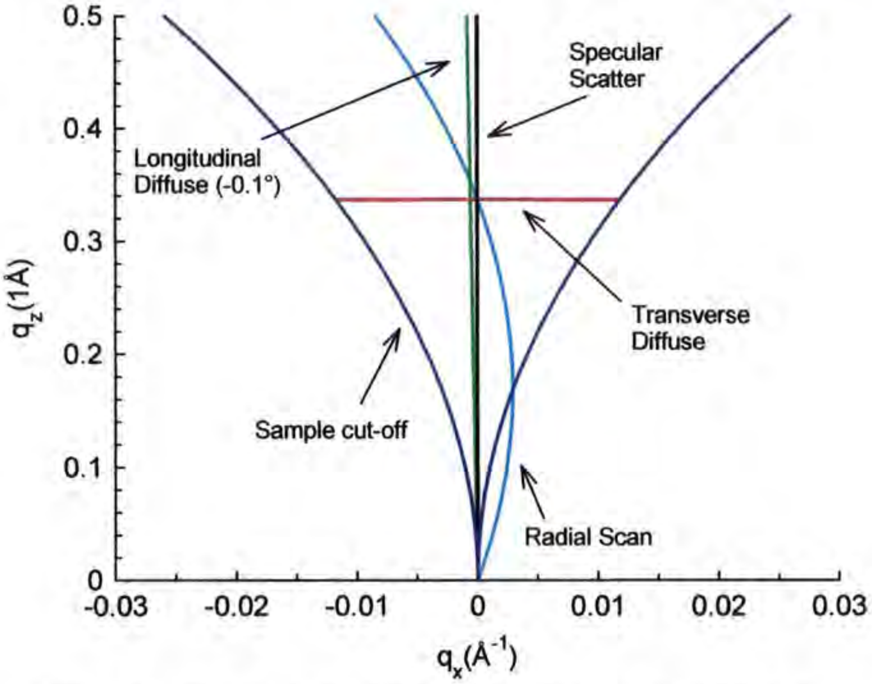

Figure 2-4: Standard grazing incidence reflectivity scans in reciprocal space

Moving out of this x-z plane to include a horizontal detector angle as well as a vertical ψ allows the y-component of **q** to be probed. The scattering geometry is illustrated in Figure 2-5 below with the equations for the components of **q** given in equations (2-29) and (2-30).

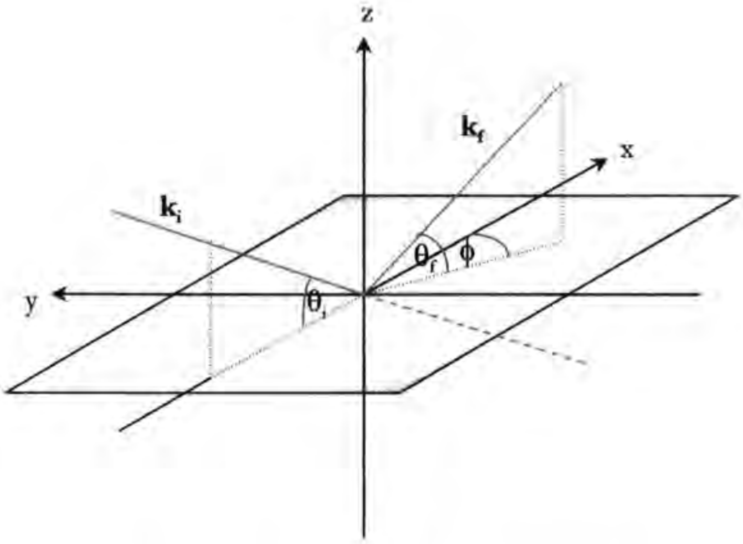

Figure 2-5: Scattering geometry in three dimensions

Resolving the expression for the scattering vector, equation (2-25), into components using the angles defined in Figure 2-5, and assuming elastic scatter, gives the **q** components in three dimensions:

$$\begin{pmatrix} q_x \\ q_y \\ q_z \end{pmatrix} = \frac{2\pi}{\lambda} \begin{pmatrix} \cos\theta_f \cos\phi - \cos\theta_i \\ \cos\theta_f \sin\phi \\ \sin\theta_f + \sin\theta_i \end{pmatrix} \tag{2-29}$$

This can be written in terms of the angles measured in the experiment as;

$$\begin{pmatrix} q_x \\ q_y \\ q_z \end{pmatrix} = \frac{2\pi}{\lambda} \begin{pmatrix} \cos(\psi - \theta)\cos\phi - \cos\theta \\ \cos(\psi - \theta)\sin\phi \\ \sin(\Psi - \theta) + \sin\theta \end{pmatrix} \tag{2-30}$$

The path of a complete circle of the detector in a horizontal (x-y plane) only scan in a horizontal direction is shown in Figure 2-6 below. As the detector angle, ψ, is increased the scattering vector develops a component in the y-direction and negative x-direction. The y-component reaches a maximum when the detector is perpendicular to the incident beam. At small angles of ψ the scattering vector is predominantly in the y-direction and the x-component remains small.

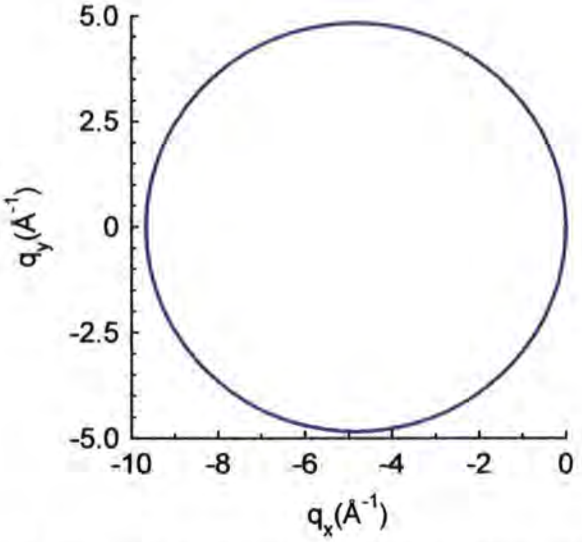

Figure 2-6: A horizontal detector only scan with an incident angle of 1° and vertical detector angle of 2° at a wavelength of 1.3Å.

At a fixed energy there are regions of reciprocal space that cannot be accessed. The boundary of the accessible region, caused by the sample surface, for scatter at a wavelength of 1.3Å, has been calculated and is shown in Figure 2-7 below for the region -5° < ψ <5. The limits shown previously in Figure 2-4 correspond to a vertical slice through Figure 2-7 at q_y=0.

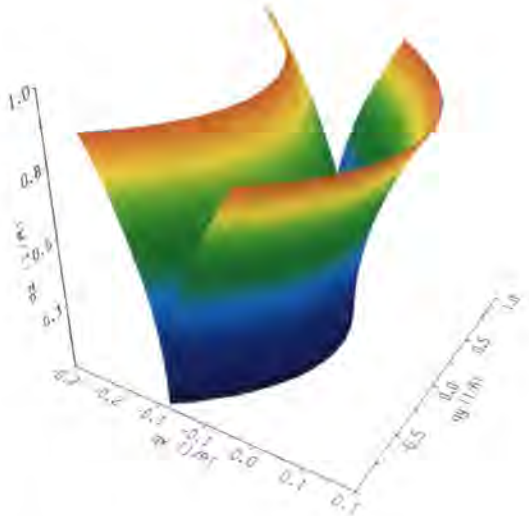

Figure 2-7: Sample cut-off in three dimensional reciprocal space for a wavelength of 1.3Å. Horizontal detector only scans sit in this 'groove'.

2.4 Grazing incidence specular reflectivity

The reflections from a single interface have been considered in section 2.2.4. Real samples can be made from many different layers and each interface will reflect and transmit the x-rays, resulting in many different ray paths through the sample. As the angle of incidence is varied so the interference effects of rays reflected from different points in the sample vary, resulting in a characteristic pattern of the specular reflectivity. This interference is restricted by the coherence length of the x-rays which sets a limit on the separation of points that can be involved in creating the interference pattern.

2.4.1 Reflectivity from a single layer

When a single layer of material is illuminated with x-rays, at the top surface the beam will be partially reflected and partially transmitted according to the Fresnel coefficients in equations (2-23) and (2-24). The transmitted ray continues to the next interface with the substrate where the same thing happens. The transmitted ray into the substrate never emerges, but the reflected ray meets the top surface and again is partially transmitted out of the sample to be detected, and partially reflected back again. This is illustrated in Figure 2-8 below.

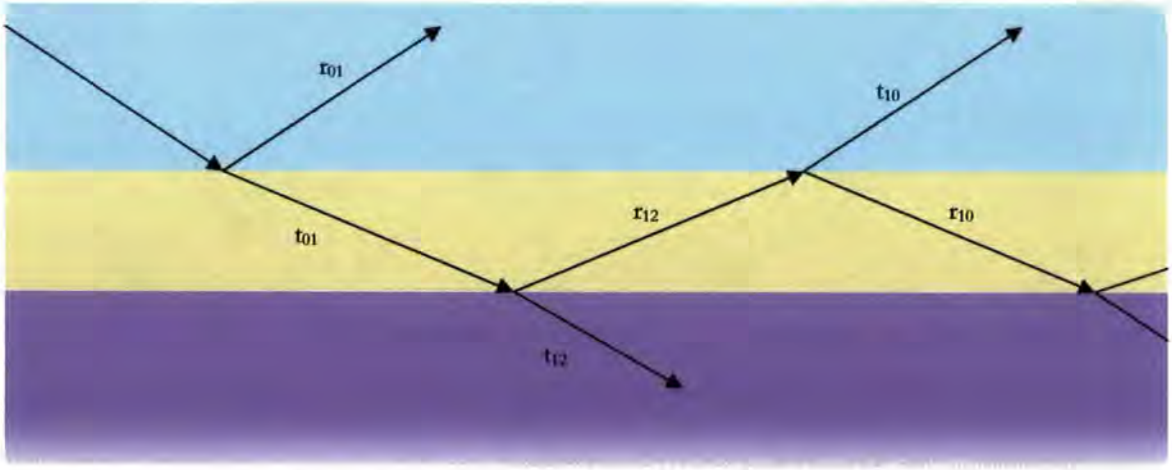

Figure 2-8: Rays through a single slab of material on a substrate with reflection and transmission at each interface

To calculate the total reflected intensity it is necessary to include the phases of the waves on reflection and transmission, and the path lengths which depend on the layer thicknesses and angle. The total reflectivity (amplitude) is given by:

$$r_{TOTAL} = r_{01} + t_{01} p r_{12} p t_{10} + t_{01} p r_{12} p r_{10} p r_{12} p t_{10} + \ldots.. \qquad \textbf{(2-31)}$$

$$r_{TOTAL} = r_{01} + t_{01} t_{10} r_{12} p^2 \sum_{m=0}^{\infty} \left(r_{10} r_{12} p^2 \right)^m \qquad \textbf{(2-32)}$$

Where p is the phase factor given by $p = e^{iq\Delta}$ where Δ is the thickness and $\mathbf{q}$ the scattering vector. Recognising this as a geometric series the sum is given by:

$$r_{TOTAL} = r_{01} + t_{01}t_{10}r_{12}p^2 \frac{1}{1 - r_{10}r_{12}p^2} \tag{2-33}$$

Using the fundamental relationships $r_{01} = -r_{10}$ and $r_{01}^2 + t_{01}t_{10} = 1$ the expression is simplified further to give:

$$r_{TOTAL} = \frac{r_{01} + r_{12}p^2}{1 + r_{01}r_{12}p^2} \tag{2-34}$$

The reflectivity for a single slab is shown in Figure 2-9 below.

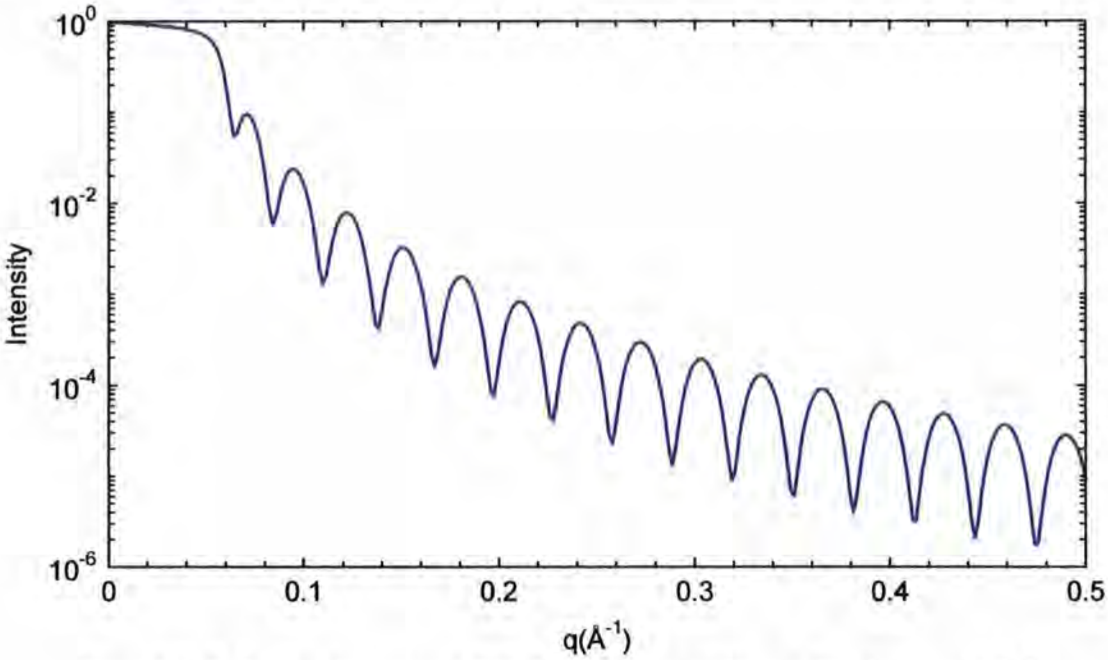

Figure 2-9: Reflectivity from a single 200Å smooth layer of Fe on a Si substrate at 1.3Å

The reflectivity from a single slab on a substrate shows distinct fringes originating from the interference effects of rays reflected from the top surface and the interface with the substrate. These are Kiessig fringes, and where they are present it is an indication that the x-rays are penetrating through the whole thickness of the sample, and are being reflected out again. The scatter is nearly constant below the critical angle where the beam is totally externally reflected and is attenuated only by absorption. At the critical angle the x-rays begin to penetrate into the sample and the Kiessig fringes start to appear.

2.4.2 Reflectivity from a stratified sample

An exact method of working out the reflectivity from a many layered sample was developed by Parratt [6]. This formalism has several stages and relies on recursively working up from the lowest interface of the bottom layer with the substrate, where there is no reflection from a lower layer coming up into the layer.

Initially the refractive index of each layer is calculated, followed by the reflection and transmission coefficients at each interface. Then the wavevector transfer, or magnitude of the **q** vector, in each layer is calculated to take into account refraction effects between layers. The Fresnel reflection coefficient (2-23) between two layers j and $j+1$ can be rewritten in terms of the wavevector transfer in the materials on either side of the interface.

$$r_{j,j+1} = \frac{q_j - q_{j+1}}{q_j + q_{j+1}} \tag{2-35}$$

This is first evaluated for the substrate/lowest layer interface where there are no multiple reflections to consider. Then this is used to calculate the reflectivity coefficient for the next interface up from the substrate where equation (2-34) is used:

$$r_{TOTAL} = \frac{r_{N-1,N} + r_{N,substrate}\, p_N^2}{1 + r_{N-1,N}\, r_{N,substrate}\, p_N^2} \tag{2-36}$$

This can then be used recursively until the reflectivity from the top surface is calculated. The phase factors p have to be calculated for each layer at all incident angles. Although Parratt in his paper worked through the calculations manually for simple structures the use of computer code to execute this operation is invaluable. An example specular reflectivity profile from [Al(25Å)/Fe(25Å)]x5 multilayer on a silicon substrate is shown in Figure 2-10 below.

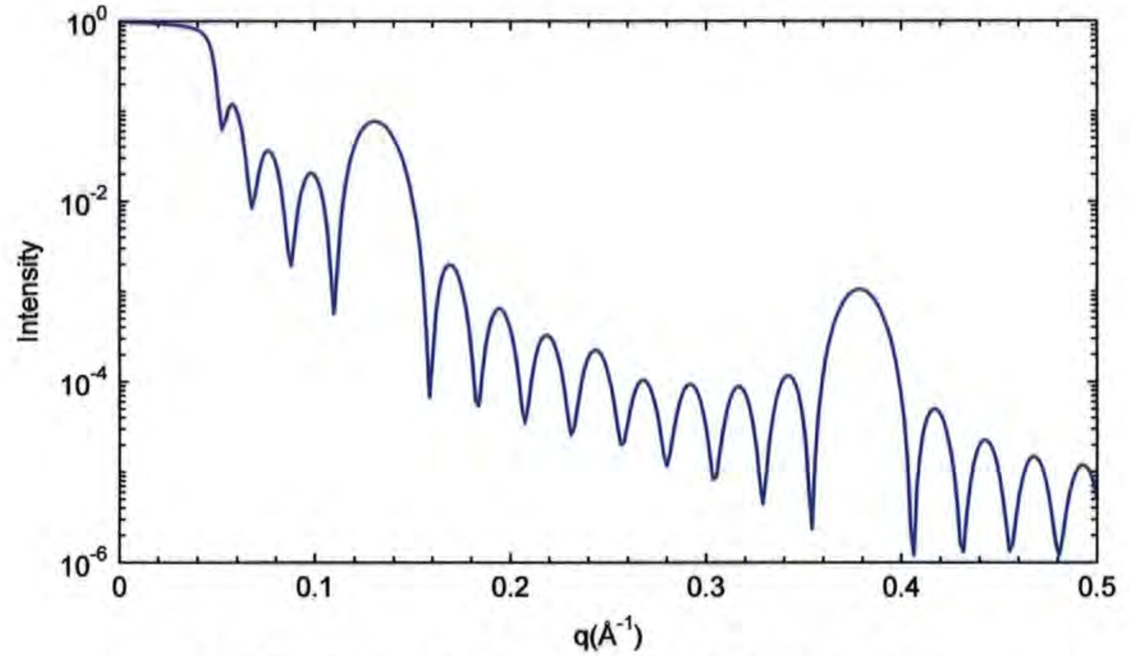

Figure 2-10: Simulated reflectivity from a [Al(25Å)/Fe(25Å)]x5 multilayer on a Si Substrate showing two clear Bragg peaks

The repeated structural unit in the sample produces Bragg peaks which are analogous to diffraction peaks, although at grazing incidence they come from the interfaces between layers forming an artificial crystal lattice, and not from the atomic planes as they do in crystal diffraction. Bragg's law, $n\lambda = 2d\sin\theta$, where d is the spacing of the reflecting planes, takes the simplified form when converted into reciprocal space:

$$q_{z,B} = n\frac{2\pi}{d} \qquad \textbf{(2-37)}$$

This clearly shows that both the position of the first Bragg peak, and spacing between subsequent Bragg peaks, is directly related to the distance between interfaces. As with crystal structures certain Bragg peaks can be missing as a result of destructive interference. This has occurred in Figure 2-10 above, where the second order Bragg peak is missing, and is understandable when the scatter is viewed in the light of being closely related to the Fourier Transform of the layer structure.

2.4.3 Brillouin zone in x-ray reflectivity

The formal definition of a Brillouin zone is defined, in diffraction, in terms of a primitive cell of the reciprocal lattice of a crystal structure, which in turn determines where the Bragg peaks exist. In the same way, in reflectivity from a multilayer, the Bragg peaks form a reciprocal 1D 'lattice' and the Brillouin zone is the region in reciprocal space bounded by points half way between Bragg peaks. This is important where diffuse scatter is being considered, as conformal roughness between layers will cause scatter at the diffuse Bragg peaks and non-conformal roughness causes a general background in the diffuse scatter. Thus by integrating the diffuse scatter over a Brillouin zone both the conformal and non-conformal components can be sampled equally. This is discussed more fully in chapter 4.

2.5 Interface widths and diffuse scatter

The scattering described in the previous section has assumed perfectly smooth interfaces. However, as noted earlier, roughness causes diffuse scatter. This will be considered in more detail in this section.

2.5.1 Sample topological roughness and compositional grading

Pictorially, an interface can be visualised in several different configurations, as shown in Figure 2-11 below. The interface can be atomically sharp and flat, or it can be sharp but show topological roughness undulations. It can also exhibit inter-diffusion which is also called grading.

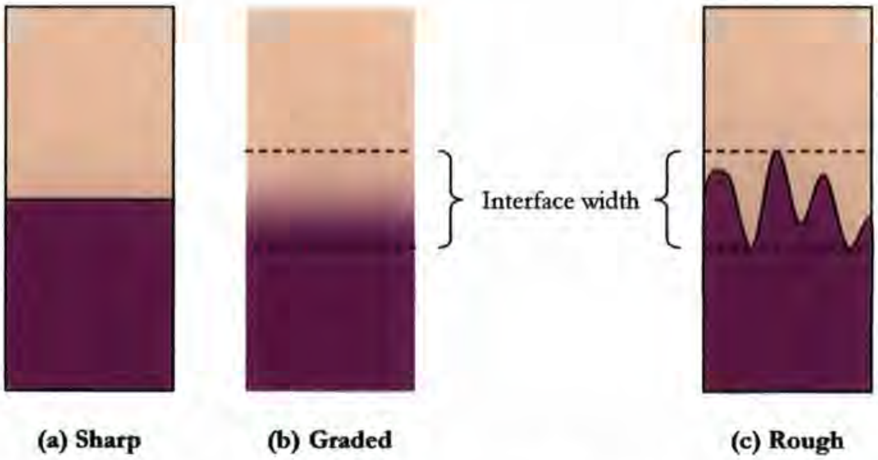

Figure 2-11: Interfaces between two materials

For both the graded and rough interfaces the laterally averaged electron density profile with depth is identical, making it impossible to distinguish the two by measurements that are only sensitive to this profile, such as specular scattering. The RMS roughness of an interface, σ_{rms}, is defined as the RMS fluctuation in height from the mean height, as given in equation (2-38) below:

$$\sigma_{rms} = \sqrt{\frac{1}{d}\int_{-d/2}^{d/2}\left(h(x)-\bar{h}\right)^2 dx} \qquad \textbf{(2-38)}$$

where d is the sample dimension and *h(x)* is the surface height function. It is also possible, and more physically realistic, that a combination of both grading and topological roughness occurs at the same time within the interface. Where this occurs, and if the interfaces are modelled using an error function profile, erf(z), the two can be combined in quadrature to measure the full interface width, as shown in (2-39).

$$\sigma^2_{rms\ interface\ width} = \sigma^2_{rms\ roughness} + \sigma^2_{rms\ grading} \qquad (2\text{-}39)$$

In multiple layered structures the growth of a layer on another can strongly influence the interface formed on the top of that layer. Roughness from one layer to the next can be either perfectly replicated, which is called correlated or conformal roughness, random, or a mixture of the two. These are illustrated in Figure 2-12 below.

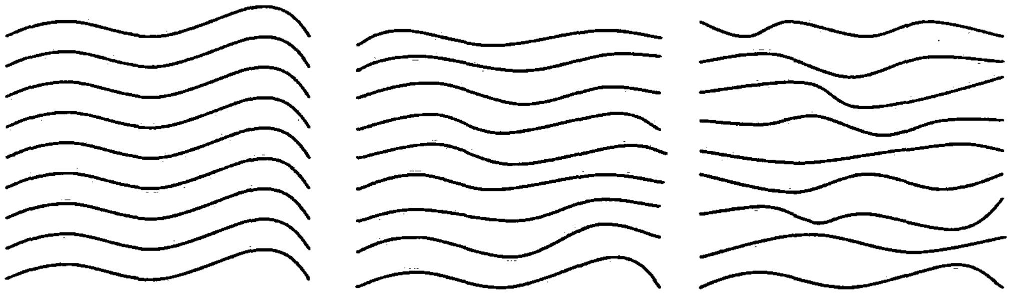

(a) (b) (c)

Figure 2-12: Examples of interface structures in multilayers:
(a) Perfectly correlated interfaces – all interfaces are identical
(b) partially correlated interfaces – an interface is similar to the previous one but not an exact copy
(c) no correlation between interfaces – all interfaces are different and bear no relation to the previous one.

The correlation of this roughness is important for scattering. In perfectly correlated systems the distances between interfaces are constant whereas any non-conformality gives a variation in the thickness. For Bragg peaks originating from multilayers, this causes broadening of the Bragg peaks. Correlation lengths can be defined for both in-plane and out-of-plane structure to give a description of the length scales over which the roughness is related. This is discussed more fully in section 2.5.7 below.

2.5.2 The effect of interface width on the specular scatter

Roughness will scatter photons away from the specular condition and the specular scatter falls off at a greater rate with increasing angle than it would for the smooth case. In a wide interface the scattering occurs over a range of distances from the mean position of the interface. This results in a variation in the phase of the scattered x-rays which must be summed over the whole interface to obtain the total reflection coefficient from that interface. This leads to the inclusion of so called 'static Debye-Waller factors' in the expressions for the Fresnel coefficients of each layer, i.e. they are modified as:

$$R(\mathbf{q}) = R_F(\mathbf{q})e^{-q^2\sigma^2} \tag{2-40}$$

A rigorous derivation of this is provided in [5]. These factors are easily incorporated into the recursive theory of Parratt described in section 2.4.2 above.

2.5.3 Transverse diffuse scans and longitudinal diffuse scans

The transverse diffuse scan has been briefly mentioned in section 2.3 above. An example is provided in Figure 2-13 below. The detector is kept at a fixed angle and the sample is rocked from being parallel to the incident beam to being aligned at the detector angle. Outside this range the sample itself either blocks the incident beam or casts a shadow on the detector. At the centre of the scan is the specular ridge where the angles are such that the specular reflection from the surface is directed into the detector. This specular peak is usually centred on a broader peak of diffuse scatter. The width of this contains information about the correlation of the roughness within the sample.

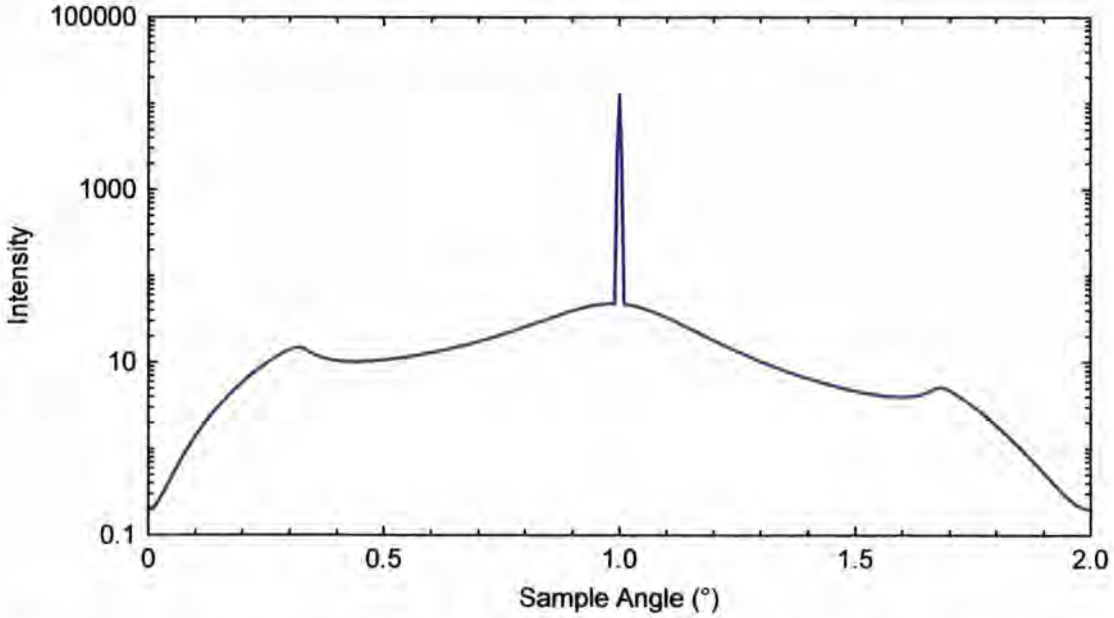

Figure 2-13: A transverse diffuse scan at a detector angle of 2°, from a 3Å rough Fe surface, with correlation length 2000Å and fractal parameter 0.5.

At the critical angles there is an enhancement in the diffuse scatter, which are known as Yoneda wings [7]. These occur from the electric field profile causing an enhancement at the surface. When second-order multiple scattering events are included in the theory modelling the diffuse scatter, the increased intensity at the surface enhances the scattering giving rise to the wings. A similar effect is sometimes seen when at certain incident angles a standing wave is produced in a multilayer which enhances the field at the interfaces and causes an enhancement to the diffuse scatter [8,9].

A longitudinal diffuse scan is shown below in Figure 2-14. This is similar to the specular scan except that an off-set is maintained between the specular reflection and the detector position. It therefore gives a measure of the diffuse scatter just off the specular ridge. Again correlations in the roughness play a part in determining the profile of this curve as Bragg peaks can extend out into the diffuse scatter and their widths are strongly dependent on the correlation lengths.

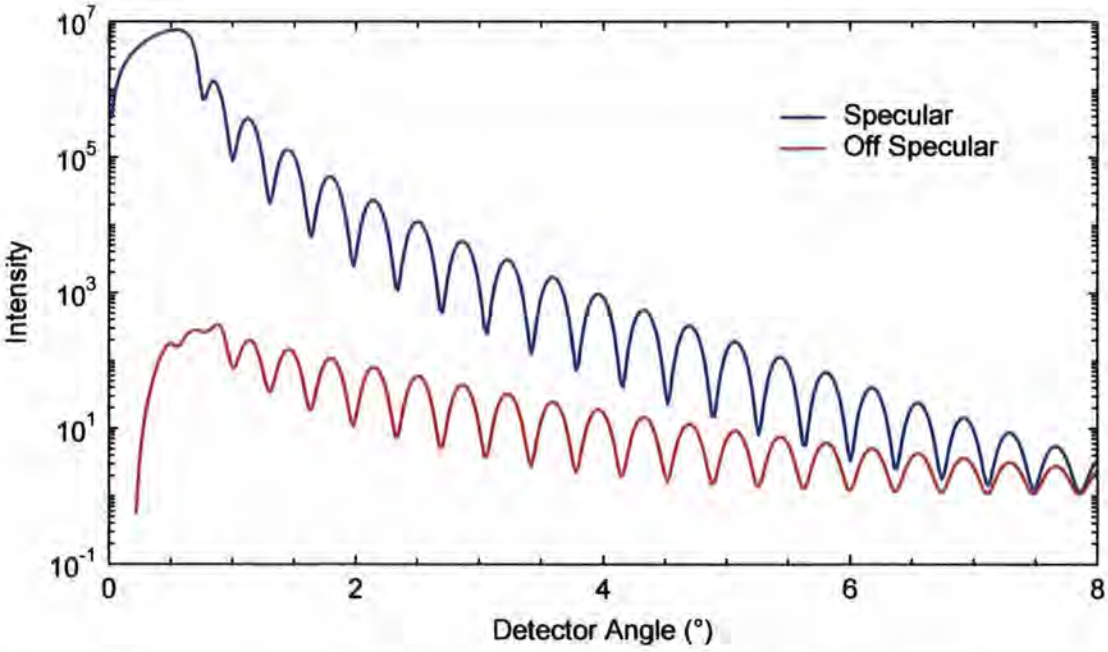

Figure 2-14 Specular and off specular scatter from a 200Å Fe layer on Si substrate with the same roughness parameters as in Figure 2-13 above.

2.5.4 Kinematical theory

To describe the diffuse scatter various methods are available at different degrees of complexity and sophistication. Approximations can be made to the scattering theory to simplify the calculations which are valid under different circumstances. One simplifying regime is the kinematical approximation, which makes the following assumptions:

a) the intensity of the beam is constant throughout the sample, i.e. absorption is ignored;
b) the scattered intensity is small, so multiple scattering events can be ignored;
c) the waves can be considered in the far-field (Fraunhofer) regime, and the scattering occurs from point scatters;
d) all scattering is elastic, and scattered photons all move in parallel directions.

This had advantages in terms of simplicity of calculations and speeding up processing. However, it fails when the scattering is strong, such as around the critical angle by not predicting the Yoneda wings.

2.5.5 (First) Born wave approximation

The Born Wave approximation is a simple kinematical theory on which it is relatively easy to perform calculations. Using kinematical theory the differential cross-section for scattering is given by equation (2-41) below [10]:

$$\frac{d\sigma}{d\Omega} = N^2 r_0^2 \int_V d\mathbf{r} \int_V e^{-i\mathbf{q}\cdot(\mathbf{r}-\mathbf{r}')} d\mathbf{r}' \qquad \text{(2-41)}$$

where N is the number density of scattering particles, and r_0 is the Thomson scattering length. Using Stoke's theorem this can be re-written in terms of surface integrals, equation (2-42):

$$\frac{d\sigma}{d\Omega} = \frac{N^2 r_0^2}{q_z^2} \iint_{S_0} dx dy \iint_{S_0} e^{-iq_z(z(x,y)-z'(x',y'))} e^{-i(q_x(x-x')+q_y(y-y'))} dx' dy' \qquad \text{(2-42)}$$

where S_0 is the surface of the x-y interface plane. It is assumed that the difference in height between any two points, the height-height correlation function, follows a Gaussian profile as a function of the separation of the points. i.e.:

$$\left\langle \left(z(x',y') - z(x,y) \right)^2 \right\rangle = g(X,Y) \qquad \text{(2-43)}$$

where $X = x' - x$ and $Y = y' - y$ are relative coordinates of the separation of two points. The scattering cross-section for an irradiated area of $L_x L_y$ is given by (2-44) below:

$$\frac{d\sigma}{d\Omega}=\frac{N^2 r_0^2}{q_z^2}L_x L_y \iint_{S_0} e^{-\frac{1}{2}q_z^2 g(X,Y)} e^{-i(q_x X+q_y Y)}dXdY \qquad \textbf{(2-44)}$$

S(q), the scattering function, is defined by equation (2-45) below:

$$S(q)=\frac{1}{N^2 r_0^2}\frac{1}{L_x L_y}\frac{d\sigma}{d\Omega} \qquad \textbf{(2-45)}$$

If *g(X,Y)*, the height-height correlation function defined in equation (2-43) is zero, which is true for a perfectly smooth surface, this equation reduces to equation (2-46):

$$S(\mathbf{q})=\frac{1}{q_z^2}\iint_{S_0} dXdYe^{-i(q_x X+q_Y Y)} \qquad \textbf{(2-46)}$$

$$=\frac{4\pi^2}{q_z^2}\delta(q_x)\delta(q_y) \qquad \textbf{(2-47)}$$

The delta functions impose the specular condition; a perfectly smooth interface does not produce any diffuse scatter, it is all specular. In the case of a multilayered sample the scattering function takes the form given in equation (2-48) [11]:

$$S(q)=\frac{1}{q_z^2}\sum_{i,j}^{N}\Delta\rho_i\Delta\rho_j e^{-\frac{1}{2}q_z^2(\sigma_i^2+\sigma_j^2)} e^{-iq_z(z_i-z_j)}\iint_{S_0}\left(e^{q_z^2 C_{ij}(R)}-1\right)e^{-i(q_x X+q_y Y)}dXdY \qquad \textbf{(2-48)}$$

where z_i-z_j is the vertical separation of layers *i* and *j*, $\Delta\rho_1$ is the contrast in scattering density of layer *i* and $C_{ij}(R)$ is the correlation function which is non-zero only when there is conformal roughness. This model breaks down when the scattering is strong, such as at the critical angle.

2.5.6 Calculating roughness within the Born approximation

It is easily observed that the greater the roughness in a sample the greater the amount of diffuse scatter. Therefore by measuring the total diffuse scatter and comparing it to the specular intensity an estimate can be made of the average RMS roughness of the interfaces in the sample. From equation (2-40) above the effect of roughness on the reflection amplitudes for the specular scatter is:

$$F^{R}_{layer} = F^{R}_{smooth-layer} e^{-\frac{1}{2}\left(Q_z^2\sigma_t^2\right)} \qquad \text{(2-49)}$$

The intensity is therefore reduced by a factor of $e^{-Q_z^2\sigma_t^2}$.

$$I_{specular} = I_{smooth-layer} e^{\left(-Q_z^2\sigma_t^2\right)} \qquad \text{(2-50)}$$

where there is no roughness all the scatter will be specular and there will be no diffuse scatter and therefore $I_{total}=I_{smooth\text{-}layer}$. Using this together with conservation of photons (and assuming the absorption in the sample is not roughness related):

$$\begin{aligned} I_{diffuse} &= I_{total} - I_{specular} \\ I_{diffuse} &= I_{smooth-layer} - I_{specular} \\ I_{diffuse} &= I_{specular} e^{Q_z^2\sigma_t^2} - I_{specular} \end{aligned} \qquad \text{(2-51)}$$

$$\frac{I_{diffuse}}{I_{specular}} = e^{Q_z^2\sigma_t^2} - 1 \qquad \text{(2-52)}$$

In applying the above equation it should be remembered that at low angles the scatter is restricted by the critical angles of the incident and exit beams. In a transverse diffuse scan the amount of diffuse scatter recorded is therefore less than the total. Strictly speaking the diffuse scatter should be collected by a detector only scan. The enhancement at the critical angles is not predicted by the Born Approximation and so this also leads to errors. However the benefit of using this equation to provide an estimate of the roughness in samples and as a method of comparing samples is undoubted. There is also a q_z dependence found when applying this equation and ideally the scatter should be integrated over a Brillouin zone [12].

2.5.7 Height difference functions and correlation functions

Different forms of the height-difference function, defined in equation (2-43) above, have been proposed. A fractal self-affine surface has a height difference function [10]:

$$g(X,Y) = AR^{2h} \qquad \text{(2-53)}$$

where $R=\sqrt{\left(X^2+Y^2\right)}$, and *h* is the fractal parameter which measures the jaggedness of the surface and is related to the fractal dimension by *D=3-h*. A value of *h*=1 gives a smooth surface confined to two dimensions and as h decreases to 0 the surface becomes more three dimensional in nature. This gives the physical limits imposed on the *h* parameter.

Unfortunately this form of height difference function has the disadvantage that for very large *R* the value of *g*(*X*,*Y*) blows up. This is not physically realistic given that samples are often grown on near-perfectly flat polished substrates and the maximum height difference between two points is limited. A form with cut-off, to avoid the divergence at large distance, was first proposed by Sinha *et al.* in 1998 [10] and this height difference function takes the form:

$$g(X,Y)=2\sigma^2\left(1-\exp\left[-\frac{R}{\xi}\right]^{2h}\right) \qquad \textbf{(2-54)}$$

where σ is the RMS roughness, ξ, is the correlation length and *h* is the fractal parameter. The in-plane correlation length, ξ, provides a characteristic cut-off distance and prevents the correlation function blowing up at large distances. In the limit of small R this form becomes the same as equation (2-53) without a cut-off and with $A=2\sigma^2/\xi$. Thus h can be interpreted in both cases to be the same.

The height difference function is related to the correlation length by:

$$C(X,Y)=\langle z(X,Y)z(0,0)\rangle=\sigma^2-\tfrac{1}{2}g(X) \qquad \textbf{(2-55)}$$

This gives a correlation function in the Sinha self-affine model of:

$$C(X,Y)=\sigma^2\exp\left[-\left(\frac{R}{\xi}\right)^{2h}\right] \qquad \textbf{(2-56)}$$

The form of this is shown in Figure 2-15 below for various values of ξ and *h* and makes it clear that *h* changes the shape of the profile and ξ sets a characteristic length.

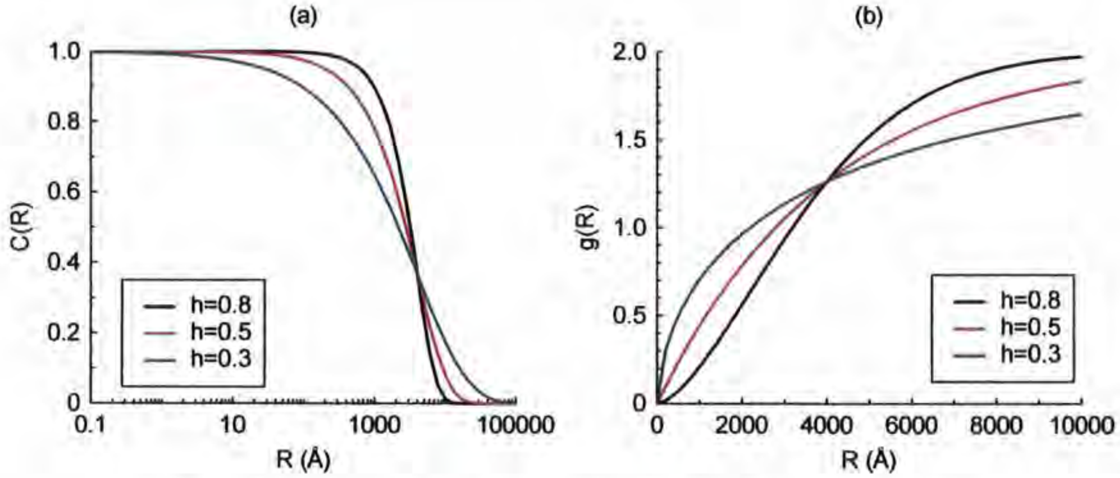

Figure 2-15: the correlation function (a) and height-difference function (b) for an interface with 1Å roughness and a correlation length of 4000Å

2.5.8 Distorted Wave Born Approximation (DWBA)

The assumptions in kinematical theory, given in section 2.5.4, restrict it to single scattering events. Often these are perfectly valid for diffuse scatter, but on occasions multiple scattering events have to be observed, such as around the critical angle and when simulating diffuse Bragg sheets. By secondary diffraction, or reflection, x-rays which are coherent with the incident beam are returned to the same direction as the incident beam and so a coupling of the wave-fields results. These are knows as dynamical effects. The Distorted Wave Born Approximation (DWBA) models these and is a semi-kinematical approach in that the ideal structure is treated dynamically and the roughness is treated kinematically.

To model the diffuse scatter the disorder, i.e. roughness, of the interface is taken as a perturbation to the ideally smooth interface. The interaction potential is split into two separate parts, V_1 and V_2, for the undisturbed smooth system and the perturbing disturbance respectively. The transition probabilities are then given by:

$$T_{1\to 2} = \left\langle \widetilde{\Psi}_2 \middle| V_1 \middle| \phi_1 \right\rangle + \left\langle \widetilde{\Psi}_2 \middle| V_2 \middle| \Psi_1 \right\rangle \tag{2-57}$$

where ϕ_1 is the incident plane wave, Ψ_1 is an eigenstate from Fresnel theory, and $\widetilde{\Psi}_2$ are time reversed eigenstates. The differential cross-section for diffuse scatter is found to be [10]:

$$\frac{d\sigma}{d\Omega} = L_x L_y \frac{\left|k_0^2 (1-n)^2\right|^2}{16\pi^2} \left|T(k_1)\right|^2 \left|T(k_2)\right|^2 S(q') \tag{2-58}$$

where $T(k_1)$ and $T(k_2)$ are the incident and scattered Fresnel Coefficients respectively. The $S(q')$ term is the scattering function, or structure factor, which is a Fourier transform of a function incorporating the correlation function described in section 2.5.6 above. This Fourier transform has to be performed numerically making it a very slow process computationally. This equation is able to model the enhancement at the critical angle of the diffuse scatter (Yoneda wings) that arises because the $|T(k)|$ terms reach a maximum at the critical angle of the incident or exit beams.

When multilayers are under investigation there are many interfaces all contributing to the diffuse scatter. The above DWBA theory was applied by Holý in 1994 to multilayers, together with a description of the dynamical effects of Bragg peaks in the diffuse scatter and the now famous Holý bananas [13].

2.5.9 Distinguishing topological roughness and compositional grading

As noted earlier specular scatter cannot distinguish between roughness and grading. Grading does not directly cause scattering in the off specular direction. Therefore looking at the diffuse scatter allows the two to be separated. For an interface of a particular fixed width, as the relative contributions of roughness and grading are altered in quadrature according to equation (2-39), the specular scatter will remain constant but the relative amount of diffuse scatter will fall as the amount of roughness falls. If the interface roughness is constant and the amount of grading changes, changing the total interface width, then the grading will alter the amount of diffuse scatter. As the grading increases so the specular scatter intensity will fall and the diffuse scatter will also fall. The intensity calculated by Wormington [14] is given by:

$$I_{diffuse} = I_{incident}\frac{k_0^3\delta\theta_2}{8\pi\sin(\theta_1)}\left|T(k_{1z})T(k_{2z})(1-n^2)\int_{-\infty}^{\infty}\left[\frac{d\rho(z)}{dz}\right]e^{iQ_z^t z}dz\right|^2 \times\frac{e^{-\left[(Q_z^t)^2+(Q_z^{t*})^2\right]\frac{\sigma_i^2}{2}}}{|Q_z^t|^2}\int_0^{\infty}\left(e^{|Q_z^t|^2C(X)}-1\right)\cos(Q_xX)dX \tag{2-59}$$

The integrand of the first integral, which depends on the differential of the electron density profile, will be lower for a wider and therefore less sharp interface profile. As the grading width increases so the intensity, of the diffuse scatter falls. The sin(θ_1) term in the prefactor takes into account the changing beam footprint as a function of angle, and the detector angular acceptance is $\delta\theta_2$.

2.6 Sample growth

The growth of thinly layered samples can be done by numerous techniques, including chemical vapour deposition, the thermal processes including MBE and thermal evaporation, and sputtering, which is the technique used to grow the samples studied in this work.

2.6.1 Sputtering

The technique of sputtering is illustrated in Figure 2-16 below. The equipment is within a vacuum chamber into which a small amount of sputtering gas, usually argon, is introduced. The substrate, on which the layers will grow, is connected to the anode and a target of the material to be deposited is attached to the cathode. A potential difference is applied to form a 'glow discharge' and the argon ions are accelerated towards the target cathode. When the Ar^+ strikes the target some of the target material is ejected, called sputtering, and travels towards the substrate where it attaches, eventually building up a layer of material. This is so called DC sputtering and slight variations to the process are often made. If the target material is an insulator then charge would rapidly build up on it preventing further sputtering. By using a RF voltage applied to the target this charge can be removed, allowing insulators to be sputtered directly from an insulating target. In magnetron sputtering a magnetic field is used to confine electrons from the glow discharge in a torus shaped volume above the target. These then increase the plasma density, which increases the rate of sputtering at the target.

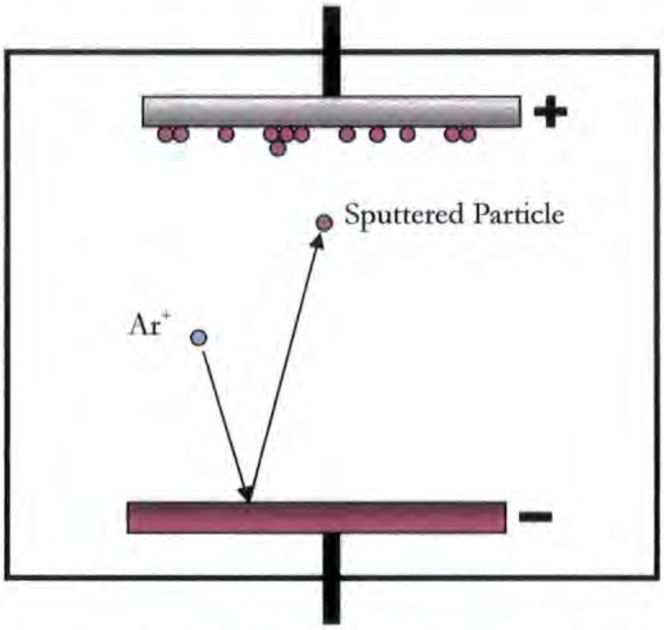

Figure 2-16: Diagram of sputtering apparatus

When the sputtered atom lands on the surface it is first adsorbed and then surface diffusion, assisted by temperature, occurs. Small clusters form, which can diffuse and collide with other clusters or break apart. When a cluster reaches a certain size it stabilises and nucleates. At this point islands start growing, predominantly laterally along the surface although slower vertical growth can also exist. The islands coalesce, to reduce their surface area, forming spaces where holes and channels of substrate are exposed. Eventually a continuous film forms and a second layer begins to be deposited. A fuller discussion is provided in reference [15].

The way in which the sputtered atoms land and become attached to the substrate is dependent on many factors. The potential difference between anode and cathode affects the energy of the sputtering argon ions and hence the energy of the sputtered atoms impinging on the substrate surface. The temperature of the substrate will affect the amount of surface diffusion of atoms when they first land on the substrate, which is also dependent on the particular materials involved. If the initial nucleation density is high then many small grains will form, which become continuous at low thicknesses and form smooth deposits. Shadowing, from the impinging atoms landing at angles to the surface normal, can lead to deep valleys forming as layers are sequentially deposited. The influence of the under-layer on the growth of the upper layer cannot be ignored and strongly influences the growth of the upper layers, leading to the correlations in the roughness that are important for the diffuse x-ray scatter.

2.6.2 Growth models

Different models describing the growth have been proposed. The simplest is ballistic deposition where atoms are dropped in random positions on the substrate and become attached to the first neighbour they meet. This is illustrated for 20,000 particles on a 200 particle wide substrate in Figure 2-17 on the left. The porosity of the structure is not physically realistic, however it is easy to see that the roughness of the surface increases in time. Eventually the roughness saturates and stays constant. The variation in the roughness with deposition time shows power-law, or scaling, behaviour in both the initial stages and later saturation stages with a different exponent in the power law for the two stages [16]. These types of scaling laws, arising from the stochastic nature of the deposition, are fundamental to the nature of the roughness with all growth mechanisms.

A more realistic deposition model is shown on the right of Figure 2-17 where the atom again is dropped in a random position on the surface but is allowed a small amount of surface diffusion to find the lowest point. This leads to dense layers with much smoother interfaces. The scaling behaviour is still present in these interfaces. A full discussion of scaling for these different models is provided in [16].

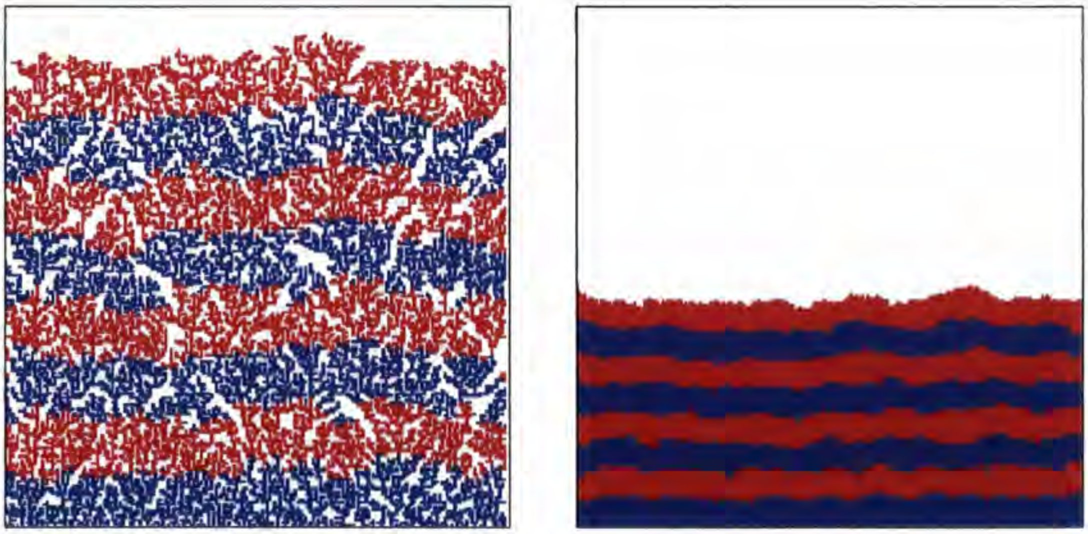

Figure 2-17: Different models of layer growth. Simple ballistic deposition (left) and random deposition with surface relaxation (right). The substrate is 200 particles wide. 20,000 particles have been deposited and the colour is changed every 2,500 particles.

More complex descriptions can be made to model the evolution of the interface as successive layers are deposited, such as the Edwards-Wilkinson equation [17] which takes into account a 'surface-tension' type parameter, or the KPZ model [18] which adds non-linear terms to account for growth along the local surface normal.

In their paper written in 1990 Tang, Alexander and Bruinsma applied a Huygens type principle, familiar from propagating wave-fronts in geometric optics, to surface evolution during layer deposition [19]. An example of this Huygens type growth is shown in Figure 2-18 below. From an initial random substrate subsequent layers are deposited and it is seen that the higher spatial frequencies in the layers propagate less well from one layer to the next than the longer wavelength features. This results in broad columns appearing which increase in width as the sample grows. They characterise this growth with a time dependent characteristic length, $\xi(t)$, for an evolving interface, which is interpreted as the average width of a column. In a simple power law dependence on time, equation (2-60), they predict values for the scaling exponent, p, for different initial starting surfaces. If the deposition rate is constant the thickness will increase linearly with time and so the same scaling laws and exponents will describe the scaling of the characteristic length with thickness.

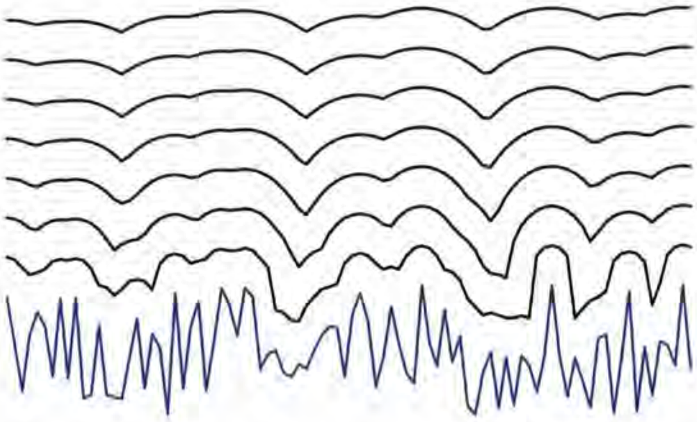

Figure 2-18: Example of Huygens type growth from a random initial surface

$$\xi(t) \propto t^{p} \tag{2-60}$$

For a correlated and self-similar starting surface (see section 2.5.6) they predict a scaling exponent of between 0.44 and 0.9 depending on the degree of correlation initially present. Furthermore, for self-similar surfaces they show, in agreement with other authors, that the scaling exponent relates to the fractal parameter by:

$$p = \frac{1}{2-h} \tag{2-61}$$

2.7 Magnetic tunnel junctions

A Magnetic Tunnel Junction (MTJ) is a device which exhibits a change in resistance depending on the direction of an external magnetic field. Integral to their operation is the interaction of the intrinsic spin of the electron with a magnetic field causing a change in the energy levels and a very thin insulating barrier across which electrons can tunnel. They are found primarily as sensors in magnetic storage media, such as hard disk drives, but they can also be information storage elements in their own right [20,21] and have already been incorporated into commercially available MRAM since July 2006 by Freescale Semiconductor Inc [22].

2.7.1 Structure and operation

Structurally, MTJs are formed from very thin layers of metals and metal oxides and are a development of the spin-valve [23]. MTJs include a very thin (typically 18Å) tunnelling barrier between two ferromagnetic electrodes through which the electrons tunnel. This has the advantage that it increases the resistance of the device, and reduces the coupling of the two electrodes. To measure the direction of the external field the magnetisation direction of one of the electrodes is pinned so that it is unable to move and forms a fixed reference. The other electrode is free to rotate to align with the external field. This arrangement is shown diagrammatically in Figure 2-19 below.

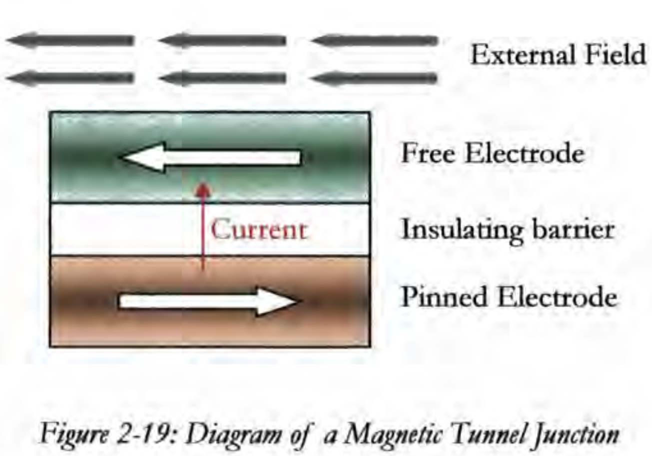

Figure 2-19: Diagram of a Magnetic Tunnel Junction

The electron spins are polarised when passing through the magnetised electrodes in the device into either spin-up or spin-down states, leading to two distinct conduction channels [24]. Whether the spin-up channel or the spin-down channel contains more electrons depends on the magnetisation direction of the first electrode the electrons encounter. The electrons then tunnel through the barrier and reach the other electrode. Ignoring any spinflip events occurring in the barrier, the electrons can only tunnel into an empty state of the same spin. The direction of the magnetisation of the second electrode determines which conduction channel will have more available states. If that matches the polarisation from the 1st electrode the device will be in a low resistance state, and if it opposes then the device will exhibit a larger resistance. This is illustrated in Figure 2-20 below. The spin dependent scattering is proportional to the density of states at the Fermi level and so different materials will exhibit different rates of spin dependent scattering. The resistance of the device falls as the temperature increases because more states are made available.

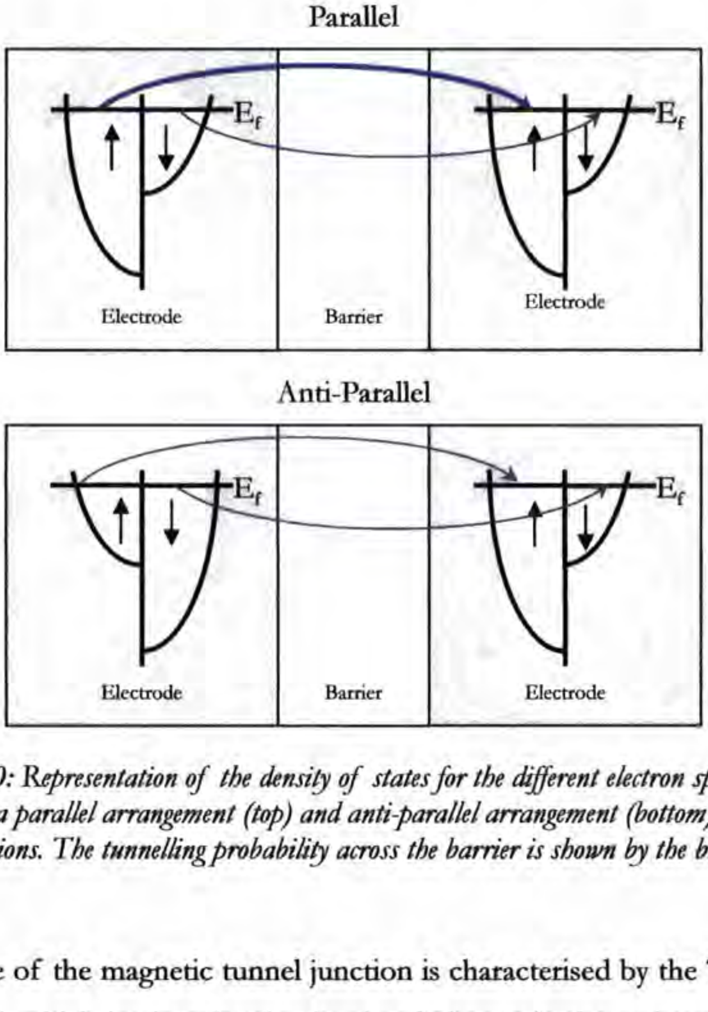

Figure 2-20: Representation of the density of states for the different electron spin channels in the MTJ for a parallel arrangement (top) and anti-parallel arrangement (bottom) of the electrode magnetisations. The tunnelling probability across the barrier is shown by the blue arrows.

The performance of the magnetic tunnel junction is characterised by the Tunnel Magneto-Resistance (TMR) which is given by the fractional change in the resistance when moving from a state where the electrode magnetisation is aligned parallel, $R_{\uparrow\uparrow}$, to an anti-parallel alignment, $R_{\uparrow\downarrow}$:

$$TMR = \frac{R_{\uparrow\downarrow} - R_{\uparrow\uparrow}}{R_{\uparrow\downarrow}} \tag{2-62}$$

Initially the TMR effect was only seen at very low temperatures, and was restricted to a few percent. Later, through improved growth methods, MTJs were observed to exhibit TMR at room temperature [25].

2.7.2 Pinning the reference electrode

The magnetisation direction of the pinned ferromagnetic layer in the structure is kept in place by the antiferromagnetic layer immediately below it in the structure shown in Figure 2-19 above. This exchange anisotropy, or exchange bias, was first identified by Meiklejohn in 1956 [26]. A thorough review of exchange bias is available in reference [27]. In 2000 it was reported by Nolting that the exchange coupling of individual domains between an antiferromagnetic material $LaFeO_3$ and ferromagnetic Co had been directly observed with polarization-dependent X-ray magnetic dichroism spectro-microscopy, which, by tuning to either the Co or Fe edge, is able to observe the magnetisation of either layer [28]. The exchange biasing was clearly observed.

2.7.3 Models of MTJs

Several models exist to describe the variations in TMR observed in MTJs. Julliere's model describes the TMR as a function of the polarisation of the electrons in both the spin channels [29].

$$TMR = \frac{2P_1P_2}{(1-P_1P_2)} \qquad \text{(2-63)}$$

Where P_1 and P_2 are the polarisations in the two electrodes given by $(n_\uparrow - n_\downarrow)/(n_\uparrow + n_\downarrow)$ where $n_\uparrow$ and $n_\downarrow$ are the number of electrons in the different spin states. Simmons' model [30] describes the operation of the MTJ from a current-voltage perspective and looks at the tunnelling probability as a function of both the potential barrier of the oxide as a certain height and thickness, and also the energy of the electrons. Eventually the current density as a function of applied voltage is given by the expression:

$$J = J_0\left[\bar{\psi}e^{-A\sqrt{\bar{\psi}}} - (\bar{\psi} + eV)e^{-A\sqrt{\bar{\psi}+eV}}\right] \qquad \text{(2-64)}$$

Where J is the current density, A is the width of the barrier region, $\bar{\psi}$ is the mean height of the barrier above the Fermi level, and eV is the difference in height of the Fermi levels between the two electrodes. Quantum mechanically, the tunnelling probability between the two electrodes depends on the number of tunnel electrons and the number of final states available into which the electrons may tunnel. This density of states is split into the spin-up and spin-down components.

2.7.4 Considerations for practical devices

As the thickness of the tunnel barrier reduces, the phenomena at the interfaces become more significant [31]. Thin barriers may also lead to MTJs that are more likely to form a conductive short, or pinhole, between the two electrodes [32]. The patterned size of the MTJ device also has important considerations for the external stray magnetic fields from the electrodes causing coupling. As the MTJs get smaller this becomes more significant [33].

Where the interface is non-ideal and roughness is included in the models, then certain considerations need to be taken into account. There will be scattering at the interfaces, caused by surface states and modification to the energy levels at the interfaces. As Tsymbal observed, "Spin polarisation is primarily determined by the electric and atomic structures of the interfaces, rather that the bulk properties" [34]. Where the roughness over the insulator is conformal then Néel "orange-peel" coupling, where uncompensated poles near the interfaces couple [33,35,36], can become important. This provides a mechanism by which there is an energy advantage in the magnetisation of the two electrodes aligning, making switching of the free electrode more difficult. It is illustrated in Figure 2-21 below.

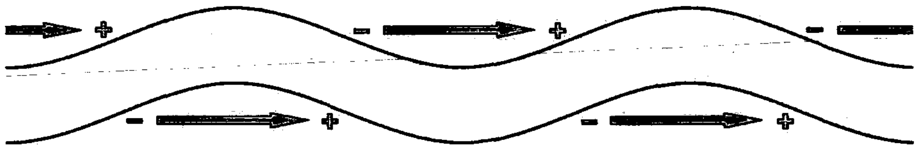

Figure 2-21: Conformal roughness across the barrier leads to so called orange-peel coupling of the electrodes through the barrier. The magnetic poles involved are shown by the + and – symbols on the figure.

The interfaces between layers are fundamental to the successful operation of a magnetic tunnel junction. As shown above, the interface nature, and replication of interfaces between layers, is determined during the growth. X-ray scattering is an ideal tool for examining these interfaces to measure the layer structure and interface properties.

References for Chapter 2:

[1] Röntgen, W. C., Nature, **53** (1896) 274

[2] Friedrich, W., *et al.*, Proceedings of the Bavarian Academy of Sciences, (1912) 303

[3] Laue, M., Proceedings of the Bavarian Academy of Sciences, (1912) 363

[4] Bragg, W. L., "X-rays and Crystal Structure", 1st Edition (1915), G. Bell and Sons, London

[5] Als-Nielsen, J., "Elements of Modern X-Ray Physics", Reprint March 2004, John Wiley & Sons, Chichester.

[6] Parratt, L. G., Phys. Rev., **95** (1954) 359

[7] Yoneda, Y., Phys. Rev., **131** (1963) 2010

[8] Kortright, J. B., J. Appl. Phys., **3620** (1991) 3620

[9] Kortright, J. B., J. Appl. Phys., **61** (1987) 1130

[10] Sinha, S. K., *et al.*, Phys. Rev. B., **38** (1988) 2297

[11] Sinha, S. K., J. Phys. III France, **4** (1994) 1543

[12] Savage, D. E., *et al.*, J. Appl. Phys., **69** (1991) 1411

[13] Holý, V., *et al.*, Phys. Rev. B., **49** (1994) 10668

[14] Wormington, M., *et al.*, Phil. Mag. Lett., **74** (1996) 211

[15] Wasa, K., "Handbook of sputter deposition technology", Noyes Publications, Reprint Edition (1992), Westwood, New Jersey,

[16] Barabási, A.-L., *et al.*, "Fractal concepts in surface growth", Cambridge University Press, 1st Edition (1995) , Cambridge

[17] Edwards, S. F., *et al.*, Proc. R. Soc. London A, **381** (1982) 17

[18] Kardar, M., *et al.*, Phys. Rev. Lett., **56** (1986) 2087

[19] Tang, C. S., *et al.*, Phys. Rev. Lett., **64** (1990) 772

[20] Parkin, S. S. P., *et al.*, J. App. Phys., **85** (1999) 5828

[21] Gallagher, W. J., *et al.*, IBM J. Res. & Dev., **50** (2006) 5

[22] Freescale Semiconductor Inc., 6501 William Cannon Drive West, Austin, Texas 78735. USA.

[23] Dieny, B., *et al.*, Phys. Rev. B., **43** (1991) 1297

[24] Stearns, M. B., J. Magn. Magn. Mat., **5** (1977) 167

[25] Moodera, J. S., *et al.*, Phys. Rev. Lett., **74** (1995) 3273

[26] Meiklejohn, W. H., *et al.*, Phys. Rev., **102** (1956) 1413

[27] Nogués, J., *et al.*, J. Magn. Magn. Mat., **192** (1999) 203

[28] Nolting, F., *et al.*, Nature, **405** (2000) 767

[29] Julliere, M., Phys. Lett., **54A** (1975) 225

[30] Simmons, J.G., J. Appl. Phys., **34** (1963) 1793

[31] Dimopoulos, T., *et al.*, J. App. Phys., **89** (2001) 7371

[32] Schrag, B. D., *et al.*, App. Phys. Lett., **84** (2004) 2937

[33] Schrag, B. D., *et al.*, App. Phys. Lett., **77** (2000) 2373

[34] Tsymbal, J. App. Phys., **97** (2005) 10C910

[35] Egelhoff, W. F., *et al.*, App. Phys. Lett., **88** (2006) 162508

[36] Kools, J. C. S., *et al.*, J. App. Phys., **85** (1999) 4466

3 Experimental Details

The experimental work included within this thesis was conducted at both the European Synchrotron Radiation Facility (ESRF) in Grenoble, France, and also at the UK Synchrotron Radiation Source (SRS) at Daresbury in Cheshire. In this chapter the beam-lines at these synchrotrons are described, and the important instrumental considerations for the results in the latter chapters discussed.

3.1 X-ray generation

The earliest x-rays investigated by Röntgen came from the wall of a vacuum discharge tube when cathode rays struck the glass sides. The x-rays are produced by two mechanisms. Firstly, as the incident electrons approach the nuclei in the target they are deflected and radiate energy in the form of x-rays. This Bremsstrahlung forms a continuous spectrum of energies. Secondly, large spikes occur in the emission spectrum when the incoming electron (cathode ray) removes an inner electron from the atoms of the target material. As the other electrons cascade down to fill the hole and reduce the energy of the atom and they emit radiation characteristic of the quantum-mechanical transition they have made. The nomenclature given to the characteristic x-rays from a target refer to the quantum electron shell to which the cascading electrons fall. Transitions to n=1, the innermost electrons in the atom, correspond to K radiation. Most laboratory based x-ray sources still use this same principle of an evacuated x-ray tube and a metallic target.

At national and international central facilities, large synchrotron radiation sources are available, where electrons are accelerated around an evacuated ring by large magnets. As the direction of the electrons is altered so they emit synchrotron radiation, which for the correct electron energy and ring radius, is in the form of x-rays and can be gathered and utilised by scientists around the ring. Experiments using synchrotron radiation began by utilising the synchrotron radiation emitted as a by-product of high-energy physics accelerators; however, the amount of useful synchrotron x-rays was severely limited. The first of the second generation of synchrotron sources, specifically designed for producing synchrotron radiation and incorporating a storage ring, was the SRS at Daresbury, Cheshire, UK, which opened for experiments in 1981. The third generation of machines began with the ESRF which was designed to maximise brightness and also to include straight sections in the ring for insertion devices, such as wigglers and undulators, producing even more intense x-rays and with a greater degree of coherence. The Daresbury SRS began a staggered shut-down in 2006 and the first experiments by the Durham group were conducted on the replacement UK synchrotron, the Diamond Light Source, in 2007.

3.2 X-ray detectors

Originally scientists were restricted to fluorescent screens and photographic films and emulsions for recording x-rays. These had many drawbacks from cost, to developing time, to being easily saturated and difficult to record an accurate intensity. Later gas or proportional detectors were introduced which measure the ionisation of a gas by measuring a current flow. The most common detector of today is a scintillation counter where the scintillator produces a flash of light for every x-ray photon it receives. These are then amplified and counted to measure the intensity. Solid State detectors are also common and involve an incident x-ray producing a characteristic number of electron-hole pairs, depending on the energy of the x-ray, in a doped semiconductor. The pulse height produced after a photon is recorded is then measured and counted in a multi-channel analyser so that a spectrum of the incident photon energies can be produced. CCD cameras have more recently become more common and have the advantage of being comprised of a two dimensional array of elements for recording scatter, both in the scattering plane, defined by the specular reflection, and also the out of-plane scatter.

3.3 Synchrotron beamlines

The beamline on a synchrotron where the experiments are conducted is illustrated below in Figure 3-1 for the case of x-ray reflectivity. Bending magnets within the synchrotron ring emit a cone of radiation tangentially to the electron path with a broad range of energies. This then passes through a shutter assembly which can be closed to prevent radiation from entering the experimental area. From the range of energies a narrow band is usually selected for the particular experiment by using a monochromator. Often a specially cut crystal is used, which, depending on the angle, allows only a narrow band of energies to pass. This is achieved by using the angular dependence of a diffraction peak with energy to first spread out the synchrotron beam into a spectrum and then select a particular energy with slits. The size and energy resolution of the incident beam on the sample is thus defined by the set of slits after the beam exits the monochromator, and the divergence and energy selection of the beam passed through the monochromator. Other beam optics can be introduced, such as focussing mirrors or phase plates, to further condition the beam that hits the sample.

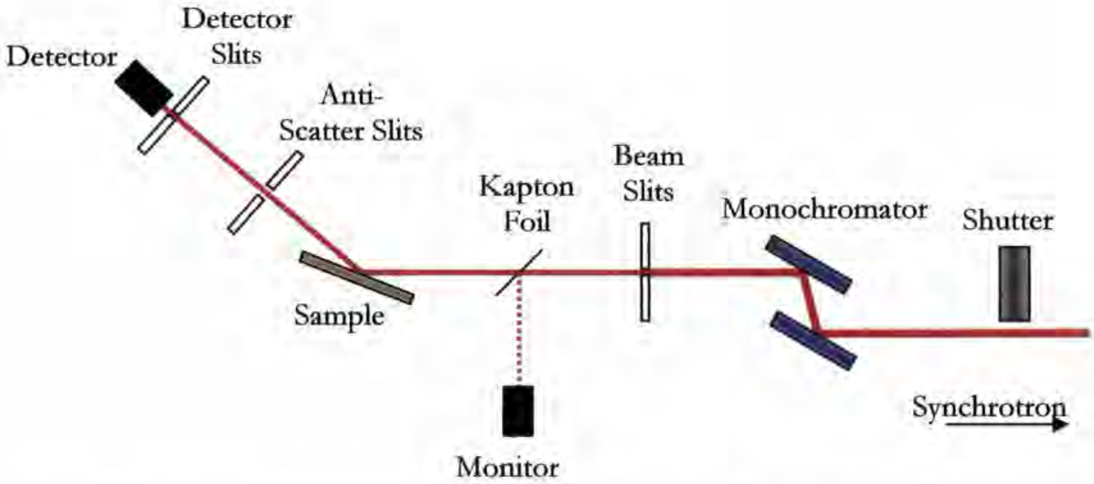

Figure 3-1 Diagram of an x-ray reflectivity synchrotron beamline, based on Daresbury station 2.3

The electron current in the synchrotron ring decays after injection with time leading to a reduction in x-ray intensity at the sample. A monitor is used to measure the incident intensity on the sample so that any variation in the intensity can be removed from the data. This can either be an ion chamber, or a kapton foil is used to partially scatter photons out of the beam to a monitor detector. After the beam hits the sample and is scattered the x-rays are measured by the detector. In the case of a reflectivity measurement a set of slits is placed next to the detector to define the resolution, or angular acceptance, of the detector, and front anti-scatter slits are used to reduce the background noise.

The specular scatter is the mirror reflection of the incident beam, and if the detector slits are larger than the beam dimensions then the whole specular reflection can be recorded. If the detector slits are widened further, more of the diffuse scatter at the specular point is measured. However, for smooth samples this is usually orders of magnitude lower than the specular. Widening the slits has the advantage that where there are slight imperfections in the initial alignment of the equipment it is harder to fall off the specular ridge during a specular scan. When it comes to recording the off-specular scatter, however, the effect of larger detector slits is that the scatter in larger area of reciprocal space is collected at the same time, reducing the resolution of the measurement of features in the diffuse scatter.

The choice of beam slits determines both the total intensity of the incident beam the beam footprint at low angles, which is an important consideration when fitting the scatter.

3.4 Instrument alignment errors

Aligning the beamline accurately is crucial for making accurate measurements. Ideally, in a reflectivity experiment the sample is infinite in size and the centre of rotation of the sample and detector rotation axes lie in the centre of the incident beam. Experimentally, once the diffractometer is aligned on the centre of rotation, each new sample will need adjustment to put its top surface at the correct point in the beam to take into account different sample and substrate thicknesses. In addition to effects caused by the finite size of a sample and the varying size of the beam footprint at different angles, any errors in the alignment of the diffractometer, and sample, in the beam can affect the measured scattered intensity. Although alignment errors should be minimised by setting up the experiment carefully, with some of the equipment used in this work thermally induced height misalignments were difficult to eradicate and so consideration must be paid to the effect on the scatter.

3.4.1 Changes in the scattering centre

If the sample's top surface is not placed at the centre of rotation, when the sample is rotated the centre of the sample will trace out a circular path around the centre of rotation. This causes both the beam to move along the surface of the sample, so a different part of the sample is probed at different angles, which may cause variations if the sample is inhomogeneous laterally or slightly curved. These are considered in more detail in Appendix A. However, at small angles the errors induced are relatively small.

3.4.2 Footprint effects

The greatest changes in the intensity occur from beam footprint effects. At very low angles the footprint is largest and a significant fraction of the incident radiation can miss the sample. A height alignment error will affect the vertical positions of the extremes of the sample and thus the part of the beam intersected by the sample and the effective incident intensity.

The heights relative to the centre-of-rotation of the edges of a sample of length l, offset from the centre-of-rotation by a displacement s and at a sample angle θ, are given by (see Appendix A for more details);

$$height_{\text{far edge}} = \frac{l}{2}\sin\theta + s\cos\theta \tag{3-1}$$

$$height_{\text{near edge}} = -\frac{l}{2}\sin\theta + s\cos\theta$$

The intensity hitting the sample is then found by integrating the beam intensity profile between these two points. Assuming a beam profile of a Gaussian line shape with a normalised area of 1, of standard deviation 0.2mm, chopped by slits at ±0.1mm, that passes through the centre of rotation, and a sample 10mm in length which is offset from the centre of rotation, the profiles shown in Figure 3-2 below for the intensity impinging on the sample surface are obtained:

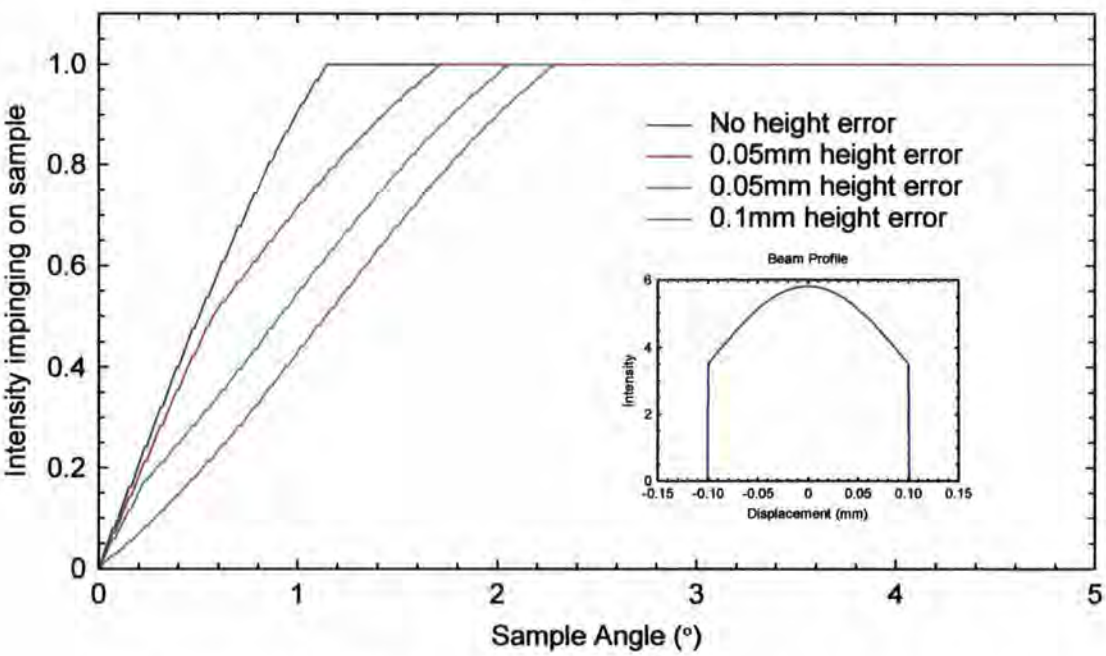

Figure 3-2 Simulated change in the incident intensity impinging on the top sample surface for different misalignments of a 10mm sample from the centre of a 0.2mm beam.

The effect of one edge of the sample moving out of the beam before the other can be clearly seen on the curve for 0.05mm error, where there is a noticeable change in gradient at around 0.5°. These intensity adjustments are applied to specular and transverse diffuse profiles below in Figure 3-3 and Figure 3-4.

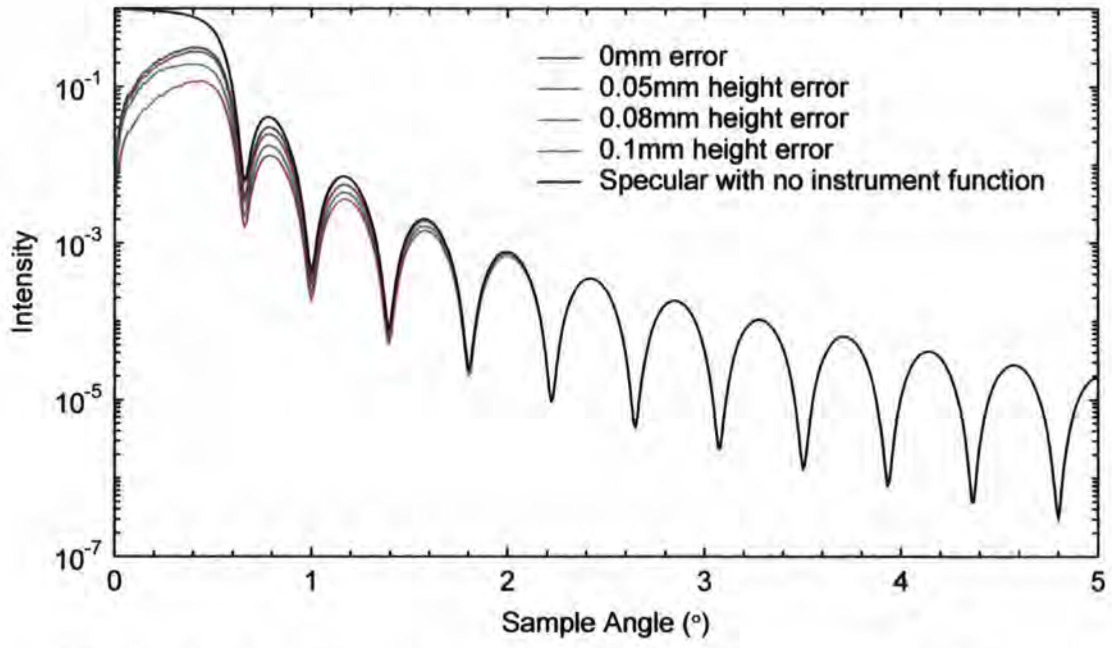

Figure 3-3: Simulated reflectivity profiles for the different footprint functions in Figure 3-2above. Note at high angles there are no differences

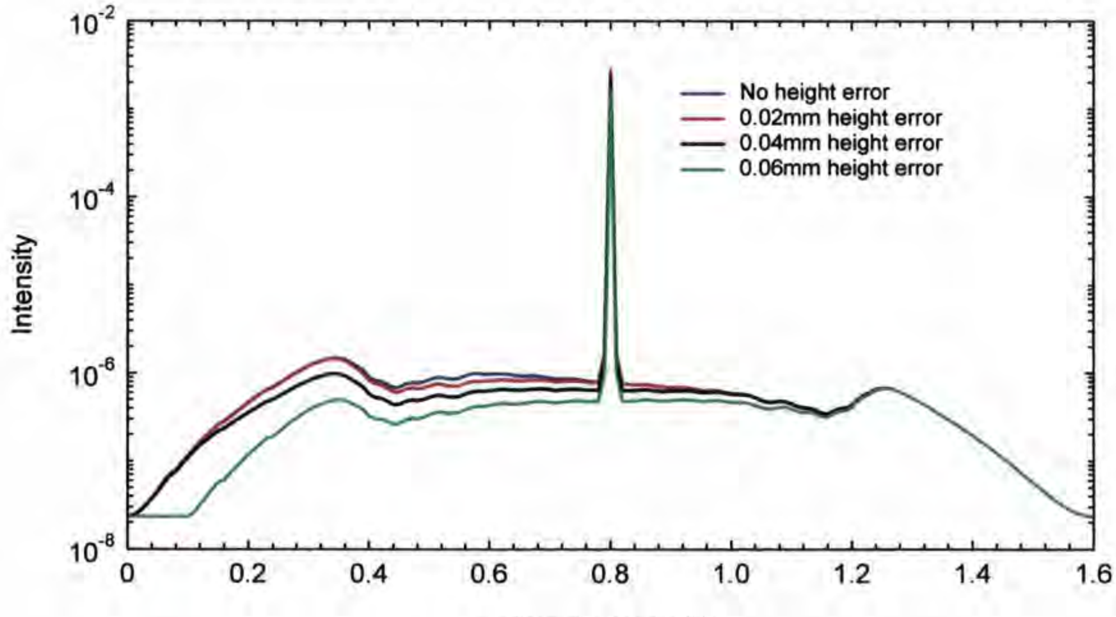

Figure 3-4: Simulated transverse diffuse scatter with different height misalignments.

The effect of the beam footprint is predominantly at low angles, as above a certain angle all the beam usually impinges on the sample. If the modified scatter is fitted without taking into account the height misalignment then the sample structure deduced will appear smoother on account of the reduced fall in intensity with increasing scattering angle.

3.5 Daresbury Station 2.3

Station 2.3, now closed, at the UK Synchrotron Radiation Source (SRS), based in Daresbury, Cheshire, was positioned 12m from a 1.2T bending magnet. It received x-rays in the range 0.7Å to 3Å radiation and was monochromated by a water-regulated channel cut Si(111) monochromator which was kept at a constant 30°C. Detection was done with a Bede EDRa detector [1]. To prevent the detector saturating at high incident intensities an attenuator disk was mounted on the detector arm which could be rotated to select different thicknesses of attenuation. Between the detector and anti-scatter slits there was an evacuated tube to reduce air absorption. This detector arm assembly is shown in Figure 3-5 below. Further details on the diffractometer can be found in reference [2].

Figure 3-5: SRS Station 2.3 detector arm assembly showing the anti scatter slits, attenuator, evacuated beam path, detector slits and detector.

An RF induction furnace [3,4] could be mounted on the diffractometer, see Figure 3-6 below. It contained a coil to generate an RF field which coupled with a tungsten crucible inside causing heating, and is shown in Figure 3-7 below. It was powered by a 1kW supply unit and was capable of reaching temperatures of up to 1,500K. The temperature of the crucible was measured by placing a thermocouple in a purpose drilled hole on its top surface. The power supplied to the coils was controlled by a Eurotherm 900 unit which was linked to a computer so it could be operated remotely. The surfaces were cooled by circulating water inside the body. The chamber of the furnace could either be evacuated to a pressure of 10^{-3}mbar, or connected to an external gas supply to create, for example, a nitrogen or argon atmospheres Kapton windows in the side of the furnace allowed the x-rays to enter and exit the sample environment.

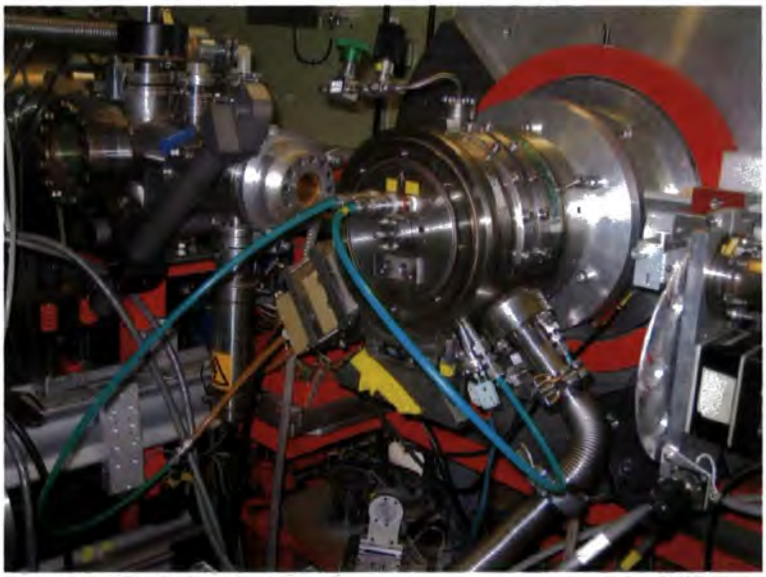

Figure 3-6: The RF induction vacuum furnace mounted on the diffractometer at the Daresbury SRS station 2.3.

Figure 3-7: The furnace chamber with sample mounted in the centre. The RF induction coils are clearly visible around the sample stage and column.

The crucible was designed for powder diffraction work and so contained a crucible to hold a powdered sample. This had to be modified for it to be suitable for reflectivity measurements by making a copper disk that sat inside the crucible to provide a flat sample stage. This is illustrated in Figure 3-8 below.

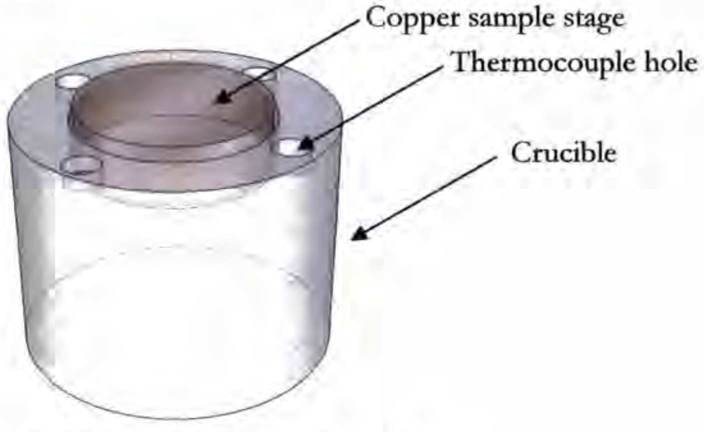

Figure 3-8: Diagram of the sample stage design

Although temperature control was managed through a computer, it was not linked in with the Daresbury Pincer control software, so it is was not possible to write an automated macro to change temperatures. Height adjustment was also performed by manually turning a screw tread on the sample stage shaft. This adjusted the sample stage height but also rotated the sample. It was very time consuming aligning samples with such equipment.

3.6 ESRF Beamline BM28 (XMaS)

The XMaS beamline (BM28) is a UK funded CRG based on a bending magnet at the European Synchrotron Radiation Facility (ESRF), in Grenoble, France. It is specially designed for high-resolution and magnetic single crystal diffraction, although it is ideally suited to reflectivity work as well, and with its excellent monochromation and energy selection it is capable of variable energy work in the range 3keV to 15keV. A detailed description of the development of the instrument is given in references [5-7].

The diffractometer is an 11-axis Huber instrument and is shown in Figure 3-9 below. Intensity measurements in one dimension were made using a CyberStar scintillation detector. For two dimensional work a cooled MAR CCD camera with a circular array of pixels of diameter 2048 pixels was used. Exposure times are relatively short, allowing a large amount of scatter to be recorded in a very short time. The incident spot size of the beam was 0.2mm square and an energy of 10keV was used. At a distance of 90cm the angular size of each pixel is ~0.005° or 18". The MAR CCD camera mounted on the diffractometer is also shown in Figure 3-9 below. A thermal sample stage can be fitted on the diffractometer, shown in Figure 3-10 below, which can be surrounded by a beryllium shroud to prove a space which can be connected to vacuum pump and evacuated.

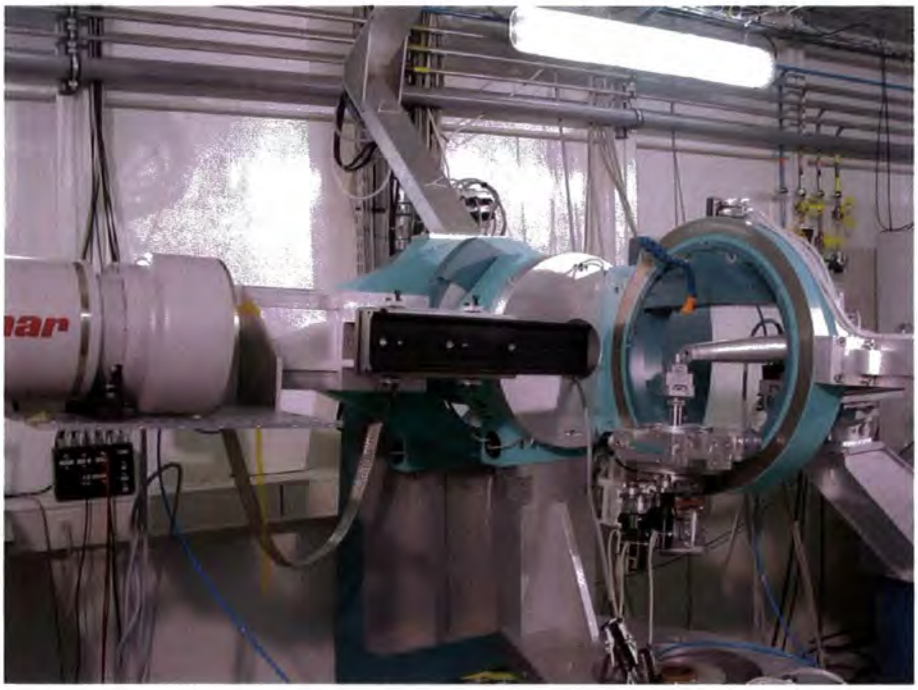

Figure 3-9: The Huber Diffractometer on the XMaS Beamline

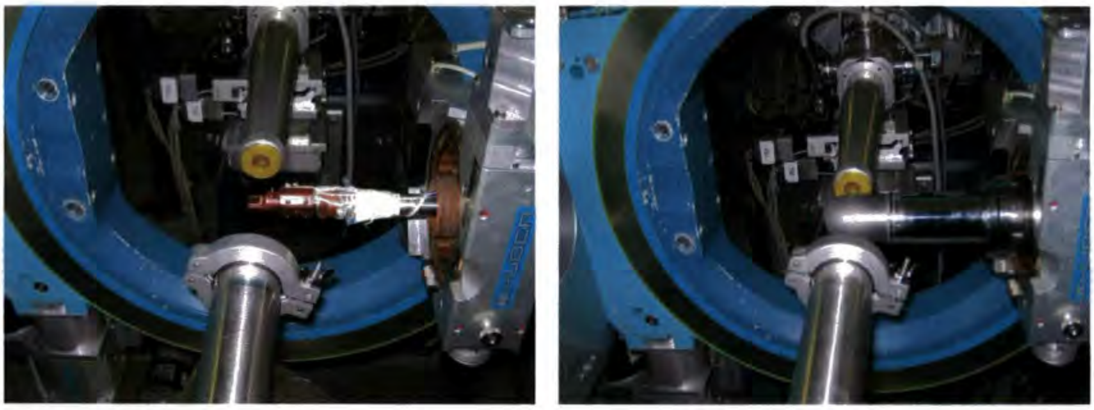

Figure 3-10 The cryofurnace sample stage without the beryllium shroud (left) showing the sample mounted at the centre, and sealed up (right).

3.7 Computer Software

3.7.1 Bede REFS

The commercially available Bede REFS software was used to simulate the reflectivity scatter from samples. This uses the recursive theory of Parratt to simulate specular reflectivity and the Distorted Wave Born Approximation (DWBA) for simulation of the diffuse scatter. Refinement of the sample structure from the specular reflectivity profile is achieved by use of genetic algorithms, in particular Differential Evolution, the details of which can be found in [8].

References for Chapter 3:

[1] Cockerton, S. and Tanner, B.K., Advances in X-ray Analysis., **38** (1995) 371

[2] Tang, C. C., *et al.*, Rev. Sci. Inst., **69** (1998) 1224

[3] Tang, C. C., *et al.*, J. Synchrotron Rad., **5** (1998) 929

[4] Tang, C. C., *et al.*, Advances in X-ray analysis, **40** (1997) 656

[5] Paul., D. F., *et al.*, Rev. Sci. Inst., **66** (1995) 1741

[6] Brown, S. D., *et al.*, Nucl. Inst. and Methods in Phys. Res. A, **467-468** (2001) 727

[7] Brown, S. D., *et al.*, J. Synchrotron Rad., **8** (2001) 1172

[8] Wormington, M., *et al.*, Phil. Trans. R. Soc. Lond. A, **358** (1999) 2827

4 Evolution of interfaces in repeated bi-layer structures of Co/Pd and Co/Ru

This chapter looks at the interfaces that cobalt forms with palladium and ruthenium. The way in which the interfaces change as successive layers are deposited is investigated by a detailed analysis of the diffuse x-ray scatter at grazing incidence, recorded by a CCD detector. In particular the behaviour of the roughness at different spatial frequencies is investigated.

4.1 Introduction

The performance of a range of thin film devices, ranging from those exhibiting perpendicular magnetic anisotropy (PMA) to spin-valves and magnetic tunnel junctions (MTJs), is known to be strongly influenced by the nature of the interfaces buried below the top surface [1, 2]. The influence of the interface characteristics can affect the coupling between magnetic layers [3], or affect the current flowing through the layers as electrons are scattered by the interfaces [4]. Obtaining the right interfacial qualities is an important consideration in both the design and growth of the devices.

The nature of the interface originates from the kinetics of the deposition process during the deposition of the layers, although it may subsequently be changed by post-deposition processes such as ion-bombardment or thermal annealing. Sample growth involves many different physical processes, all of which combine to produce an interface. The commonly used technique of sputter deposition has been described in section 2.6.1. The main factors determining the nature of the interface are the surface kinetics of ad-atom mobility, which determines whether monolayers grow and smoothing occurs, or whether the atoms clump together forming islands, and also the propensity of the impinging atoms to be incorporated into the existing layer, which leads to interdiffusion [5]. The existing roughness on the surface, on which the atoms are incident, must also be taken into account. Shadowing is often encountered, and leads to columnar growth [6].

Once roughness is established it is often seen that it will propagate up from one layer to next as further layers are deposited and replicate the layer below. The dependence of layer-growth on the underlying layer is a fundamental consideration when designing devices. The roughness is not the only physical property of the under-layer that has an effect on the nature of the deposited layer. Matching of the crystalline lattice to minimise the energy associated with the interface can cause materials to grow in preferential orientations, which has an effect on the granularity of the layers. Similarly, growing a layer on an amorphous or nano-crystalline layer can influence the upper-layer.

The random factors of the deposition process arising from the variations in position, energy and direction of impinging atoms give rise to variations in the statistical nature of the surface. Describing the properties of the roughness has already been discussed in relation to correlation functions. In the case of the Sinha self-affine fractal model [7], two parameters are used to describe the interface nature: a characteristic length scale, and a fractal Hurst parameter (see section 2.5.7). These are in addition to the RMS roughness amplitude of the layer.

Diffuse x-ray scatter provides an excellent tool for probing the nature of the interfaces as it is generated by the imperfections from a perfectly smooth interface. Since Sinha's work in the late 1980s on single interfaces to first order within the DWBA [7], the modelling of interfaces has progressed to include partially correlated interfaces in multilayers [8-10], and more rigorous mathematical methods, such as de Boer's work including second order terms in the Distorted Wave Born Approximation [11]. However, the original Sinha model and self-affine correlation function remain in widespread use, and appears valid for most systems being investigated.

Most correlation functions use only a single characteristic length scale, but different spatial frequencies of the roughness can be correlated differently. This arises from factors in the growth mechanisms affecting the interface width at different length scales. Short wavelength roughness arises mostly from the random nature of the incident atoms whereas longer wavelength roughness arises from geometric considerations arising from the nature of the existing layer on which the material is being deposited [12]. A discussion on different growth models leading to scaling, that is power law behaviour, in various roughness parameters is given in reference [6].

The work of Salditt *et al.* in the mid 1990s showed that the variation in the diffuse scatter at different distances from the q_z specular scattering rod parallel to the surface is strongly dependent on the form of the correlation function [13]. However, interpretation of this scatter does not rely on choosing a particular correlation function, such as when modelling transverse diffuse scans. Instead, the scatter is directly related to the actual correlation of the roughness present in the sample, allowing it to be probed directly. In conventional q_z-q_x scatter this in-plane component is rapidly obscured by the critical angle which restricts the parts of reciprocal space available (see section 2.3), although this has been overcome in looking at some W/C multilayers, used as x-ray mirrors, which have a very high reflectivity out at higher angles [12]. By moving out of the specular scattering plane into q_y this restriction is relaxed and a larger region of reciprocal space is accessible, as discussed in section 2.3 and Figure 2-7 above. This scatter in q_y can be probed by using a conventional 1D detector. However, this is extremely cumbersome. Two-dimensional CCD detectors are ideally suited to these sorts of measurement and allow the diffuse scatter in the q_zq_y plane to be recorded quickly and easily.

The first high-resolution experiments on the diffuse scatter in the q_y direction from a multilayer were reported in 1996 by Salditt *et al.* on sputtered W/Si multilayers [14]. A thorough analysis of Fe/Au multilayers using diffuse x-ray scatter was performed by Paniago *et al.* in 1997 [15]. Away from continuous films the correlation of self-assembled gold nano-particles on a surface has also been investigated using a CCD detector [16]. Another study using a CCD camera is reported in reference [17] where a very large sample to detector distance of 12m was used to study very fine detail. In this chapter a series of repeated bi-layer structures of cobalt-palladium and cobalt-ruthenium, with a differing number of repeats, were used so that the surface at particular stages of growth was 'frozen' and preserved.

4.2 Background theory: scaling behaviour in diffuse scatter

4.2.1 Origin of scaling in surfaces

A simple ballistic deposition model of surface growth will naturally lead to scaling or power-law behaviour [18]. Starting from an perfect surface initially there will be roughening, following a scaling law; the so called dynamic scaling exponent. Then after a time the roughness will saturate and a second static scaling regime will be reached. This process is described by the Family-Vicsek law [19], equation (4-1) below, which applies to any growth model where scaling is expected, such as the linear Edwards-Wilkinson model [20], the non-linear KPZ Model [21] and also the TAB [22] Huygens type growth model, all of which have been discussed previously in section 2.6.2.

$$\sigma(\mathrm{R},t) \sim \mathrm{R}^{\mathrm{h}} f\left(\frac{t}{R^{z}}\right) \tag{4-1}$$

Here *f* is a general function whose form is dependent on the model being used but it is a function of the growth time and separation of points. The height difference function for the self affine fractal model given in chapter 2 above, $\left\langle (z(\mathrm{R}') - z(\mathrm{R}))^2 \right\rangle = AR^{2b}$, equation (2-53), is a scaling equation in its own right with the average height-difference between two points scaling with 2h, where h is the fractal parameter of the surface. This fractal parameter is the same as the static scaling exponent in the Family-Vicsek law above.

4.2.2 Scaling in the Bragg sheet intensity

Bragg peaks arise from conformality in the interfaces. The intensity of a Bragg sheet moving out into q_y gives information on the propagation of spatial frequency components from one layer to the next. In particular it is related to the Fourier transform of the height-height correlation function [17]. Scatter at high q_y results from short length scale roughness between layers. This technique thus examines the in-plane correlations of the roughness as a function of the spatial frequency of the roughness.

Within the Distorted Wave Born approximation for the diffuse scatter a structure factor is introduced to incorporate the nature of the roughness within the differential cross-section for scattering (section 2.5.8). Writing this structure factor with the simplification of restricting it for the situation of momentum transfer parallel to the surface, gives [13]:

$$S(Q,q_z) = F(q_z)\xi^2 \int_0^\infty x\left(e^{-q_z^2\sigma^2 C(x/Q)} - 1\right) J_0(Q)\,dx \tag{4-2}$$

where J_0 is a Bessel function of the 1st kind, Q is rescaled reciprocal space scattering vector expressed it in terms of a correlation length $Q = q_{\|}\xi$, x is expressed in terms of Q and a characteristic length $\mathrm{R} = \mathrm{r}/\xi$, $x = QR$, and all the prefactors are contained together in:

$$F(q_z') = \frac{e^{\mathrm{Re}(q_z')^2 \sigma^2}}{\left|q_z'\right|^2} \tag{4-3}$$

The structure factor, S, which is essentially what is measured when the diffuse scatter is recorded, is proportional to the square of the in-plane correlation length, ξ, and the function F(q). From (4-3) it can be seen that q_z has to be kept small to obtain a high intensity.

There is no general solution to the integral in (4-2) above and Salditt *et al.* used numerical methods to study the function, with various different forms of the correlation function, C(r) [13]. A diagram of the structure factor as a function of Q, based on a figure in [13], is shown below in Figure 4-1, clearly demonstrating the scaling at high Q.

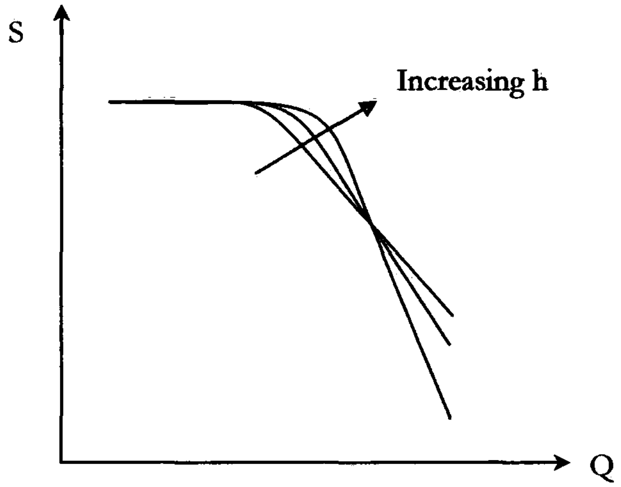

Figure 4-1: Structure factor in the limit of weak roughness for different values of h, the fractal parameter. After [13]

For Q values greater than 1 the structure factor shows scaling behaviour, ie $S(Q) \propto Q^{-\gamma}$, where Q >> 1 and the scaling parameter, γ, is a function of h, q_z and σ. There is no dependence at these higher q values on the in-plane correlation length. It was reported that only for a logarithmic correlation function, $c(r) = A - B \ln r$, does an analytical function for the scaling exponent, derived within the first Born approximation, exist [13] and it is given in equation (4-4) below.

$$\gamma = 2 + 2h - \left(|q_z|\sigma\right)^2 \qquad \text{(4-4)}$$

Saldit *et al.* state that their numerical simulations show that this form still holds in the Distorted Wave Born Approximation. Within the approximation of weak roughness,

$(|q_z|\sigma)^2 < 1$, the integral in equation (4-2) above can be replaced by the Fourier Transform of C(r). They showed that by using a Taylor expansion to 1st order the $(q_z\sigma)^2$ dependence vanished for all correlation functions, and in all cases:

$$\boxed{\gamma = 2 + 2h} \qquad \textbf{(4-5)}$$

Where the roughness is not weak the intensity profile measured will depend on the value of q_z chosen within the Brillouin zone. By integrating over the entire Brillouin zone both the coherent and incoherently contributions to the scattering are equally sampled [23] and any q_z dependence is negated (See section 2.4.3).

4.2.3 Scaling in the Bragg peak FWHM

The out-of plane correlation length of conformal roughness is inversely proportional to the full-width at half-maximum (FWHM) of the Bragg sheets in the q_z direction [24], and is given by the relation [15]:

$$\Delta q_z = \frac{2\pi}{\xi_\perp} \qquad \textbf{(4-6)}$$

The width varies with the $q_{parallel}$ vector as a result of different spatial frequencies of roughness being correlated differently. For example, short wavelength surface fluctuations typically propagate between layers in a multilayer less well compared to longer wavelength features. In another publication Salditt *et al.* examine the scaling in the FWHM, using it to find the dynamic growth exponent which relates the correlation length to the deposition time, or thickness, of a layer.[25].

4.3 Samples

4.3.1 Co/Pd repeated bi-layers

Cobalt palladium multilayers exhibit perpendicular magnetic anisotropy (PMA), where the easy magnetisation direction aligns along the surface normal when the cobalt layer is less than 8Å thick [26], and are interesting for the high-density magnetic recording industry because it enables the physical size of a 'bit' to be dramatically reduced. The effect of the interfaces on the PMA is identified in references [27] and [28].

The samples were grown by magnetron sputtering on single crystal (001) orientated silicon at the University of Leeds with nominal structure:

SiO_2 / Pd(30Å) / {Co(5Å) / Pd(30Å) $\}_{xN}$ where N=12, 20, 24, 26, 28, 30. The sputtering conditions were a base pressure of 3mTorr Ar and with 100mA and 33W on the Co target and 50mA and 17W on the Pd target. The x-ray penetration depth at the XMaS beamline, where measurements were made, was estimated within Bede REFS (see section 3.7.1) to be greater than 1500Å which is sufficient to penetrate the thickest sample.

The series used has already been extensively characterised by Amir Rozatian for the relationship between anisotropy and interface structure using scattering in the q_x-q_z plane [29][30]. Reference [31] gives details of the full characterisation from specular reflectivity of these samples. The thickness was found to be within a few Ångstroms of the nominal values and they show an average roughness of 5.25Å on both the cobalt and palladium layers.

4.3.2 Co/Ru repeated bi-layers

Cobalt and ruthenium layers display an oscillatory exchange coupling, where the cobalt layers couple antiferromagnetically. The coupling is dependent on the thickness of the ruthenium layer and oscillates with a period of around 10Å [32,33]. They also demonstrate PMA in a similar way to Co/Pd systems [1, 34]. These structures are currently of much interest for forming synthetic antiferromagnetic pinning layers within magnetic tunnel junctions [35] (see section 2.7 and later chapters).

Samples were grown by magnetron sputtering on single crystal (001) orientated silicon at the University of Leeds. The nominal structures were:

SiO_2 / Ru(11Å) / {Co(10Å) / Ru(11Å) $\}_{xN}$ where N=5, 15, 20, 60, 80. Unlike the CoPd series this sample set has not been characterised before.

4.4 Experimental details

Grazing incidence measurements were taken on beamline BM28 (XMaS) at the ESRF with a 10keV incident beam constrained to 0.2mm diameter both horizontally and vertically. Diffuse scatter was recorded using a cooled MAR CCD camera. The beamline has been discussed in detail in section 3.6 above.

4.4.1 Scattering geometry recorded using a CCD detector

The sample was inclined at a small angle to the incident beam and a CCD detector positioned to record the diffuse scatter from the sample at a similarly low detector angle, as illustrated in Figure 4-2 below.

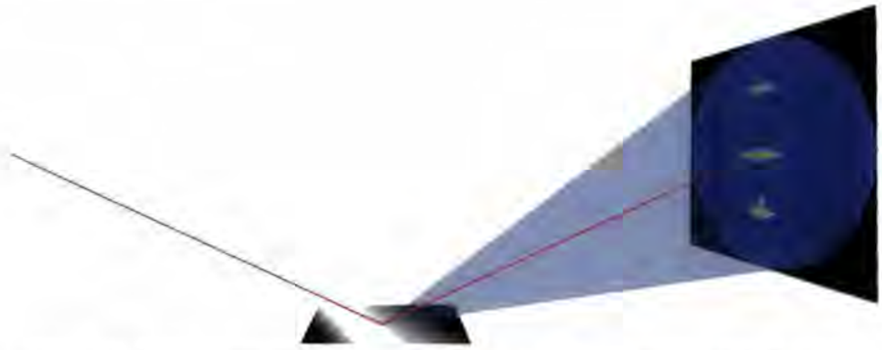

Figure 4-2: The geometry of recording the diffuse scatter using a CCD camera

The transformations of angles into reciprocal space has been given in section 2.3. In reciprocal space the CCD camera extends mainly in q_z and q_y. There is only a very small component in q_x which adds a slight curvature into the detector. The q_x value is very small and so the q_y value is effectively equal to $q_{||}$ and the scaling behaviour described in 4.2.2 above applies to the scatter measured as a function of q_y in this regime. The region of reciprocal space probed by a flat plate detector centred on the specular reflection of a 1.3Å incident beam meeting the sample at an angle of 1° has been calculated and is shown in Figure 4-3 below.

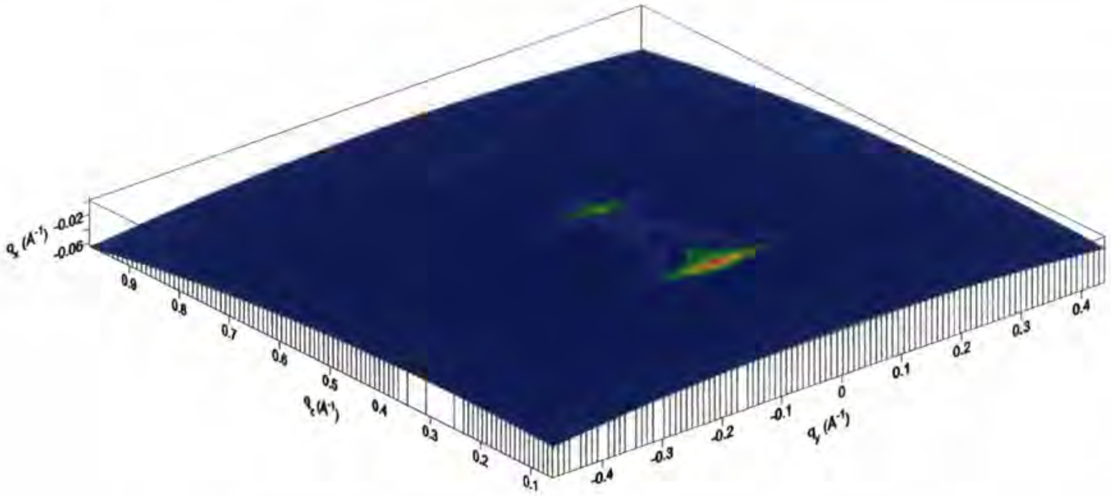

Figure 4-3: The curvature of the CCD image in reciprocal space (for 10keV radiation at a sample angle of 1°)

It should be noted that the quality of the images is sensitive to the quality of the incident beam which should be narrow in both directions and have a low divergence.

4.4.2 Features in the diffuse scatter

Typical diffuse scatter recorded by the MAR CCD camera is shown in Figure 4-4 below. Many of the features present in a q_z specular scan, such as a Bragg peak, Kiessig fringes and a Yoneda wing, are present, and exist entirely in the diffuse scatter. There is only one point of specular scatter in the image. These features, usually associated with the specular scatter from multilayers, only exist in the diffuse scatter if the roughness from one layer to the next shows a degree of conformality [12].

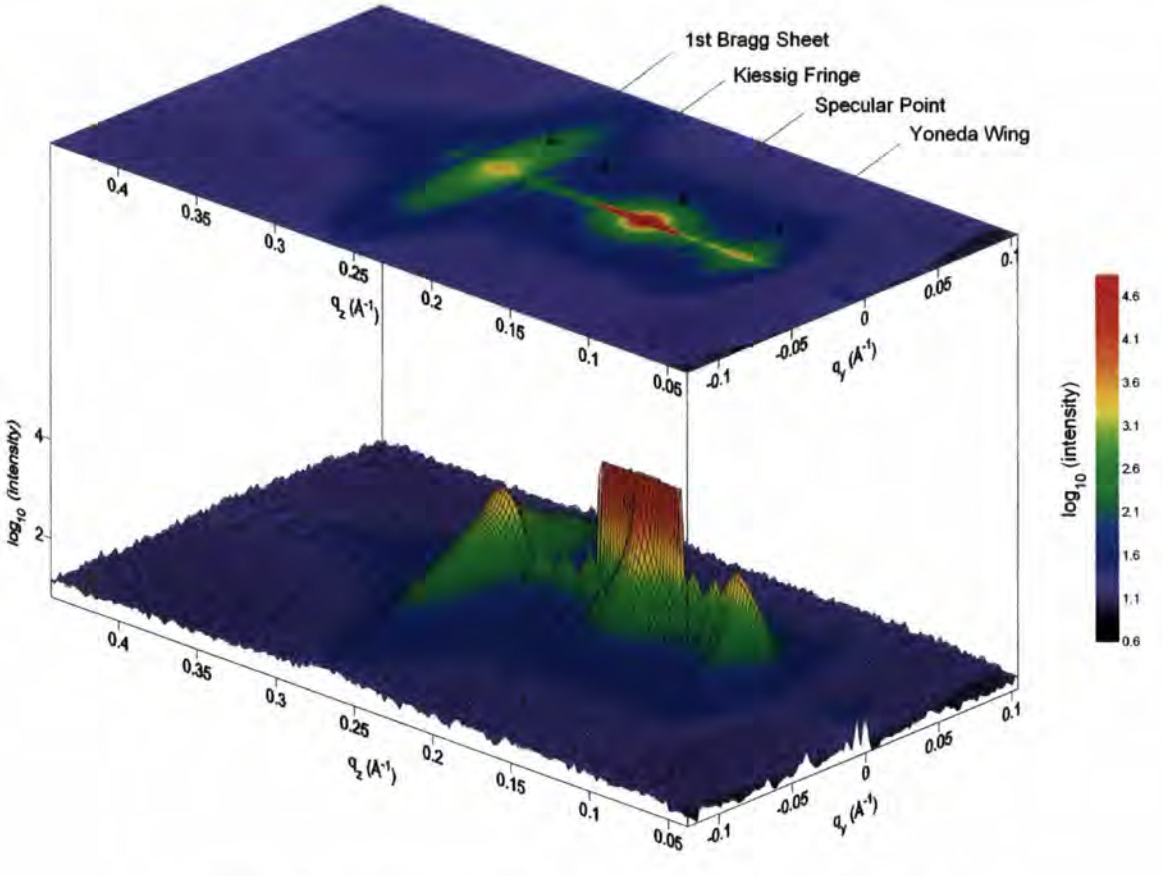

Figure 4-4: Diffuse scatter from a [Co/Ru]$_{x15}$ sample at sample angle of 1° and incident energy of 10keV

The Bragg sheets in the diffuse scatter form planes in reciprocal space above, and parallel to the sample surface. In this chapter the profile of these Bragg sheets, which gives information on the interfaces in the repeated structure, are examined closely. The spatial extent of these depends on the nature of the correlation of the roughness between interfaces. In particular the scaling or power law variation of both the intensity and the width in q_z as q_y is increased is examined.

The diffuse scatter is many orders of magnitude less than the specular scatter. To record the diffuse scatter it is necessary to count for longer periods to resolve the features. However, when using a CCD detector, the CCD array elements at the specular condition saturate because of the low dynamic range of each pixel. There is also a 'bleeding' effect where neighbouring elements also saturate, primarily in the vertical direction, obliterating the diffuse scatter at these points. Another associated instrument effect with the particular CCD camera on the XMaS beamline is that it is comprised of four separate arrays and a saturated pixel gets reflected weakly in all four quadrants in the array. These reflections are clearly visible and easy to exclude when interpreting the images recorded.

4.4.3 CCD image file analysis

The images from the CCD camera were first converted into a text file of a grid of 2048 x 2048 numbers representing the intensity at each camera pixel using the Fit2D software from the ESRF [36]. C++ code, included in Appendix B, was written to convert this grid of intensities into reciprocal space, using the transforms given earlier in equation (2-30). This same program then fitted cross sections of the Bragg sheets in q_z to a Pearson VII peak with a linear background. This peak profile, equation (4-7), can be used as an approximation to a Voigt profile and is much simpler to calculate as it does not contain any integrals.

$$f(x)=\frac{a_0}{\left[1+4\left(\frac{x-a_1}{a_2}\right)^2\left(\frac{1}{2^{a_3}}-1\right)\right]^{a_3}} \qquad (4\text{-}7)$$

where a_0 is the amplitude, a_1 is the peak centre, a_2 is the width and a_3 is the shape parameter. For a shape parameter of 1 the profile is Lorentzian and as the parameter increases the profile becomes progressively more Gaussian. The program gives a text output of the value of q_y where the cross-section has been measured, the four Pearson VII peak parameters, and details of the linear background. Example cross-sections and the respective fits though a Bragg sheet are shown in Figure 4-5 below.

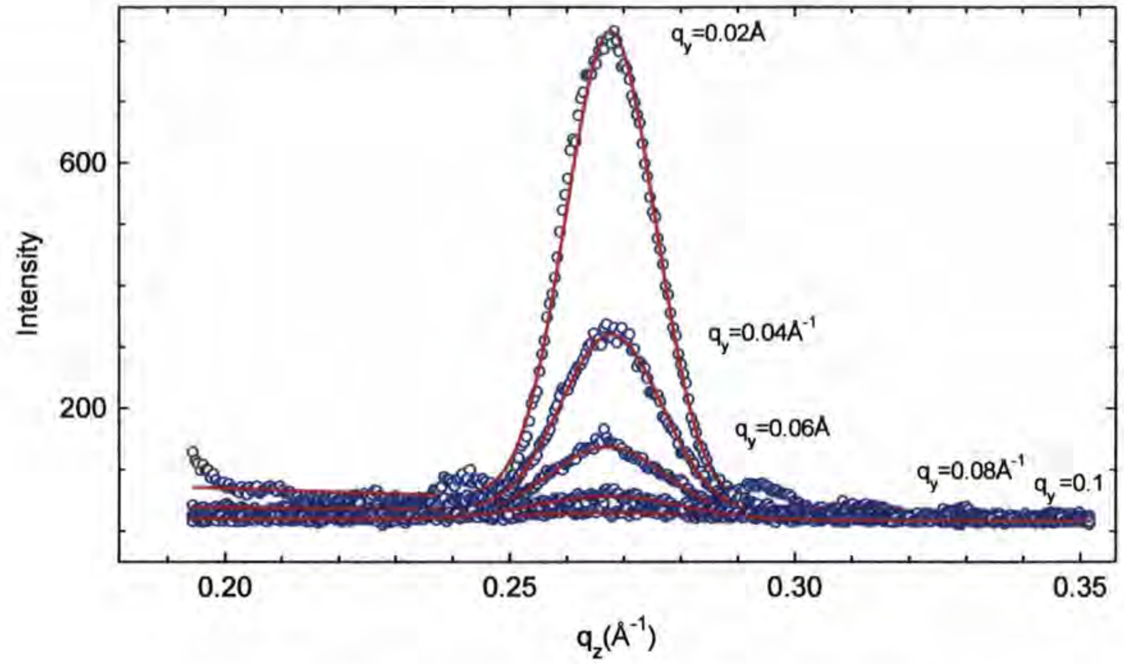

Figure 4-5: Example fits to cross sections through the 1^{st} *Bragg Sheet at different* q_y *values of a Co/Ru ×12 multilayer*

A typical Pearson VII with linear background fit to the measured scatter over the entire Bragg sheets is shown below in Figure 4-6. The linear background is sufficient to take into account the raised background from the Kiessig fringes at low q_z. A line is visible in the fit at q_z=0.43Å^{-1} which is where the two different linear backgrounds, from the two visible orders of Bragg sheet, meet at the Brillouin zone boundary.

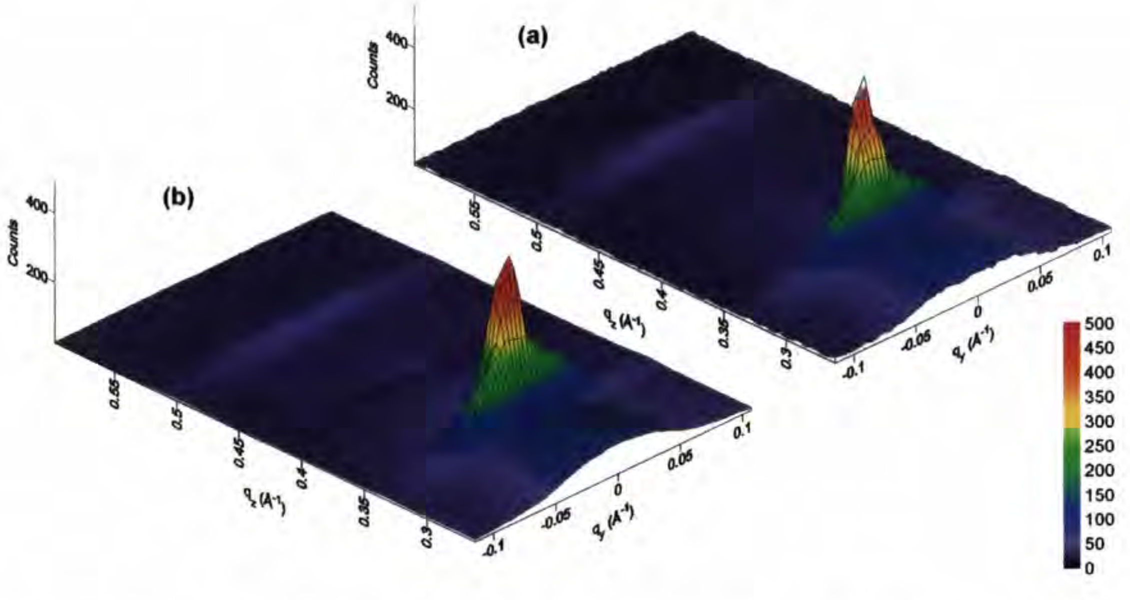

Figure 4-6: (a) measured intensity of the 2^{nd} and 3^{rd} Bragg sheets from the $[Co/Pd]_{\times 12}$ sample (b) fit to the measured data of a Pearson VII peak and linear background for each Brillouin zone separately.

Once the FWHM as a function of q_y is known, analysis of the scaling behaviour was performed in Excel spreadsheets, where Chi^2 minimisation was used to fit a power-law to the high q_z scatter, see Figure 4-7 below. Errors in the FWHM scaling were calculated from the estimated errors in the FWHM and using visual-basic macros in Excel to find the limits of the scaling parameters giving a minimised sum of Chi^2+1.

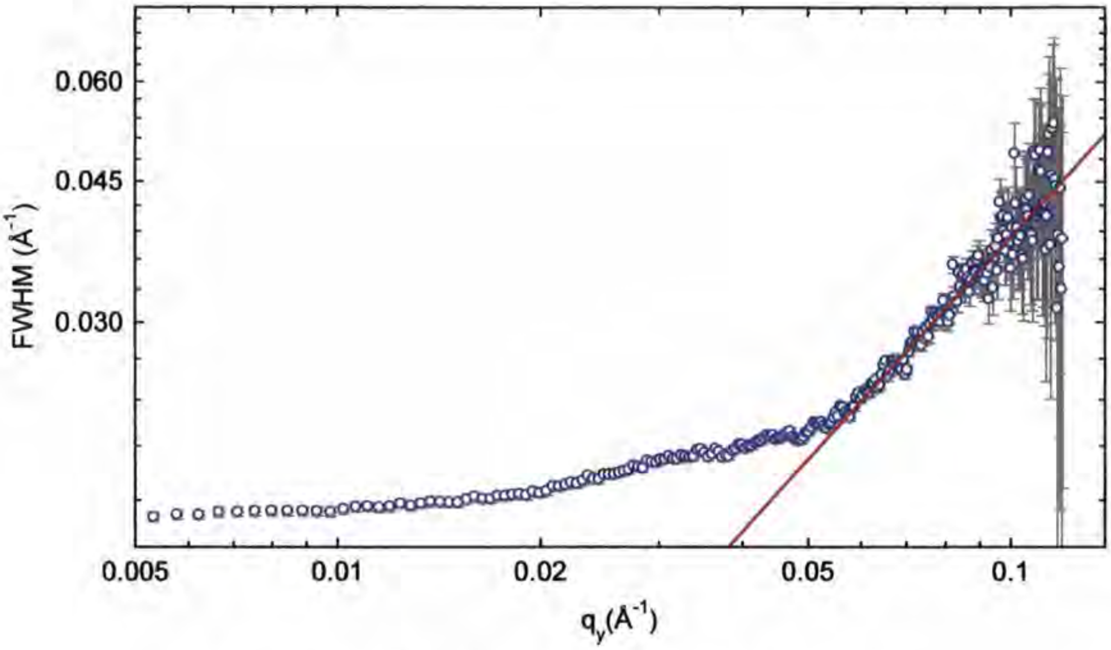

Figure 4-7: A log-log plot construction to find the FWHM scaling of the 1st Bragg Sheet from a Co/Ru x12 multilayer.

The scaling of the FWHM is independent of the incident angle, although the FWHM at a particular position in q_y decreases as the sample angle is increased. This is illustrated in graph Figure 4-8 below where the only difference between the experimental curves recorded at different angles is a vertical off-set in the data.

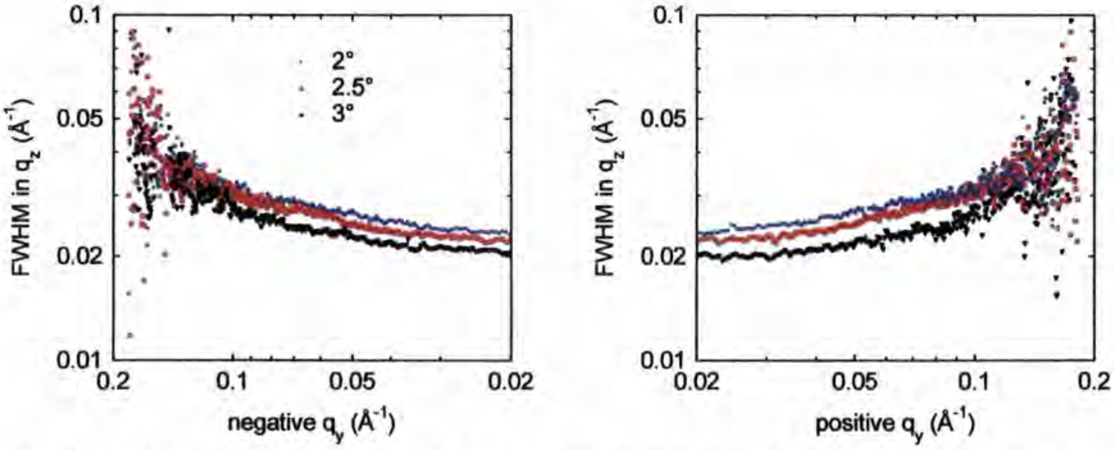

Figure 4-8: Measured FWHM in q_z of the 2nd Bragg Sheet from a $[Co/Pd]_{x20}$ repeated bilayer as a function of position in q_y along the Bragg sheet for three different incident angles. The FWHM falls with increasing angle but the scaling behaviour is unaltered.

Also included in the C++ program is the ability to output a text file of the integrated intensity in q_z over a Brillouin zone as a function of q_y. Again, once the intensity as a function of q_y was found, the data was processed in Excel. A linear (nearly constant) background was subtracted from the data and power-law fits made at low and high q_y, see Figure 4-9 below. Errors in the intensity analysis were calculated using $\sqrt{N}$ counting statistics, and, again, Chi^2+1 fitting was used to get the errors on the scaling parameters. For consistency and to introduce some objectivity the 'knee' of the distribution giving the characteristic length scale was measured by the intercept of the two power laws at low and high q_y. The error on this value was calculated from the errors on the two respective power laws.

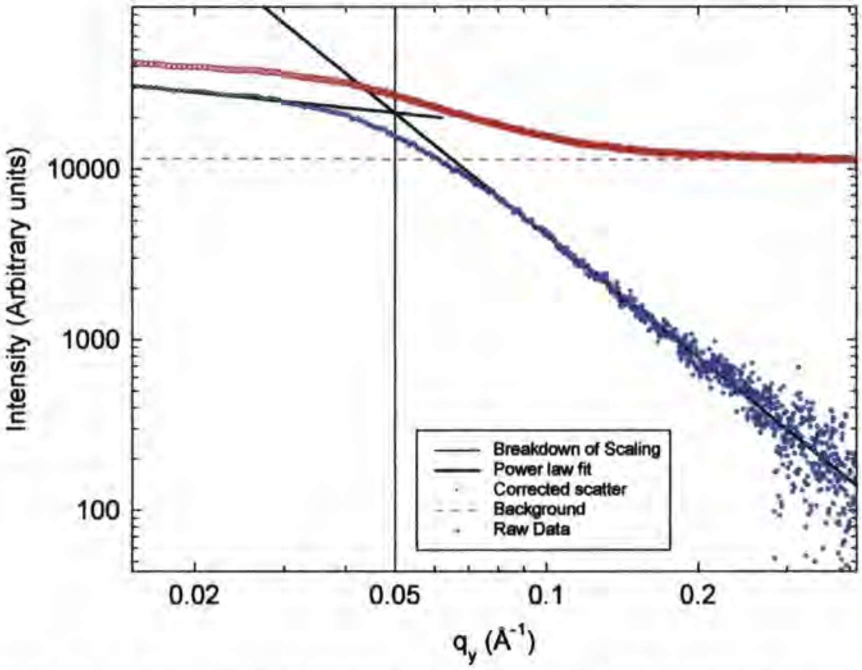

Figure 4-9: Red data – the intensity profile through the diffuse Bragg sheet for positive q_y,
Blue data – the data after a linear background has been subtracted
clearly showing two areas of scaling behaviour.

This intensity analysis is not affected by the incident angle of the x-rays on the sample, as shown in Figure 4-10 below, where the curves recorded at different angles all follow the same form. For clarity the curves on a log scale have had to be shifted in intensity.

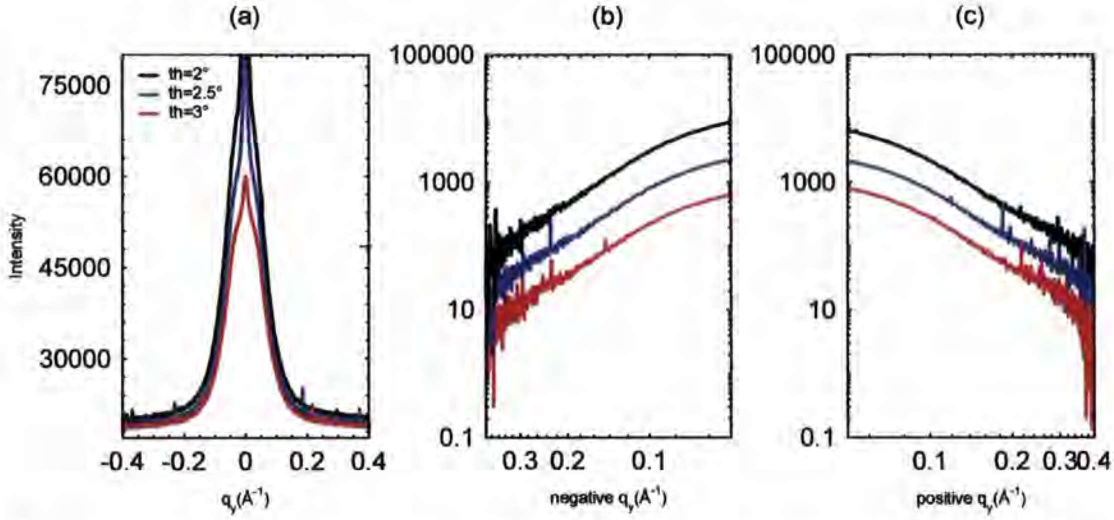

Figure 4-10: (a) Intensity of the 2^{nd} Bragg Sheet integrated over q_z from $[Co/Pd]_{x20}$ repeated bi-layer. (b) + (c) The same intensities for positive and negative q_y after the subtraction of a linear background across the whole peak and plotted on a log-log scale showing that the scaling behaviour at high q_y is independent of the incident angle of the sample. (The curves in (b) and (c) have been shifted in intensity for clarity.)

4.5 Analysis of the Bragg sheets from the Co/Pd samples

4.5.1 CCD images analysed

The CCD images of the diffuse scatter from the CoPd samples, at a sample angle of 2°, are shown in Figure 4-11 below. Looking at these images in more detail reveals that Kiessig fringes are present in the multilayers with 12, 20 and 24 repeats between the Yoneda scatter at $q_z \sim 0.2$Å and the first visible Bragg sheet. This has been shown for the sample with 12 repeats in Figure 4-12 below. This is only the case if the top and bottom surfaces are conformal over the thickness of the sample. For the other samples the resolution of the measurement is not good enough to resolve the Kiessig fringes which become narrower as the sample thickness increases.

In some of the images, such as the sample with 12 repeats, a diagonal streak moving away from the origin is present. This is associated with scatter from the beam defining slits on the beamline and was later blocked by placing a washer around the beam exit. It is sufficiently distant from the Bragg sheets for it not to be a hindrance, although it does feature in some of the intensity profiles shown later.

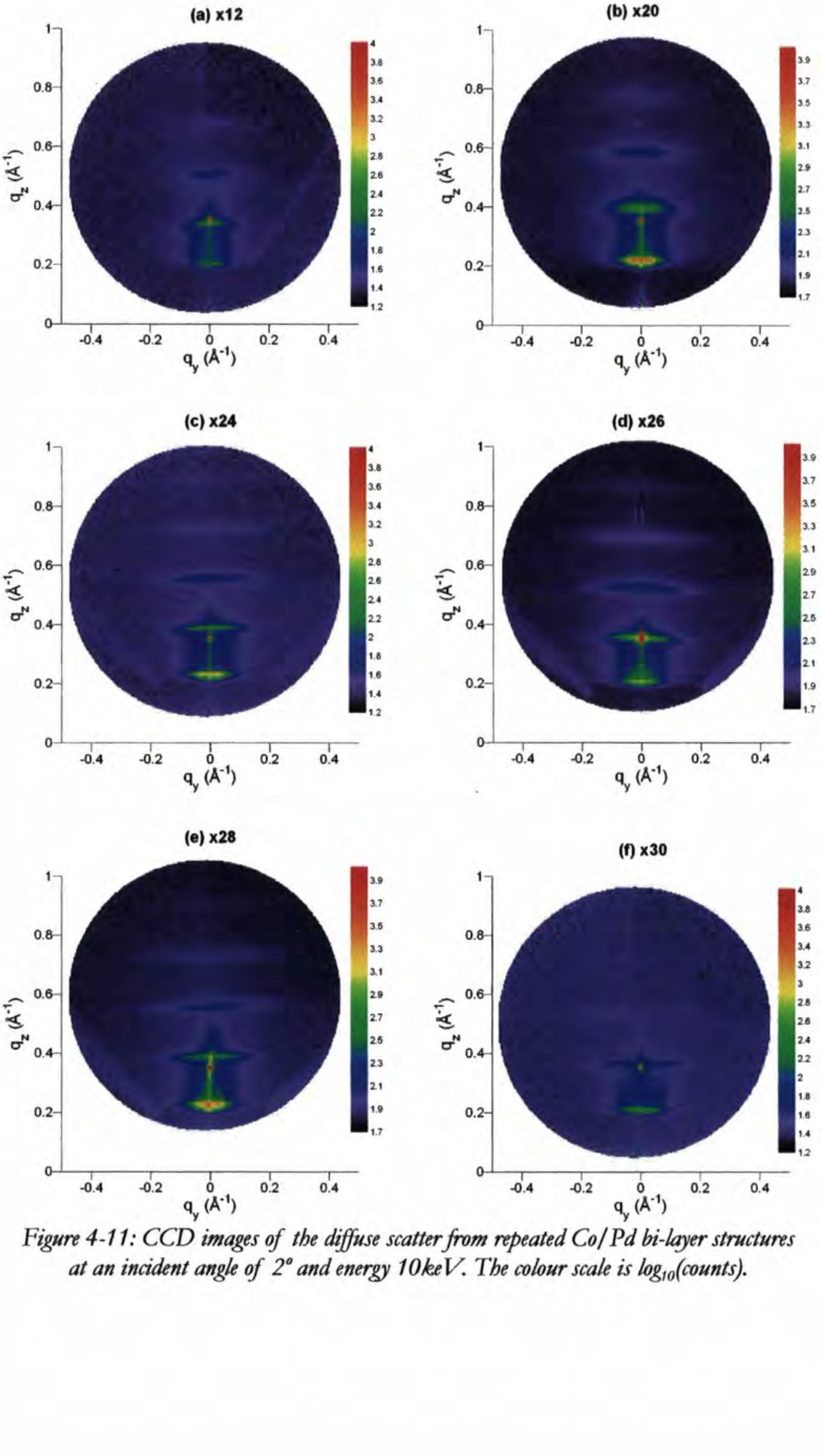
(a) x12

(b) x20

(c) x24

(d) x26

(e) x28

(f) x30

Figure 4-11: CCD images of the diffuse scatter from repeated Co/Pd bi-layer structures at an incident angle of 2° and energy 10keV. The colour scale is $\log_{10}$(counts).

Figure 4-12: Close in view of the Kiessig fringes visible in the sample with 12 repeats

4.5.2 Scaling in the Bragg sheet width

The full-width at half-maximum (FWHM), measured by taking cross-sections in q_z as a function of distance in q_y, is shown below, in Figure 4-13, for each of the six samples. Both the second and third order Bragg sheets were analysed. The first-order Bragg sheet was obscured by the critical angle at the sample angle used for these measurements. The existence of scaling behaviour as a function of q_y is unclear in all these data sets. For clarity only the error bars on the 2nd Bragg sheet and scaling law fit for the x12 repeat sample have been shown. However, the spread in the data points as the FWHM is measured further out in q_y is a good indicator of the errors inherent in the data.

The blue data relating to the second-order Bragg sheet is often broadened at low q_y as a result of the specular point falling close to the centre of the Bragg sheets and the tails of this point affecting the Bragg sheet width. As the distance away from the zero of q_y increases the widths tend to increase. The Bragg peak arises from conformal roughness between the layers, and thus the width is a measure of the out-of-plane correlation length of the roughness within the sample [24]. As q_y increases, the spatial frequency (in the plane of the interface) of the roughness being measured increases and the higher spatial frequencies tend to show a greater width. This is particularly evident in this second-order Bragg sheet and shows that the out-of-plane correlation length is less for higher spatial frequency roughness components compared to lower frequency components. From this observation that the longer-wavelength features in the interfaces are better replicated between layers it cannot be inferred that the layers are getting smoother. This measurement is only looking at the conformal roughness and the high-frequency components may still be present in the interfaces but are simply non-conformal.

The 3rd order Bragg sheet is not affected by the tails of the specular point and at low q_y the FWHM is almost constant. The higher order Bragg sheet is always wider than the lower order one, and does not always follow the same form with increasing q_y. This variation with q_z is not expected within the weak roughness assumption and shows that at these higher q_z values the model is breaking down.

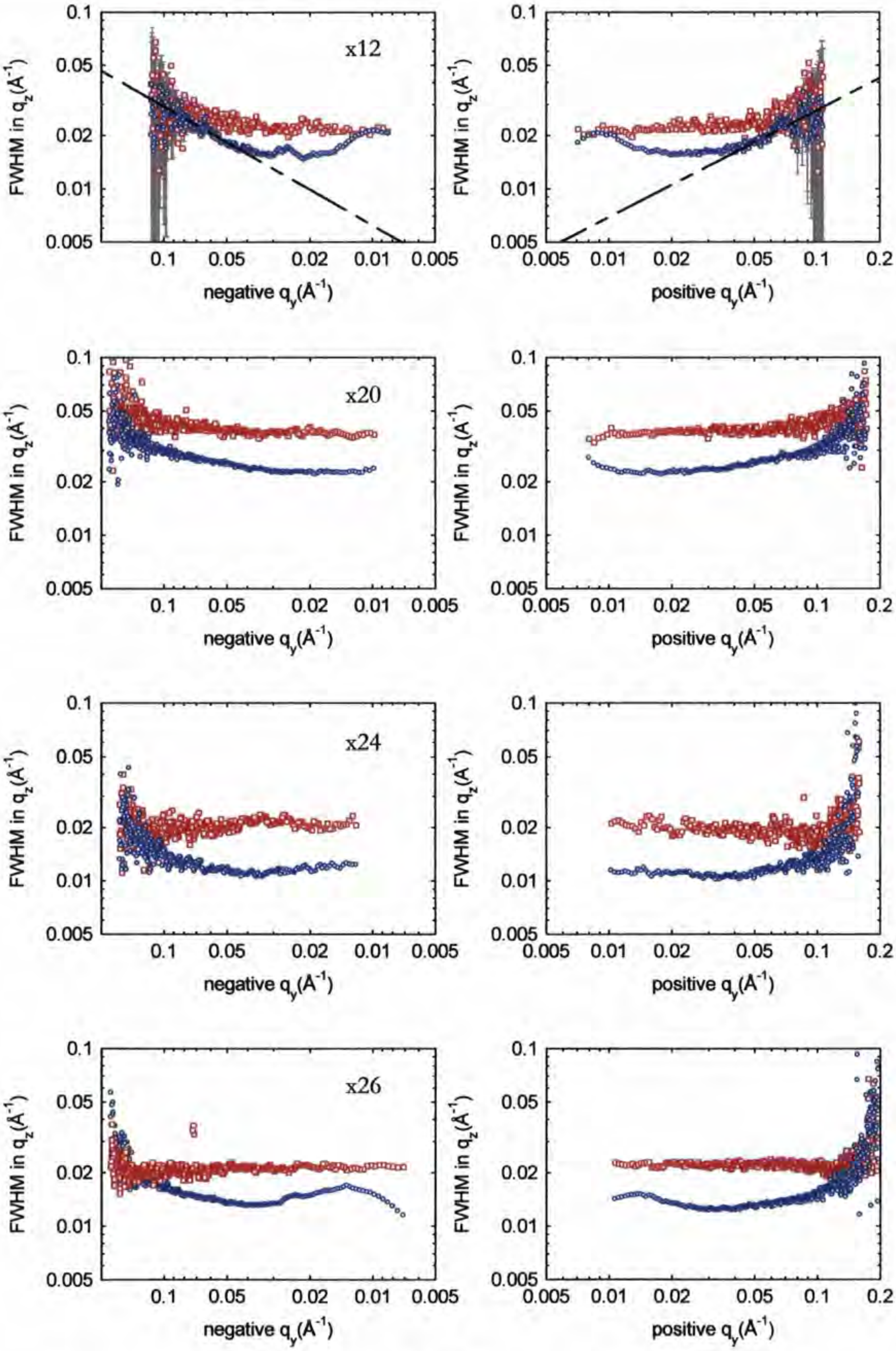

Figure 4-13: Measured FWHM in q_z of the 2nd (blue data) and 3rd (red data) Bragg Sheets as a function of q_y (continued overleaf)

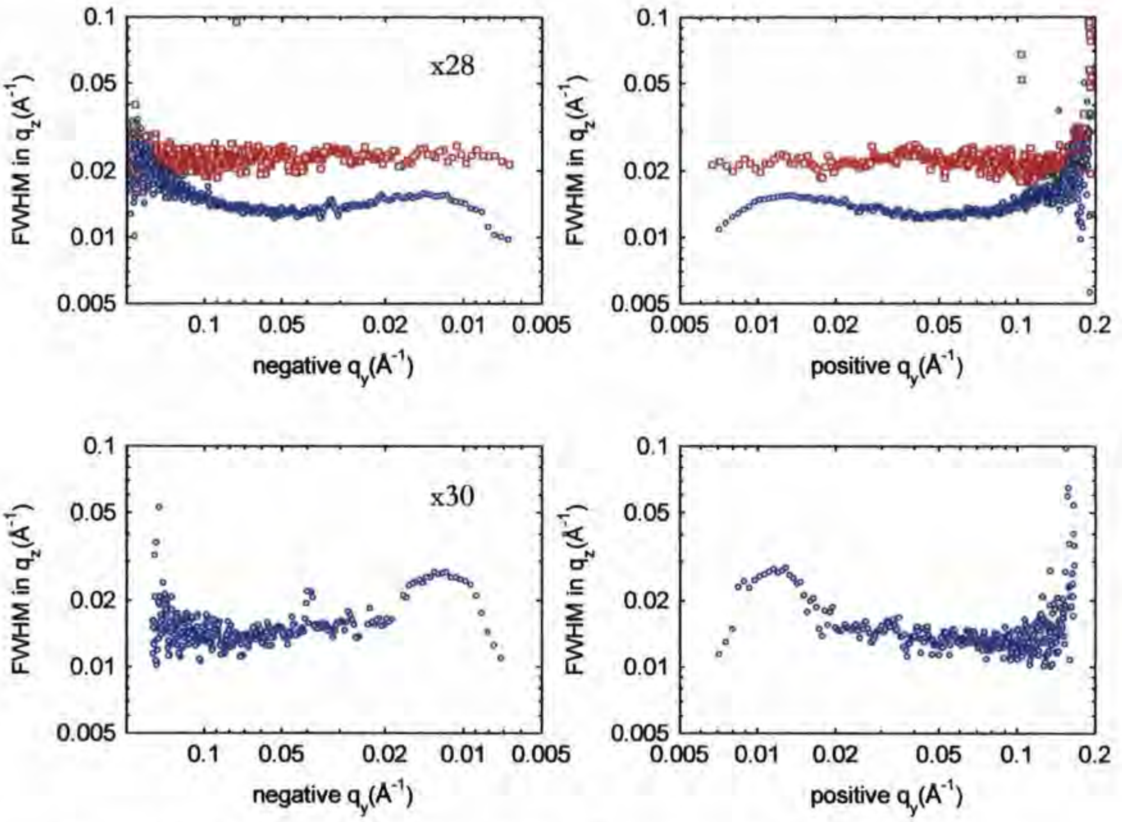

Figure 4-13 Measured FWHM in q_z of the 2^{nd} (blue data) and 3^{rd} (red data) Bragg Sheets as a function of q_y (continued from previous page)

The scaling exponent fitted to these sets is summarised in Figure 4-14 below. A power law fit to the FWHM data is not a good fit, and the exponent determined depends strongly on the range over which the data are fitted. For the multilayer with 30 repeats it is very unclear that any scaling at all exists and the FWHM appears to be constant within the spread of the data until the Bragg sheet intensity falls below that which is detectible. The errors bars have been increased from that given by chi^2 fitting to take into account the range of scaling exponents deduced from selecting different ranges in q_y over which to fit the scaling law. No fit seems reasonable for the x30 multilayer and it has not been included.

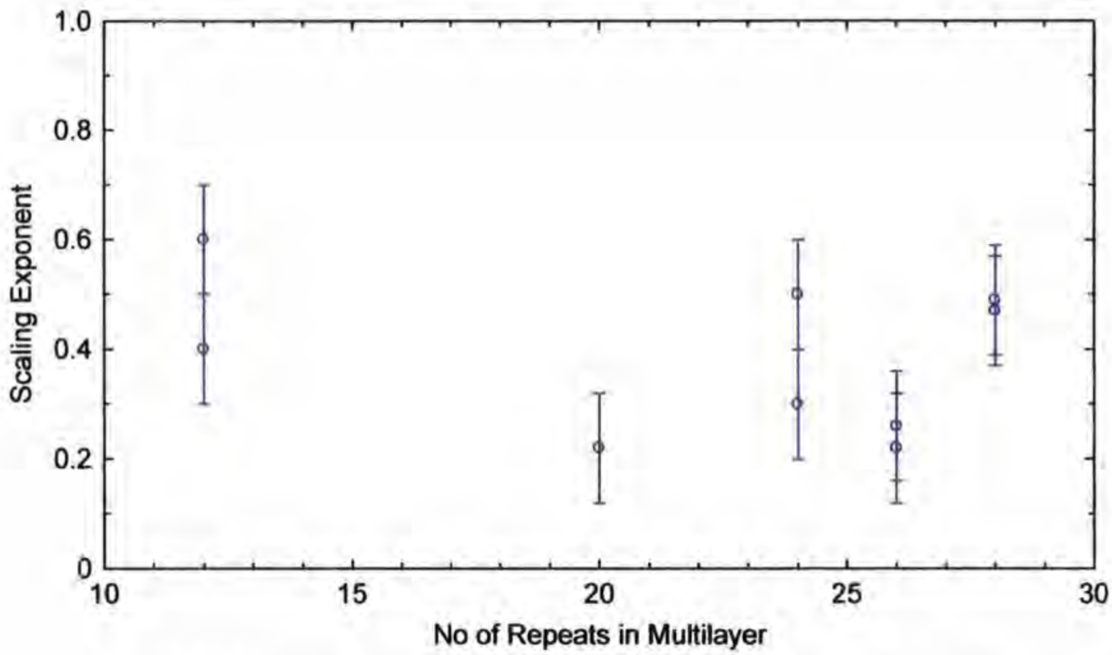

Figure 4-14: Scaling exponent in the FWHM with number of repeats in the multilayer.

As successive layers are deposited and the number of repeats in the multilayer increases, so the profile of the interfaces is expected to change, especially if the higher frequency components of the roughness are propagating less well. The absence of variation in the scaling exponent suggests that the correlation length associated with each frequency component is not changing as more and more layers are deposited.

4.5.3 Scaling in the intensity

The intensity profiles, integrated in q_z, over the first visible Brillouin zone, are plotted below in Figure 4-15. Also plotted are the data after a linear background has been subtracted and to which a scaling relation has been fitted. The geometric construction fitting a scaling law at low q_y and finding the 'knee' of the profile is also shown.

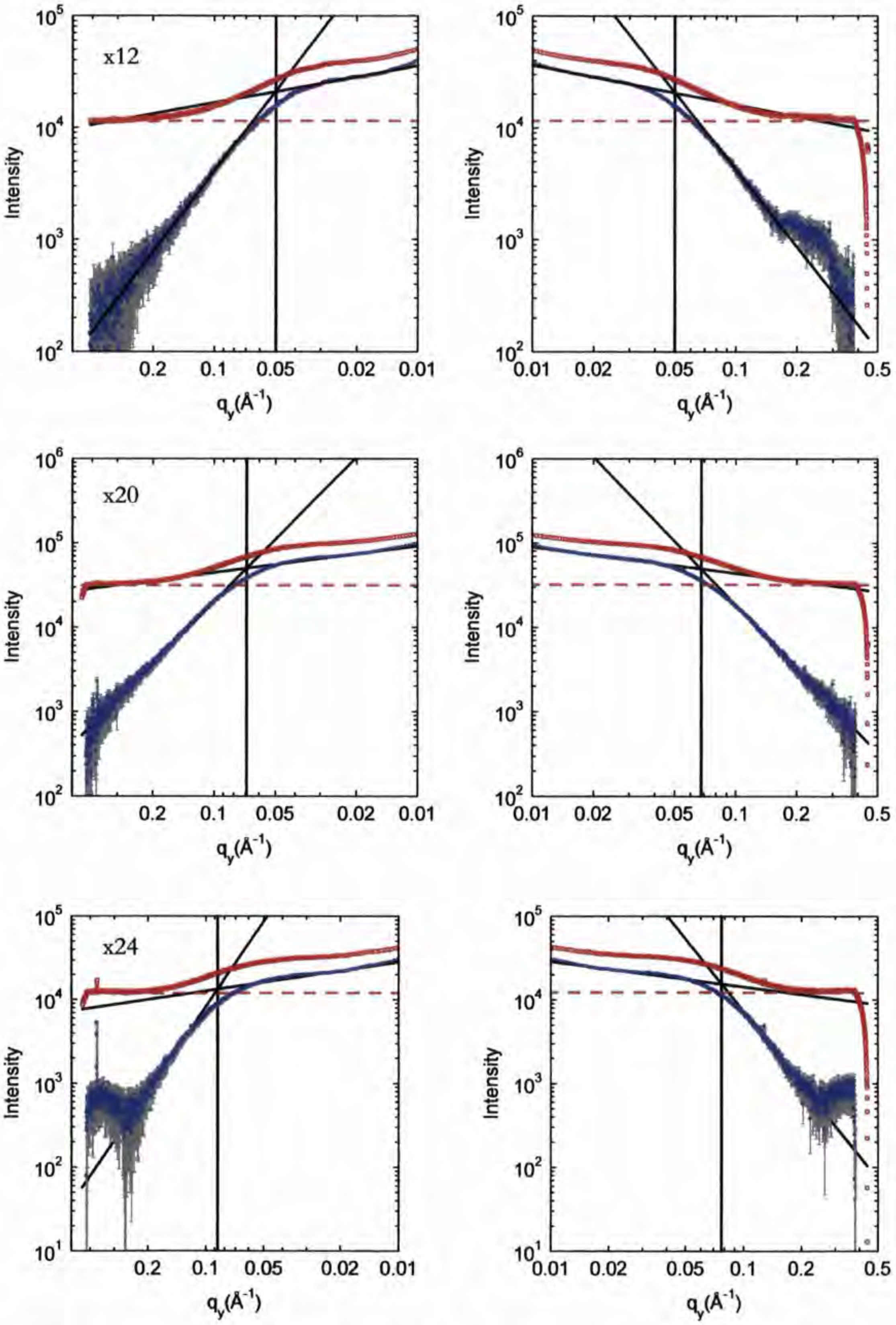

Figure 4-15: Intensity scaling in the six samples. Red data – the intensity profile integrated in q_z over the Brillouin zone. Blue data – the data after a linear background (dashed red line) has been subtracted showing two areas of scaling behaviour where power laws (black lines) have been fitted.
(Figure continued on next page)

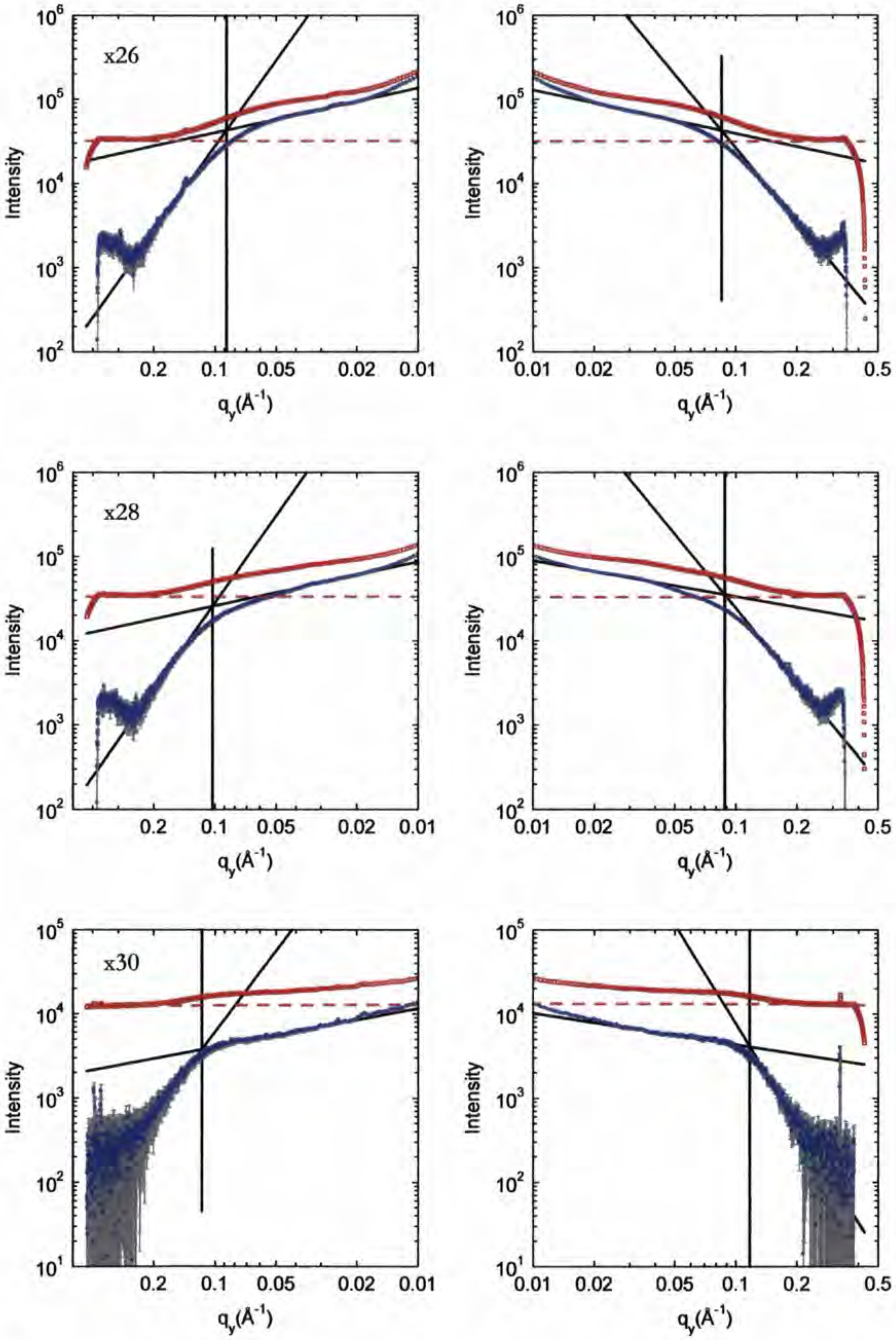

Figure 4-15: Intensity scaling in the six samples. Red data – the intensity profile integrated in q_z over the Brillouin zone. Blue data – the data after a linear background (dashed red line) has been subtracted showing two areas of scaling behaviour where power laws (black lines) have been fitted. (continued from previous page)

In the cross-sections through the Bragg Peak, used to measure the FWHM (Figure 4-13) the peak is not detectable above 0.2Å^{-1}. However, the scaling behaviour begins at around 0.1Å^{-1} and continues into the background scatter. The purpose of integrating the scatter over the Brillouin Zone is to sample both the coherent and incoherent contributions to the diffuse scatter equally. The incoherent parts, which are not measurable in the Bragg peak, thus extend to even higher spatial frequencies within the roughness profile.

The fractal parameter as deduced using equation (4-5) from the scaling of the intensity profile at large values of q_y is shown in Figure 4-16 below. The fractal parameter approaches unity as the number of repeats increases, hence the surfaces are becoming smoother and more two dimensional as more layers are being deposited. These data fit well to a scaling law in their own right, although the fractal parameter cannot exceed 1, a perfectly 2D surface, and the h value should saturate at some higher values. Without samples containing more repeats the form of the relation between h and number of repeats at higher repeat numbers cannot be found.

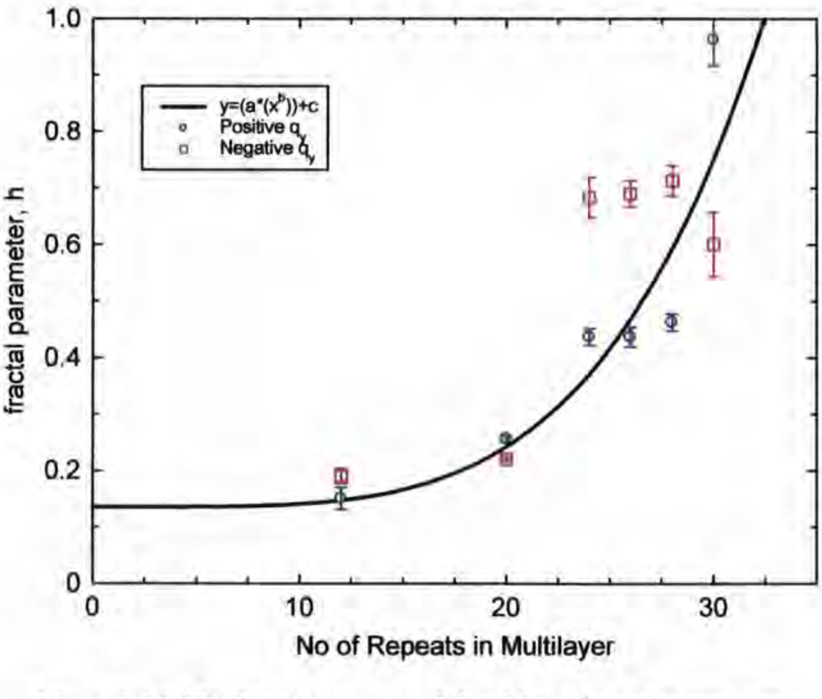

Figure 4-16: The fractal parameter, deduced from the scaling exponent of the intensity profile at high values of q_y

The value of q_y at which scaling ceases shows a linear increase with number of repeats in the multilayer, or the film thickness (Figure 4-17 below). This relates to a shortening in real space of a characteristic length as the sample grows. Error bars were calculated from chi-squared minimisation of the two power-law fits at high and low q_y to find 68% confidence limits on the fitted parameters and these were propagated through to find the error on the q_y value of the intercept of the two power laws.

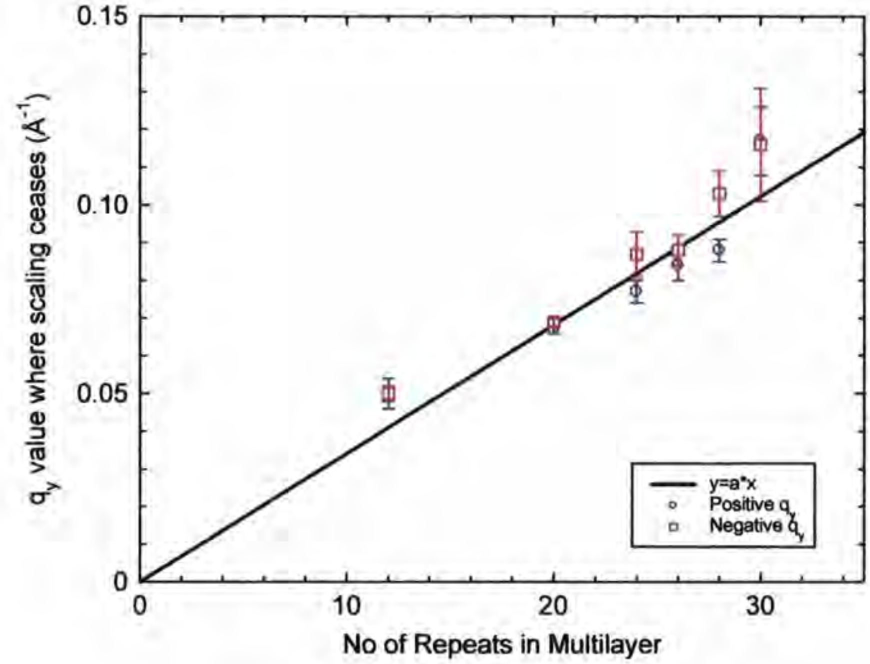

Figure 4-17: The length at which scaling ceases

The increase in the q_y values at which scaling behaviour ceases with the number of repeats. At the same time the fractal parameter increases with the number of repeats. This is in line with the predictions of Salditt, reproduced in Figure 4-1 above, where the position of the 'knee' of the distribution changes with *h*. This was based on the Sinha self-affine fractal model, and, given that the measurement performed here is not dependent on any assumptions of the particular form of the correlation function, the analysis verifies that this correlation function is good for describing the interfaces.

The interpretation of the q_y value where scaling ceases in terms of a correlation length is difficult. Measurements performed by A. Rozatian to establish the in-plane correlation length included in the Sinha model from fits to the transverse diffuse scatter from this same sample set show an increase in the in-plane correlation length as the number of repeats increases [31,37]. These length scales cannot therefore be the same.

4.6 Analysis of the Bragg sheets from the Co/Ru samples

Following on from the Co/Pd layers, a series of Co/Ru multilayers with 15, 20, 60 and 80 repeats were examined.

4.6.1 Specular scatter and simulation

No previous characterisation had been performed on these samples and so the specular, and off specular scatter was recorded and fitted to establish the structure. The experimental data and simulated fits are shown below in Figure 4-18, with the deduced parameters being shown in Table 4-1 below.

Co/Ru Periods	SiO_2 Substrate Roughness (Å)	Cobalt		Ruthenium	
		Thickness (Å)	Roughness (Å)	Thickness (Å)	Roughness (Å)
x5	4.0 ± 0.5	11 ± 2	4 ± 2	12 ± 2	6 ± 2
x15	2.1 ± 0.5	10 ± 2	5 ± 2	13 ± 2	3 ± 2
x20	1.0 ± 0.5	12 ± 2	5 ± 2	12 ± 2	3 ± 2
x60	4.3 ± 0.5	13 ± 2	4 ± 2	10 ± 2	3 ± 2
x80	7.0 ± 0.5	12 ± 2	3 ± 2	12 ± 2	4 ± 2

Table 4-1: Sample structures deduced by fitting the true-specular scatter for the Co/Ru multilayer series

The thicknesses are slightly larger than the nominal values of 10Å for the cobalt layers and 11Å for the ruthenium. The layer roughness values are similar to the values measured on the Co/Pd layers. The variation in the roughness of the SiO_2 substrate is surprisingly large.

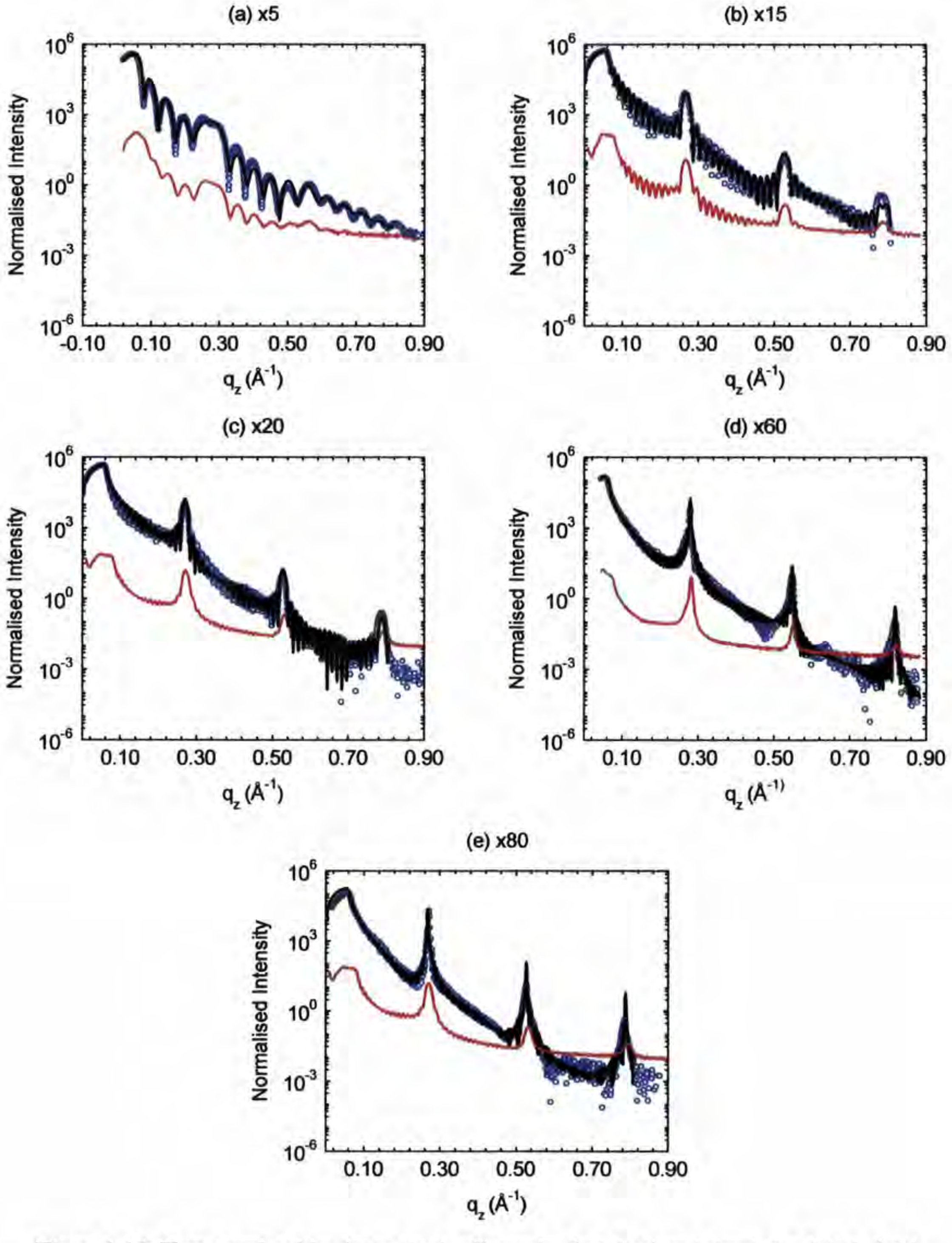

Figure 4-18: True specular (blue data points), off-specular (red data) and simulation (black data) from the five Co/Ru multilayers (a) x 5, (b) x15, (c) x 20, (d) x60, (e) x80.

4.6.2 CCD images analysed

The images recorded from the Co/Ru samples are shown in Figure 4-19 below. The sample angle chosen was 1° and the Yoneda scatter is now sufficiently low to allow the first-order

Bragg sheet to be viewed. This sheet is also at a higher q_z value than the Co/Pd series as a result of the thinner repeated bi-layer unit in the multilayer. The Bragg sheets from the sample with only 5 repeats is poorly defined, and only the first-order sheet is visible, and so no further analysis was performed on this sample.

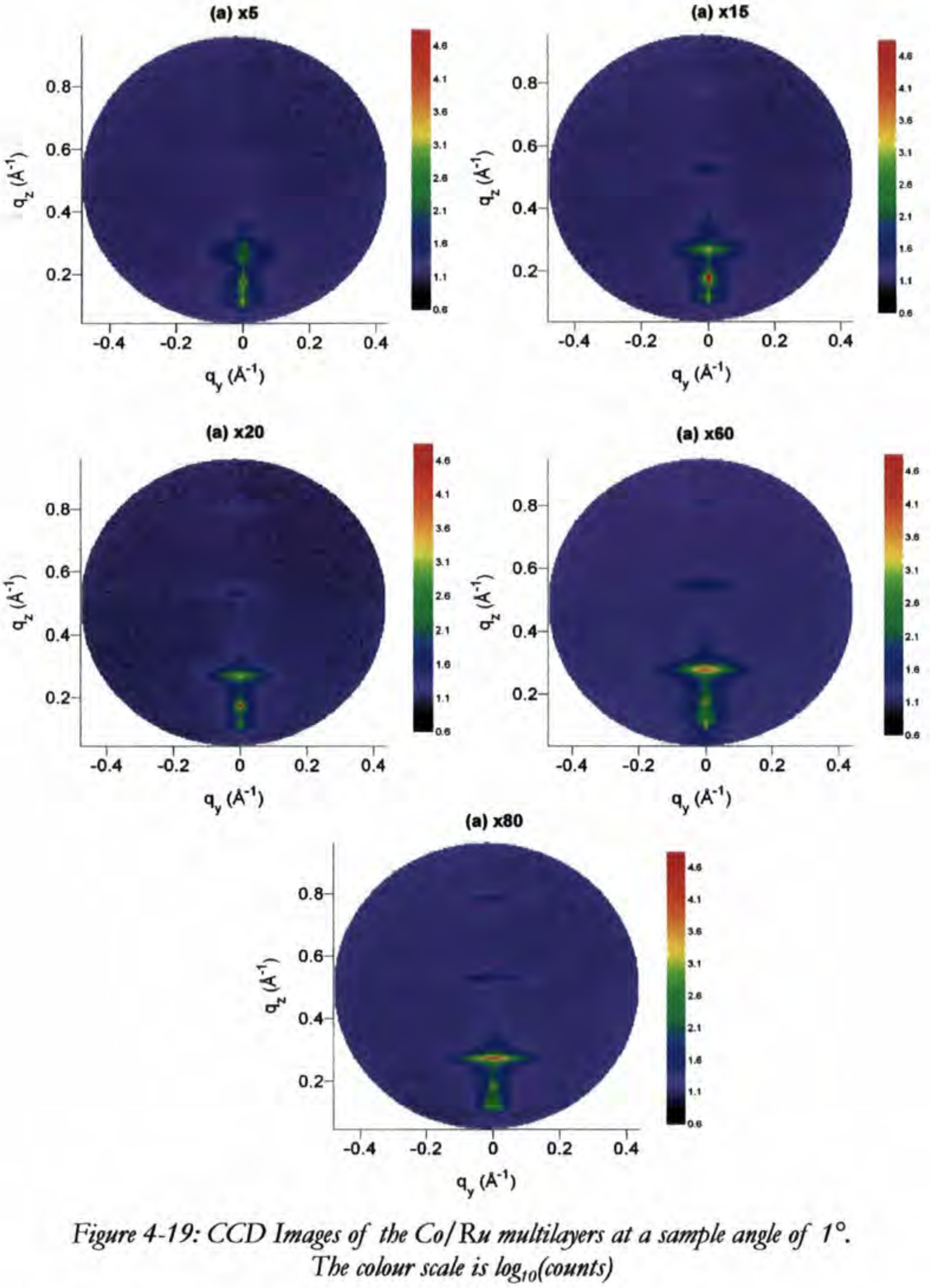

Figure 4-19: CCD Images of the Co/Ru multilayers at a sample angle of 1°. The colour scale is log_{10}(counts)

4.6.3 Scaling in the Bragg sheet width

The FWHM of the first and second Bragg sheets are shown in Figure 4-20 below. The error bars on the data are similar to those shown in Figure 4-13 and have not been shown again for clarity. In the first-order Bragg sheet there is clear scaling visible at higher values of q_y which can easily be fitted to a power-law. This scaling relation cannot be seen in the much weaker second-order Bragg sheet. In some of the samples, such as the x80 repeat sample, the widths appear to show several distinct regions of power law behaviour.

The trend in the scaling exponent as a function of the number of repeats is shown in Figure 4-21 below and shows a fall in the scaling exponent as the number of repeats is increased. With only four samples to analyse a more precise form of the relation is not obvious. Comparing the 15 and 20 repeat samples to the 60 and 80 repeat samples it can be seen that there is a reduction in this scaling parameter.

Interpreting the widths in terms of the out-of-plane correlation lengths of the conformal roughness for different spatial frequencies, as was done with the Co/Pd series before, the change in scaling represents a change in the way the higher frequency components are correlated between layers. The scaling parameter falls when the number of repeats are increased and the roughness becomes more evenly correlated across the range of roughness component frequencies. Between 20 repeats and 60 repeats there is a change in the way the interfaces replicate in the bilayer stack, indicating a change in the predominant growth mechanism.

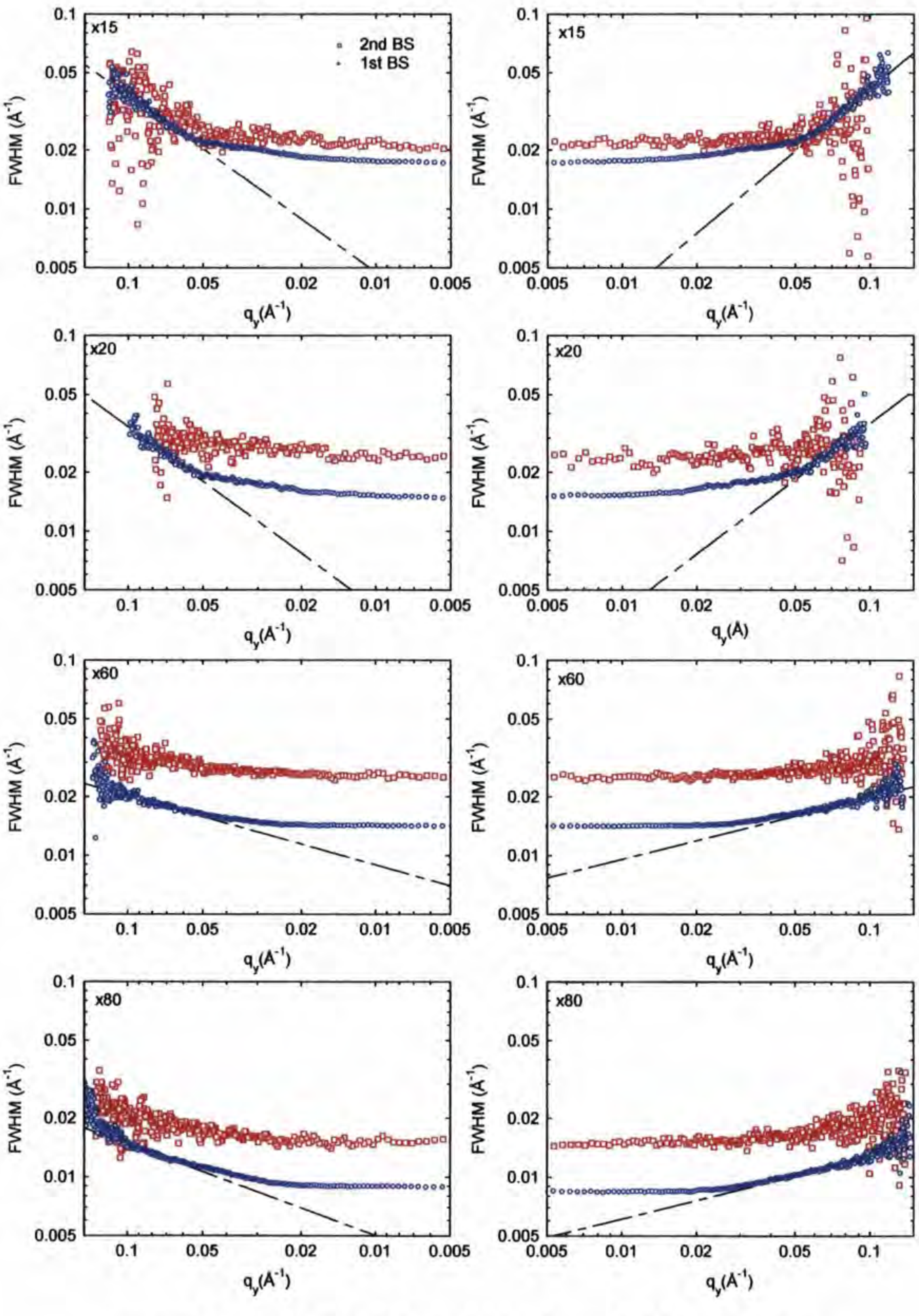

Figure 4-20 FWHM of the first (blue data) and second (red data) Bragg sheet as a function of qy for the Co/Ru multilayers with 15, 20, 60 and 80 repeats

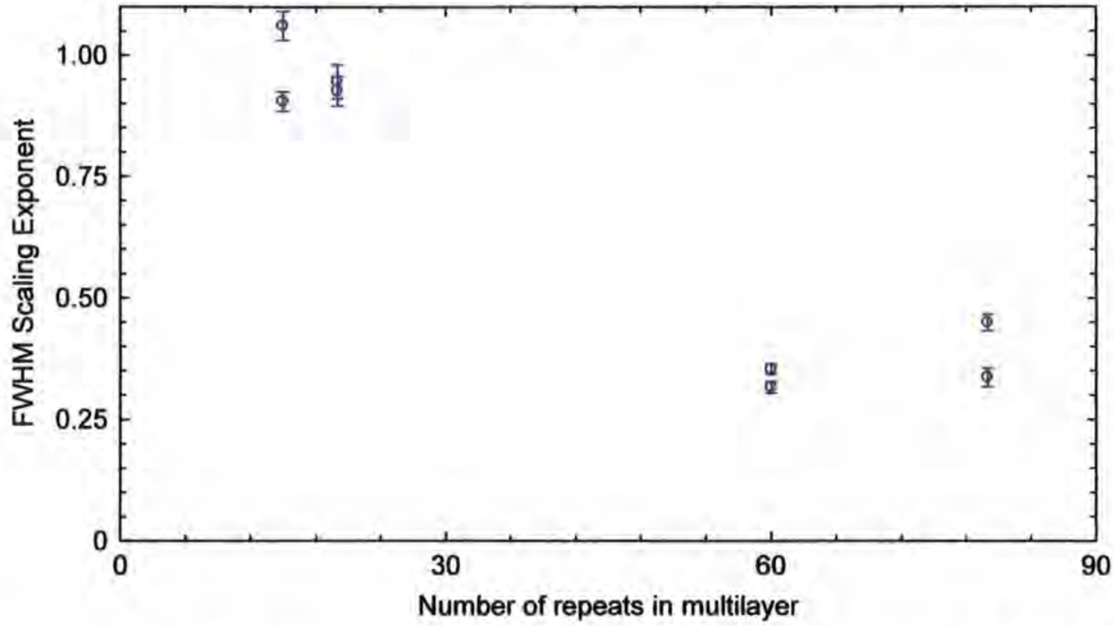

Figure 4-21: Scaling parameter from the FWHM of the 1st Bragg Sheet as a function of the number of repeats in the multilayer

4.6.4 Scaling in the intensity

The intensity profiles of the 1st Bragg sheets are shown in Figure 4-22 below. Immediately a clear change in the shape profile is seen as the number of repeats is increased from 20 to 60. The two scans at 15 and 20 repeats look very similar, as do the scans at 60 and 80 repeats.

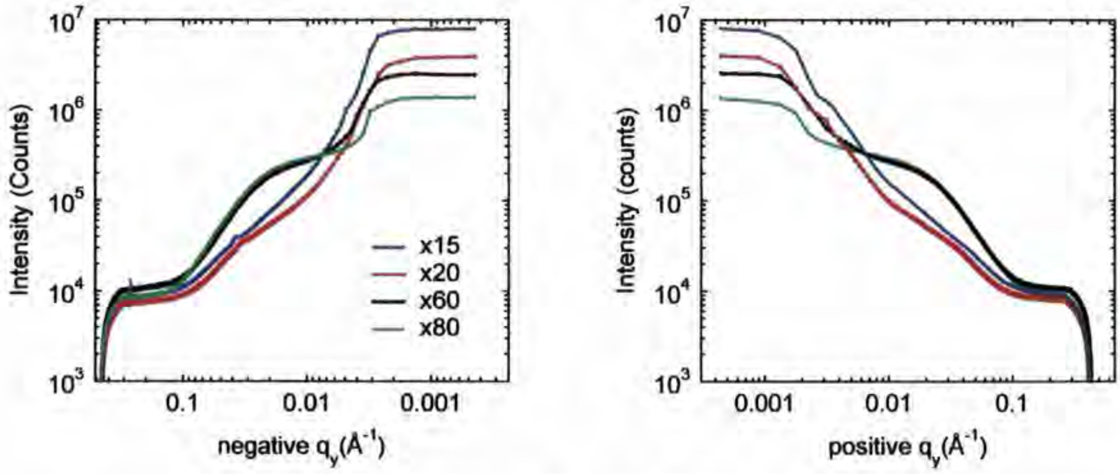

Figure 4-22: Intensity profiles of the 1st Brillouin Zone.

This observed changed in the shape profile is in contrast to the 2nd Brillouin zone, Figure 4-23 below, where no change in shape is observed.

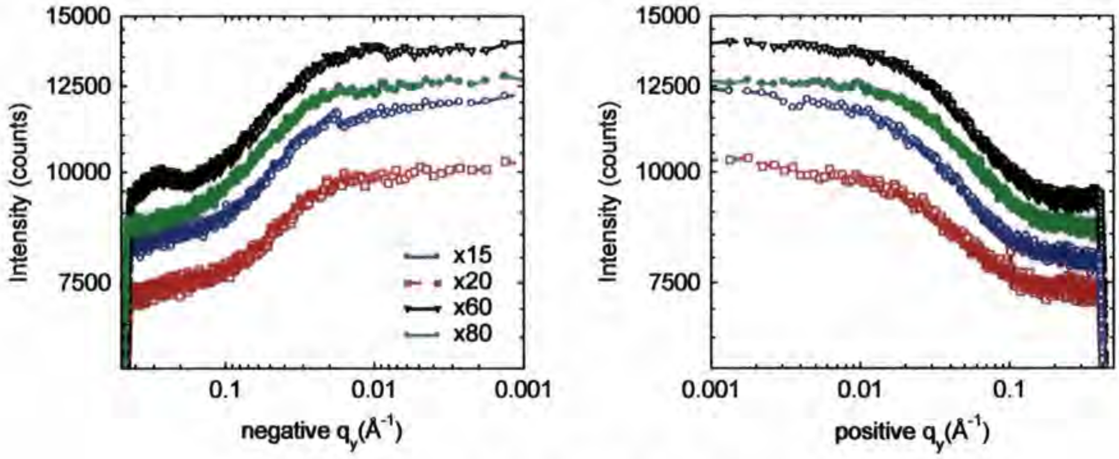

Figure 4-23: Intensity profiles of the 2nd Brillouin Zone.

This first-order Bragg sheet is giving very different information to the second order one. Returning to the first-order Bragg sheet, and subtracting a linear background to extract the scaling behaviour generates the constructions shown in Figure 4-24 below. Again scaling behaviour is clearly found at higher q_y values. The scaling behaviour at low q_y is unclear in the case of the samples with 15 and 20 repeats.

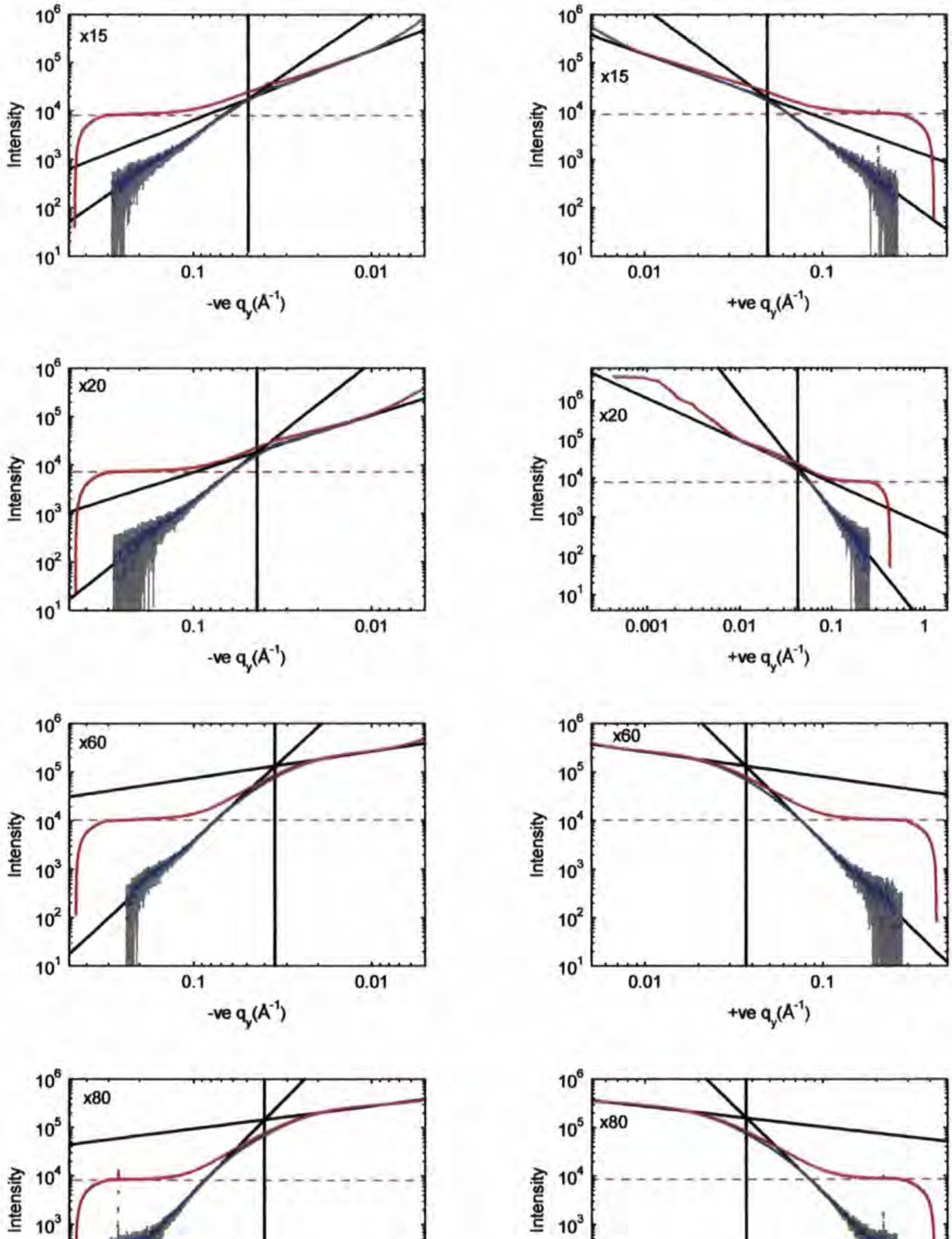

Figure 4-24 Intensity scaling in the CoRu samples. Red data – the intensity profile integrated in q_z over the Brillouin zone. Blue data – the data after a linear background (dashed red line) has been subtracted showing two areas of scaling behaviour where power laws (black lines) have been fitted.

As with the CoPd series the scaling parameter shows a systematic fall (Figure 4-25), corresponding to an increasing fractal parameter (Figure 4-26), as the number of repeats increases.

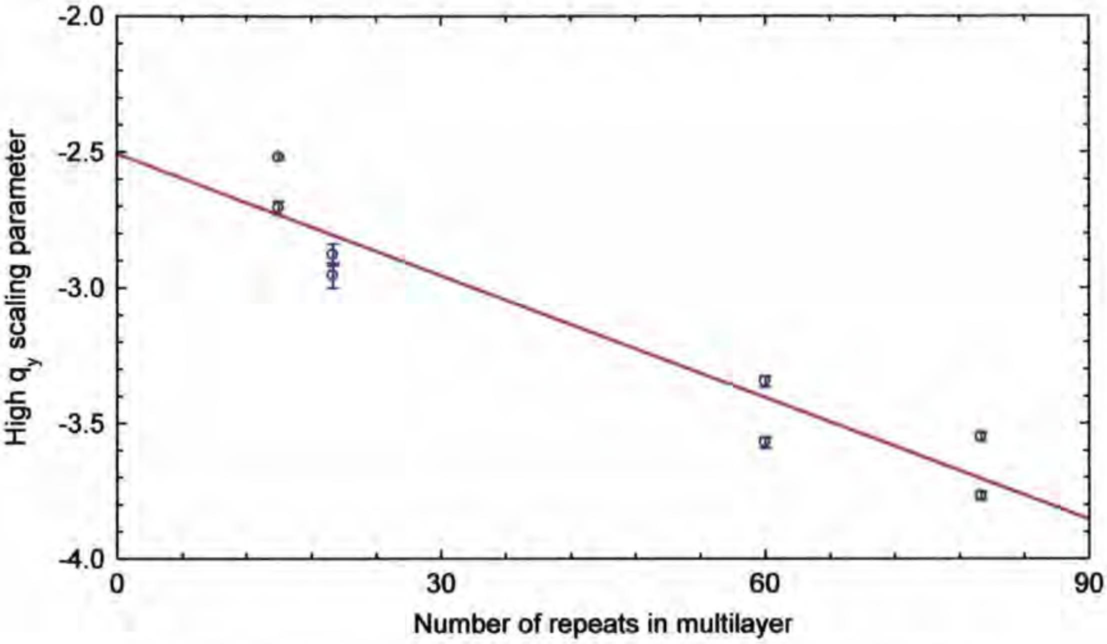

Figure 4-25: Scaling parameter from the scaling in the intensity at high angles.

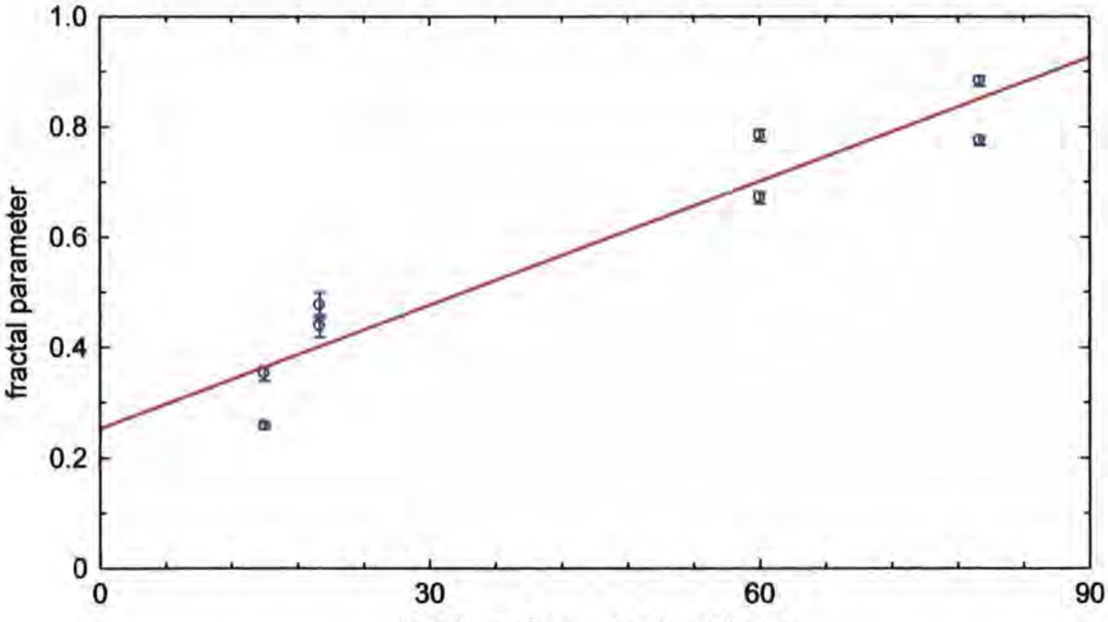

Figure 4-26: Fractal parameter deduced from the scaling in the intensity at high angles.

Looking at the q_y value associated with the 'knee' of the distribution is difficult for the 1st Bragg sheet, especially for x15 and x20 repeat samples where the scaling behaviour at low

q_y is unclear. This fall in q_y value with increasing number of layers, Figure 4-27 below, is opposite to the behaviour of the CoPd system, but with the uncertainly in the low q_y scaling fit it is difficult to interpret this apparent fall. The value of q_y where scaling ceases is more precisely defined for the x60 and x80 repeats and in comparison to the CoPd data occurs at a much lower value of q_y. This is a larger real-space in-plane distance, although as noted before the interpretation of this is unclear.

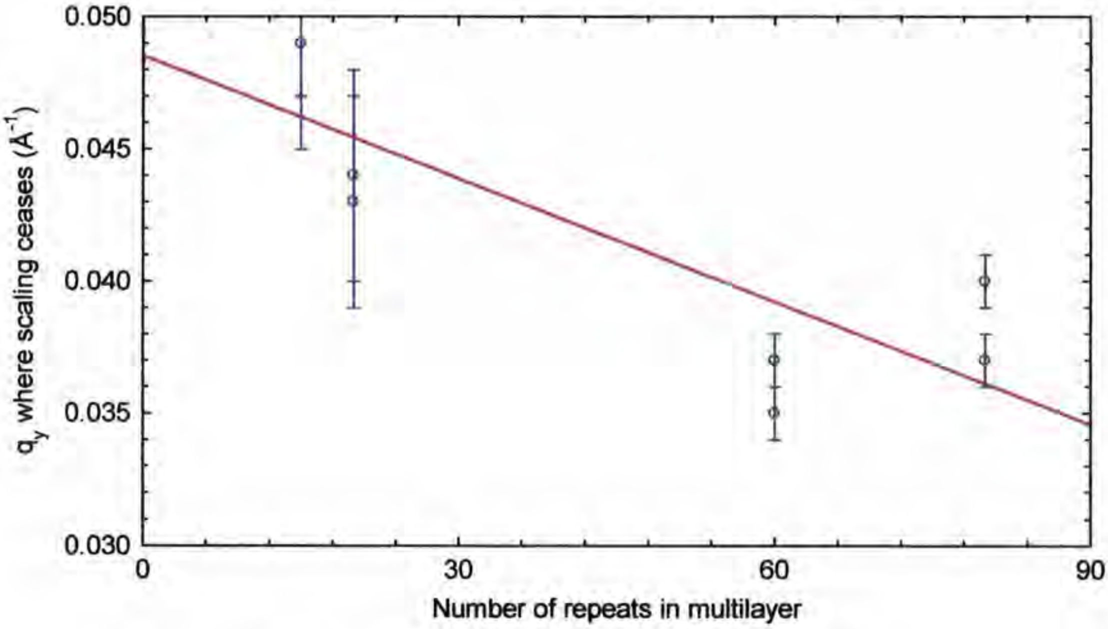

Figure 4-27: q_y where scaling ceases vs. number of repeats

4.7 Interpretation and discussion

The reduction in the Bragg sheet width with increasing number of layers has to be viewed in the context of it originating from more interfaces. In the samples with less repeats there will be broadening of the Bragg sheets caused by there being fewer reflecting planes, in much the same way as diffraction peaks are broadened from materials composed of small grains. Whether or not the peaks measured are limited by size effects or broadening from the correlation length is hard to say. The out-of-plane correlation length for the roughness frequency components is shorter for higher frequency components, showing that they replicate less well than longer wavelength features, which is a prediction within the TAB model [22]. This is shown by both material systems. The Fe/Au layers of Paniago [15] demonstrate a very similar scaling exponent in this FWHM as the Co/Ru x15 and x20 samples.

In comparison to the CoPd series the Bragg sheets from the CoRu look much more rounded in shape. The absence of observed scaling in the FWHM from the CoPd series may be because the first-order Bragg sheet was not accessible. Weak roughness is defined as being where $|q_z\sigma| < 1$. With RMS roughness around 5Å the limit of weak roughness is at q_y of 0.2Å, just below the positions of the Bragg sheets examined. Some variation in properties with q_z and Bragg sheet order is therefore not surprising.

Both sets of samples have been seen to exhibit scaling behaviour in the intensity of diffuse scatter moving away from the plane in which specular scattering occurs ($q_y = 0$). This is a direct measurement of the structure factor of the scatter and does not rely on any assumed form for the correlation function for interpretation. The cobalt palladium system took about 30 repeats, or 1000Å, for the fractal parameter to approach 1, whereas the cobalt ruthenium system takes much longer, nearly 80 repeats, or 1700Å, although the form between the 20 and 60 repeat samples is not known. The low initial value of the fractal parameter, for both the CoRu and CoPd samples, of around 0.2 is entirely consistent with the Kardar-Parisi-Zhang (KPZ) model which is a ballistic model [21], and as successive layers are deposited the dimensionality of the interfaces falls and the fractal parameter increases. This is in line with the Tang-Alexander-Bruinsma (TAB) model which assumes growth along the local surface normal [22].

The change in the dimensionality of the interface is an important form of smoothing which is not picked up in the determination of the RMS roughness deduced from fitting the specular scatter (Table 4-1). This RMS roughness parameter will be dominated by the longer wavelength features. For PMA and exchange coupling the length scale of the interface features which affect the performance are likely to be very short, and this fractal smoothing likely to be more significant than a reduction in the RMS roughness.

4.8 Conclusions

This has demonstrated that, as the layers grow, the nature of the roughness is altered, predominantly in the fractal parameter of the roughness. Choosing the right parameters to understand the samples is very important, and making a measurement of only the RMS roughness may not be sufficient to probe the actual roughness features that are important for the physical processes responsible for determining the performance of a device. Thicker layers in both the CoPd and CoRu system gives a more two dimensional interface, but without any change to the longer wavelength features.

References for Chapter 4:

[1] Dinia, A., *et al.*, J. Magn. Magn. Mat., **104** (1992) 1871

[2] Bailey, W. E., *et al.*, J. Appl. Phys., **79** (1996) 6393

[3] Zoll, S., *et al.*, Phys. Rev. B., **57** (1998) 4842

[4] Miller, C. W., *et al.*, App. Phys. Lett., **90** (2007) 043513

[5] Wasa, K., "Handbook of sputter deposition technology", Noyes Publications, Reprint Edition (1992), Westwood, New Jersey,

[6] Bales, G. S., *et al.*, J. Vac. Sci. Technol. A, **9** (1991) 145

[7] Sinha, S. K., *et al.*, Phys. Rev. B., **38** (1988) 2297

[8] Phang, Y. H., *et al.*, J. Appl. Phys, **72** (1992) 4627

[9] Sinha, S. K., *J.* Phys. III France, **4** (1994) 1543

[10] Holý, V., *et al.*, Phys Rev. B., **49** (1994) 10668

[11] de Boer, D. K. G., Phys. Rev. B., **49** (1994) 5817

[12] Phang, Y. H., *et al.*, J. App. Phys., **74** (1993) 3181

[13] Salditt, T., *et al.*, Phys. Rev. B, **51** (1995) 5617

[14] Salditt, T., *et al.*, Physica B, **221** (1996) 13

[15] Paniago, R., *et al.*, Phys. Rev. B, **56** (1997) 13442

[16] Roth, S. V., *et al.*, App. Phys. Lett., **82** (2003) 1935

[17] Müller-Baschbaum, P., *et al.*, Europhys. Lett., **42** (1998) 517

[18] Barabási, A. -L., and Stanley, H. E., "Fractal Concepts in Surface Growth", Cambridge University Press (1995), chapter 2.

[19] Family, F., and Vicsek, T., "Dynamics of Fractal Surfaces", World Scientific, Singapore, (1991)

[20] Edwards, S. F., and Wilkinson, D. R., Proc. R. Soc. London A, **381** (1982) 1759

[21] Kardar, M., *et al.*, Phys. Rev. Lett. **56** (1986) 889

[22] Tang, C., *et al.*, Phys. Rev. Lett., **64** (1990) 772

[23] Salditt, T., *et al.*, Phys. Rev. Lett., **73** (1994) 2228

[24] Salditt, T., *et al.*, Europhys. Lett., **36** (1996) 565

[25] Salditt, T., *et al.*, Phys. Rev. B, **54** (1996) 5860

[26] den Broeder, F. J. A., *et al.*, J. App. Phys., **61** (1987) 4317

[27] Bruno, P., J. Phys. F: Met. Phys., **18** (1998) 1291

[28] Bruno, P., J. App. Phys., **64** (1988) 315

[29] Rozatian, A. S. H., PhD Thesis, University of Durham (2004), chapter 8

[30] Rozatian, A. S. H., *et al.*, J. Magn. Magn. Mat., **256** (2003) 365

[31] Rozatian, A. S. H., *et al.*, J. Phys: Condens. Matter, **17** (2005) 3759

[32] Ounadjela, K., *et al.*, Phys. Rev. B, **45** (1992) 7768

[33] Fassbender, J., *et al.*, Phys. Rev. B, **46** (1992) 5810

[34] Hamada, S., *et al.*, J. Magn. Magn. Mat., **240** (2002) 539

[35] Bal, K., *et al.*, J. App. Phys., **90** (2001) 5228

[36] Fit 2D software written by A. Hammersley of the ESRF, Grenoble, France

[37] Pym, A. T. G., *et al.*, J. Phys D: Appl. Phys., **38** (2005) A190

5 Interfaces with amorphous CoFeB

This chapter moves from the Co/Ru multilayers of the previous chapter by looking first at CoFe/Ru multilayers before boron is incorporated to form CoFeB/Ru multilayers. Finally the ruthenium is replaced by an oxide layer in multilayers of CoFeB/AlO_x which are used to investigate the interfaces often found in the active regions of Magnetic Tunnel Junctions.

5.1 Introduction

Metallic alloys mixed with a combination of metalloids such as boron, silicon or phosphorus, to produce an amorphous or nano-crystalline structure were first studied in the 1970's and became known as metallic glasses [1]. Industrial methods, involving quickly quenching a molten alloy on a cooled spinning drum to maintain an amorphous state, have enabled the production of continuous ribbons of the amorphous metals. One such brand is Metglas®, manufactured by Metglas® Inc., part of the Hitachi group of companies [2].

Magnetically, the Co-Fe-Metalloid amorphous metals show no significant directional anisotropy and have a very low coercivity making hysteretic losses extremely small. They have thus been used in transformer cores, amongst other applications [3]. In 1975 the first glassy cobalt-iron based materials using only boron as the metalloid were reported by O'Handley from the Allied Chemical Corporation [4]. They reported that these materials had a higher Curie temperature and room temperature saturation magnetisation than glassy alloys formed with the same content of cobalt and iron but several different metalloids.

At around the same time as the development of metallic glasses Julliere published the paper on tunnelling between ferromagnetic films and spin dependent scattering that led to the first spin valves [5]. However, it was twenty years before amorphous $CoFeB_{20\%}$ was grown by sputtering and included in spinvalves by Jimbo [6]. Until this time most of the Giant Magneto Resistive (GMR) structures used NiFe alloy films. Later Jimbo reported a maximum room temperature magneto-resistance of 6.5% in CoFeB/Cu/Co sandwiches when the amorphous CoFeB magnetic layer was 20Å thick [7].

With the invention of magnetic tunnel junctions in 1995 [8], cobalt-iron soon became an important electrode material and later, in 2002, the advantages of amorphous electrodes were incorporated into the structures [9]. TMRs as high as 70% at room temperature were reported in 2004 with CoFeB electrodes and an aluminium oxide based tunnel barrier [10]. Even more recently CoFeB has been employed with MgO barriers to give TMR values of 230% [11] and up to 500% in 'pseudo-spin-value' magnetic tunnel junctions [12].

The spin polarisation required for the operation GMR and TMR has been shown to be highly influenced by the electronic and structural nature of the interfaces [13] and thus it is crucial for the optimisation of device performance that the interface growth be under precise control. It is believed that the addition of boron improves the perfection of the interfaces by creating an amorphous structure that does not replicate the crystalline grain growth from the layer underneath. This has been confirmed by HRTEM measurements [10].

A low temperature annealing stage in the manufacture of the devices is often used to enhance the TMR performance in the manufacture of the MTJ devices [14]. Various explanations have been proposed, all relating to changes at the interfaces responsible for the spin-polarisation. In this chapter the structural nature of the interfaces is examined in detail using low-angle x-ray scattering, this time without a CCD detector, and confined to the q_zq_x plane.

Variations in the design of the MTJ electrodes, ranging from single layers to more complicated synthetic ferrimagnets, taking advantage of the oscillatory exchange coupling of Co, CoFe or CoFeB across non magnetic spacer layers, such as ruthenium as examined in the previous chapter, have been investigated by several researchers. Enhanced TMR has been reported and attributed to higher spin polarisation at the interface with the tunnel barrier in structures with CoFeB [10] and CoFe [15].

Instead of looking particularly at the frequency dependence of the correlated nature of the interfaces, as was done in the last chapter, now the emphasis is shifted to examine the changes occurring in the layers during relatively low temperature annealing (less than 500°C) of multilayers replicating the interfaces commonly found in magnetic tunnel junctions.

5.2 Samples under investigation

Multilayers were chosen to increase the amount of diffuse scatter, a crucial factor in separating the roughness and grading components within the interface width, and also the in-plane correlation length of the sample. They also have the advantage of producing Bragg peaks in the scatter, from the repeated bi-layer units, which are sensitive to the interfaces in the layers, a property that was used in the previous chapter to examine the correlation lengths of the interfaces. The multilayers also have both material A on B and B on A which are unlikely, through the growth kinetics, to have the same properties. In MTJs built with the same electrode material on both sides of the tunnel barrier both these interface configurations will be present and any breaking of symmetry will be of interest.

5.2.1 CoFe/Ru multilayer

This sample was grown by Susana Cardoso at INESC MN [16] on a Si/Al_2O_3 substrate and has a nominal structure:
Si/Al_2O_3/[$Co_{80\%}Fe_{20\%}$ (30Å)/Ru (7Å)]$_{x13}$/ $Co_{80\%}Fe_{20\%}$ (30Å)/Ru(30Å). It was grown by ion beam deposition in a Nordiko 3000 system, the details of which are reported in reference [17]. Both the CoFe and Ru layers are expected to show polycrystalline structure. The samples were grown on an Al_2O_3 buffer giving one interface in the structure that is present in an actual MTJ which can be studied by changes in the Kiessig fringes in the scatter.

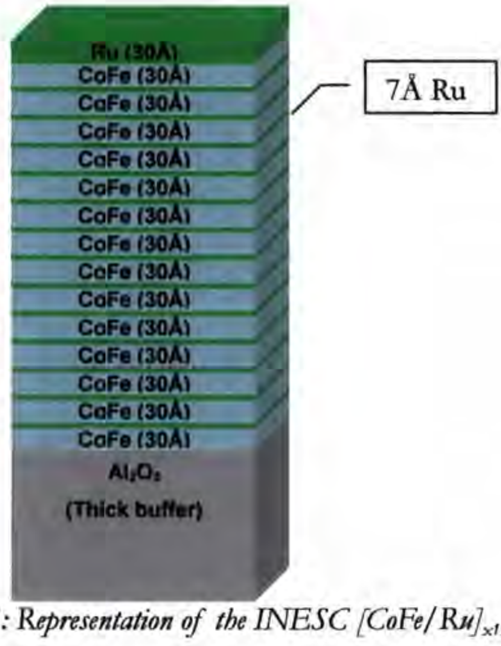

Figure 5-1: Representation of the INESC [CoFe/Ru]$_{x13}$ multilayer

The bulk equilibrium phase diagram of the Cobalt-Iron system predicts that at 80% Co composition the system adopts a mixed fcc and disordered bcc phase although in thin films this is known to stabilise into either an fcc [18] or a bcc phase [19] depending on the conditions. The lattice parameter varies nearly linearly for cobalt compositions between 30% and 80% and therefore obeys Vegard's law [20,21]. At 80% Co concentration a lattice parameter of 2.833Å is expected [22]. Cobalt has the highest magnetostriction coefficient of any element but by alloying it with iron this is dramatically reduced making it more suitable as an electrode material. Cobalt and ruthenium are miscible, however when cobalt is alloyed with iron the chemical affinity between the two reduces the miscibility with ruthenium [15] so the interfaces in the sample are expected to be relatively sharp.

5.2.2 CoFeB/Ru multilayer

This sample is the same as the previous CoFe/Ru multilayer except that the CoFe has been replaced by amorphous CoFeB. It was also grown at INESC MN under the same conditions as before. It has a nominal structure:
$Si/Al_2O_3/[Co_{64\%}Fe_{16\%}B_{20\%}$ (30Å)/Ru (7Å)$]_{x13}$/ $Co_{64\%}Fe_{16\%}B_{20\%}$ (30Å)/Ru(30Å).

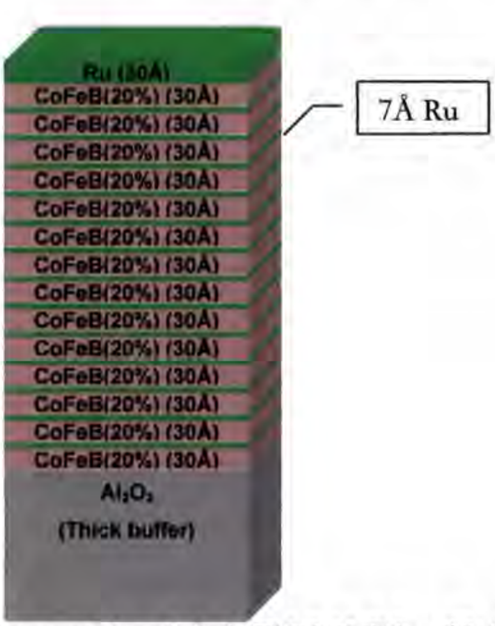

Figure 5-2: Representation of the INESC $[CoFeB_{20\%}/Ru]_{x13}$ *multilayer*

Boron is added to the CoFeB to prevent it crystallising and to form an amorphous or 'nano-crystalline' layer where no appreciable long range crystal structure is established. The ruthenium layers are expected to be polycrystalline. Above a certain temperature the amorphous CoFeB will crystallise into a polycrystalline state and the boron, which is known to dissolve appreciably in cobalt and iron transition metals, will sit in the interstitial sites. This phase is a true alloy exhibiting metallic properties [23]. If the proportion of boron is high then it will be expelled to the grain boundaries where mechanisms exist for longer range diffusion than is possible in thermally assisted diffusion either through an amorphous bulk material or through a crystal structure. The crystallisation temperature, not surprisingly, depends on the quantity of boron present in the sample. Reported crystallisation temperatures range from 280°C up to 320°C [24-26] depending on the exact boron content. The crystallisation process has been examined in detail for iron-rich (in contrast to the samples examined here) bulk $Co_xFe_{85-x}B_{15}$ where a two stage crystallisation process was observed. At a temperature of about 410°C iron was precipitated, followed at a higher temperature by the formation of metastable Fe_3B and crystalline cobalt (cubic and hexagonal) [27].

5.2.3 CoFeB/AlO$_x$ multilayer

The sample investigated was grown by magnetron sputtering by Theo Dimopoulos at Siemens, Erlangen, on a thermally oxidised Si substrate and has the nominal structure: SiO_2 / Ta (50Å) / $[Co_{60\%}Fe_{20\%}B_{20\%}(30Å)/ Al(12Å)+oxidation]_{x5}$ / Ta(50Å). Five repeats were chosen because of time constraints on the crystal growers.

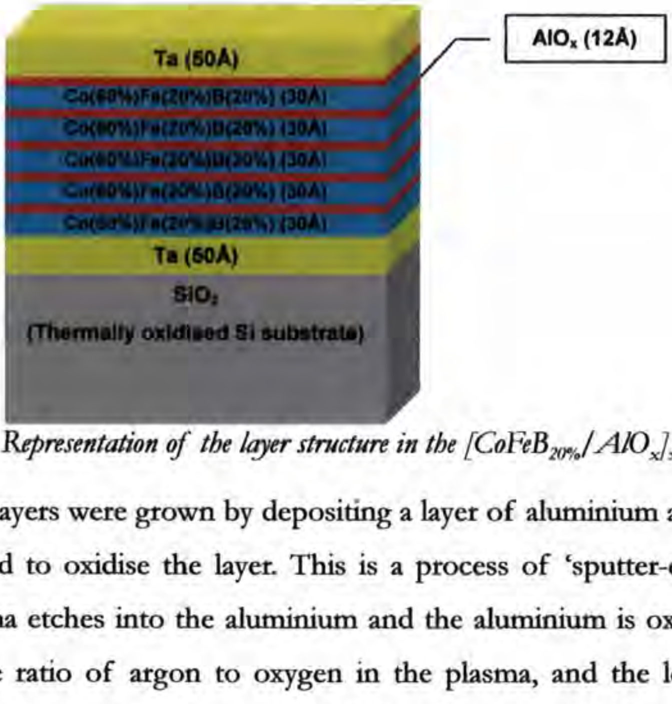

Figure 5-3: Representation of the layer structure in the $[CoFeB_{20\%}/AlO_x]_{x5}$ *multilayer*

Aluminium oxide layers were grown by depositing a layer of aluminium and then an Ar/O_2 plasma was applied to oxidise the layer. This is a process of 'sputter-etching' where the argon in the plasma etches into the aluminium and the aluminium is oxidised at the same time [28,29]. The ratio of argon to oxygen in the plasma, and the length of time the plasma is applied to the sample, are crucial in achieving complete oxidation of the aluminium without oxidising the under-layer as well. The thickness of the AlO$_x$ is typically 30% more than that of the Al originally deposited [30]. The stoichiometry of such layers is not exactly Al_2O_3 and so the material is commonly referred to as AlO$_x$ in the literature.

5.3 Experimental details

Grazing incidence reflectivity measurements, with *in-situ* annealing, were performed on station 2.3 of the Daresbury SRS, the details of which have been given in section 3.5. The benefits of performing the experiment *in-situ* include;

a) the use of an identical sample throughout the experiment avoiding any effects from variations between samples;

b) any time dependent variation can be examined through making repeated measurements over a long period of time; and

c) the incident intensity can be accurately known and any variation normalised out (assuming no movement of the incident beam on the slits).

During annealing the sample stage column expands with temperature, moving the sample's position relative to the centre of the beam. The thermal expansion coefficient of iron is 1.2×10^{-5} °C^{-1}[31], so for 1cm , which is roughly the length of the column in the RF coils, being heated by 100°C the change in length will be around 12μm. In a beam of width 200μm this will be a noticeable movement off the centre-of-rotation. The individual layer thicknesses within the sample are so small, typically 30Å, that thermal expansion can be ignored. Periodically throughout the following annealing experiments the half-cut of the sample in the beam was adjusted to prevent the movement off the centre of rotation having a significant effect on the measured data. To change the sample height the whole column has to be rotated which affects the positioning of the sample in the beam and hence also the beam footprint at low angles. The sample's height was always aligned out of vacuum and then the chamber pumped down, or filled with argon, before the height was checked again to avoid large rotations of the sample. During the annealing experiments it was never necessary to rotate the sample by more than a few degrees to set the height. At these angles the change in footprint at low angles will be negligible.

CoFe/Ru and CoFeB/Ru multilayers:

Measurements were recorded for the CoFe/Ru and CoFeB/Ru multilayers in vacuum to prevent oxidation of the top surface. The vacuum chamber available, however, was not able to sustain a very high vacuum, and the pressure rose to typically around 5 to 10mbar. The sample height adjusting mechanism involves an O-ring being under compression. As the sample's height was lowered to compensate for thermal expansion at higher temperatures the compression on this ring was reduced and the quality of vacuum was seen to fall. The wavelength selected for the experiments was 1.3Å.

CoFeB/AlO$_x$ multilayers:

In the later experiments on a CoFeB/AlO$_x$ multilayer a high purity argon atmosphere was used at a slight overpressure to prevent atmospheric oxygen entering the furnace. This has the disadvantage of increasing the level of x-ray attenuation within the experiment but eliminates any effects of oxidation from the poor vacuum. The chamber, after being sealed, was typically flushed through with argon for 20minutes before measurements were taken. The wavelength chosen for the experiments was 1.3Å.

5.4 CoFe/Ru multilayer

5.4.1 Room temperature specular scatter and simulation

The specular scatter is shown in Figure 5-4 below and fitting was performed in Bede REFS software (see details in section 3.7.1). The fitted parameters are shown in Table 5-1 below. Good specular scatter was observable up to a sample angle of 4° with four Bragg peaks visible. It was not possible to fit all the Bragg peaks with constant interface widths in the repeated bi-layer stack. The number of free parameters in the fit was gradually increased until a satisfactory fit to the data was achieved with all the parameters being physically plausible. The simplest structure found was when the CoFe/Ru layers were split up into three sub-stacks. This is sufficient to allow for dispersion in the sample structure and accounts for the Bragg peak broadening at higher angles. The Kiessig fringes are seen to disappear above the 2nd Bragg peak, which has been found, through simulating many different structures, to be indicative of a structure where the interfaces widths either systematically increase or decrease through the stack.

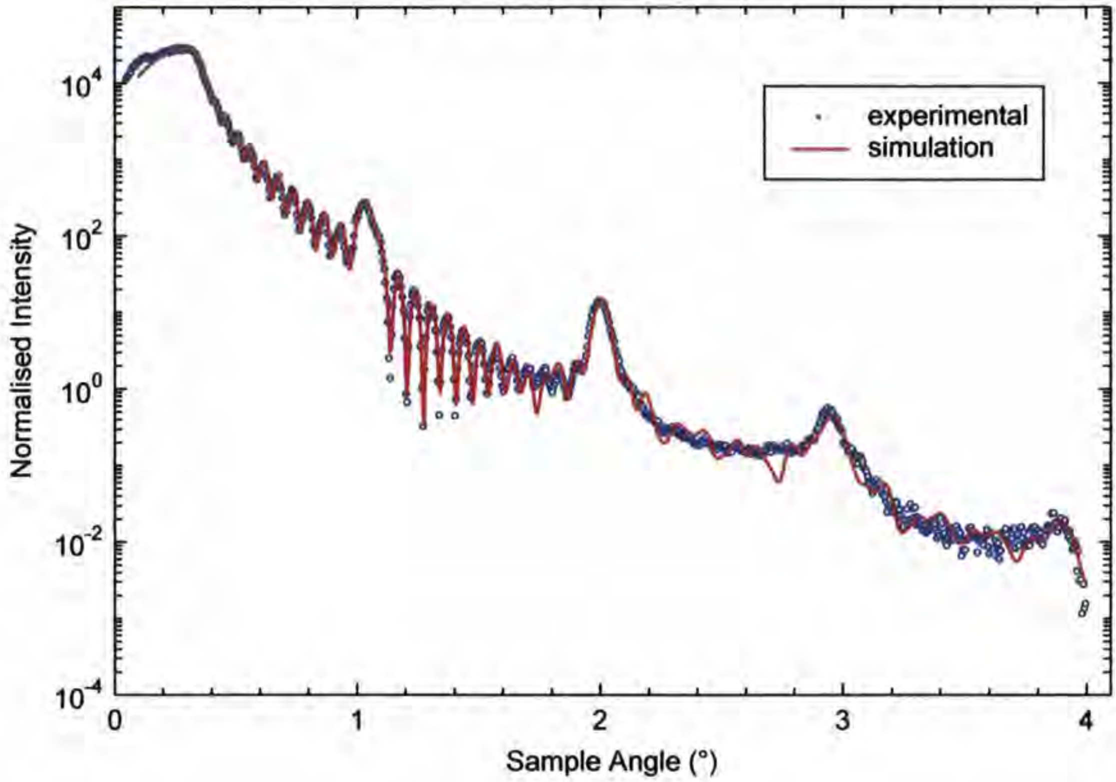

Figure 5-4: Specular scatter and simulation of a $[CoFe/Ru]_{x13}$ *multilayer.*

Layer		Material	Thickness (Å)	Density (% of bulk)	Upper Interface Width (Å)
29		RuO_2	1.2 ± 1.9	89 ± 62	6.61 ± 0.85
28		Ru	26.5 ± 1.9	90.5 ± 3.3	10.6 ± 4.3
27		$Co_{0.8}Fe_{0.2}$	28.56 ± 0.97	100 ± 1.8	6.18 ± 0.61
17-26	x5	Ru	6.7 ±3.7	91 ± 11	4.80 ± 0.38
		$Co_{0.8}Fe_{0.2}$	30.9 ± 3.7	98.9 ± 1.6	6.7 ± 1.8
9-16	x4	Ru	6.8 ± 1.4	91.3 ± 4.5	3.54 ± 0.17
		$Co_{0.8}Fe_{0.2}$	30.9 ± 1.3	97.5 ± 1.8	5.35 ± 0.81
1-8	x4	Ru	6.87 ± 0.28	90.4 ± 1.8	2.88 ± 0.16
		$Co_{0.8}Fe_{0.2}$	30.82 ± 0.29	94.5 ± 2.0	3.77 ± 0.25
Thick buffer		Al_20_3	∞	90.8 ± 4.6	2.57 ± 0.06

Table 5-1: Model to fit the specular scatter from a $[CoFe/Ru]_{x13}$ *multilayer. The multilayer has been split into three separate repeated structures to allow evolution of the interface width as the sample grows.*

The densities of the ruthenium layers are low, being near 91% of the value of single crystal bulk ruthenium. This is not surprising given the thin and polycrystalline nature of the layers. The thickness values are very close to the nominal values of 30Å and 7Å for CoFeB and Ru respectively. The interface widths are plotted in Figure 5-5 below and show an increase in the widths of the CoFe and Ru layer interfaces as the stack thickness increases, the Ru/CoFe interface being smoother than the CoFe/Ru interface. The relation appears to be linear, although with only the limited number of free parameters this may be fortuitous. There is no observable dispersion in the layer thicknesses or densities within the error bars.

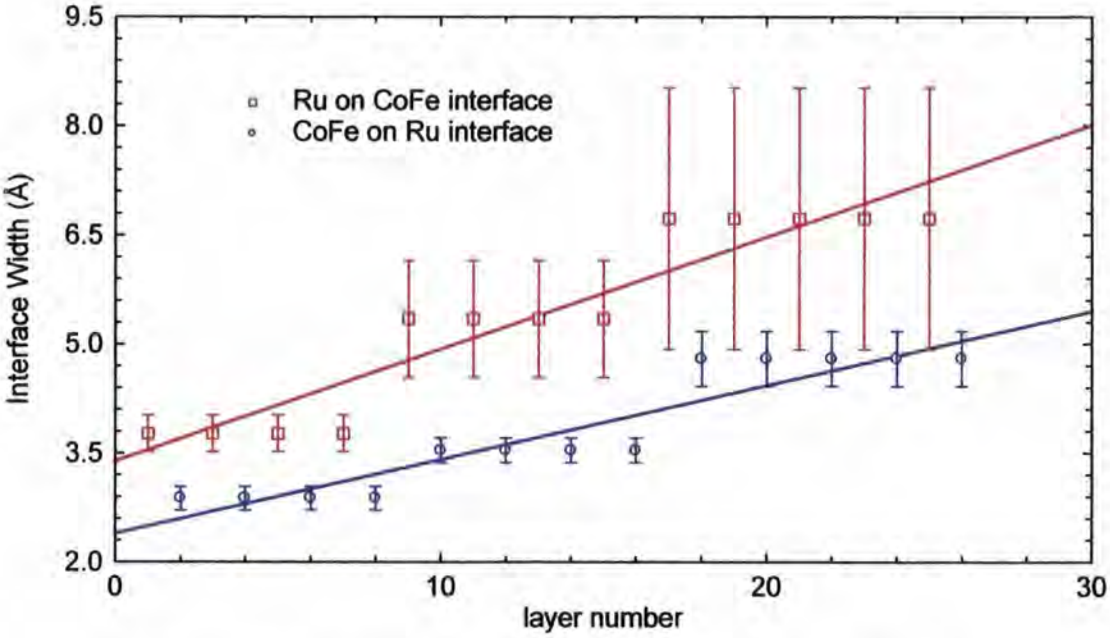

Figure 5-5: Interface widths derived from the fitting of the specular scatter.

5.4.2 Room temperature diffuse scatter

Bragg peaks are visible in the off specular scatter, shown below in Figure 5-6, indicating a relatively large out-of-plane correlation length. The Kiessig fringes are not visible indicating that the top and bottom surfaces are not correlated and that the out-of-plane correlation length does not extend through the whole height of the repeated stack.

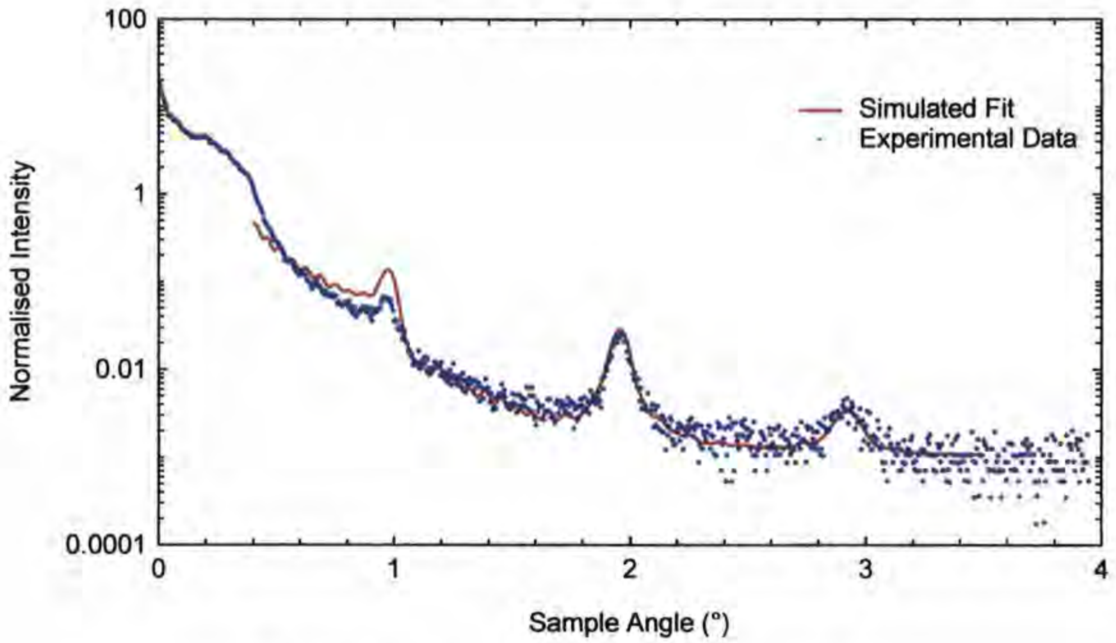

Figure 5-6: Off specular scatter and simulation from the CoFe/Ru multilayer at room temperature.

Fitting of this curve has been achieved with the identical parameters to those in Table 5-1 above but with the interface widths broken down into topological roughness and inter-diffusion as shown in Table 5-2 below. Simulations of an interface solely formed of topological roughness produce too much diffuse scatter and so there must be an element of grading, or inter-diffusion, between layers. The fit has been obtained manually by setting the roughness values and adjusting the amount of grading to compensate in quadrature and keep the interface width constant. This way the specular scatter is unaltered. The scatter below 0.4° is heavily dominated by geometrical considerations and the simulated scatter has not been plotted.

In-plane correlation length: 140Å ± 30Å

Out-of-plane correlation length: 300Å ± 100Å

Fractal parameter: 0.7 ± 0.3

Layer		Material	Roughness(Å)	Grading (Å)	Total Interface Width (Å)
29		RuO_2	5	4.3	6.61 ± 0.85
28		Ru	5	9.3	10.6 ± 4.3
27		$Co_{0.8}Fe_{0.2}$	5	3.6	6.18 ± 0.61
17-26	x5	Ru	3	3.8	4.80 ± 0.38
		$Co_{0.8}Fe_{0.2}$	5	4.5	6.7 ± 1.8
9-16	x4	Ru	3	1.9	3.54 ± 0.17
		$Co_{0.8}Fe_{0.2}$	4	3.6	5.35 ± 0.81
1-8	x4	Ru	1.5	2.5	2.88 ± 0.16
		$Co_{0.8}Fe_{0.2}$	1.5	3.5	3.77 ± 0.25
Thick buffer		Al_2O_3	1.5	2.1	2.57 ± 0.06

Table 5-2: Roughness and inter-diffusion properties of the interfaces for the CoFe/Ru multilayer at room temperature

Using the identical model as that used to fit the specular and off-specular data, the transverse diffuse simulations, shown in Figure 5-7 and Figure 5-8 below, are in good agreement with the experimental data.

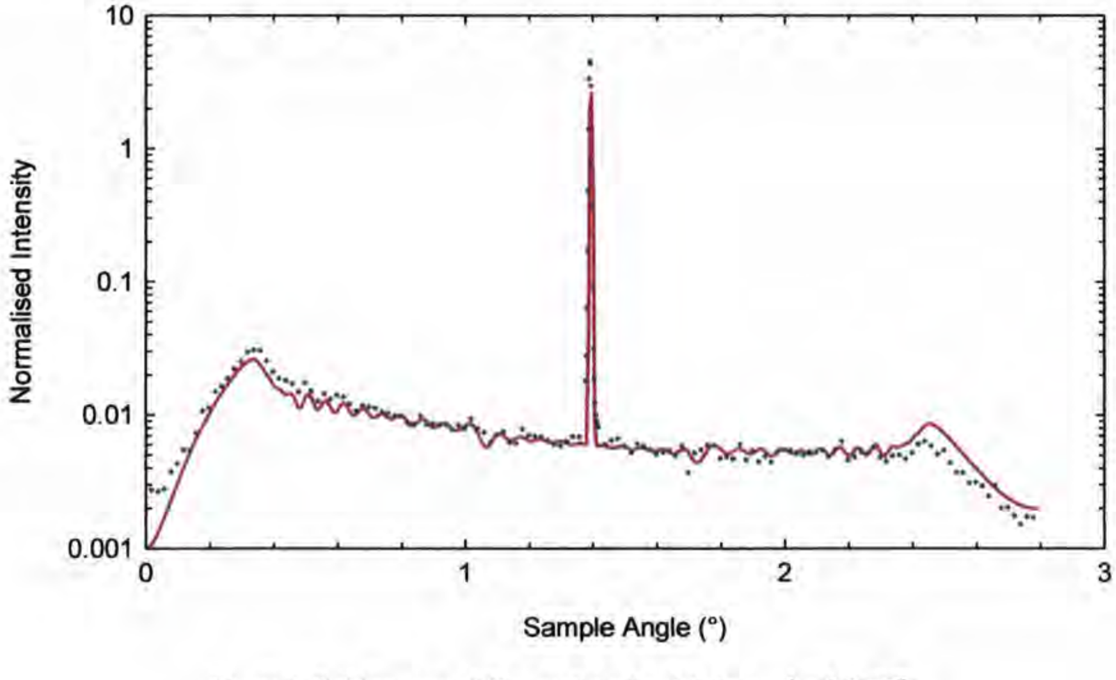

Figure 5-7: Transverse diffuse scatter at a detector angle of 2.79°

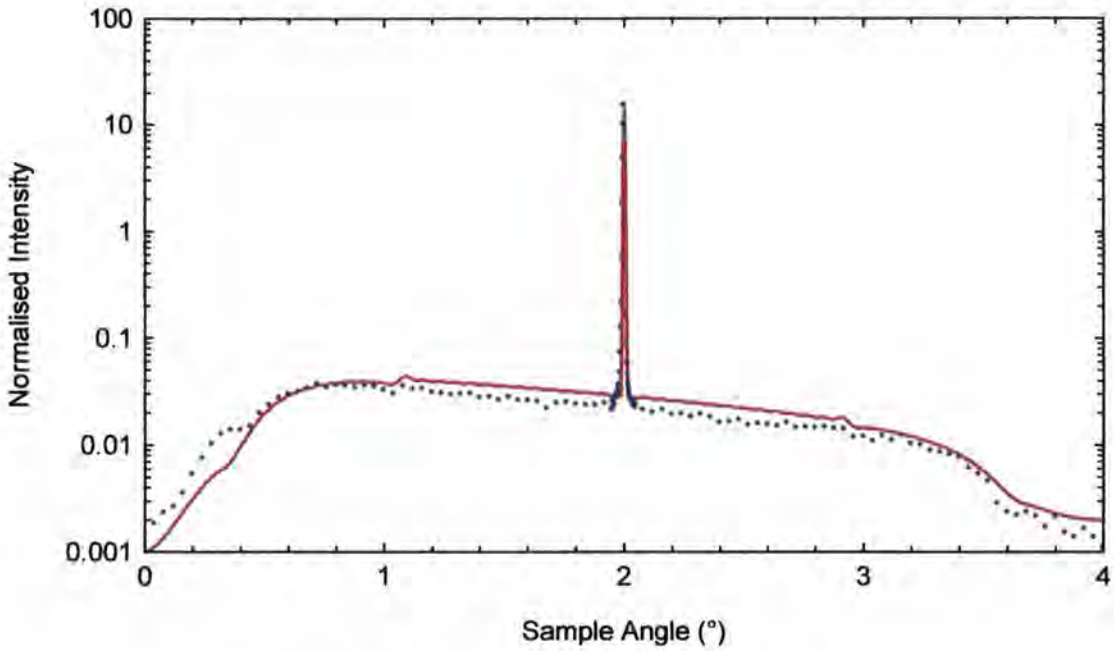

Figure 5-8: Transverse diffuse scatter at a detector angle of 4°

From the shape of both these curves it is seen that the in-plane correlation length is very short indeed and has been fitted to 140Å ± 30Å. At these short distances the fractal parameter has very little influence on the scatter and hence the precision of ±0.3 is low. The characteristic oscillation at 1° from the extreme values of both transverse scans is a dynamical effect of the first Bragg peak showing in the q_x diffuse scatter. This feature is present in both the simulation and the experimental data and arises from purely dynamical effects [32]. These features have been discussed more fully in section 2.5.3 above.

5.4.3 Effect of annealing on the specular and off-specular scatter

The specular and off-specular scatter is shown in Figure 5-9 and Figure 5-10 below for various temperatures from room temperature up to 300°C.

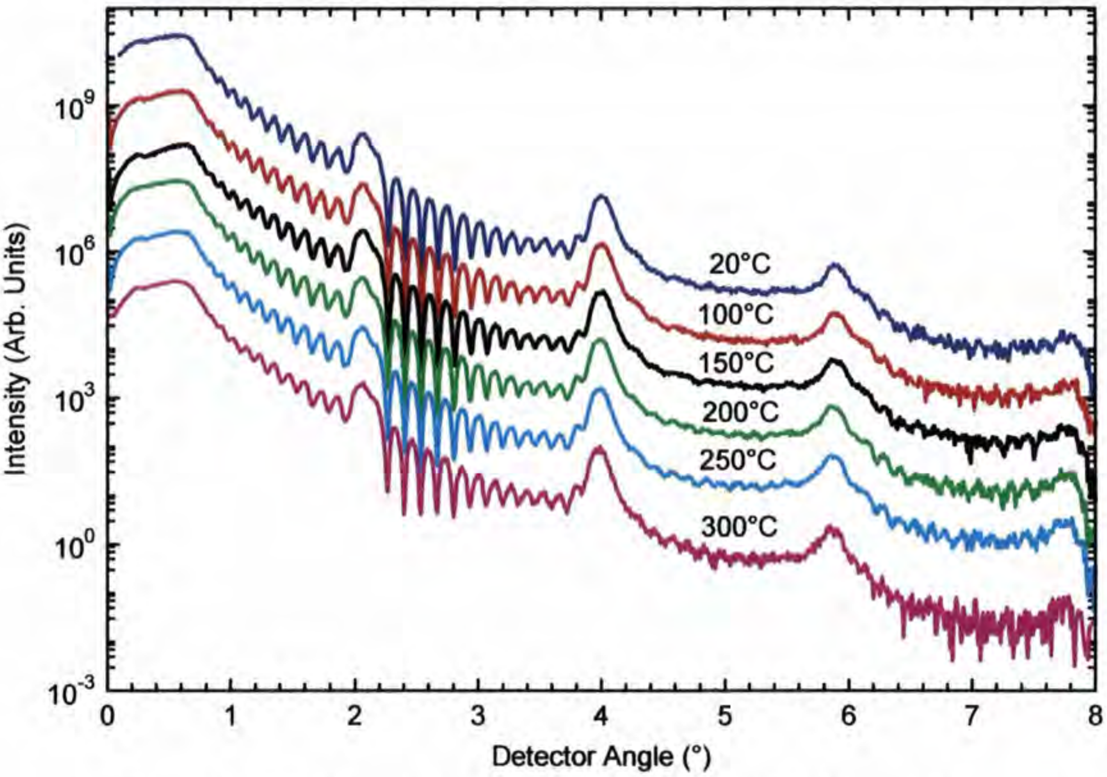

Figure 5-9: Effect of annealing on the specular scatter in a CoFe/Ru multilayer. The curves have been offset by factors of 10 for clarity

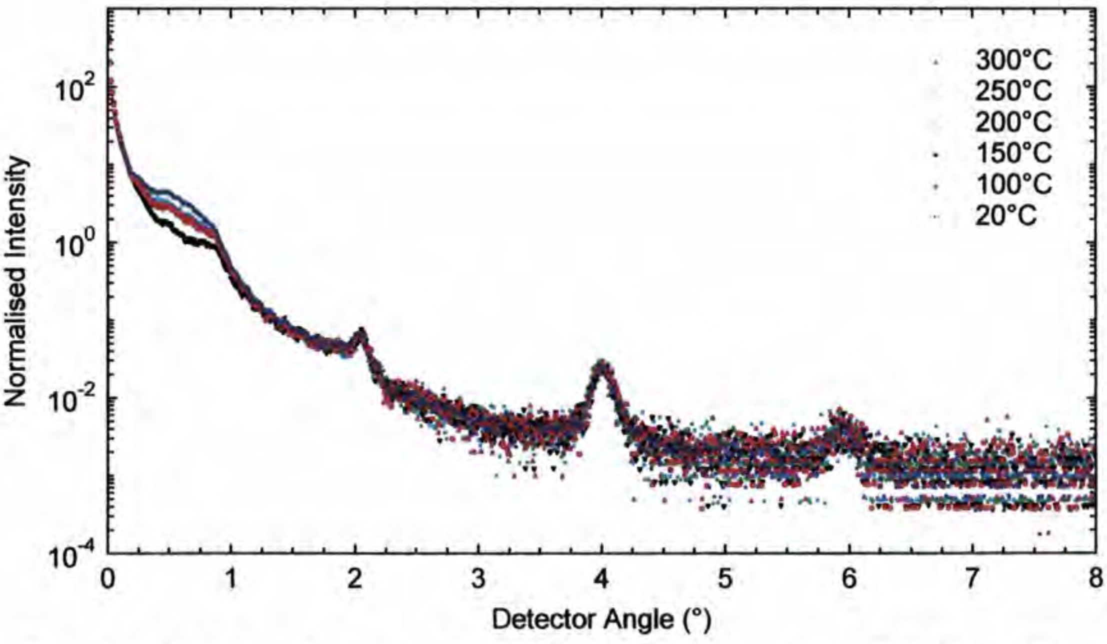

Figure 5-10: The off-specular scatter at different annealing temperatures from a CoFe/Ru multilayer

No variation of the specular or off-specular scatter is observed and therefore no change of the sample structure can be measured on annealing. The changes occurring below the critical angle are associated with small changes in the sample alignment. Within the furnace the sample is mounted on a copper plate to conduct the heat from the crucible, which couples to the RF field, to the sample. The temperatures shown are those measured with a thermocouple in contact with the crucible through a drilled hole in the top rim. Full details of the experimental setup have been given in section 3.5.

5.4.4 Effect of annealing on the transverse diffuse scatter

The transverse diffuse scans at different temperatures are shown in Figure 5-11 and Figure 5-12 below.

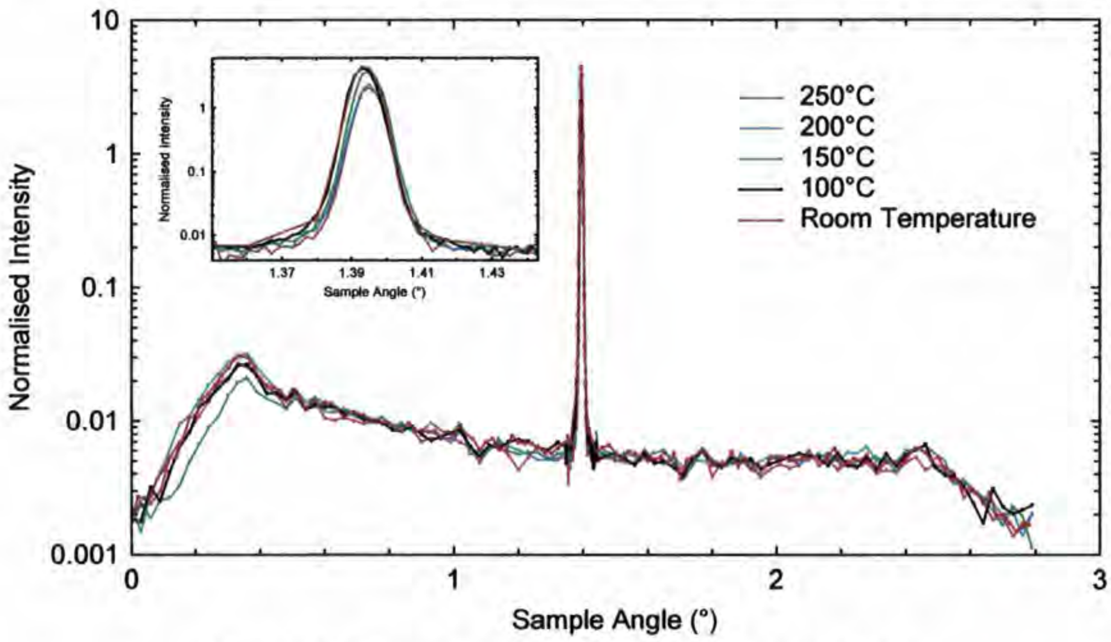

Figure 5-11: Transverse diffuse scatter at a detector angle of 2.79°

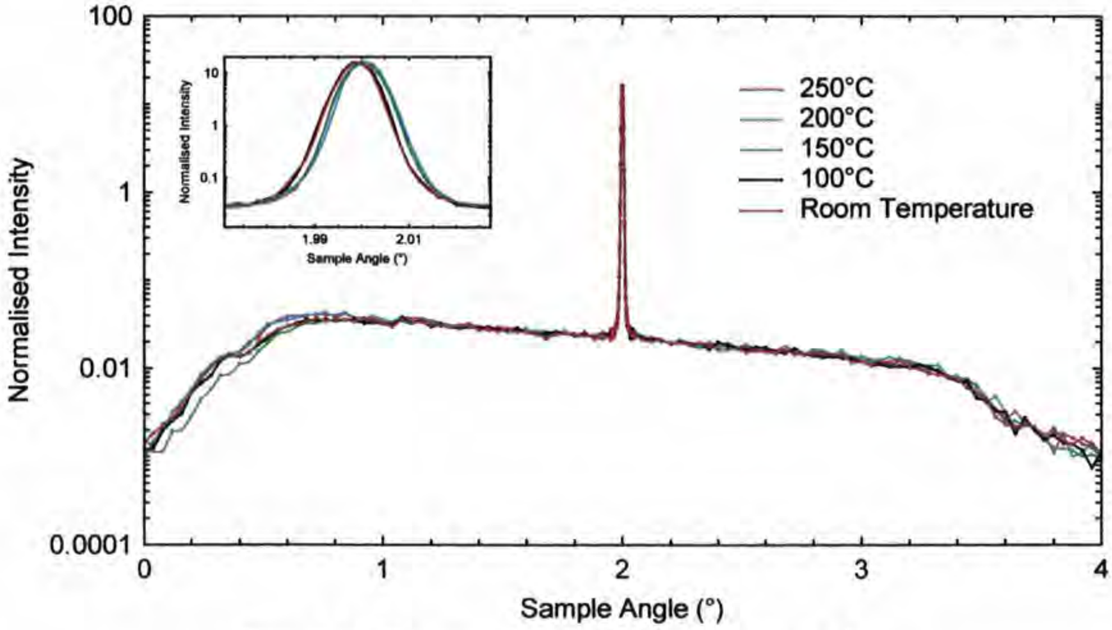

Figure 5-12: Transverse diffuse scan at a detector angle of 4°

The scatter recorded at 150°C at low angles is less intense than the other scans which is a result of slight height misalignments through thermal expansion. This has been described more fully in section 3.4. No significant changes are seen in the diffuse scatter at different temperatures, showing that the interfaces are stable and there is no change in the roughness or grading components of the interface widths, and also the associated fractal parameters and correlation lengths.

5.4.5 Interpretation and discussion

The evolution of the interfaces with thickness is observed and shown by the increase in the RMS roughness as the stack is grown. It is not possible to separately identify an h or ξ value for each layer. As shown in Figure 5-5 above, there is a systematic difference when the CoFe/Ru and Ru/CoFe interfaces are compared, with the latter being smoother. However, there are two competing processes; the deposition of the Ru appears to be having a smoothing effect on the underlying surface whereas the growth of iron-cobalt leads to roughening. The roughness remains correlated from one surface to the next as demonstrated by the existence of Bragg peaks in the longitudinal diffuse scatter. There is a very small in-plane correlation length, evident from the transverse diffuse scans, indicative of very small crystallites in the samples.

No change in the scatter, and therefore the structure, has been seen on annealing the CoFe/Ru samples up to 300°C. This is understandable as both the CoFe and Ru layers are in stable polycrystalline states. No evidence is observed of there being any change in the interface between the substrate and the bottom CoFe layer. The whole structure appears to be thermally stable. Importantly for the work presented later in the thesis is the observation that there is no measurable change to the top surface oxide layer during the annealing, even in the relatively poor vacuum present.

The work of Svedberg *et al.* at Seagate on diffusion in $Co_{90\%}Fe_{10\%}$/Ru multilayers, heated in the temperature range 450°C to 540°C, showed that inter-diffusion between layers, resulting in the decrease in intensity of higher order specular reflectivity Bragg peaks, only becomes appreciable at temperatures approaching 500°C [33]. They reported a high activation energy of 4.95eV. The results here confirmed that at lower temperatures in the slightly different $Co_{80\%}Fe_{20\%}$ system there is no indication of inter-diffusion and the structure is thermally stable.

5.5 CoFeB/Ru multilayer

5.5.1 Room temperature specular scatter and simulation

The room temperature specular scatter of the CoFeB/Ru multilayer and the specular scatter from the multilayer examined previously without boron are compared in Figure 5-13 below.

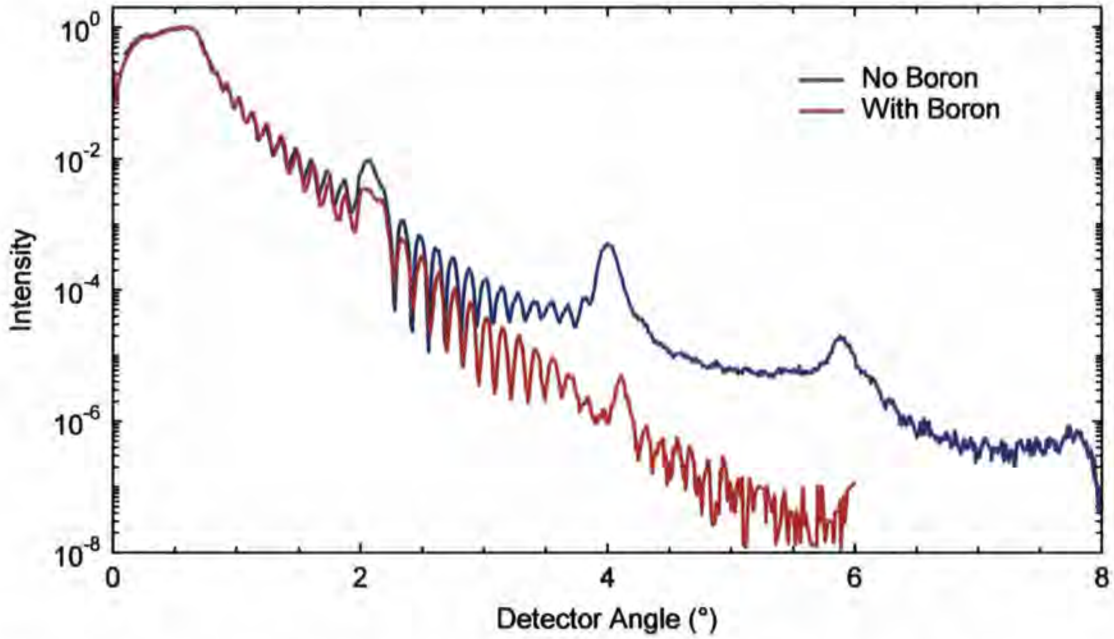

Figure 5-13: Comparison of the true specular scatter from the multilayers with and without boron added. Both curves have been normalised to 1 at the critical angle.

The increased rate of fall of the specular scatter in the CoFeB/Ru multilayer compared with that from the CoFe/Ru multilayer indicates that the addition of boron has led to much wider interfaces. The specular scatter has been fitted in Figure 5-14 below and the fitted parameters are shown in Table 5-3 below. It was necessary to break the multilayer into separate repeated units to get agreement with the Bragg Peak widths, as was the case with the CoFe/Ru multilayer. Within the errors no systematic dispersion in either layer thickness or the interface widths could be identified.

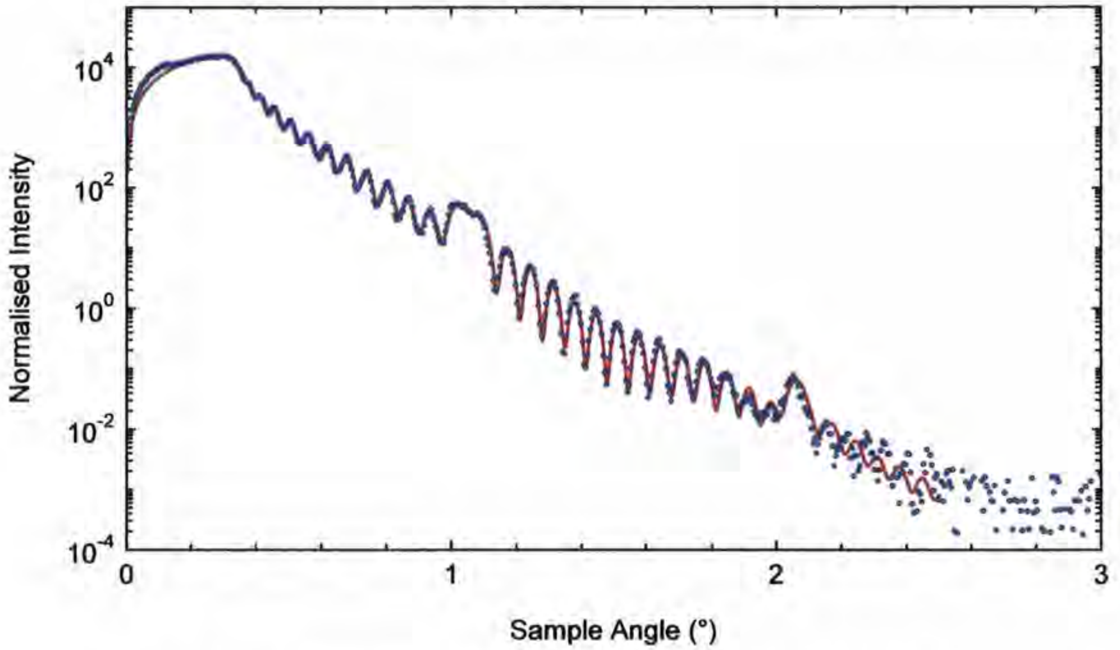

Figure 5-14: experimental data and simulation of the true specular scatter.

Layer		Material	Thickness (Å)	Density (% of bulk)	Interface Width (Å)
29		RuO_2	9.7 ± 3.3	79 ± 33	5.83 ± 0.43
28		Ru	29.2 ± 3.9	88.2 ± 2.2	8.4 ± 1.8
27		$Co_{0.64}Fe_{0.16}B_{0.2}$	26.6 ± 1.4	102.1 ± 5.0	8.68 ± 0.63
17-26	x5 {	Ru	10.9 ± 1.1	86.2 ± 4.1	11.7 ± 2.4
		$Co_{0.64}Fe_{0.16}B_{0.2}$	26.2 ± 1.1	99.8 ± 4.1	7.05 ± 0.25
9-16	x4 {	Ru	10.6 ± 1.0	83.8 ± 3.8	10.0 ± 2.3
		$Co_{0.64}Fe_{0.16}B_{0.2}$	26.5 ± 1.0	103.0 ± 4.0	6.83 ± 0.23
1-8	x4 {	Ru	12.1 ± 1.3	84.3 ± 4.1	8.05 ± 0.83
		$Co_{0.64}Fe_{0.16}B_{0.2}$	26.0 ± 1.2	103.3 ± 5.6	7.76 ± 0.67
Thick buffer		Al_20_3	∞	95 ± 17	7.22 ± 0.30

Table 5-3: Model to fit the specular scatter from a $[CoFeB/Ru]_{x13}$ multilayer.

Again the ruthenium densities are low, at around 91%. If this was not viewed in the light of the CoFe/Ru multilayer discussed earlier then it would be tempting to ascribe this to boron incorporation into the layers. However, they are consistent with this previous sample and appear to result from the deposition conditions.

5.5.2 Room temperature diffuse scatter

The off-specular scatter is compared with the previous sample in Figure 5-15 below and with a simulation in Figure 5-16 below.

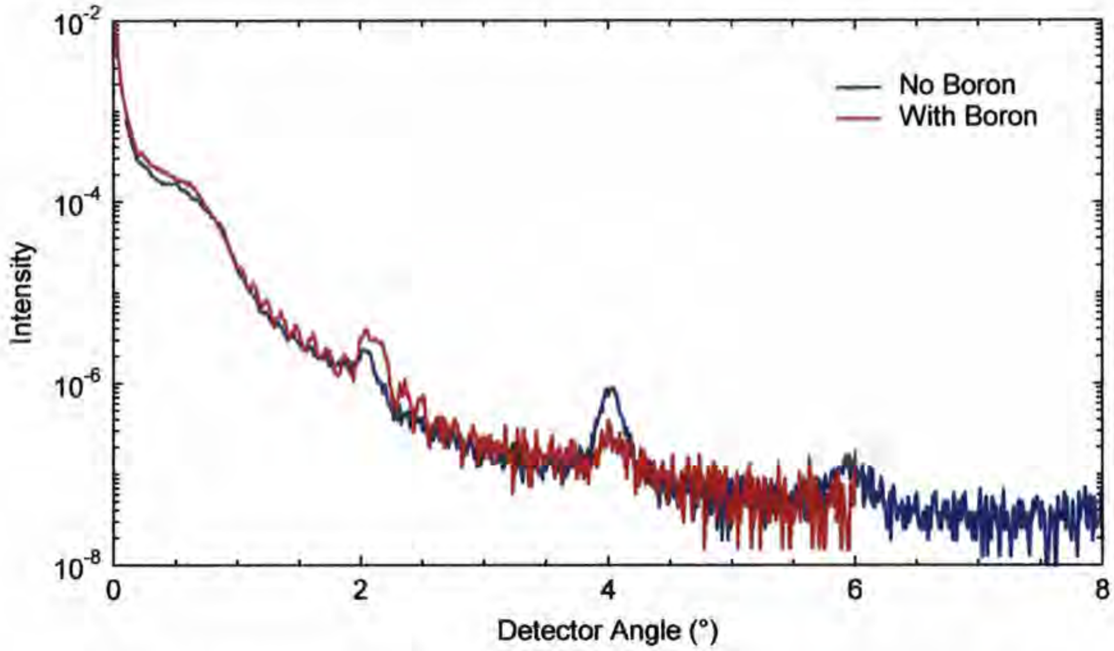

Figure 5-15: Comparison of the off-specular scatter from the multilayers with and without boron. Both curves have been normalised by applying the same factor as that used to normalise the corresponding true specular scatter.

The intensity profile of the off-specular scatter is broadly the same between the two samples, suggesting that the topological roughness is similar. The additional interface width from the specular scatter must therefore be a result of increased grading, or inter-diffusion, in the sample containing boron.

The Kiessig fringes are clearer in the sample with the boron which implies that the out-of-plane correlation length is greater in this sample. The boron, whilst causing a wider interface, appears to be improving the conformality between the layers. By disrupting the formation of small crystallites the interfaces appear to have grown more evenly, with a greater conformality being propagated through the stack. The second order off-specular Bragg peak from the sample without boron is of higher intensity than with boron which is related to the interfaces being narrower, as has been identified from the rate of fall of the specular scatter. The simulated fit to the off-specular scatter is shown in Figure 5-16 below and the tabulated parameters used are shown in Table 5-4 below.

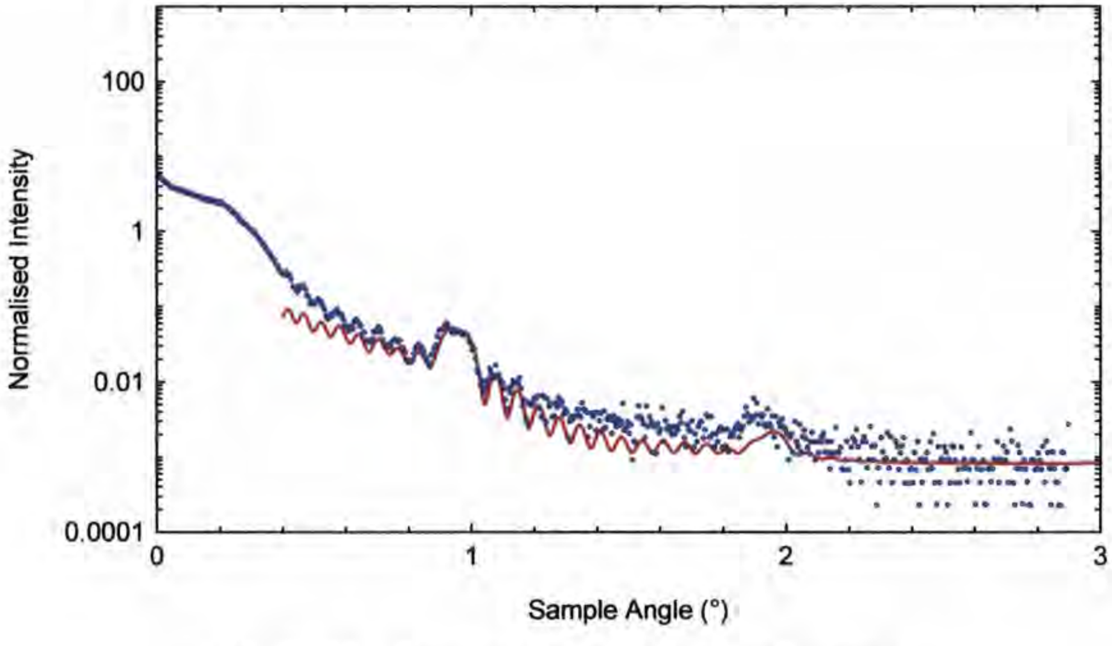

Figure 5-16: Experimental off-specular scatter and simulation

In-plane correlation length: 80Å ± 20Å

Out-of-plane correlation length: 1500Å ± 250Å

Fractal parameter: 0.7 ± 0.3

Layer		**Material**	**Roughness(Å)**	**Grading (Å)**	**Total Interface Width (Å)**
29		RuO_2	5	3.0	5.83 ± 0.43
28		Ru	6	5.8	8.4 ± 1.8
27		$Co_{0.64}Fe_{0.16}B_{0.2}$	6	6.3	8.68 ± 0.63
17-26	x5	Ru	7	9.4	11.7 ± 2.43
		$Co_{0.64}Fe_{0.16}B_{0.2}$	6	3.7	7.05 ± 0.25
9-16	x4	Ru	7	7.2	10.0 ± 2.3
		$Co_{0.64}Fe_{0.16}B_{0.2}$	6	3.3	6.83 ± 0.23
1-8	x4	Ru	6	5.4	8.05 ± 0.83
		$Co_{0.64}Fe_{0.16}B_{0.2}$	6	4.9	7.76 ± 0.67
Thick buffer		Al_2O_3	6	4.0	7.22 ± 0.30

Table 5-4: Roughness and inter-diffusion properties of the interfaces for the CoFeB/Ru multilayer at room temperature

The transverse diffuse scans measured at detector angles of 1.6°and 2.1° are shown in Figure 5-17 and Figure 5-18 below.

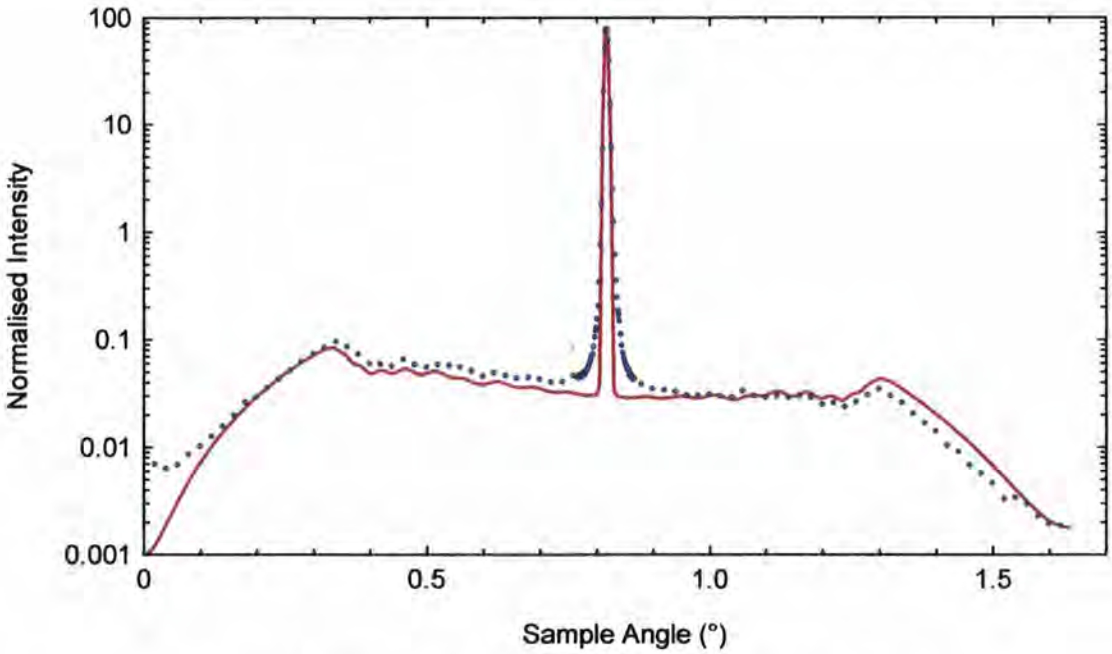

Figure 5-17: Transverse Diffuse scatter at a detector angle of 1.6°

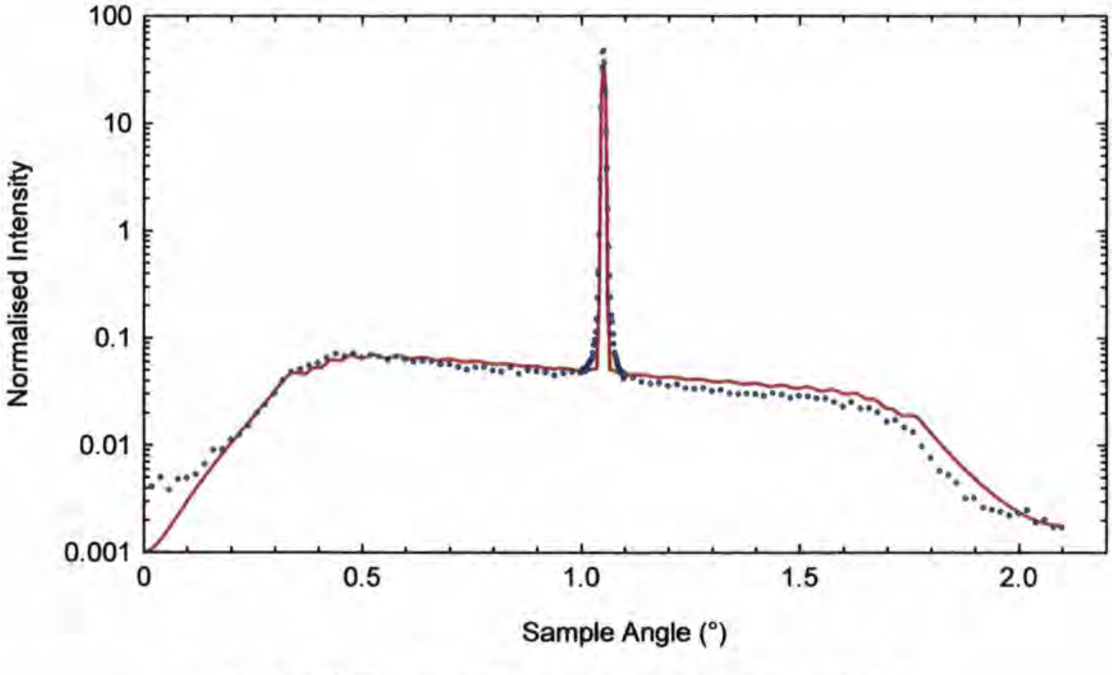

Figure 5-18: Transverse diffuse scatter at a detector angle of 2.1°

Again the transverse scans show that a very short in-plane correlation length is present in these samples. The out-of-plane correlation length, however, is much greater, showing there is much more conformality between the layers despite the increased interface width.

5.5.3 Effect of annealing on the specular and off-specular scatter

The specular scatter recorded at different temperatures ranging from 20°C to 400°C is shown in Figure 5-19 below.

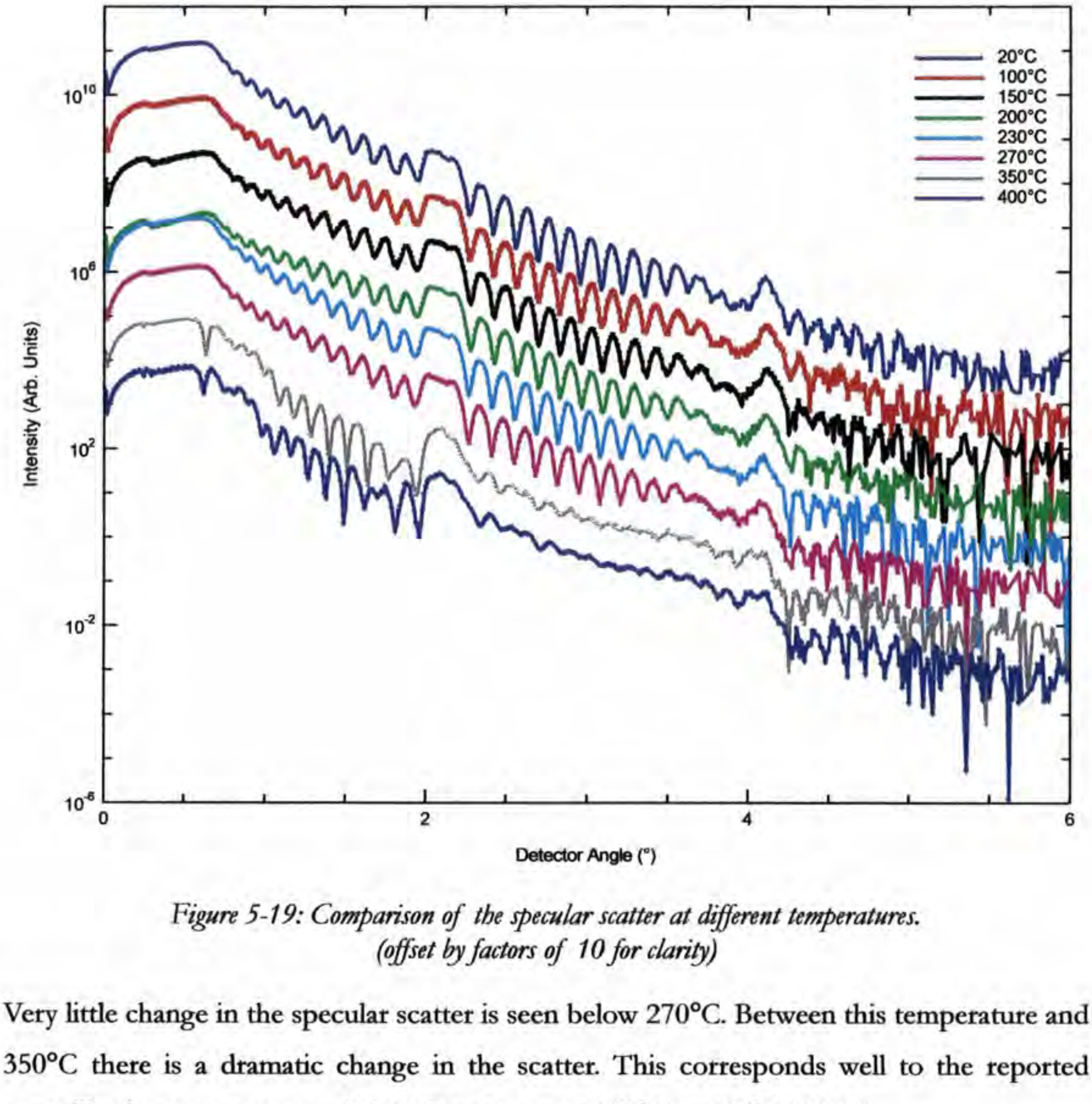

Figure 5-19: Comparison of the specular scatter at different temperatures. (offset by factors of 10 for clarity)

Very little change in the specular scatter is seen below 270°C. Between this temperature and 350°C there is a dramatic change in the scatter. This corresponds well to the reported crystallisation temperature of CoFeB of between 280°C to 320°C [22-24].

There are some small changes in the specular scatter between 20°C and 350°C in isolated regions, such as immediately before the 2nd Bragg Peak. These Kiessig fringes originate from interference between the top surface and bottom interface in the stack. The small changes are unlikely to be a result of changes in the top surface as nothing was seen in the Ru/CoFe, suggesting that the sample is not oxidising, therefore it has most probably been caused at the bottom CoFeB/Al_2O_3 interface.

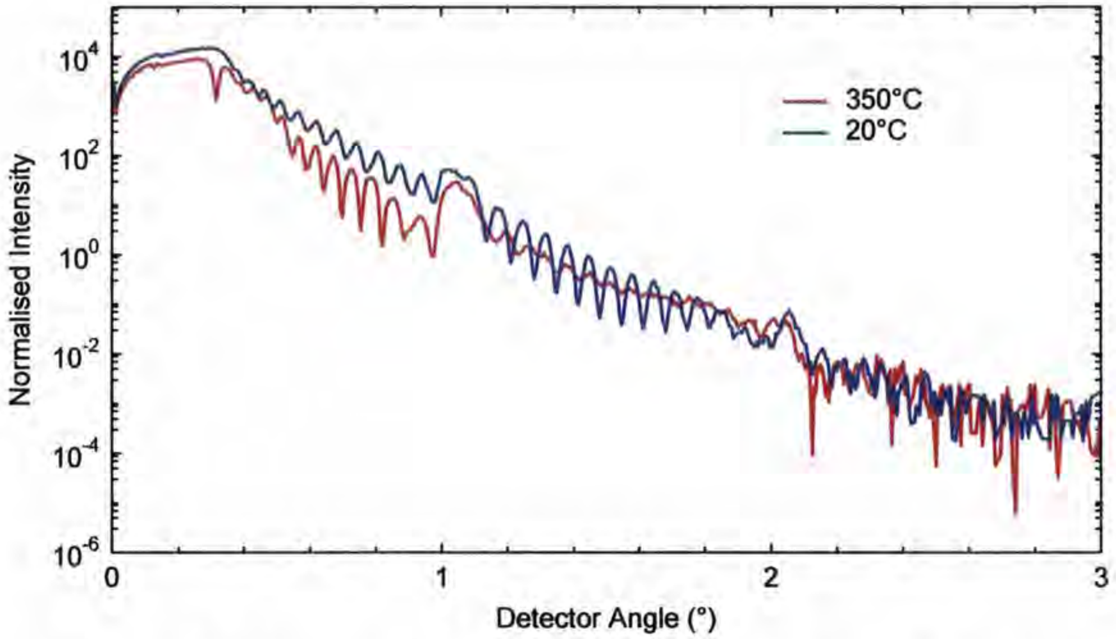

Figure 5-20: Comparison of the specular scatter above and below the crystallisation temperature of the CoFeB.

Kiessig fringes are still visible at 350°C showing that there is still conformality between the top and bottom layers after crystallisation. Indeed the Kiessig fringes below the 1st Bragg peak have increased in amplitude. Also, the Bragg peak stays in the same position. However, the most significant changes occur at the critical angle, where there is a sharp fall in the intensity before a second critical angle appears, and between the 1st and 2nd Bragg peaks where the Kiessig fringes are all but lost. The intensity at the critical angle is also reduced. However, low angle scatter is particularly sensitive to the beam footprint, which may, through thermal expansion of the sample stage assembly, have been reduced through spill-off onto the sample stage. This has been discussed more fully in section 3.4.

From the initial decrease in the specular scatter it is deduced that the interface widths have increased as a result of the annealing. However as there is little change in the scatter below 350°C the abrupt change appears to be due to crystallisation rather than increased atomic diffusion.

5.5.4 Simulation of the 350°C specular scatter

Simulation of the specular scatter for the high temperatures has proven difficult. The simulation of the specular scatter at 350°C is shown in Figure 5-21 below.

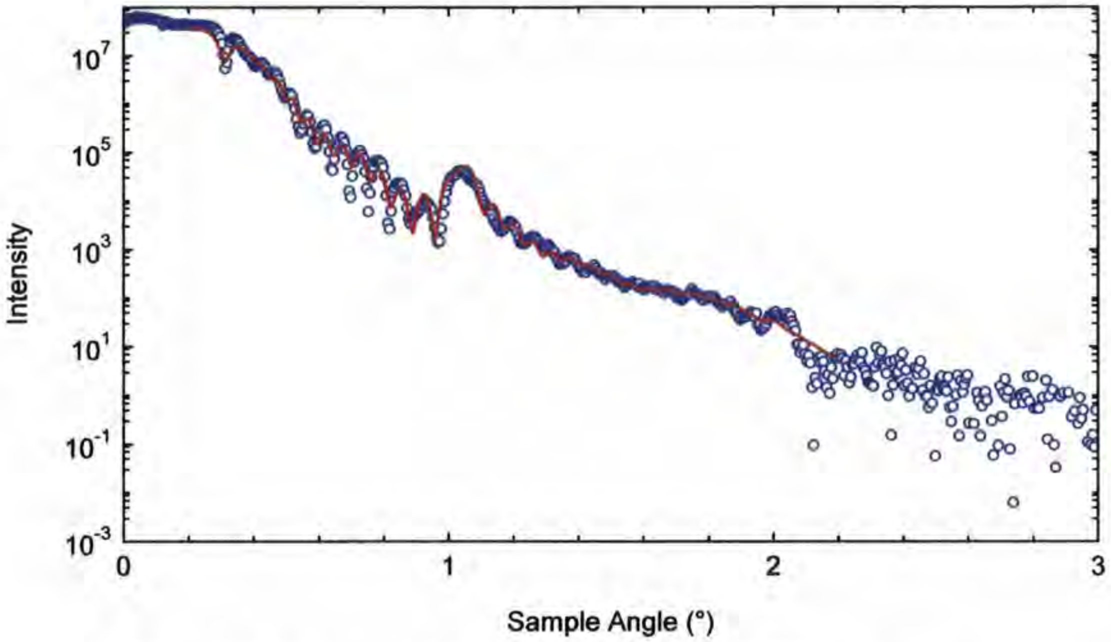

Figure 5-21: Experimental data and simulation of the 350°C specular scatter

The characteristic sharp dip at the critical angle gives an insight into the electron density profile within the sample and only occurs if there is a low electron density region (such as an oxide layer or boride layer) beneath a high electron density layer (such as a transition metal layer). The electron density profile shown in Figure 5-22 was found to best fit the data presented above.

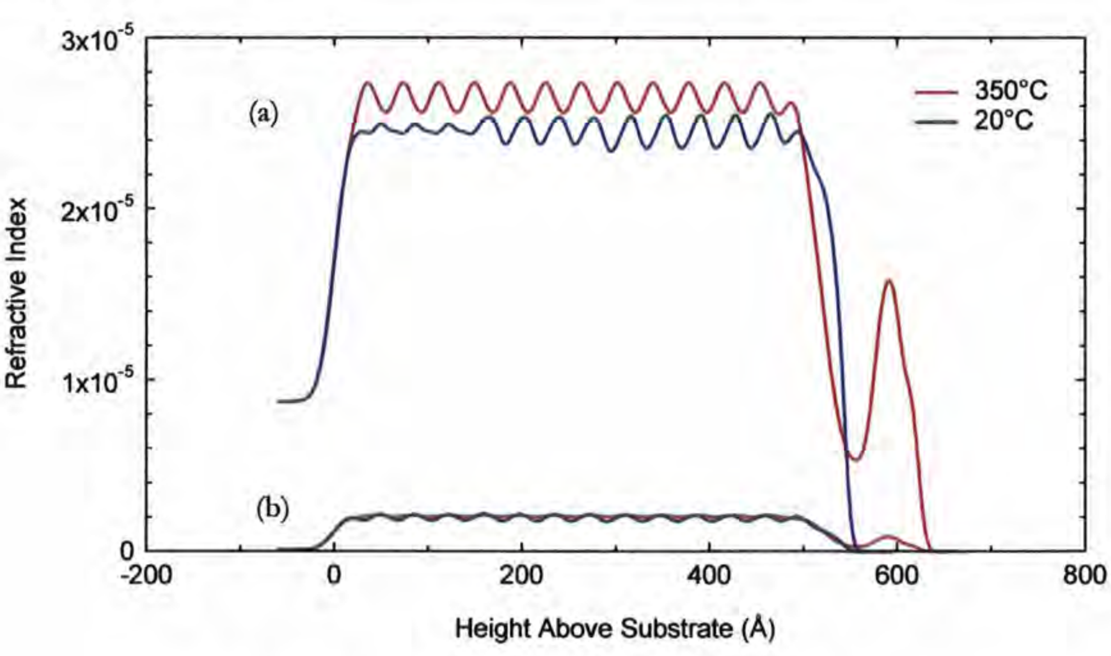

Figure 5-22: The dispersion (a) and absorption components (b) of the refractive index used to model the scatter at room temperature and at 350°C.

In the fitted structure, the sample thickness has increased by 80Å, or approximately 15% at 350°C. This is too large to be accounted for by thermal expansion. The vacuum in which the experiment was conducted was relatively poor and it is possible some oxygen has been incorporated into the sample. When the CoFeB crystallises, crystallites of CoFe will be formed and boron expelled to the grain boundaries. The presence of grain boundaries allows for relatively long distance grain boundary diffusion [34] and could allow for a thin low electron density layer to form.

To identify the composition of this low electron density layer is very difficult. The x-rays are predominantly sensitive to the electron density distribution within the sample, modified by the anomalous dispersion corrections (see section 2.2.2) which are element specific. To the x-rays at this energy both boron and oxygen will appear very similar with low electron densities and anomalous dispersion corrections giving low refractive indices.

There is no indication that densities have fallen dramatically to account for the expansion. The variation in layer parameters needed to model the 20°C data is no longer needed for the higher temperature, and it appears some homogenisation has occurred.

5.5.5 Effect of annealing on the transverse diffuse scatter

The transverse diffuse scatter recorded at different temperatures is shown in Figure 5-23 and Figure 5-24 below.

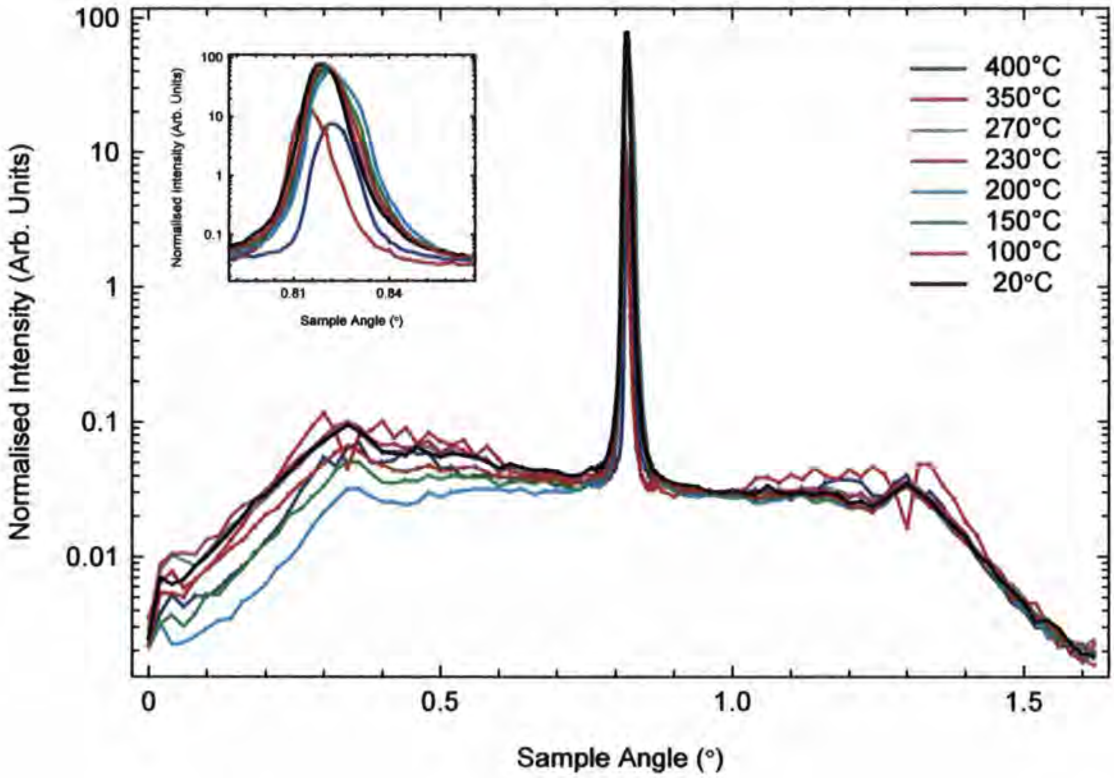

Figure 5-23: Transverse diffuse scans from the $CoFeB_{20\%}$ multilayer at a detector angle of 1.6° at different temperatures. The intensity variations at low angle are from changes in the beam footprint.

The change in intensity at the low angle Yoneda Wing is indicative of height alignment errors leading to footprint changes as discussed in section 3.4. However the high angle scatter is not sensitive to these misalignments and here it can be seen there is very little change in the diffuse scatter until 350°C, indicating that up to that temperature there is no change to the topological roughness. Above 350°C the sharp downward spike observed near the critical angle in the specular scatter is also present in the diffuse scatter at both the critical angles for incident and exit beams. This confirms that a critical angle associated with a distinct low density layer is present and that the dip is not an interference effect.

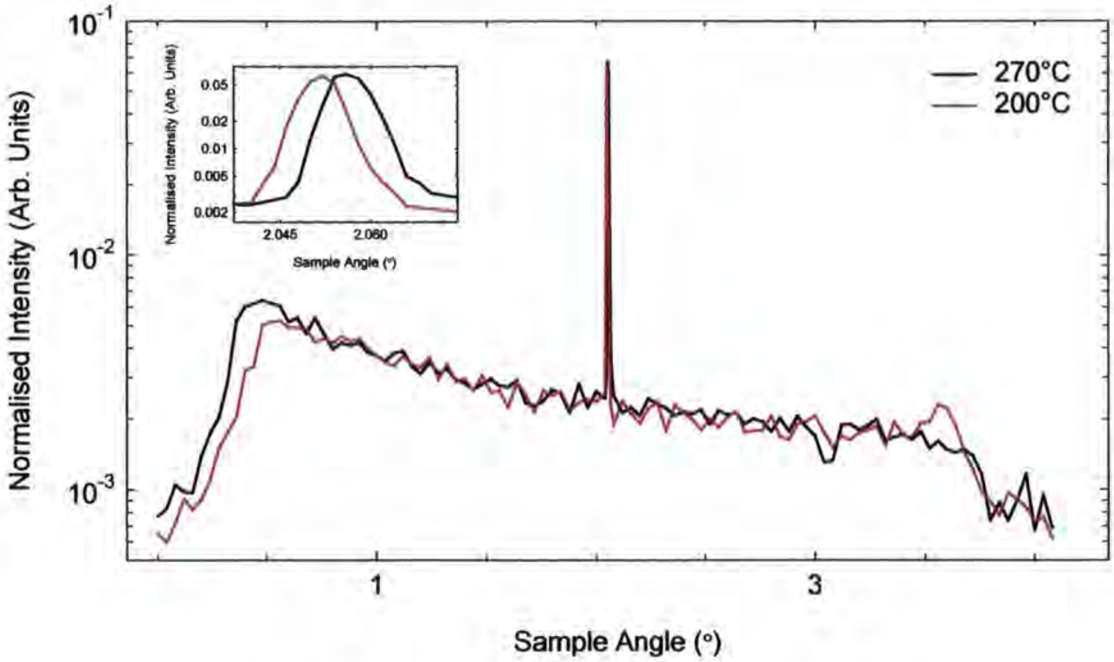

Figure 5-24: Transverse diffuse scans at a detector angle of 4.1°

The dynamical effects observed in the transverse diffuse scatter from the CoFe/Ru multilayer (Figure 5-7 and Figure 5-8 above) are not visible in this sample. The dip arises from multiple scattering when the standing wave set up in the sample enhances the coherent scatter from all the interfaces. The absence of the effect here is ascribed to the increased widths of the interfaces.

5.5.6 Interpretation and discussion

The fitted model to the scatter before crystallisation shows that although the total interface width is greater, this is primarily due to grading rather than pure topological roughness. It is possible that the boron, being small and interstitial, can diffuse through the boundary either on deposition or afterwards at room temperature. The poorer fit between simulation and experiment compared with the CoFe/Ru multilayer could be as a result of different components of the CoFeB material having a different interface widths, which cannot be accommodated in the REFS simulation software.

However, boron is a very small and light element, with anomalous dispersion corrections several orders of magnitude smaller than the other transition metals in the sample. Its contribution to the refractive index profile is thus very small and only when it is separated and concentrated to form a low electron density region at the surface or an interface does it make a significant modification to the refractive index profile.

Postulating that during the deposition, the kinetics are such that the boron on a deposited surface will easily receive large amounts of energy from the impinging heavier atoms of cobalt and iron, it is possible for the boron to move up the layer and be more concentrated at the top growing surface. When the sputtering target is changed to ruthenium the same process can continue and some of the boron will be incorporated into the ruthenium layer. However, with the cobalt iron being amorphous, and not in the most stable and energetically favourable configuration of a regular crystal lattice, those atoms can also be disrupted by the deposition of the ruthenium, leading to a graded interface. With no boron being added during the deposition of the ruthenium, eventually the boron concentration will be reduced to the extent that the enhancement to the inter-diffusion is negligible and ruthenium will begin to form in a polycrystalline state.

Therefore it is more likely that the boron disrupts the growth of the CoFe, as indeed it must for it to be deposited in an amorphous state, but that it also enhances the amount of inter-diffusion at the top interface when ruthenium is grown on top. This can be explained by the atoms no longer sitting in energetically favourable small crystallites. In the amorphous arrangement it will thus be easier for the atoms to diffuse between layers during deposition.

Wang *et al.* [35] looked at sputtered samples of Ru(50Å)/$Co_{60\%}Fe_{20\%}B_{20\%}$(*x*Å)/Ru(50Å) and measured the width of the interface as characterised by a 'magnetically dead layer' from extrapolating graphs of CoFeB thickness against saturating magnetisation to find the intercept with the thickness axis at zero magnetisation. They concluded that there was an interface width of 1.7Å for both interfaces. This is very small for sputtered films and much smaller than the values presented above. Their cross sectional TEM results showed clear sharp interfaces, suggesting that intermixing is insignificant, even at 300°C with no differences between the CoFeB/Ru and Ru/CoFeB interfaces. The ruthenium layers are polycrystalline and show a clear columnar structure. With annealing above 150°C they saw an increase in the effective saturation magnetisation and a steady rise up to their maximum temperature of 300°C. This they attribute to boron diffusion away from the CoFeB layers. When boron, a magnetic impurity, moves away from the CoFeB, the magnetic moment increases. No evidence for this diffusion was seen in the x-ray scatter.

Wang *et al.* also observed crystallisation beginning in CoFeB at 250°C, whereas the change was observed in these measurements to occur above 270°C. This could however be due to the thermocouple in our experiment measuring the temperature of the crucible, as described in section 3.5, their inaccurate temperature measurement, or a result of their boron concentration in the CoFeB falling and hence changing the crystallisation temperature.

Although the addition of boron has led to wider interface widths the sample is still stable to low temperature anneals and inter-diffusion is not enhanced by annealing. The high activation energy observed in the CoFe/Ru multilayers for diffusion [33] appears still to hold.

The increased out-of plane correlation length can also be explained by the lack of crystallites. Where crystallites form there will energetically be a push towards formation of long range order, rather than simply replicating the lower interface. Thus a 'jagged' surface can more easily grow with less regard to the underlying interface.

5.6 CoFeB/AlO$_x$ multilayer

Having looked at samples where the only light element is boron, and having identified that it appears to dissociate from the CoFe on annealing, samples containing AlO$_x$ were investigated. AlO$_x$ is also a relatively low electron density material and so sharp features as seen in the CoFeB/Ru multilayer around the critical angle are typical. From the poor contrast between the boron and the aluminium oxide, identifying the position of interfacial boron becomes problematic. It is also possible that boron oxide is formed at the interfaces during the sputter etching process of fabricating the AlO$_x$.

In contrast to the CoFeB/Ru multilayer the layer grown on the CoFeB is now aluminium, a much lighter atom, and so growth kinetics are expected to be very different. Two identical samples were compared to establish the reproducibility of the deposition process employed by the sample growers, Siemens. Experiments were conducted in a high-purity argon atmosphere at slightly above atmospheric pressure to ensure no atmospheric oxygen entered the chamber. Argon has the disadvantage of being heavier than air and much more attenuating so the recorded intensity in the experiment is reduced.

5.6.1 Room temperature specular scatter and simulation

The specular scatter and off-specular scatter, recorded at an incident wavelength of 1.3Å, is shown in Figure 5-25 below, and the simulation to the data, using the parameters in Table 5-5, is shown in Figure 5-26 below.

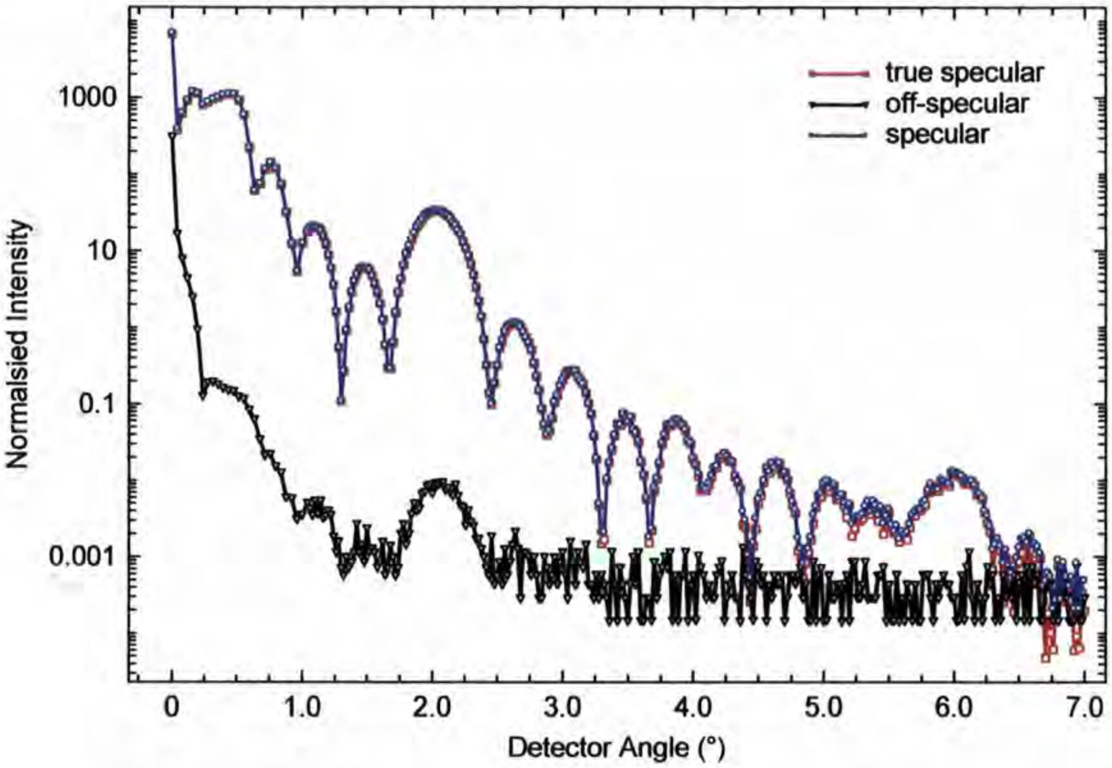

Figure 5-25: Specular and Longitudinal Diffuse scatter from a CoFeB/AlO$_x$ multilayer at room temperature and with an incident wavelength of 1.3Å.

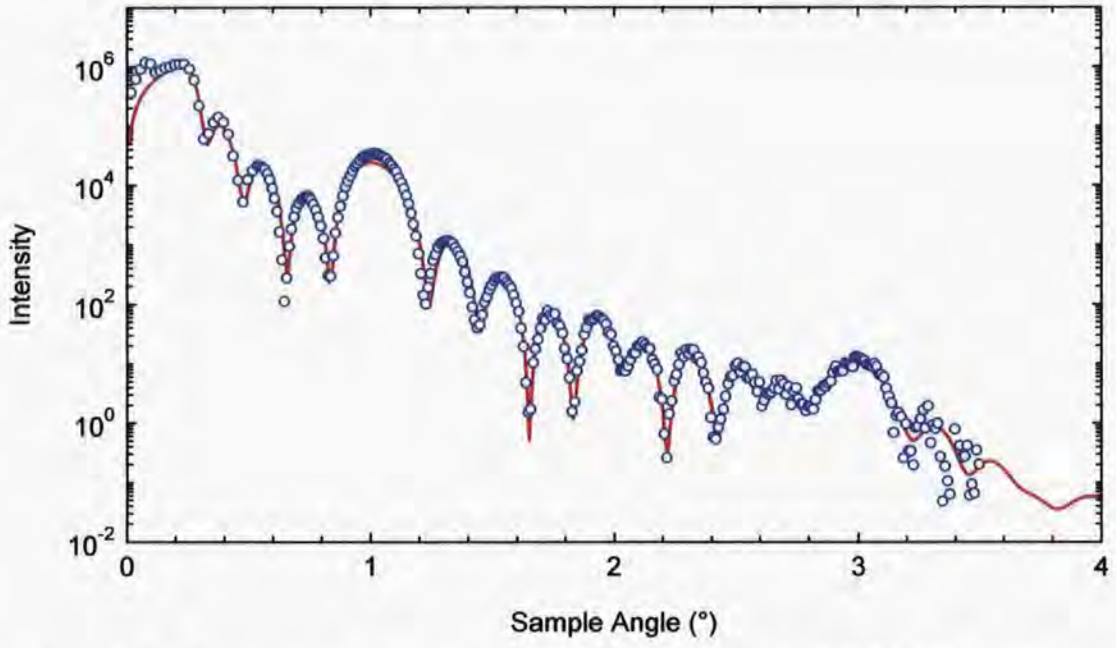

Figure 5-26: Room temperature specular scatter and simulation from the CoFeB/AlO$_x$ multilayer.

Layer	Material	Thickness (Å)	Density (% of bulk)	Interface Width (Å)
10	Al_2O_3	20.29 ± 0.48	80.0 ± 6.1	5.10 ± 0.16
9	$Co_{0.6}Fe_{0.2}B_{0.2}$	17.83 ± 0.38	84.2 ± 2.3	5.67 ± 0.28
8	Al_2O_3	17.04 ± 0.24	85.0 ± 5.0	4.81 ± 0.21
7	$Co_{0.6}Fe_{0.2}B_{0.2}$	17.96 ± 0.40	85.0 ± 2.7	5.15 ± 0.23
6	Al_2O_3	19.43 ± 0.26	80.0 ± 5.2	4.54 ± 0.15
5	$Co_{0.6}Fe_{0.2}B_{0.2}$	18.71 ± 0.23	82.7 ± 2.9	5.00 ± 0.20
4	Al_2O_3	18.51 ± 0.33	80.7 ± 6.1	4.34 ± 0.15
3	$Co_{0.6}Fe_{0.2}B_{0.2}$	18.60 ± 0.25	80.0 ± 4.0	4.84 ± 0.21
2	Al_2O_3	18.36 ± 0.26	85.0 ±9.9	4.09 ± 0.2
1	$Co_{0.6}Fe_{0.2}B_{0.2}$	18.60 ± 0.24	81.2 ± 7.8	3.92 ± 0.26
Substrate	SiO_2	∞	98.8 ± 30	3.32 ± 0.16

Table 5-5: Model to fit the specular scatter from a [CoFeB/AlO$_x$]$_{\times 5}$ multilayer.

It has proved impossible to fit the data using the nominal structure. The genetic evolution fitting routines pushed the Ta seed and cap layer thickness to zero. Diffraction experiments failed to observe any peak from polycrystalline tantalum in the sample. With a nominal total thickness of 100Å (two 50Å layers) this should have been possible. There are other reasons to believe no tantalum has been deposited. The Kiessig fringe period is related to the total thickness of the sample and suggests a thinner sample than nominal, and the positioning of the Kiessig fringes relative to the Bragg peaks also shows that all of the layers are contained in the repeated structure and there are no capping or seed layers. This has probably occurred through mechanical malfunction of the sputtering equipment. The fit was thus optimised on a structure of: Si/[CoFeB(30Å)/Al(12Å)+oxidation]$_{x5}$. The top layer of AlO_x will be stable to further atmospheric oxidation.

The equality of the thicknesses of the aluminium oxide and CoFeB layers is demonstrated by the absence of a second order Bragg peak in the scatter. Nominally the aluminium thickness deposited, before oxidation, is 12Å. Oxidation appears to have increased the thickness by 50%. This is on the large size, and previously the sample growers reported an increase in thickness of 30% from plasma oxidation [30]. What is surprising is that the CoFeB thickness is only 60% of the nominal thickness.

The densities are all constant within the error bars. Stoichiometric Al_2O_3 was used in place of AlO_x in the model and the density of the layer is coming out very low. Very little variation in the thicknesses is seen, but the AlO_x layers show more variation than the CoFeB layers. The evolution of the interface widths as the sample stack thickness increases, shown in Figure 5-27 below, shows a linear increase with layer number. As seen previously the interfaces differ depending on whether AlO_x is grown on CoFeB or *vice versa*. This asymmetry is not surprising as the growth involves the AlO_x aluminium being deposited first, and then oxidised. This will certainly alter the nature of the top interface as the material is significantly disrupted by the sputter etching process. The lowest CoFeB/AlO_x interface is very smooth and presumably results from this CoFeB being deposited directly on the SiO_2 substrate instead of on an aluminium oxide layer.

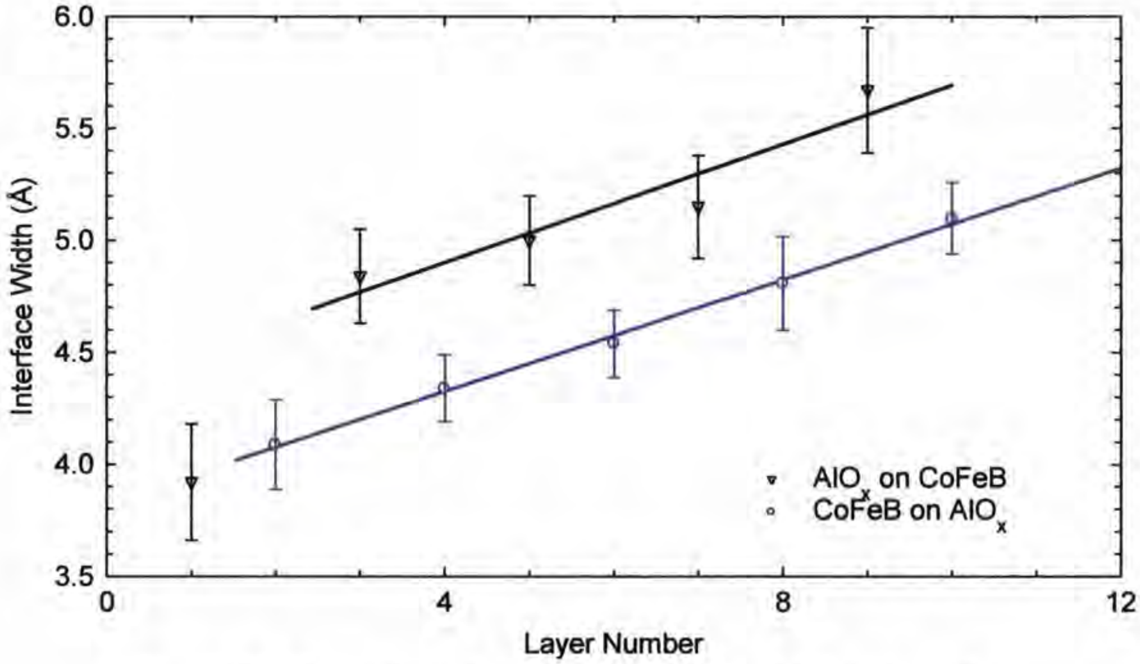

Figure 5-27: The variation in the interface width of the modelled structure with layer number counted from substrate.

5.6.2 Room temperature diffuse scatter

In the measured off-specular scatter, shown in Figure 5-28 below, the first Bragg peak is visible. Above a sample angle of 1° no scatter is measured, showing that the sample is extremely topologically smooth. The simulated fit to the data, shown in Table 5-6 below, shows the contribution to the interface widths is almost entirely from grading, or inter-diffusion, between the layers.

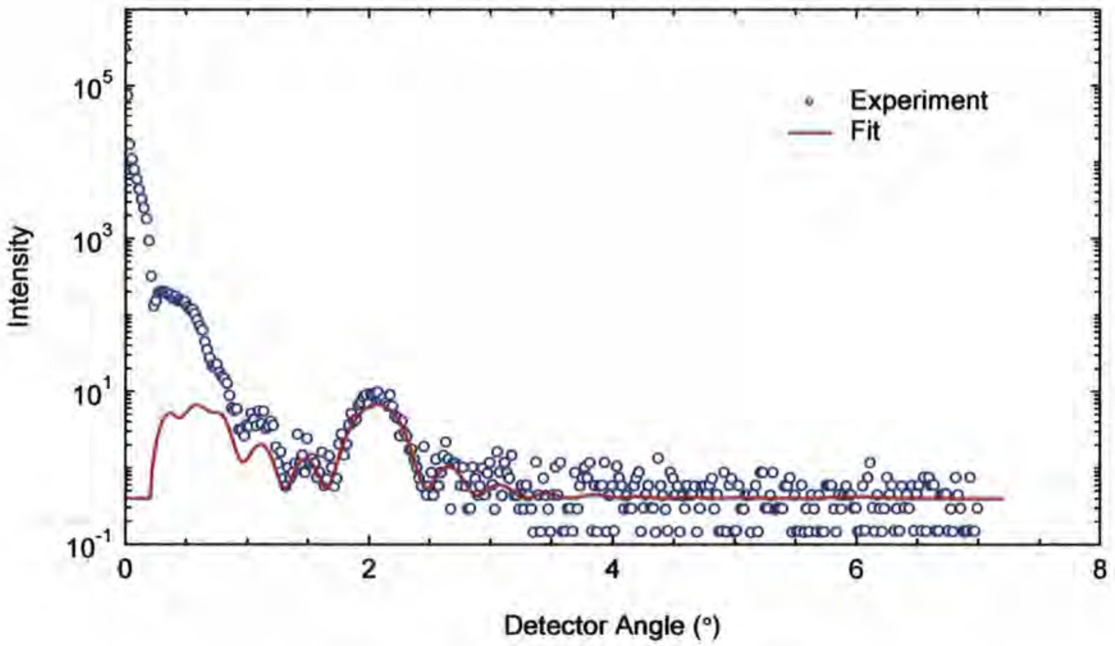

Figure 5-28: Off specular scatter and simulation

The detailed characterisation of the interface widths are shown in Table 5-6 below.

In-plane correlation length 1000Å ± 200Å

Out-of-plane correlation length 2000Å ± 1000Å

Fractal parameter 0.7 ± 0.2

Layer	Material	Roughness(Å)	Grading (Å)	Total Interface Width (Å)
10	Al_2O_3	0.55	5.07	5.10 ± 0.16
9	$Co_{0.6}Fe_{0.2}B_{0.2}$	0.55	5.64	5.67 ± 0.28
8	Al_2O_3	0.55	4.78	4.81 ± 0.21
7	$Co_{0.6}Fe_{0.2}B_{0.2}$	0.55	5.12	5.15 ± 0.23
6	Al_2O_3	0.55	4.50	4.54 ± 0.15
5	$Co_{0.6}Fe_{0.2}B_{0.2}$	0.55	4.97	5.00 ± 0.20
4	Al_2O_3	0.55	4.31	4.34 ± 0.15
3	$Co_{0.6}Fe_{0.2}B_{0.2}$	0.55	4.81	4.84 ± 0.21
2	Al_2O_3	0.55	4.05	4.09 ± 0.2
1	$Co_{0.6}Fe_{0.2}B_{0.2}$	0.55	3.88	3.92 ± 0.26
Substrate	SiO_2	0.55	3.27	3.32 ± 0.16

Table 5-6: Roughness and inter-diffusion properties of the interfaces for the CoFeB/AlO_x multilayer at room temperature

Both the in-plane and out-of-plane correlation lengths are longer than those of the previous multilayers examined, although with the sample being made in a completely different laboratory with different apparatus, different growth conditions, and on a different substrate, this difference is not surprising. The sample shows greater conformality of the roughness.

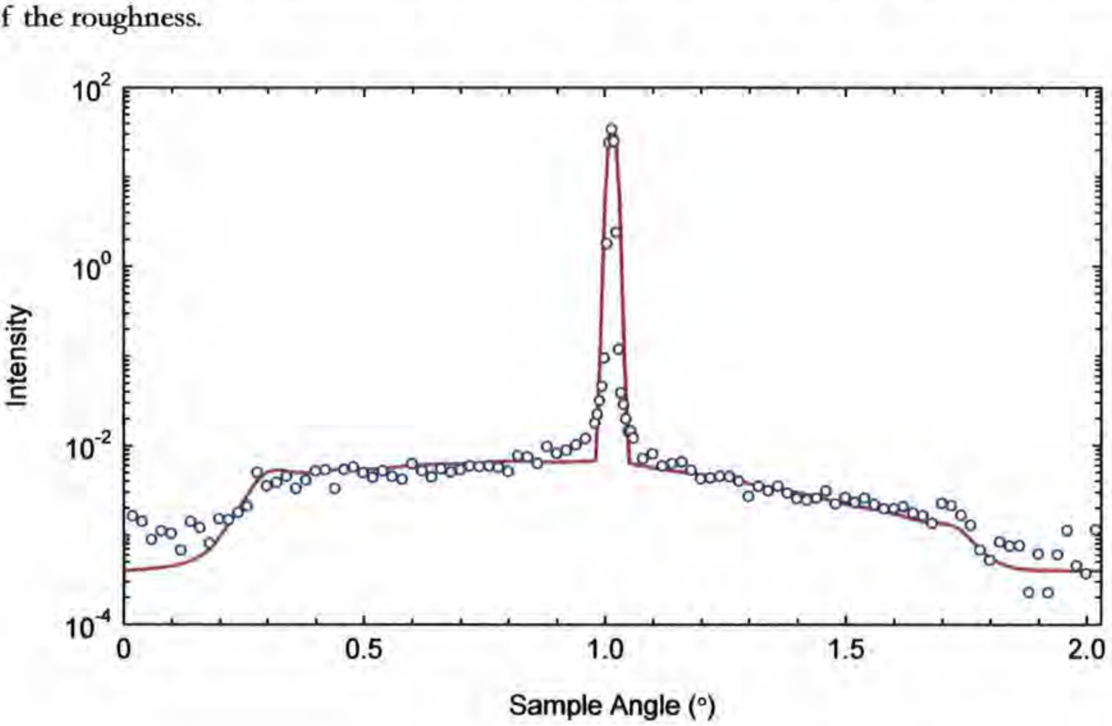

Figure 5-29: Transverse diffuse scatter and simulation at room temperature at a detector angle of 2.03° corresponding to the 1st Bragg peak.

5.6.3 Effect of annealing on the specular scatter

The intensity of the 3rd Bragg peak is seen to increase with annealing temperature, see Figure 5-30 below, and this is particularly evident when the data are plotted on a linear scale (see inset). Therefore, for the same reasoning as before, it is concluded that sharpening is occurring. No sudden changes occur that are associated with crystallisation or oxidation although a slight shift in the fringe positions is seen above 1.6°.

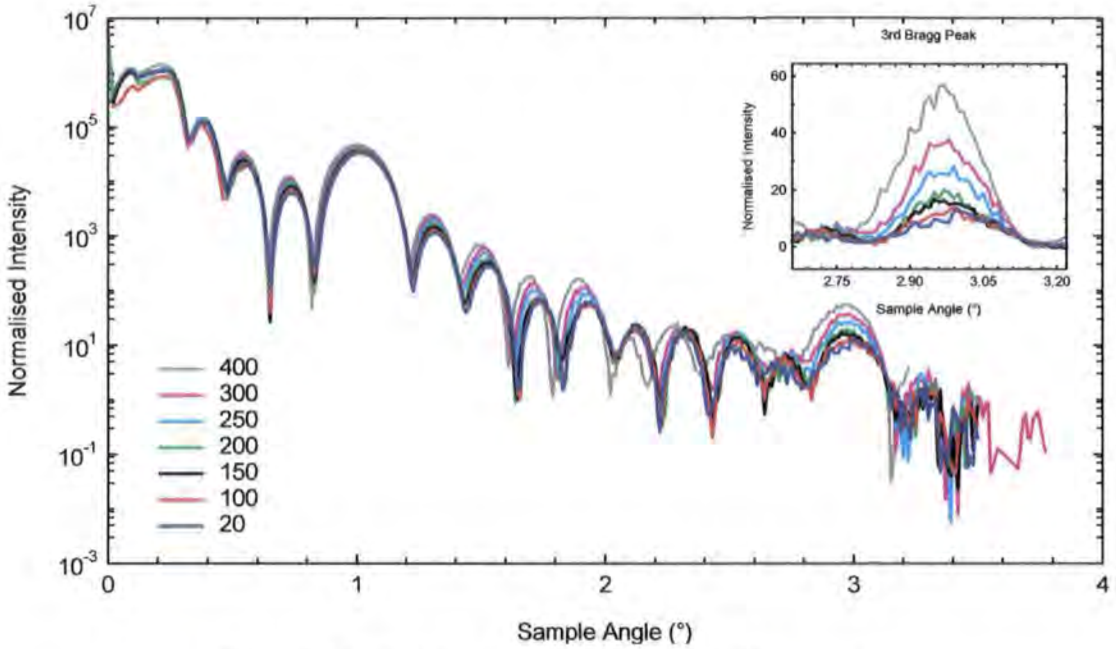

Figure 5-30: Variation in the specular scatter with temperature

Beam footprint issues will only be a factor at low angles, as has been discussed before. Variation in intensity at low angles shows no systematic variation with temperature. At higher angles where beam foot-print issues are no longer a factor the intensities systematically follow the temperature as shown in the inset in Figure 5-30.

The experiment was repeated on a further two samples; one cut from the same wafer and a second cut from a different wafer that had been grown to the same nominal structure. All samples showed the same enhancements at high angles. The fringe structure of the second sample, shown in Figure 5-31 below, was slightly different, showing the difficulty in exactly replicating a particular structure between growth runs.

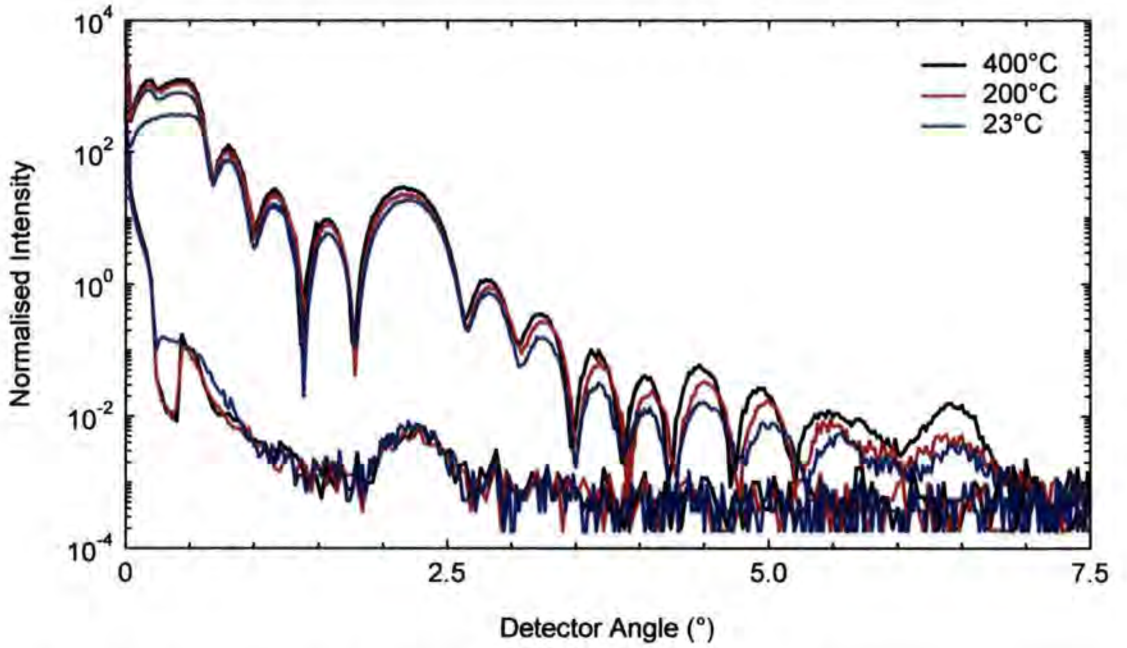

Figure 5-31: Specular and off-specular scatter from a second AlO / CoFeB multilayer also showing enhanced scatter at elevated temperatures.

Changes in the scattered intensity caused by a change in position of the beam on the incident slits or a change in the atmospheric absorption within the chamber itself can be discounted; the effect of these would be to change the intensity over the whole range of angles, and on a log scale this would appear as a constant offset in the data. Additionally, any intensity changes from the monochromator or components closer to the ring would be eliminated when the scatter is normalised to the monitor. This clearly is not the case, as can be seen in Figure 5-30.

The best-fit simulations to the specular scatter at each temperature are shown in Figure 5-32 below and the details of the average values of the interface widths, layer thicknesses and layer densities are shown in Figures 5-33, 5-34 and 5-35 respectively. In fitting all the data at different temperatures the same incident intensity has been used for all the data sets. This is particularly important when the corresponding diffuse scatter is fitted; there are multiple sets of parameters that produce the same diffuse scatter profile and only if the intensity is kept constant and consistent with the specular scatter can a unique solution be found [36].

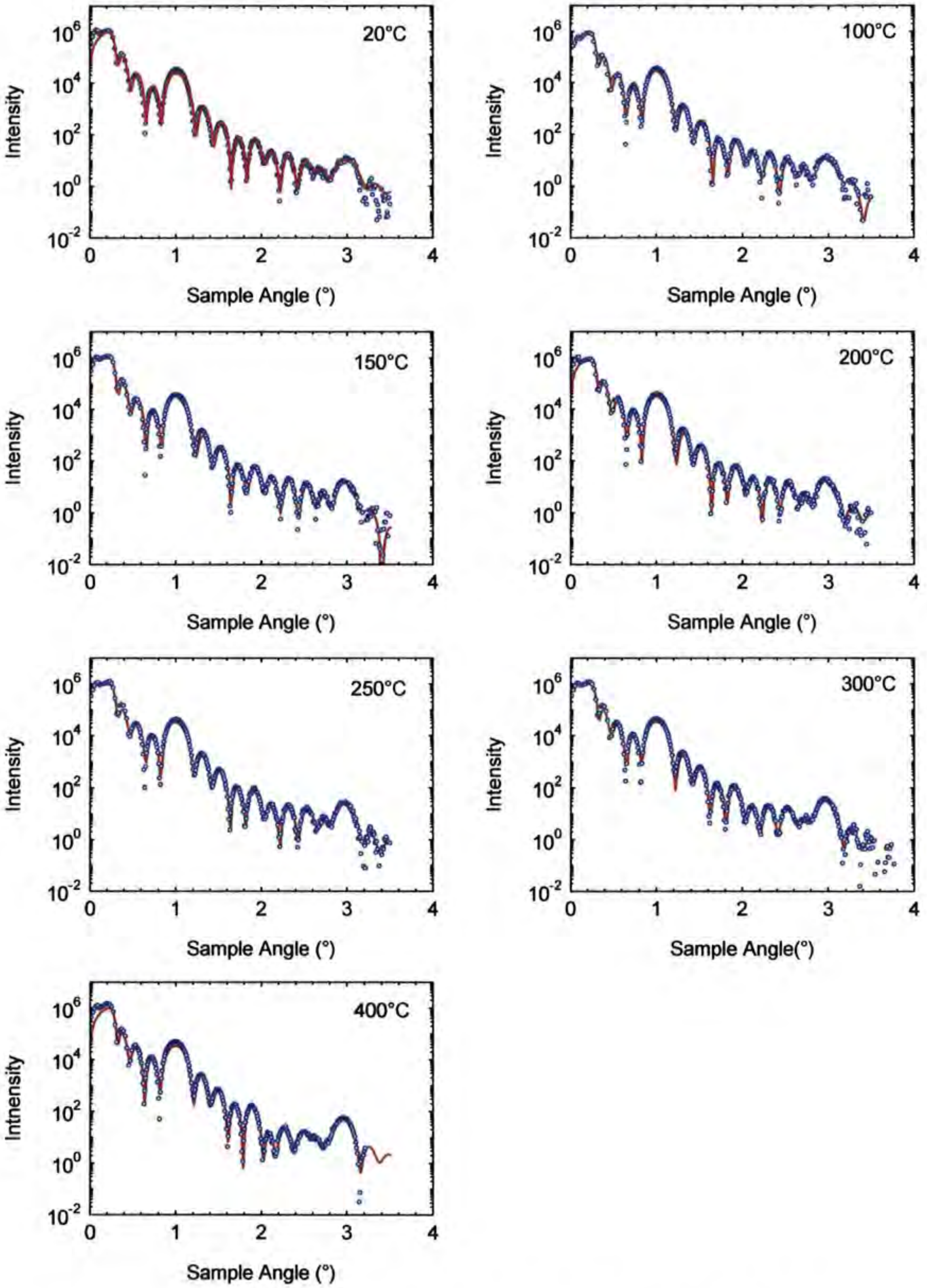

Figure 5-32: Specular scatter and simulation for the sample annealed at different temperatures

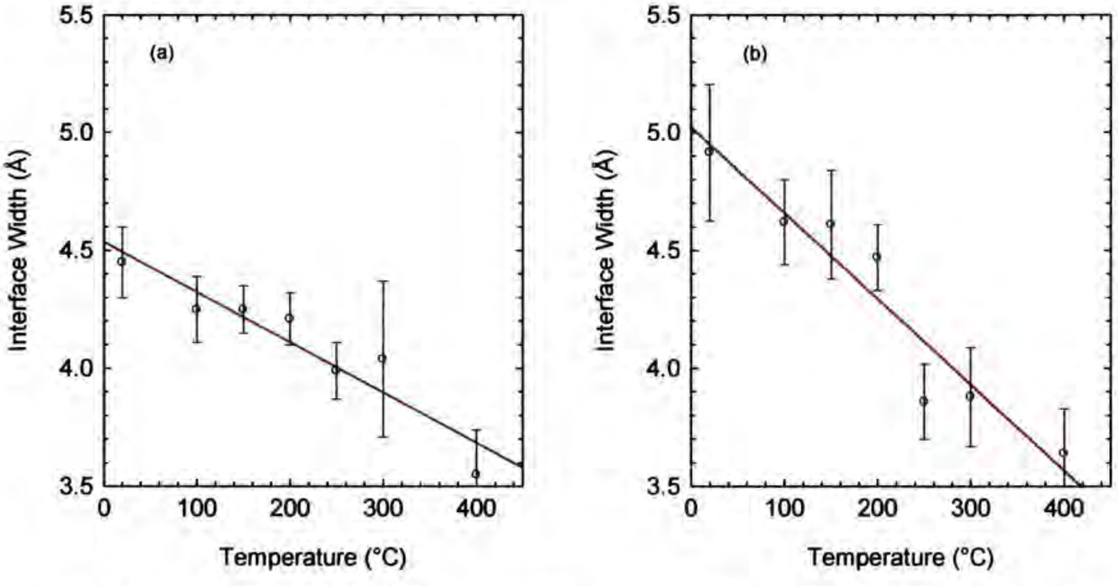

Figure 5-33: Average interface width of (a) CoFeB grown on AlO_x and (b) AlO_x grown on CoFeB

Both the interfaces show a reduction in width as the sample is annealed. As noted previously the AlO_x on CoFeB interface starts off being wider than the converse arrangement but here we see that this interface sharpens at a faster rate, so that by 400°C both configurations become equivalent with an interface width of around 4Å.

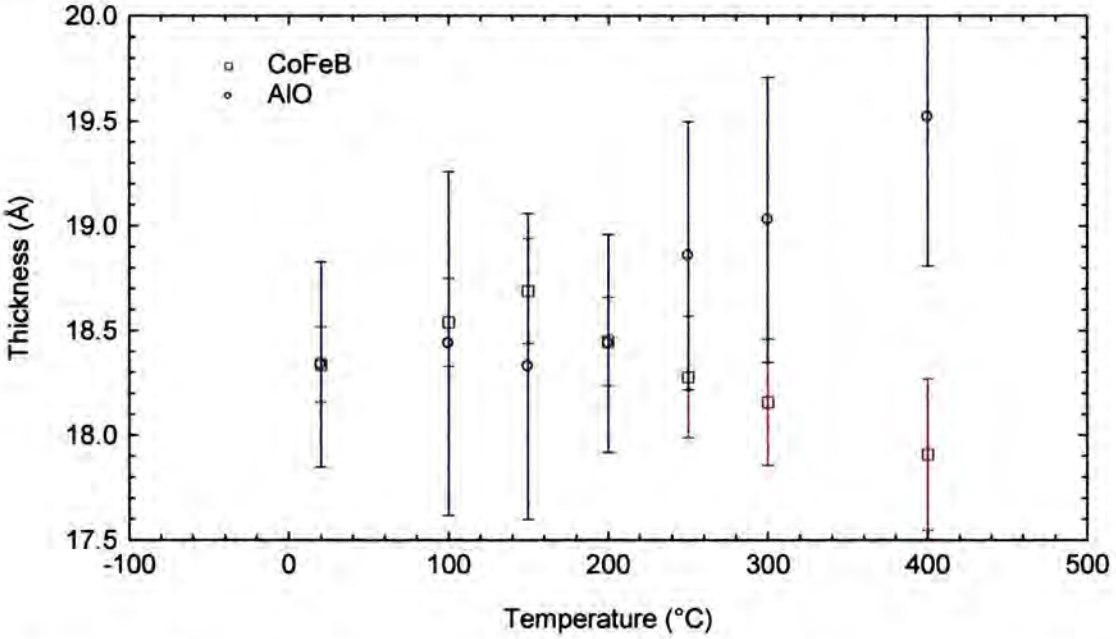

Figure 5-34: Average layer thickness of the CoFeB and AlO layers at different temperatures. Above 200°C material appears to move into the AlO layer.

Both material thicknesses are comparable until 200°C and then they appear to diverge. These thickness parameters are coupled; a change in thickness of one layer has to be compensated by a change in thickness of the other layer to prevent the total bi-layer thickness changing and the Bragg peak positions moving. The AlO$_x$ layer appears to be getting thicker and the CoFeB layer thinner.

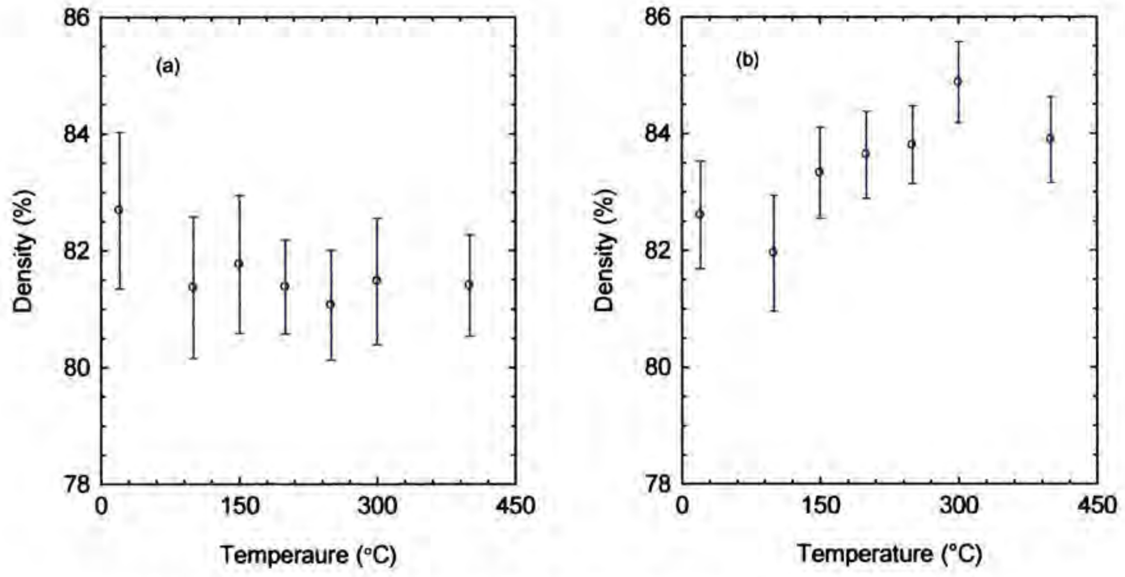

Figure 5-35: Average layer densities of the (a) AlO [based on Al_2O_3] and (b) CoFeB layers

The densities of the layers are reasonably constant. Within the models the thickness of the AlO$_x$ was seen to increase with temperature which does not appear to have been accompanied by a reduction in density. Conversely the CoFeB layer reduced in thickness which has been accompanied by an increase in the density with temperature. This raises the possibility that material has moved from the CoFeB layer to the AlO$_x$ layer as the sample has been heated. It is very difficult to be confident in this as the layers are thin and the interfacial regions make up a large proportion of the layers. Therefore density and width are effectively coupled within the modelling regime employed.

5.6.4 Effect of annealing on the diffuse scatter

The off-specular scatter is shown in Figure 5-36 below. No noticeable changes are seen in the off specular scatter on annealing. The small changes seen below the critical angle are from sample and beam alignment differences. The corresponding transverse diffuse scatter is shown in Figure 5-37 below.

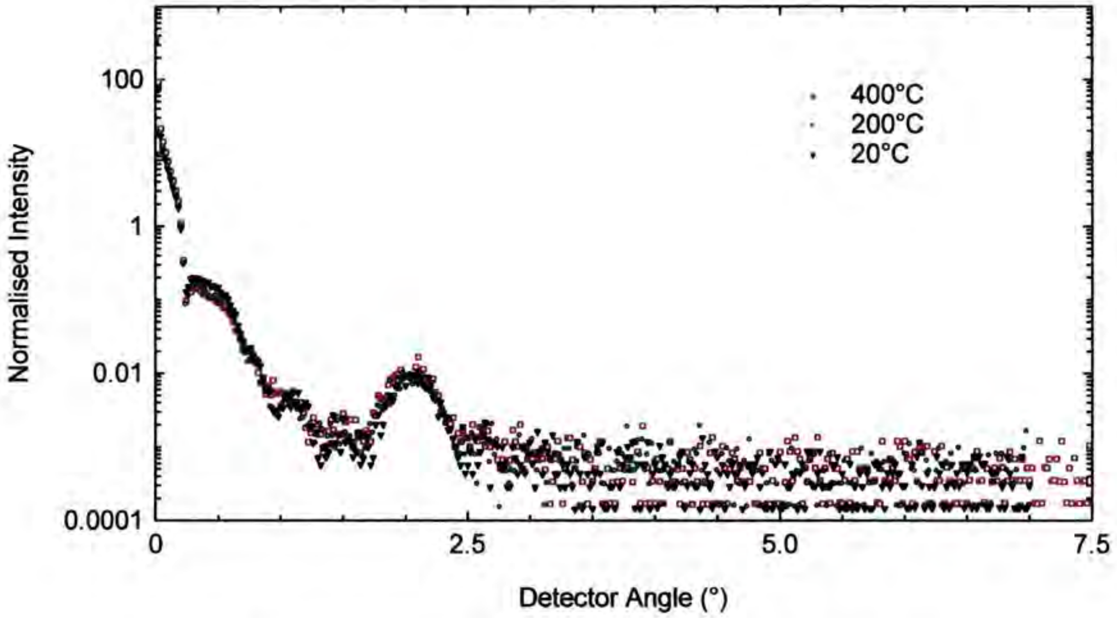

Figure 5-36: Comparison of the off-specular scatter for the sample at three temperatures over the range investigated.

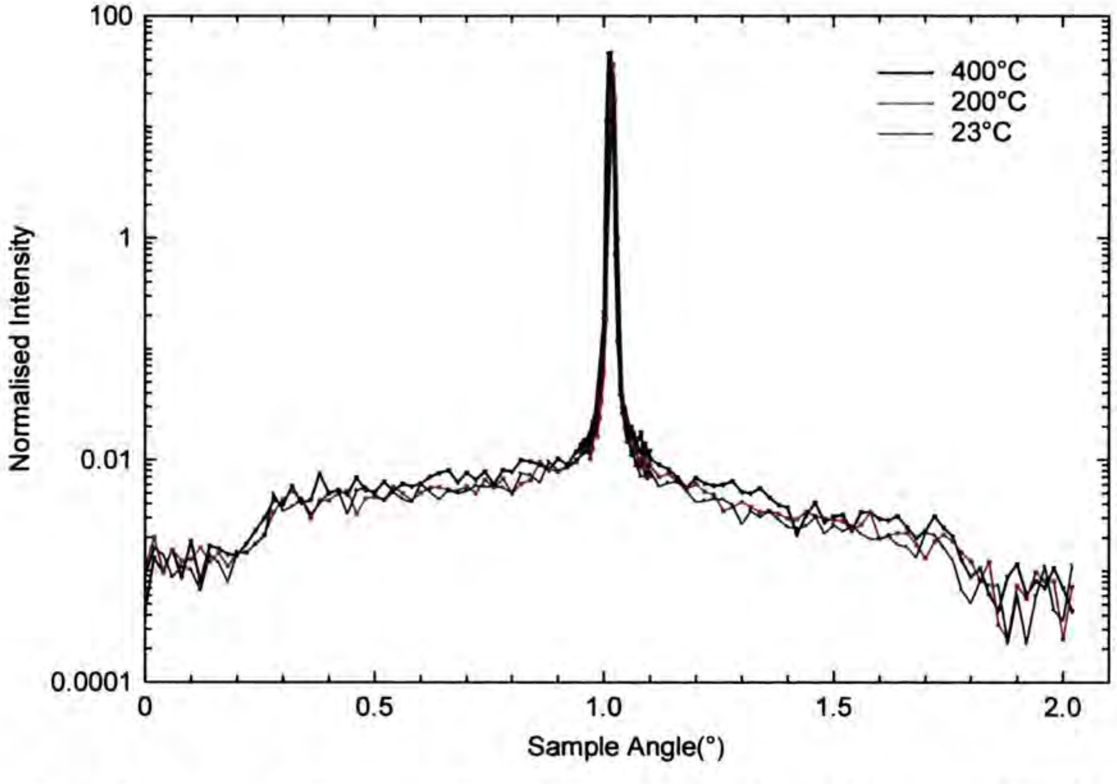

Figure 5-37: Transverse diffuse scatter from a CoFeB/AlO$_x$ multilayer at detector angle of 2.06°

These transverse diffuse scans and the associated change in the intensity of the specular ridge give the strongest evidence that the specular scatter has changed as a result of changes in the sample and not through sample-beam alignment considerations. These scans only involve the movements of the sample angle (the detector angle is fixed) unlike the specular scan where the two angles are moved simultaneously. The specular scan is susceptible to centre of rotation misalignments and it is possible to slide across the specular ridge if the experiment is not set up correctly. This artefact is not present in these scans and the specular ridge will always be found in the scans and the maximum can be measured.

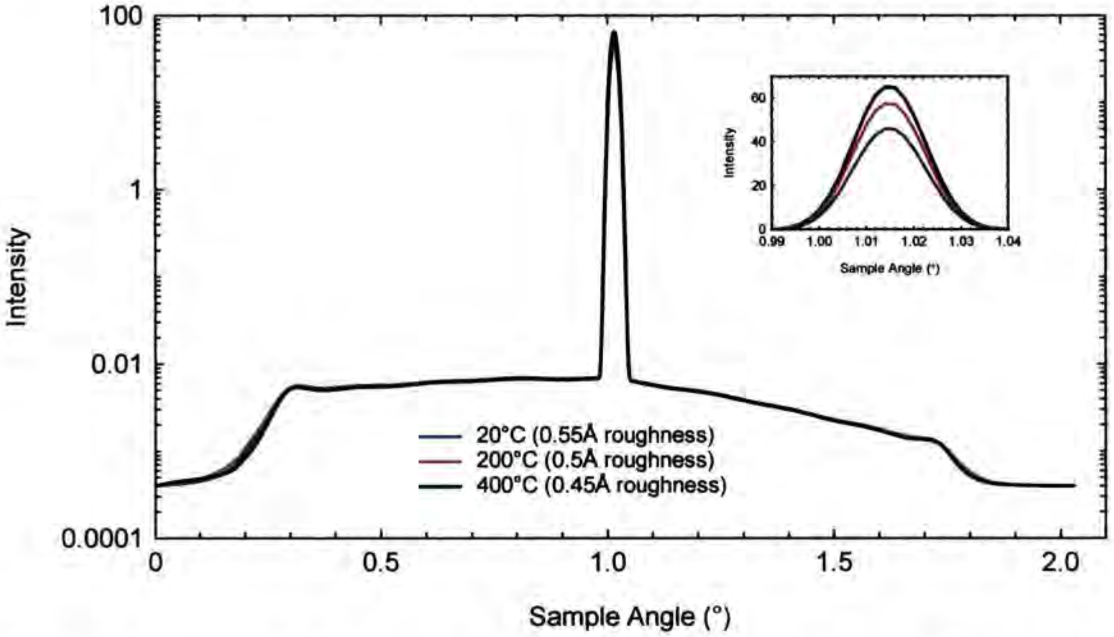

Figure 5-38: Simulations of the transverse diffuse scatter for the three different samples. The inset shows the increase of the specular ridge caused by a reduction in the interface width, primarily through grading. To keep the diffuse scatter constant a very small decrease in the roughness is required.

No change is seen in the transverse diffuse scatter. The transverse diffuse scatter has been simulated for each of the three temperatures and is shown in Figure 5-38 above. The interface width, as has already been noted, falls with increasing temperature, causing the specular scatter to increase (see inset). A reduction in grading in isolation causes the specular scatter to increase, but also causes the diffuse scatter to increase (equation (2-59)). To keep the level of diffuse scatter constant the roughness also has to increase by a very small amount to compensate. This change of 0.1Å over the full temperature range is insignificant and may arise purely as an artefact of the modelling used. The change in compositional grading when the sample is heated accounts for almost all the observed changes in the interface widths, which have fallen on average by 1.25Å over the entire temperature range.

The process of changing the interface width is continuous over the temperature range investigated. There is no minimum 'activation energy' required to start the sharpening. All the changes observed were after a thermal equilibrium had been established in the sample by holding it at temperature for at least 20 minutes before the measurements were taken over the next two hours. At the end of the two hours when measurements were repeated no further changes in the scatter were observed.

No change has been observed in the correlation lengths or the fractal parameter. These parameters all relate to the pure topological roughness. This is further evidence that there is no significant change to the interfacial roughness on annealing.

5.6.5 Interpretation and discussion

Strong evidence has been presented, based on the changes in the specular and the transverse diffuse scans, which assert that the composition profile of the CoFeB/AlO_x interface is changed by annealing. The changes in the amplitude of the specular reflectivity must have either been caused by a change in electron density, and therefore the contrast between two layers, or a change in the interface width. A change in electron density changes the visibility and position of peaks and tends to affect the whole angular range. A change in the interface width changes the rate of decay of the specular intensity as the scattering angle is increased; therefore at higher angles the effect is more pronounced. The two effects can be distinguished. In the genetic fitting routines employed the two different contributions are taken into account and a balance between them found. The results of the simulations showed that it is predominantly a change in the interface widths, in particular the inter-diffusion between layers, that is responsible for the enhancement observed in the reflectivity profile with low temperature annealing.

Seve *et al.* have observed a change in the oxidation state at the interface of $Co_{84\%}Fe_{16\%}$ and Al_2O_3 on annealing [37]. In their un-annealed samples, grown by magnetron sputtering and plasma oxidation, they observed, through x-ray absorption spectroscopy, iron and cobalt oxides at the interface, which were reduced on annealing. For an optimal Al thickness they saw a complete removal of these Fe and Co oxides by 250°C. In addition to the initial aluminium layer thickness the etching rate of the argon atoms in the Ar/O_2 plasma can determine the oxidation profile of the interfaces [30]. The results of Seve confirmed similar studies by Sousa [14,38], using Rutherford back scattering, which showed an initially oxygen rich interface, and a uniform oxygen distribution after annealing to 200°C. However these studies were unable to identify if the oxygen near the interface was confined to the aluminium layer or in both layers forming the interface. Interestingly, after the redistribution of the oxygen at 150°C Sousa then observed a reduction of the oxygen content of the aluminium oxide layer. It was not clear where the oxygen migrated.

Aluminium oxide is much more stable thermodynamically then either iron or cobalt oxide, and so it is reasonable for this to be formed preferentially provided there are sufficient aluminium atoms available to bond with the oxygen. In the CoFeB/AlO_x samples the removal of the interfacial oxygen from the CoFeB layer could account for the sharpening observed as the interface becomes less diffuse. Oxygen atoms contribute relatively few electrons to the electron density profile of the sample and so oxide layers have lower refractive indices than metallic alloys. Even with 20% Boron being present in a metallic alloy the oxide will typically have a lower refractive index. The effect of oxygen migrating out of the CoFeB layer will be to increase the refractive index of that layer and lower that of the aluminium oxide, which can plausibly effect a sharpening of the interfaces.

The active region for this, from the x-ray measurements shown above, appears to be over the 4Å interface width, which is only a few atomic layers. The x-rays are sensitive to these very small changes and there is no need for any longer range diffusion mechanisms. Detailed modelling is difficult where the individual layer components have different interface widths, or non-error function profiles.

The sharpening effect observed did not appear to reach completion up to 400°C, 150°C hotter than the temperature where Seve saw complete removal of the oxygen from their CoFe. These studies of Seve and Sousa were on Cobalt-Iron alloys, which will form a poly-crystalline structure. With the addition of boron there exists the possibility of a third oxide species being formed: boron oxide. This is more thermodynamically preferable than cobalt or iron oxide, but less so than aluminium oxide, and thus the same chemical driving force of oxygen will still be present. The activation energy required to start the process will be altered by both the higher stability of boron oxide and the amorphous or nano-crystalline structure of the CoFeB layers. The results presented above suggest that a chemical redistribution begins at a similar temperature to those reported for CoFe but continues to a higher temperature, probably on account of a greater temperature required to remove all the boron-oxide species.

This characteristic of the plasma growth mechanism to locate oxygen at the interfaces also provides an explanation for why the AlO_x on CoFeB interface is wider than the other configuration of CoFeB on AlO_x. If the plasma oxidation technique preferentially locates oxygen at the interface then there is no reason to expect that CoFeB sputtered on AlO_x would show similar sharpening properties with respect to heating.

The remaining inter-diffused components of the interface widths are either oxide species or diffused cobalt, iron, boron or aluminium for which there is insufficient, or no driving force to enable further sharpening. If there was perfect segregation of the chemically inter-diffused atoms after annealing then the limit in the smoothness of the layer is the initial topological roughness of the system when it is initially grown, which remains unaltered by the annealing.

The possibility of the formation of a boron-oxide layer at the interfaces has already been noted. This could in effect reduce the interface width by collecting together boron and oxygen atoms, depleting the surrounding area of diffused atoms, and reducing the interface width. It is easy to imagine that the boron, being comparatively small, and initially in a disordered structure, would be free to diffuse more than the heavier transition metals with which it is alloyed. During the oxygen initiated re-ordering the boron could be expelled from the AlO_x layer back into the CoFeB layer, further enhancing the sharpening of the interface.

Similar observations of sharpening have been made in the Si/W system [39] using similar measurement techniques. Jankowski *et al.* postulated briefly that structural sharpening observed in W/C multilayers may be from either segregation or compound formation at the interfaces [40]. Bai *et al.* examined Co/C multilayers and also observed enhanced Bragg peak intensities with moderate annealing [41]. They raised the possibility of expansion of the carbon layers and the corresponding change in the electron density contrast between the layers as a possible explanation. However, to achieve an appreciable change in electron density a significant change in thickness would be required, which, in changing the thickness of only one layer, would shift the Bragg peak positions, which was not observed. What is common amongst all these systems, and the CoFeB/AlO system, is that heavier atoms are interfaced with relatively light ones. Oxygen is not present in these other systems and the chemical driving forces will be different.

The work of Erdélyi *et al.* has focused on mechanisms of sharpening in binary-alloy interfaces caused by concentration dependent diffusion rates [42-45]. This has been taken further by Roussel [46] who used Kinetic Monte Carlo simulations with fewer simplifying assumptions to study a Cu-Ni system, under different initial conditions, such as sharp flat interfaces, diffuse flat interfaces, and sharp rough interfaces. Assuming sinusoidal roughness, he found that the wavelength of the roughness determines whether the interfaces sharpen or broaden. It is difficult to translate a simple sinusoidal wavelength into the correlation function parameters of ξ and h. However, the system studied here is very flat and the roughness is unlikely to be an inhibiting factor. More problematic is that the interface is most likely an inter-diffusion of five different elements, with a high chemical activity and the possibility of forming many stable oxide and boride states. It is hard to envisage how a satisfactory modelling of this interface in terms of diffusion coefficients could be performed.

5.7 Conclusions

The results above have shown that the scatter from the interfaces of both CoFe and amorphous CoFeB with ruthenium is unaltered by annealing and there is no measurable change in the interface topology or inter-diffusion with annealing up to 270°C. Therefore, any exchange coupled structures based on these layers, typically found in MTJs, will not be affected by moderate annealing.

All the samples showed that during layer growth the interfaces formed between two materials depend on which material is deposited first. This has occurred in all the three samples investigated and has implications for modelling layers where it cannot necessarily be assumed that the same in-plane correlation length applied to all surfaces in a structure. All the samples have also shown a progression in the interface properties as more layers are deposited, showing that in sample modelling it is not always possible to use a simple repeated structure without variation in the interface properties.

The addition of boron leads to wider interfaces. However, the out-of-plane correlation is much improved increasing to 1500Å ± 250Å. The addition of boron reduces the high temperature stability of the stack and a structural transition is seen between 270°C and 350°C associated with crystallisation of the CoFeB.

When the amorphous CoFeB forms an interface with aluminium oxide the thermal stability is lost and moderate amounts of heating alter the interface profiles. No time dependence was observed in the data and a static equilibrium was quickly achieved after which no further changes were observed.

Small changes were observed from the Al_2O_3 substrate interface with CoFeB in the CoFeB/Ru multilayer. This and the AlO_x layers are not comparable in that the substrate layer is carefully grown to achieve stoichiometric Al_2O_3 whereas the plasma oxidation of aluminium produces a less regulated aluminium oxide AlO_x. Nevertheless there appears to be a small effect coming from the Al_2O_3 substrate.

The changes in the scatter from these active CoFeB/AlO_x result from a reduction in the interface width between the two layers and this has been further identified, by the observation of invariant diffuse scatter, to be a reduction in the inter-diffusion between the materials. The pure topological component of the interface width is seen to remain constant, including the RMS roughness, the fractal nature and the correlations both between the layers and of the in-plane structure.

The most likely mechanism for this sharpening starts with the plasma oxidation of the aluminium, which locates oxygen at the interfaces and not in a uniform manner. This oxygen is then chemically drawn out of the CoFeB layer towards remaining metallic aluminium by the thermodynamic favourability of forming aluminium oxides over other reactions.

References for Chapter 5:

[1] Gillman, J., Physics Today, **28** Issue 5 (1975) 46

[2] Metglas® Inc. 440 Allied Drive, Conway, South Carolina, 29526, United States of America. *www.metglas.com*

[3] Squire, P. T., J. Magn. Magn. Mat, **132** (1994) 10

[4] O'Handley, R. C.,*et al.*, App. Phys. Lett., **29** (1976) 330

[5] Julliere, M., Phys. Lett. **54A** (1975) 225

[6] Jimbo, M., *et al.*, Jpn. J. Appl. Phys. **34** (1995) L112

[7] Jimbo, M., *et al.*, J. Appl. Phys. **79** (1996) 6237

[8] Moodera, J. S., *et al.*, Phys. Rev. Lett. **74** (1995) 3273

[9] Kaufler, A., *et al.*, J. Appl. Phys., **91** (2002) 1701

[10] Wang, D., *et al.*, IEEE Trans. Magn., **40** (2004) 2269

[11] Djayaprawira, D. D., *et al.*, Appl. Phys. Lett., **86** (2005) 092502

[12] Lee, Y. M., *et al.*, Appl. Phys. Lett., **90** (2007) 212507

[13] Tsymbal, E. Y., *et al.*, J. Appl. Phys., **97** (2005) 10C910

[14] Sousa, R. C., *et al.*, Appl. Phys. Lett., **73** (1998) 3288

[15] Dimopoulos, T., *et al.*, J. Appl. Phys. **87** (2000) 4685

[16] INESC Microsistemas Nanotecnologias, Rua Alves Redol, 9, 1000-029 Lisboa, Portugal

[17] Cardoso, S., *et.al.*, IEEE Trans. Magn., **35** (1999) 2952

[18] Yuasa, S., *et al.*, Appl. Phys. Lett., **87** (2005) 242503

[19] Wojcik, M., *et al.*, Z. Phys. B, **105** (1997) 5

[20] Vegard, L., Z. Phys., **17** (1921) 5

[21] Denton, A. R., *et al.*, Phys. Rev. A, **43** (1991) 3161

[22] Kasper, J., *et al.*, J. Phys. F : Met. Phys., **13** (1983) 311

[23] Cottrell, A. H., "An Introduction to Metallurgy", Edward Arnold (Publishers) Ltd. London, first edition (1967)

[24] MacKenzie, *et al.*, J. Phys. D : Appl. Phys., **38** (2005) 1869

[25] Cardoso, S., *et al.*, J. App. Phys., **97** (2005) 10C916

[26] Jimbo, M., *et al.*, J. Magn. Magn. Mat., **165** (1997) 308

[27] Stergioudis, G., *et al.*, Phys. Stat. Sol. (a), **124** (1991) 393

[28] Nassar, J., *et al.*, Appl. Phys. Lett., **73** (1998) 698

[29] Greiner, J. H., J. Appl. Phys., **42** (1971) 5151

[30] Dimopoulos, T. *et al.*, J. App. Phys., **89** (2001) 7371

[31] CRC Handbook of Chemistry and Physics, 73rd Edition, CRC Press, Boca Raton, USA

[32] Holý, V., "Nonspecular x-ray reflection from rough multilayers", Phys. Rev. B, **49** (1994) 10668

[33] Svedberg, E. B., *et al.*, J. App. Phys., **94** (2003) 993

[34] Freeland, J. W., *et al.*, Phys. Rev. B., **67** (2003) 134411

[35] Wang, Y. H., *et al.*, J. Appl. Phys., **99** (2006) 08M307

[36] Pape, I., PhD Thesis, University of Durham, 1997

[37] Seve, L., *et al.*, Europhys. Lett., **55** (2001) 439

[38] Sousa, R. C., *et al.*, J. Appl. Phys., **85** (1999) 5258

[39] Jergel, M., *et al.*, J. Appl. Crys., **30** (1997) 642

[40] Jankowski, A. F.,*et al.*, J. Appl. Phys., **68** (1990) 5162

[41] Bai, H. L., *et al.*, Appl. Phys. A., **63** (1996) 57

[42] Erdélyi, Z., *et al.*, Phil. Mag. A, **79** (1999) 1757

[43] Erdélyi, Z., *et al.*, Phys. Rev. Lett., **89** (2002) 165901

[44] Erdélyi, Z., *et al.*, Phys. Rev. B, **69** (2004) 113407

[45] Erdélyi, Z., *et al.*, Science, **306** (2004) 1913

[46] Roussel, J.-M., *et al.*, Phys. Rev. B, **73** (2006) 085403

6 Interface sharpening in magnetic tunnel junctions

This chapter examines amorphous CoFeB electrodes in Magnetic Tunnel Junctions (MTJs). The conclusions from the previous chapter, on the nature of CoFeB/AlO_x interfaces, are used to understand more clearly the structural changes that occur on annealing, which is known to enhance the MTJ performance. The sensitivity limits of the x-ray reflectivity technique, when examining complex structures, are also investigated.

6.1 Introduction

Magnetic Tunnel Junction (MTJ) architecture has been refined progressively over the last 10 years, leading to an increase in the Tunnel Magneto Resistance (TMR) value. Typical values for TMR are around the 50% level but TMRs over 400% in MgO based junctions have been reported in the literature [1,2]. For a commercially viable device the MTJs need to be highly sensitive to an external field. This requires the free layer of the MTJs to align easily with the external field direction and the whole device to exhibit a large change in resistance, depending on this external field direction. A detailed description of the working of MTJs has been given in section 2.7. Although the highest TMRs have been seen in MgO based structures, the growth of aluminium oxide tunnel barriers is now routine and well controlled and it is still a very important barrier material. To date only Freescale, a spin off company from Motorola, has put MRAM into commercial production [3]. Freescale's published 'white paper' associated with the MRAM chip indicates the use of aluminium oxide barriers in their structures [4].

Several authors report that moderate annealing enhances the measured TMR [5,6,7], with Sato identifying that the degree of improvement depends on the oxidation conditions [8]. In some structures, CoPt/AlO_x for example, the TMR initially shows no change with annealing, but then falls at higher temperatures [9]. Ultimately, when the annealing temperature is too great the TMR performance is impaired and this tends to occur around 300°C. This presents the problem that to integrate MTJ structures within existing CMOS technology, to allow for incorporation of transistors for switching, heating is a necessary part of the manufacturing process, and the MTJ structures have to be resilient to temperatures up to between 400°C and 450°C [10]. At these temperatures many MTJ structures have gone beyond their optimum annealing temperature for enhancing the TMR.

Thermal annealing permanently changes the TMR, and it is likely that the internal interface structure is affected in some way, as the performance of an MTJ is known to be highly sensitive to the interfaces themselves [11,12,13]. A change in the oxidation state at the interfaces of CoFe/Al_2O_3 on annealing has been observed via Rutherford back scattering, with cobalt and iron oxides being reduced by annealing to 250°C [14]. It is thought that modification to the surface states from which tunnelling occurs is responsible for the changes in tunnelling probability. Néel "orange-peel" coupling due to conformal roughness across the tunnel barrier will also serve to impair the performance of the MTJ [15,16,17]. Interfaces affect not only the TMR values but can also affect the resistance, reliability and ultimate degradation of devices [18].

In the pursuit of better high temperature performance, Cardoso remarked in 2000, after studying inter-diffusion within the CoFe/AlO_x system, *'Further work is needed to clarify the correlation between intrinsic barrier properties and TMR. This is most probably the key to extend the junction thermal stability above 400°C"* [19]. To date, the majority of measurements on the structure of MTJs have been done using techniques such as Auger Electron Spectroscopy, Rutherford Back Scattering, or electron microscopy techniques. Here the situation is examined using x-ray reflectivity to probe the CoFeB/AlO_x interface.

6.2 Samples under investigation

The CoFeB electrode / AlO_x barrier interface, characterised in the previous chapter in repeated bi-layer structures, is now examined on top of an actual MTJ sub-structure. In the previous chapter it was identified that this interface is sensitive to heating. The whole structure studied here is a realistic MTJ, with the top free electrode left off to simplify the scattering analysis.

The large area sample was grown by magnetron sputtering on a thermally oxidised silicon wafer at Siemens, Erlangen, by Theo Dimopoulos, and is shown diagrammatically in Figure 6-1 below. Tantalum and ruthenium are used as buffer layers, on which is deposited an 80Å anti-ferromagnetic pinning layer of $Ir_{20\%}Mn_{80\%}$. This then pins a 30Å amorphous ferromagnetic $Co_{60\%}Fe_{20\%}B_{20\%}$ electrode. The thin (12Å + oxidation) aluminium oxide barrier layer on top of the pinned electrode was grown by the same sputter etching technique as used in the CoFeB/AlO$_x$ multilayer of the previous chapter. Finally the sample was capped another tantalum-ruthenium bi-layer. The finished wafer was cut, using a diamond scribe to score along the surface and then fracturing it over an edge, into individual pieces approximately 8mm square which could be easily mounted inside a furnace, or on a diffractometer.

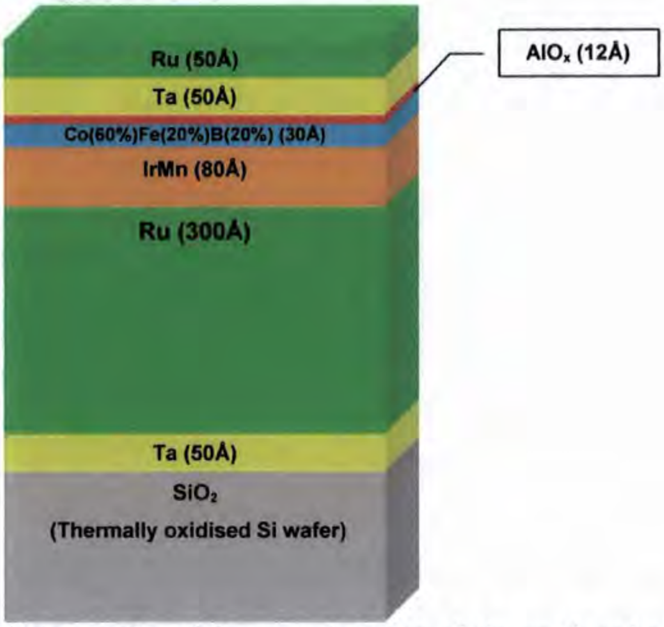

Figure 6-1: Representation of the nominal structure of the sample under investigation

6.3 Experimental details

Experimental data were collected on station 2.3 of the SRS and on BM28 (XMaS) of the ESRF. Both beamlines have been described in detail in chapter 3, and both beamlines were used with a vacuum furnace mounted on the diffractometers and set up for reflectivity measurements to allow for *in-situ* annealing during the experiment. Initial characterisation was performed at a wavelength of 1.3Å, although later the energies were changed in the range 6keV to 13keV to cover the important L and K edges of some of the elements in the sample.

6.4 Results

6.4.1 Room temperature specular scatter and simulation

Over the course of investigating these structures, different samples, all cut from the same wafer, were examined. These give a measure of both the degree of homogeneity of the sample growth over the whole surface of the wafer, and also the level of reproducibility of the x-ray reflectivity techniques used.

Four samples were initially investigated. The scans from three of the samples are presented in Figure 6-2 below and show excellent agreement with one another. Scatter is observable out to 8° and beyond showing both excellent sample growth in terms of interface perfection and the alignment of the diffractometer in staying on the specular ridge. The slightly lower intensity of sample 4 is as a result of it being cut to a slightly smaller size, resulting in less scatter at lower angles from the beam footprint considerations. This has an observable impact on intensity up to a detector angle of 3°.

The scatter from sample 2 appeared very different to the other three, partly as a property of poorer alignment resulting in a lower intensities at the critical angle (although this also arises from a smaller sample size) and possibly from being cut from the very edge of the wafer. This sample was not used for further measurements. Thus, we can assume that three out of the four samples cut from the wafer have an identical structure, and it is safe to draw conclusions from comparison of results of different samples cut from the central regions of the wafer. It also demonstrates the repeatability and reliability of this x-ray scattering technique.

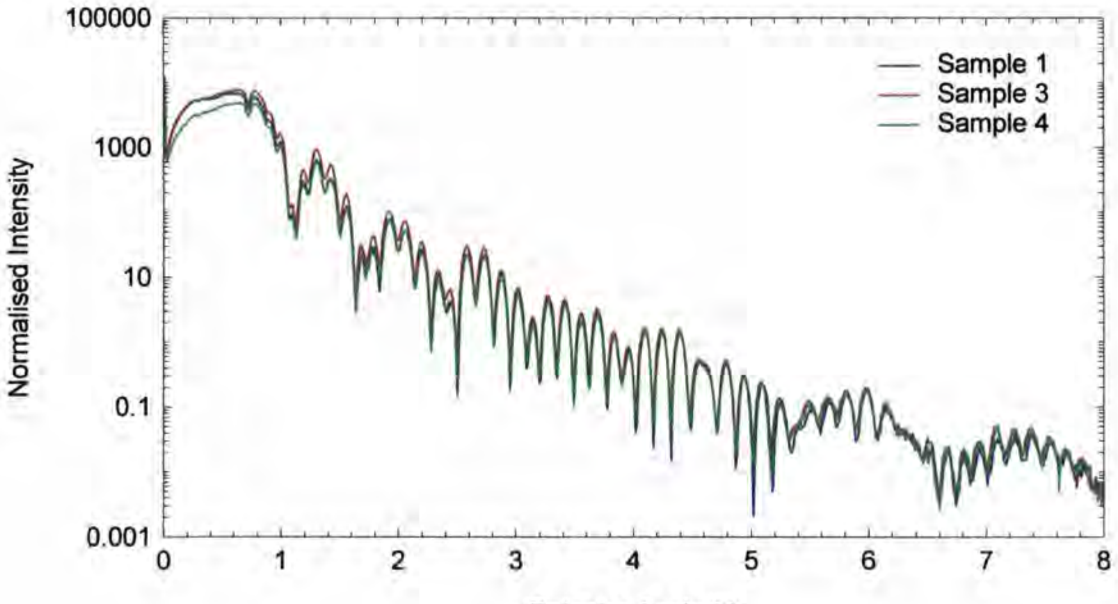

Figure 6-2: Graph of true specular scatter for three samples at wavelength 1.3Å

The simulations of the specular scatter are shown in Figure 6-3 below, and the structures used for the simulations are shown in Table 6-1 below. The fitting was done in Bede REFS, starting from the nominal structure, and refined by using a genetic algorithm. Excellent agreement is seen between the models and the experimental data over the whole range of the scatter. All curves were fitted to the same incident intensity.

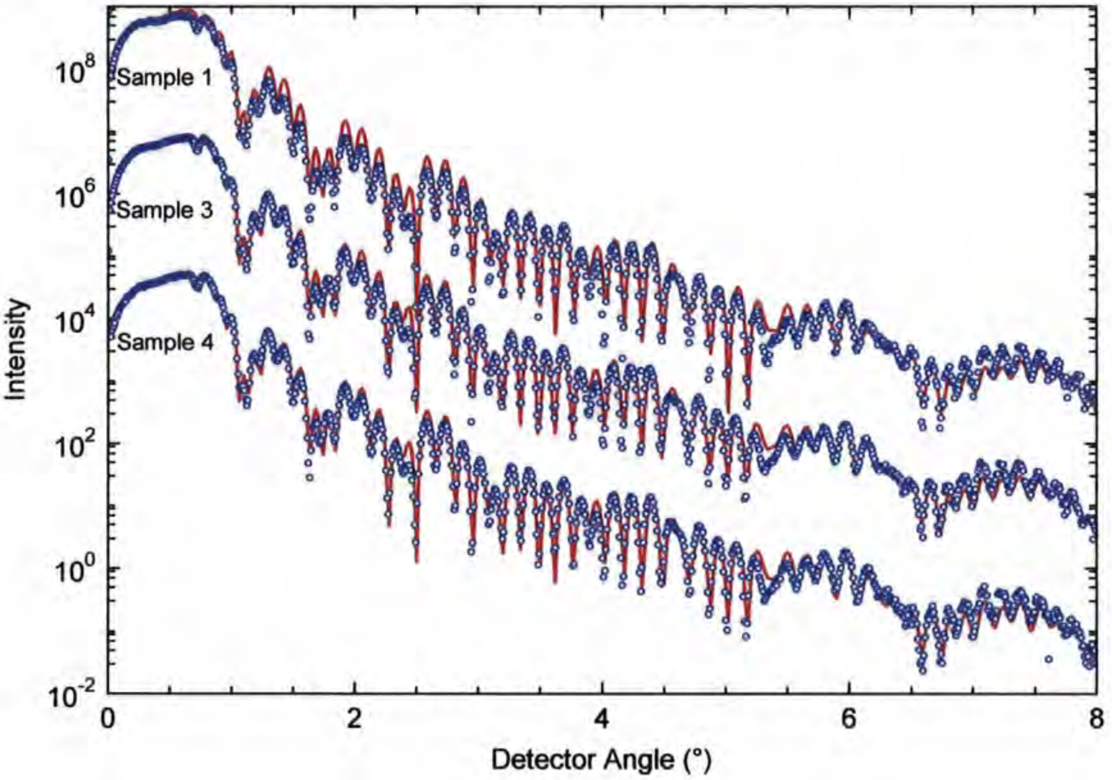

Figure 6-3: Graph of true specular scatter and simulation for the three samples.

Layer	Material	Thickness (Å)			Density (% of bulk)			Interface Width (Å)		
		Sample 1	Sample 3	Sample 4	Sample 1	Sample 3	Sample 4	Sample 1	Sample 3	Sample 4
8	RuO	5.4 ± 1.6	6.1 ± 0.8	5.8 ± 0.9	95 ± 86	95 ± 42	99 ± 43	4.3 ±1.3	4.3 ±0.8	4.1 ± 0.8
7	Ru	52.9 ± 1.8	52.9 ± 1.0	53.0 ± 0.9	95.0 ± 1.8	95.1 ± 1.2	95.0 ± 1.2	3.4 ± 0.7	3.3 ± 0.4	3.0 ± 0.5
6	Ta	42.3 ± 0.5	42.8 ± 0.4	42.6 ± 0.3	95.0 ± 2.3	95.0 ± 1.6	96.0 ± 1.5	2.9 ± 0.5	2.7 ± 0.4	2.4 ± 0.4
5	Al_2O_3	21.9 ± 0.4	20.6 ± 0.3	20.8 ± 0.3	100.0 ± 9.0	95.0 ± 6.5	96.0 ± 6.7	4.4 ± 0.1	4.8 ± 0.1	4.3 ± 0.1
4	CoFeB	15.6 ± 0.8	20.4 ± 0.6	19.8 ± 0.7	95.0 ± 5.3	99.8 ± 3.5	99.7 ± 3.5	4.9 ± 0.4	4.8 ± 0.2	4.6 ± 0.2
3	IrMn	68.8 ± 0.9	64.3 ± 0.6	64.6 ± 0.6	100.0 ± 2.6	100.0 ± 1.8	99.2 ± 1.8	5.3 ± 0.9	4.4 ± 0.5	4.3 ± 0.5
2	Ru	275.2 ± 0.4	276.3 ± 0.3	275.7 ± 0.2	95.0 ± 1.4	96.8 ± 0.9	96.4 ± 0.9	3.7 ± 0.4	3.6 ± 0.2	3.1 ± 0.2
1	Ta	44.6 ± 0.1	45.0 ± 0.1	45.0 ± 0.1	96.7 ± 1.8	100.0 ± 1.3	99.8 ± 1.4	0.5 ± 1.1	0.5 ± 0.8	0.5 ± 0.8
Sub	SiO_2	∞	∞	∞	100 ± 14	100.0 ± 9.7	99 ± 10	2.7 ± 0.1	2.6 ± 0.1	2.4 ± 0.1

Table 6-1: Comparison of the models found to give the best-fit simulation to the experimental data for the three samples.

The models show very little sensitivity to the interface width formed between the tantalum and ruthenium in the buffer, and the value of the goodness-of-fit parameter only changes by a very small amount over the range 0Å to 10Å. A lower limit of 0.5Å was chosen to be physically realistic for this interface. Between all three models there is excellent agreement in all the parameters. There is also very little sensitivity to the top oxide density or interface width.

From the refractive index profiles of the fitted structure, shown in Figure 6-4 below, it can be seen that both the δ and β terms in the refractive index (equation (2-8)) drop dramatically at the tunnel barrier layer. This lower density layer gives rise to the characteristic dip at the critical angle as a result of a second, lower, critical angle being encountered. From the increased refractive index contrast the reflectivity amplitude coefficients are greater at these interfaces and scattering shows particular sensitivity to changes in the roughness at these points. Large scattering is also observed from the top surface and substrate interfaces. The boundaries of the CoFeB electrode layer are obscured by the width of the interfaces with the neighbouring layers and the electrode merely forms a shoulder on the profile as the refractive index moves from the low value at the aluminium oxide up to a high a value at the iridium-manganese.

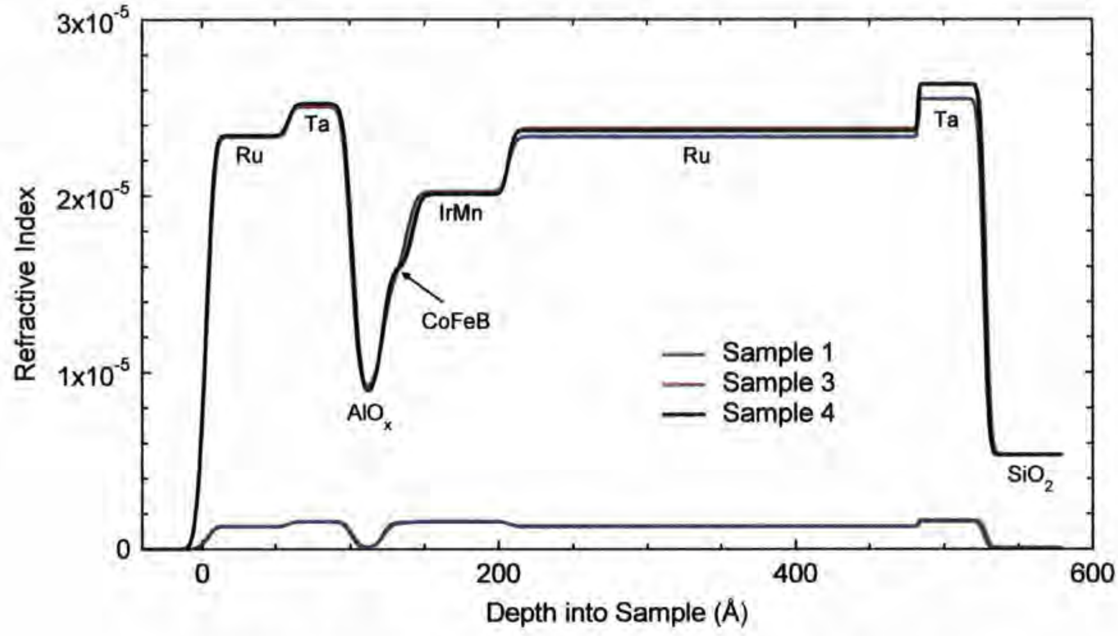

Figure 6-4: The refractive index profile of the fitted structure shown in Table 6-1 above (δ top and β bottom).

6.4.2 Room temperature diffuse scatter and simulation

The off-specular scatter recorded for sample 4, with a -0.1° offset, is shown in Figure 6-5 below, with a specular scan included for comparison. The level of diffuse scatter is very low relative to the specular, so the difference between the measured specular scatter and true specular scatter is negligible, even up to a detector angle of 8°. This low level of diffuse scatter shows that the interface topological roughness is very small. Kiessig fringes are visible in this off-specular scatter, becoming noisy after 4° and disappearing after 6°, showing that the roughness is correlated between the top and bottom layers on the sample.

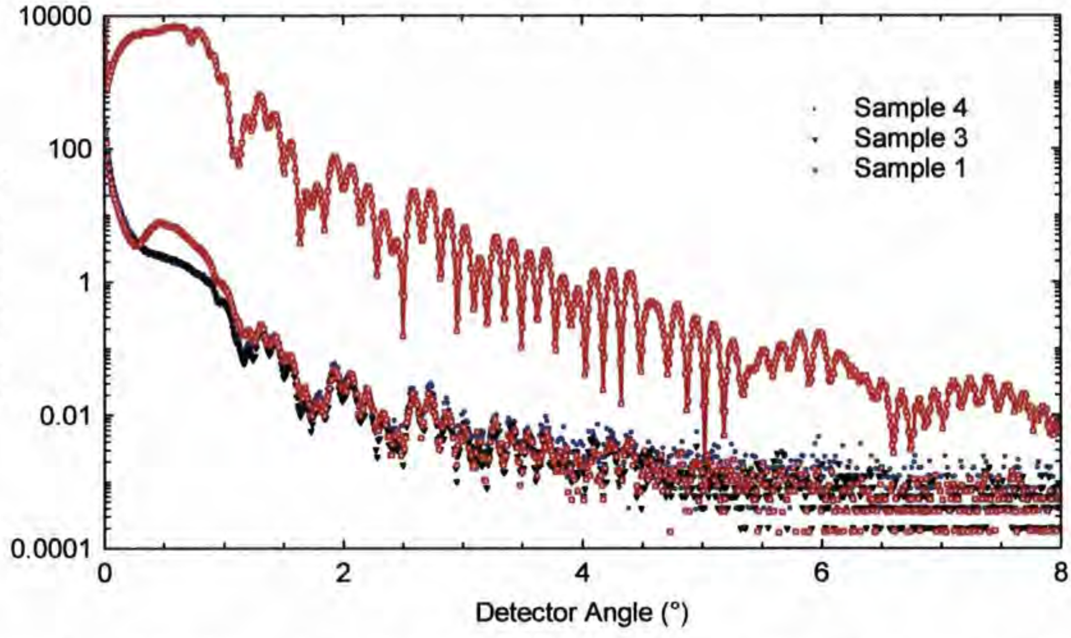

Figure 6-5: Off-specular scatter from the three samples, with the specular from sample 1 for comparison.

The transverse diffuse scatter for all three samples is shown in Figure 6-6 below. Sample 4 exhibits a specular peak that is much wider than the other two, probably because of a small variation in the sample surface angle, either from curvature or a mosaic surface. The low level of diffuse scatter again confirms the low level of topological roughness in the samples. Extra peaks inside the Yoneda wings are present in all the scans, showing that these are real and not an artefact of noise in the experiment.

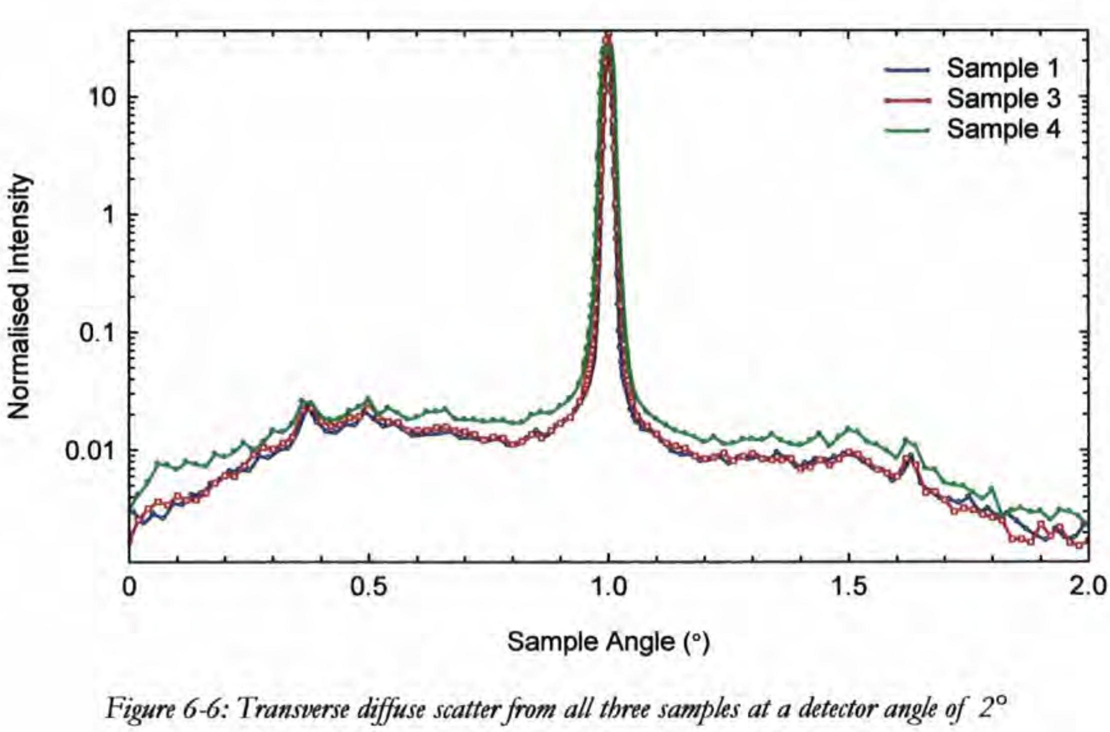

Figure 6-6: Transverse diffuse scatter from all three samples at a detector angle of 2°

The simulations of the off-specular and transverse diffuse scans are shown in figures 6-7 and 6-8 below and use the parameters shown in Table 6-2 for the interface width. It can be seen in Figure 6-7 that the tails of the central specular peak have not been fitted accurately. Within the REFS simulation software it is only possible to include a single value for the correlation length and fractal parameter that is used for all interfaces. Physically it is reasonable that each interface could have differing correlation function parameters, particularly considering the evolution of the interfaces observed previously. This broadening is ascribed to some shorter in-plane correlation lengths being present in the sample which have not been taken in account within the model.

The split between topological roughness and interface width is again difficult to assign independently to each interface present and so the topological roughness has been assumed to be the same for each interface. This has provided a satisfactory fit to the data and shows that the majority of the interface widths are from inter-diffusion. The out-of-plane correlation length is in excess of the stack thickness and increasing this parameter further has very little effect on the scatter.

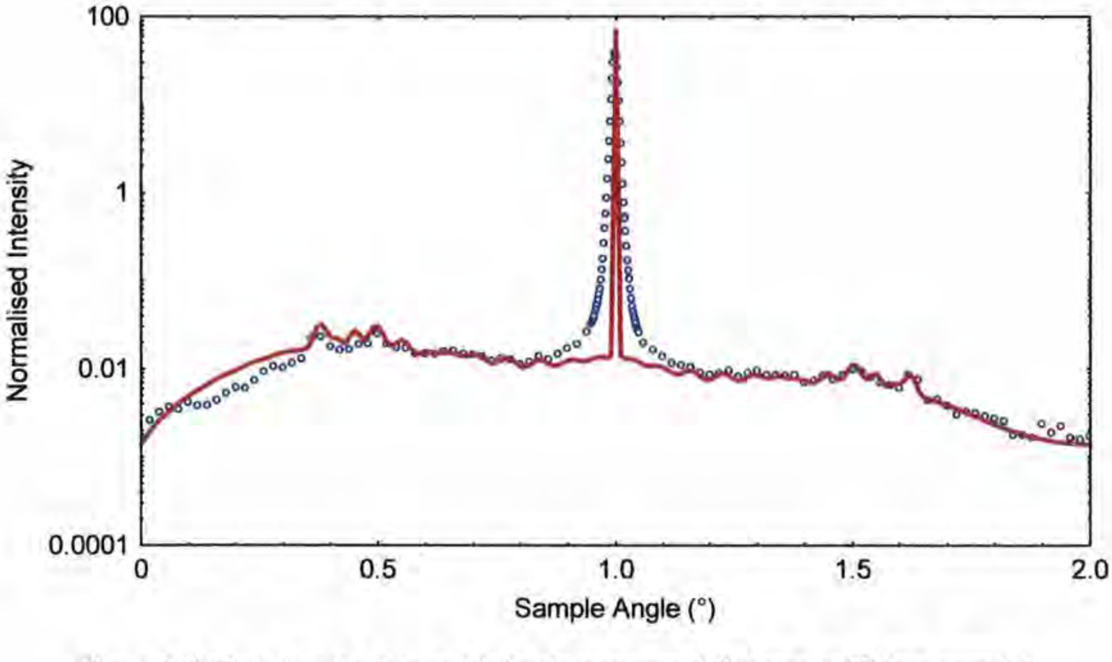

Figure 6-7: Experimental data and fit for the transverse diffuse scan at 2° from sample 3

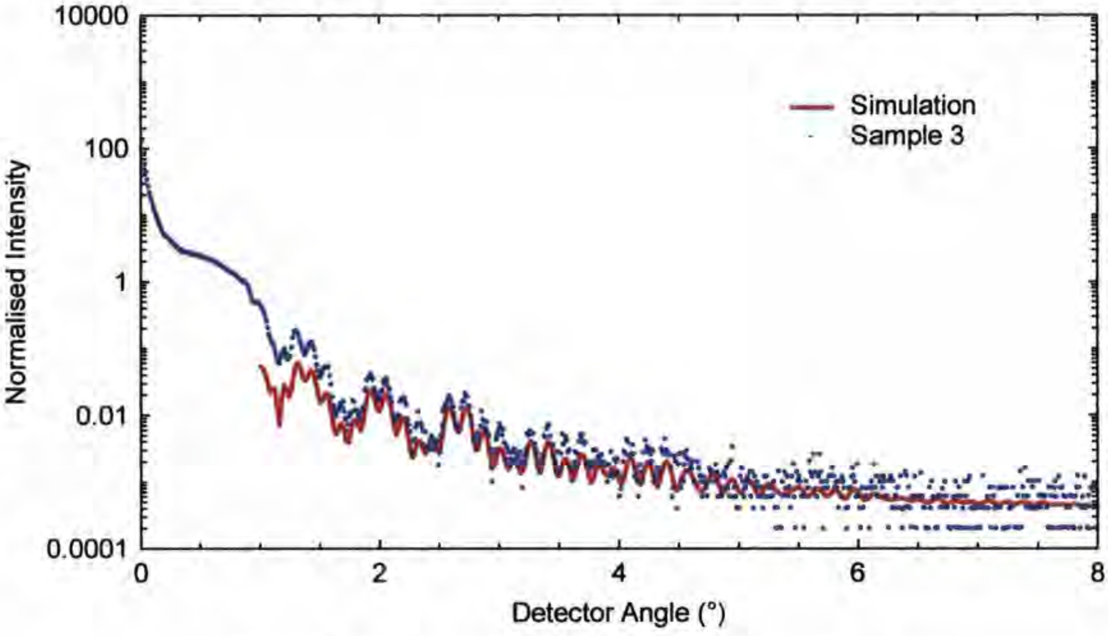

Figure 6-8: Off-specular scatter and simulation for sample 3

In-plane correlation length: 250Å ±100Å

Out-of-plane correlation length: 1000Å ± 300Å

Fractal parameter: 0.3 ± 0.1

Layer	Material	Roughness(Å)	Grading (Å)	Total Interface Width (Å)
8	RuO	1.3	4.05	4.3 ±0.8
7	Ru	1.3	3.05	3.3 ± 0.4
6	Ta	1.3	2.39	2.7 ± 0.4
5	Al_2O_3	1.3	4.38	4.6 ± 0.1
4	$Co_{0.6}Fe_{0.2}B_{0.2}$	1.3	4.66	4.8 ± 0.2
3	$Ir_{0.2}Mn_{0.8}$	1.3	4.22	4.4 ± 0.5
2	Ru	1.3	3.3	3.6 ± 0.2
1	Ta	0.2	0.46	0.5 ± 0.8
Substrate	SiO_2	1.3	2.29	2.6 ± 0.1

Table 6-2: Roughness and inter-diffusion properties of the interfaces for sample 3 at room temperature.

6.4.3 Magneto-transport measurements

Magnetic measurements as a function of temperature were made by the sample grower, T. Dimopoulos at Siemens AG, in their labs at Erlangen using a near-identical sample to that used for these x-ray measurements with the only difference being the inclusion of a 30Å CoFeB top electrode above the tunnel barrier oxide layer and below the Ta/Ru cap.

Annealing was performed in an argon atmosphere to prevent oxidation, and the samples were annealed for 15 minutes at their maximum temperature before lowering the temperature to 50°C and removing the sample from the hot plate. The cooling time varied between 1 hour and 2.5 hours. The annealing was done in a magnetic field of 400kAm^{-1} to set the exchange bias direction. Full experimental details of these measurements have been published in reference [6].

The measured TMR, shown in Figure 6-9 below and taken from [6], is seen to increase, reaching a maximum at around 230°C before degradation begins just above 300°C. At the same time Dimopoulos *et al.* saw an abrupt change in the coercivity and a rapid increase in the resistance area product, which they ascribed to the onset of crystallisation of the initially amorphous CoFeB layers [6]. These results were closely replicated by Li, of the Chinese Academy of Sciences, a year later [20].

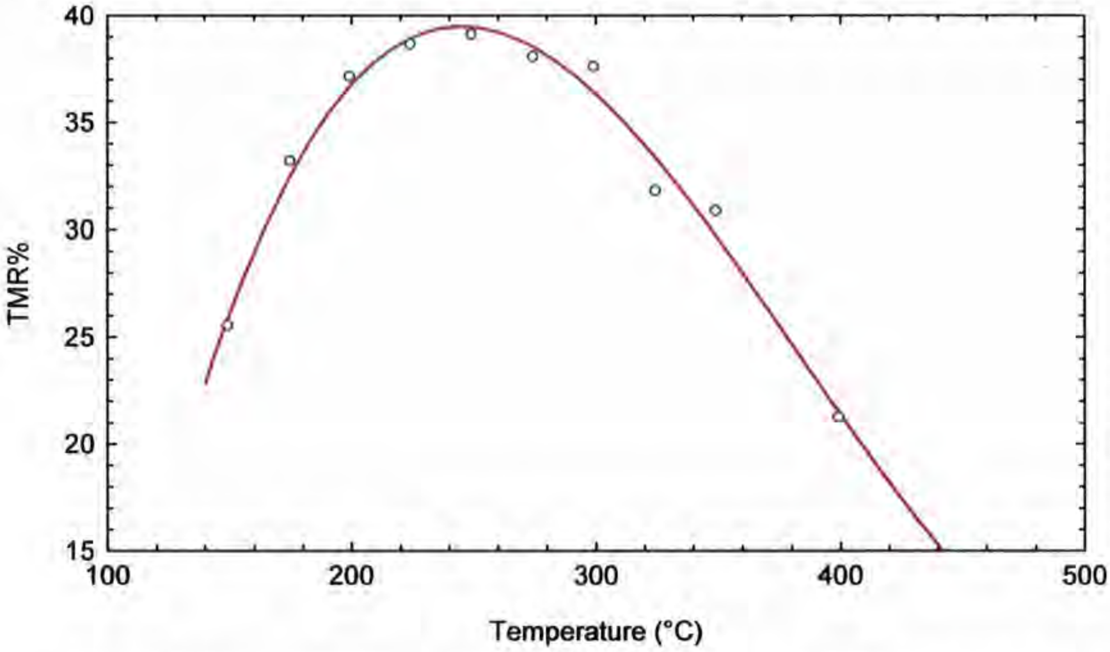

Figure 6-9: Measured TMR% as a function of temperature for the CoFeB/AlOx/CoFeB magnetic tunnel junction. The red line is a cubic fit to act as a guide to the eye only. The TMR reaches a maximum at about 230°C. Data taken from reference [6].

Within the structure there are particular interfaces where it is possible that changes during the annealing process might occur:

a) **Top Ru/Oxide interface:** It is commonly understood that ruthenium does not tarnish or react with air below temperatures of 600°C [21]. However, in examining the surface more closely, after exposure to air at room temperature for several days, it is seen that a very thin passivating oxide layer forms, which is 4Å to 8Å thick [22]. Ruthenium is often used in place of gold for electrical contacts because the most common oxide, RuO_2, is a good conductor with low (but slightly larger than that of a pure metal surface) contact resistance [23]. This oxide breaks down into its elements on heating to a temperature of greater than 600°C, either in vacuum or in an inert atmosphere [22][24]. Recently, it has been found that oxygen adsorption into the surface of both oxidised and oxide-free ruthenium surfaces occurs and at temperatures between 130°C and 230°C in a vacuum this oxygen is seen, via thermal desorption spectra, to be released [25][26]. If this oxide were to thicken then the contact resistance would change and may affect the TMR measurements. Performing the annealing in either vacuum or an inert gaseous atmosphere will prevent this from occurring.

b) **CoFeB/AlO_x interface:** From the work in the previous chapter it is known that this interface is modified on heating in the temperature range being investigated and that sharpening can occur at the interfaces. This can have two effects on the measured TMR. Firstly, a sharper interface may improve the spin-polarisation of the carriers injected into the tunnel barrier, thereby improving the TMR. Secondly, as is believed from the work of Buchanan *et al.* [27], the tunnelling occurs through the points in the structure with the thinnest barrier thickness which arise from non-conformal roughness, then a reduction in interface-width may increase the barrier thickness changing the TMR. There is also the possibility that boron, being small and interstitial, is able to diffuse into the neighbouring layers, particularly on crystallisation. There are also the effects from over and under oxidation of the Al metal which were discussed in the last chapter.

c) **IrMn/CoFeB interface:** This interface is crucial to the exchange pinning of the CoFeB electrode. Changes here may affect the strength of the exchange pinning, however as long as the CoFeB layer is still pinned, even if that pinning is weakened, then as long as the external field is not too strong the TMR should not be affected. Many studies have been performed on the manganese which has a reputation for a high mobility within structures [28-31]. Some authors have attributed a reduction in TMR between 250°C and 280°C to manganese diffusion through the electrode [32]. It was observed that at 300°C strong inter-diffusion starts in a CoFe/IrMn interface and the Mn eventually reaches the Al_2O_3/CoFe interface [10] at

> temperatures in excess of 435°C [33]. However, when Cardoso looked at systems with a thin Ta diffusion barrier to prevent the movement of manganese four years earlier it was concluded that the same reduction in TMR occurred in samples where manganese diffusion had both occurred and where it had not occurred. A small redistribution of oxygen at the electrode/barrier interface was also observed [19]. Several authors reported that manganese only reaches the barrier layer when the barrier has been over-oxidised, causing oxidation of the CoFe layer below. When samples were under-oxidised, no manganese transport to the barrier was observed [34,35]. One of the motivations for including an amorphous CoFeB layer is to act as a diffusion barrier to this Mn transport, as Mn primarily diffuses along the grain boundaries [6].

To examine these possibilities the x-ray scatter from the samples has been recorded at different temperatures to establish what structural changes are occurring when the samples are heated.

6.4.4 Effect of annealing on the specular scatter

The full range specular scatter, recorded with the sample in vacuum *in-situ* on the diffractometer at a range of temperatures from 20°C up to 400°C, is shown in Figure 6-10 below. At low angles the scatter is almost constant with heating, but above 4° the scatter begins to show changes. These are shown in more detail in Figure 6-11 where green lines have been added to show positions where extra peaks appear or existing peaks split. The amplitude of these higher angle fringes also changes with temperature, as shown in Figure 6-12 where the curves have all been plotted on top of one another and on a linear scale. There is a steady increase in fringe amplitude up to 300°C. The fringe amplitude as a function of temperature has been plotted in Figure 6-13 to show this. The data follow the same form as that of the TMR with temperature, shown in Figure 6-9, although the temperatures quoted are likely to be overstated as the thermocouple was placed on the crucible some distance away from the sample.

Between 340°C and 400°C the fringes are seen to collapse and an additional sharp depression occurs at the critical angle. These are very similar to the changes observed in the CoFeB/Ru multilayer of the last chapter, and therefore are associated with the crystallisation of the CoFeB layer in the sample. Here the CoFeB content is much less, being only nominally 30Å in total, than in the multilayer, however the crystallisation of this layer is still able to have a dramatic effect on the form of the specular scatter.

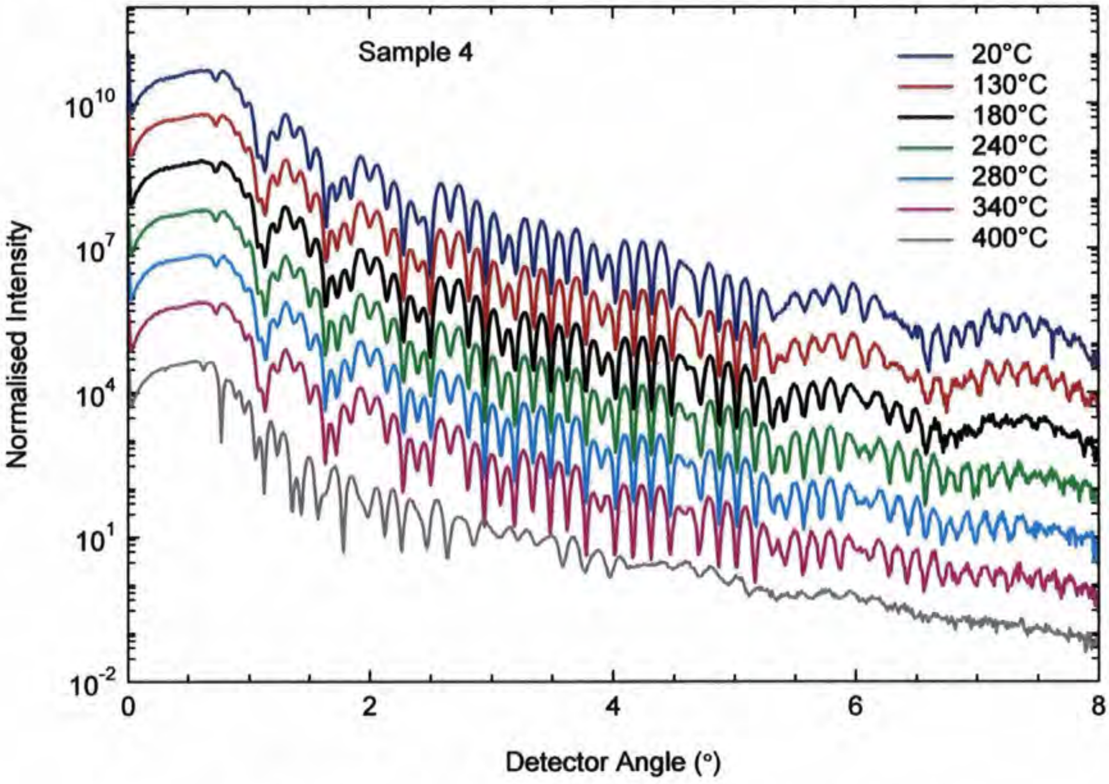

Figure 6-10: Full range specular scatter at different temperatures for sample 4.

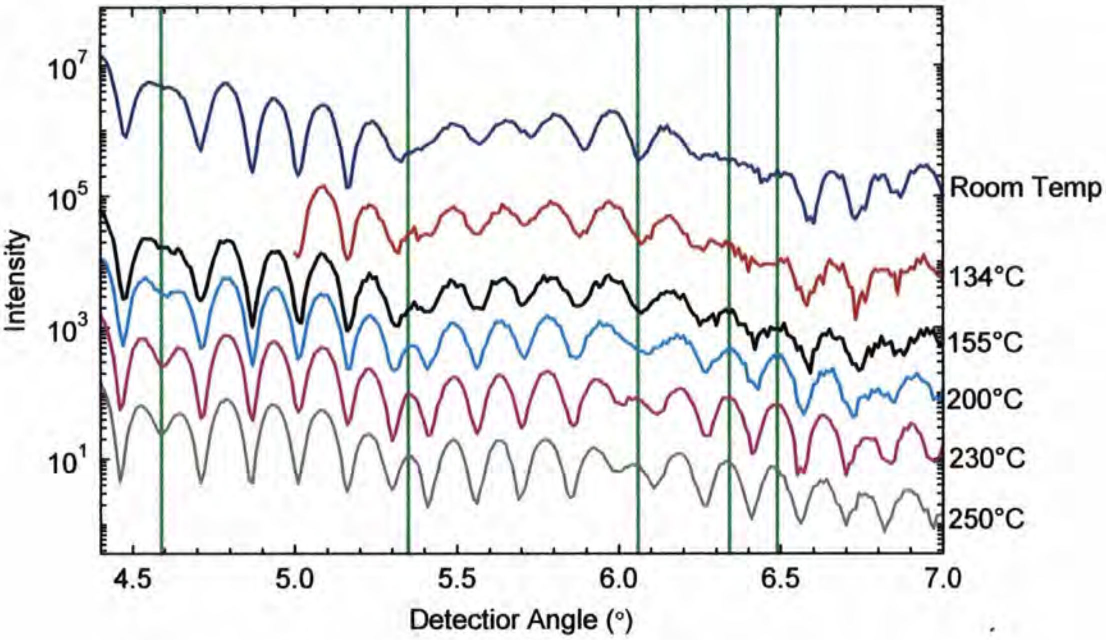

Figure 6-11: Variation in the specular scatter with annealing from sample 3.
The curves have been offset by factors of 10 for clarity.
The green lines highlight some regions where significant changes are occurring.

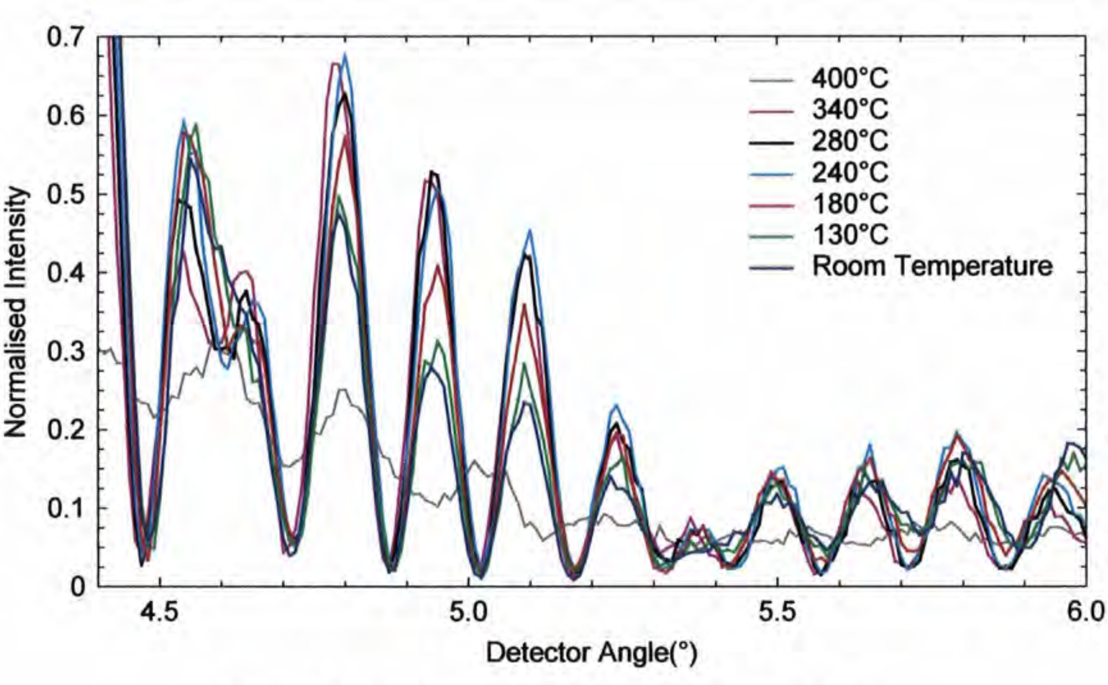

Figure 6-12: The specular scatter from sample 4 at high angles and at different temperatures on linear vertical scale.

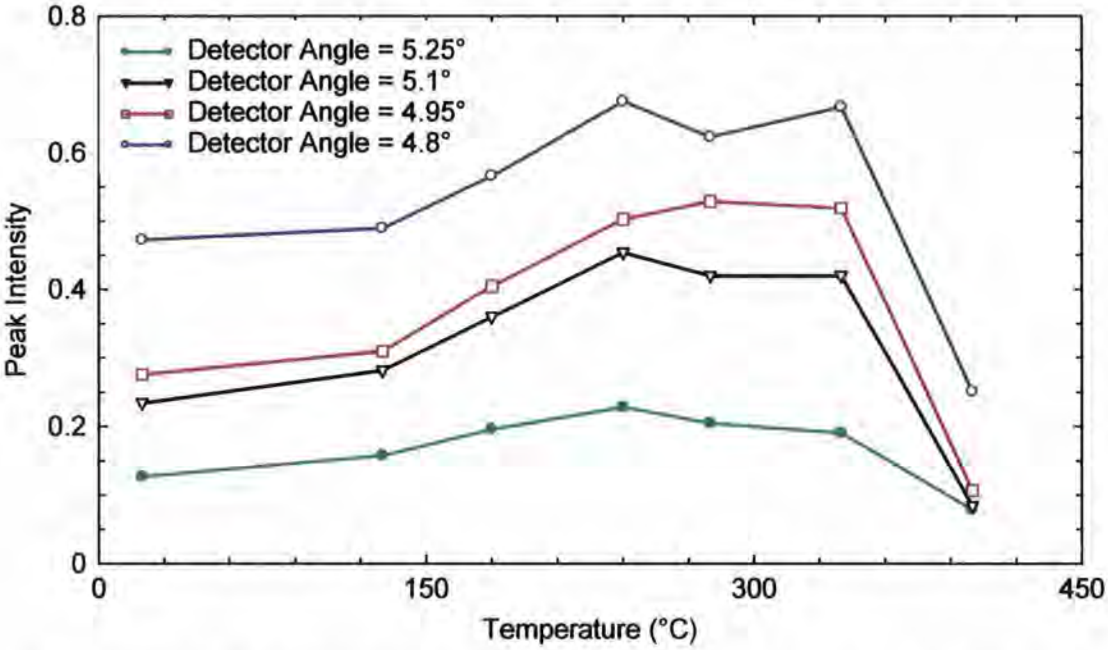

Figure 6-13: Graph of variation in specular peak intensity with temperature, taken from sample 4.

We can be sure that these changes in fringe amplitude are real and not movements up and down the specular ridge for the following reasons:

a) The detector slits were kept wide to accept the entire specular point.

b) Samples have been aligned at various points along their specular reflectivity curves using rocking scans.

c) The diffractometer has been well tested and is known to hold its alignment well, if the sample is positioned correctly in the centre of rotation.

d) The changes in fringe amplitude are systematic.

All four samples initially examined showed this same behaviour. Following from the arguments presented in the last chapter, an increase in the fringe amplitude must be related to either interface sharpening, or a contrast change between layers. These measurements were made with the sample at elevated temperatures and so, through thermal expansion or through 'healing' of defects, it is possible for densities to change. The observation that the TMR changes with annealing shows that the internal interfaces must be changing with temperature, but it is not until simulations are considered for this more complex system that a more detailed interpretation of this scatter can be provided.

6.4.5 Effect of annealing on the diffuse scatter

The off-specular scatter recorded at different temperatures is shown in Figure 6-14 and the transverse diffuse scatter shown in Figure 6-15 below. The scatter is seen to be invariant until 340°C, when the transverse diffuse scatter suddenly increases. This is associated with the onset of crystallisation of the CoFeB in the sample. In the transverse diffuse scan the scatter recorded at 340°C shows good agreement with the cooler temperatures at low angles, however at higher angles the scatter is more intense. This may be from crystallisation of the CoFeB sample during the course of the measurement. At 400°C the scatter is much more intense, showing a significant increase in the topological roughness of the interfaces. The off-specular scatter has also changed substantially, and the loss of the diffuse Kiessig fringes shows that the conformality between the top and bottom surfaces has been lost.

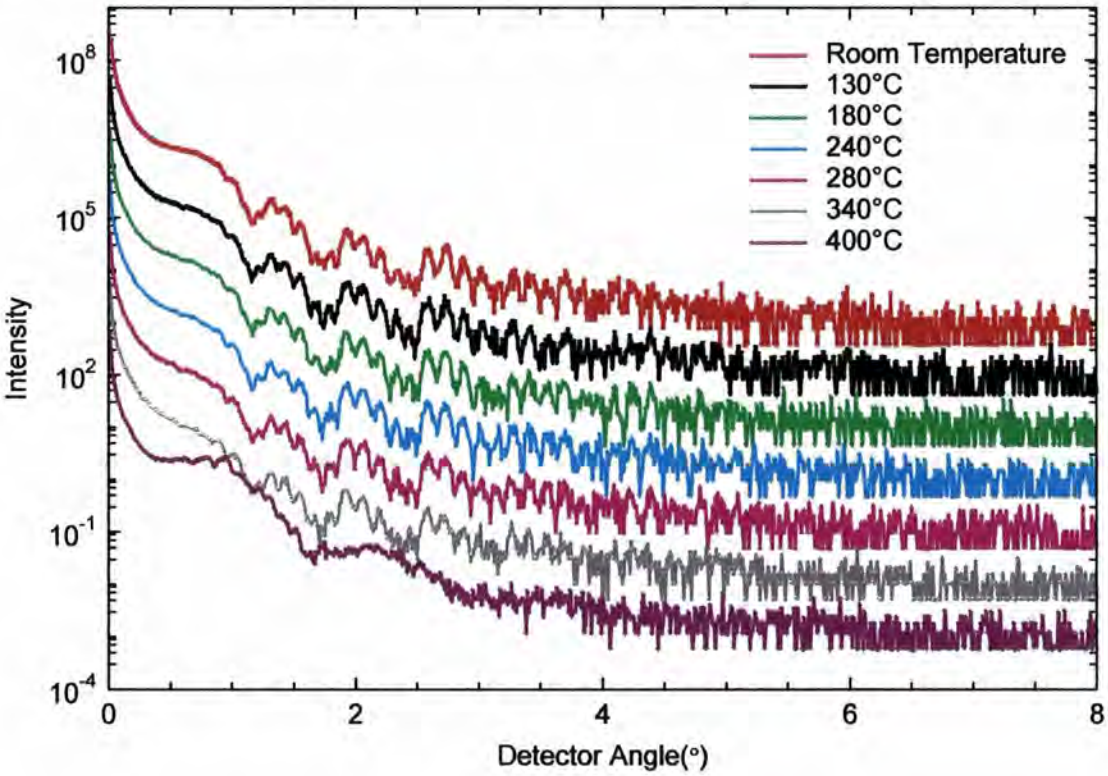

Figure 6-14: Off specular scatter from sample 4.

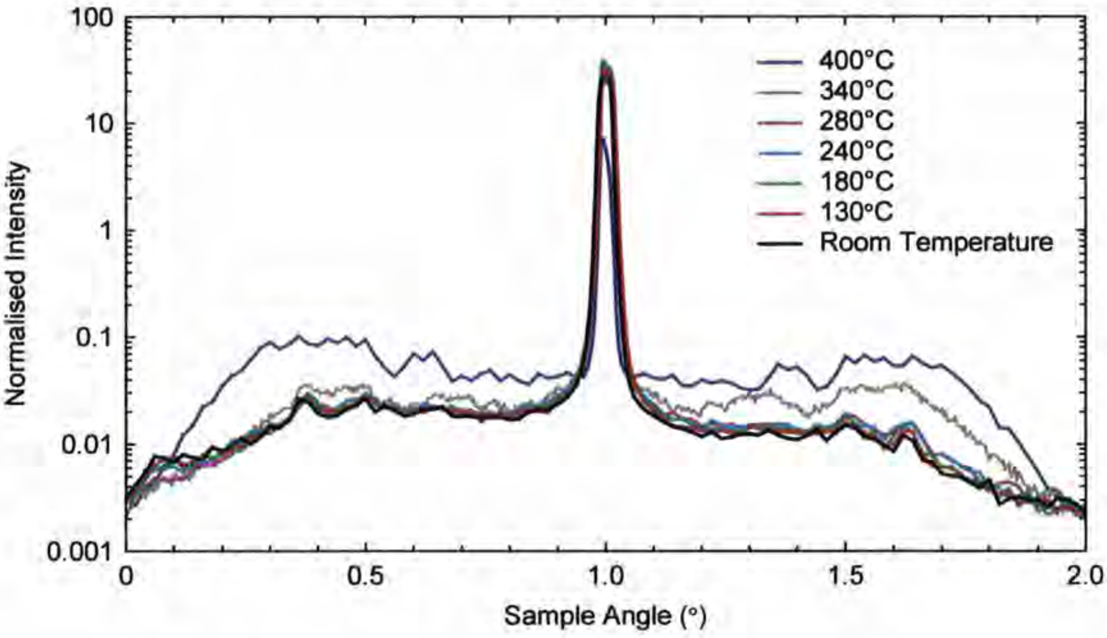

Figure 6-15: Transverse diffuse scan at 2° from sample 4

The unchanging nature of the diffuse scatter shows that until crystallisation above 340°C, no changes are occurring to the topological roughness of the sample interfaces. The change in the specular scatter must be either from density changes or a change in the chemical inter-diffusion across the interfaces.

6.4.6 Time dependence and reversibility of measurements

In the above measurements the time required to reach thermal equilibrium within the furnace is of concern, as is how quickly the changes in the specular scatter occur after the sample has reached temperature. The magnetic measurements were all made *ex-situ* at room temperature. If these changes in the specular scatter are not revisable when the sample is cooled, then there is more assurance that the sample changes giving rise to changes in the specular scatter are related to the observed changes in the TMR.

Repeated specular scans at the same temperature were performed to see how the scatter changed as a function of time after the temperature has been reached. The furnace typically took 10 minutes to change 30°C in a controlled way, avoiding any overshooting of the target temperature. The data recorded after reaching 200°C is shown in Figure 6-16 below. After 7 minutes (red markers) the data has still not fully stabilised, as is evidenced by the change in intensity after 14 minutes (dark blue markers). From 14 minutes onwards there is no noticeable change in the scatter, and it is seen that the changes occurring as a result of annealing to 200°C have occurred and the new sample structure has stabilised.

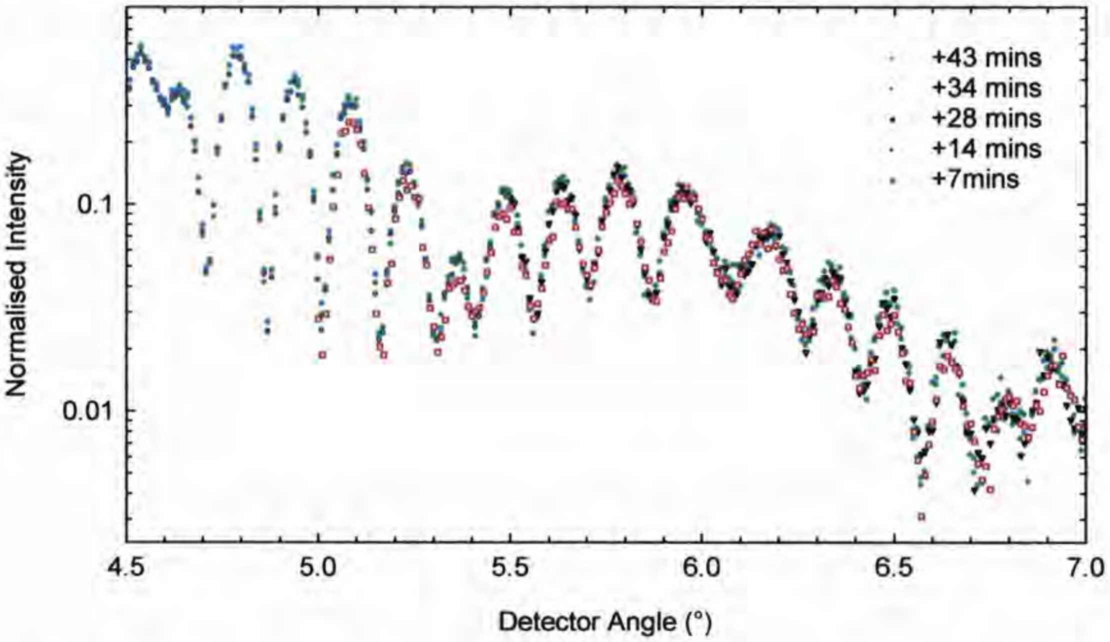

Figure 6-16: High angle scatter for different times after the temperature of 200°C was reached.

The full range specular scatter from sample 1 is shown in Figure 6-17 below. It demonstrates that the specular scatter recorded when the sample is hot is the same as the scatter recorded after the sample has been allowed to cool down after the experiment. The changes occurring on annealing are not reversible. It is therefore consistent with the assumption that the underlying structural changes causing the scatter to change are responsible for the TMR enhancement observed.

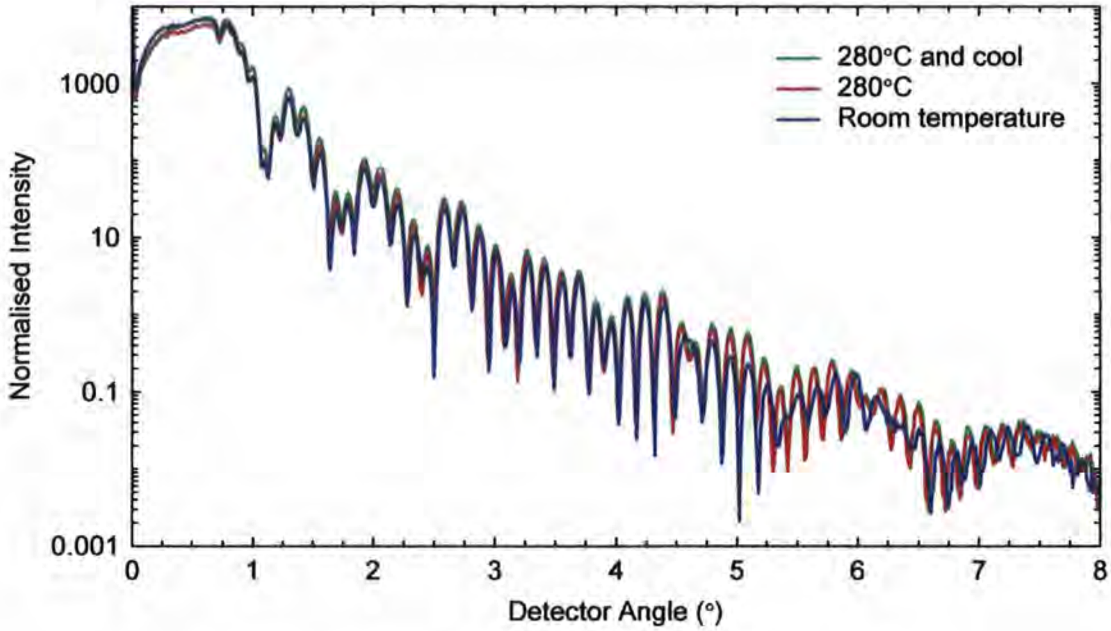

Figure 6-17: Effect of cooling the sample on the observed scatter.

6.4.7 Simulation of the specular scatter with heating

Simulation of the higher temperature scatter was initially performed in Bede REFS, allowing all the parameters to float, except for the constraint that the incident intensity must not change. The simulated scatter is shown in Figure 6-18 and the best-fit model is shown in Table 6-3 below. On this 'free' fit the errors on the widths have increased as the temperature has been raised from the room temperature models, and so the sensitivity has fallen. The refractive index profiles from these models are compared to the best fit model for the 20°C data in Figure 6-18 below. The differences in intensity at the critical angle for sample 3 is a result of a small thermally induced changes in the height of the sample.

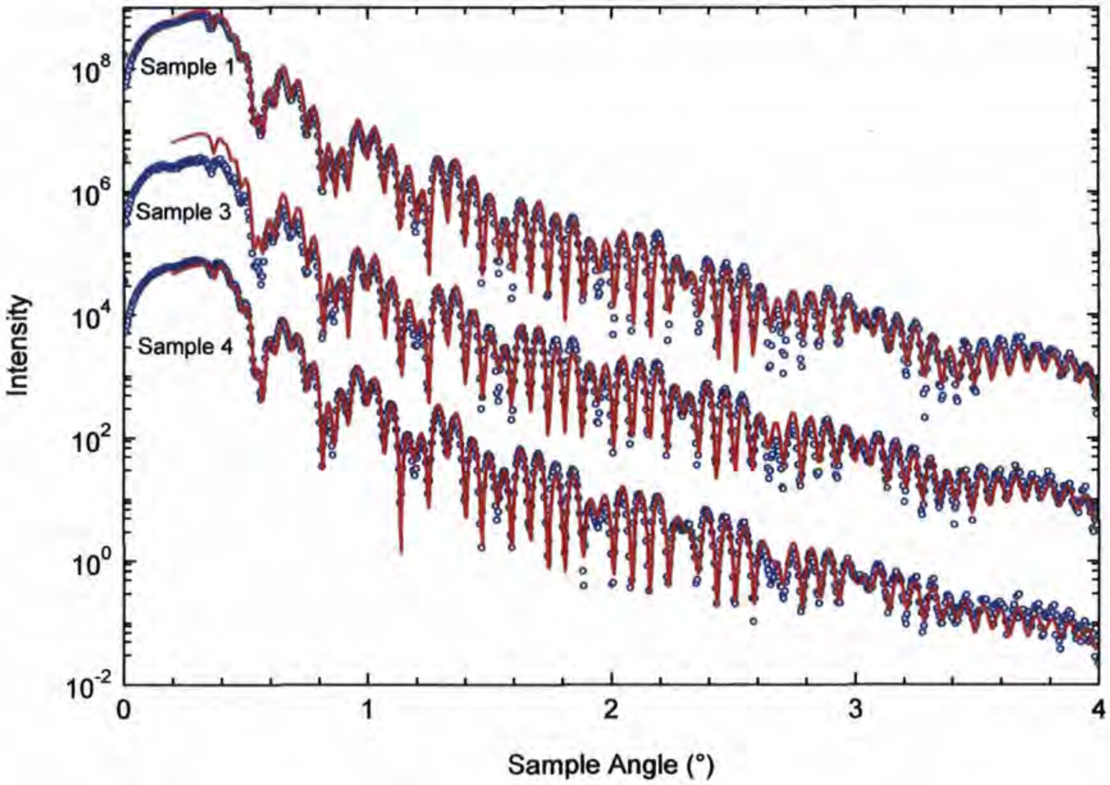

Figure 6-18: Data and best fit allowing all the parameters to float at high temperatures for the three samples. (Sample 1: 280°C, Sample 2: 250°C and Sample 3: 340°C) The curves have been off-set by factors of 100 for clarity.

Layer	Material	Thickness (Å)			Density (% of bulk)			Interface Width (Å)		
		Sample 1 (280°C)	Sample 3 (250°C)	Sample 4 (340°C)	Sample 1 (280°C)	Sample 3 (250°C)	Sample 4 (340°C)	Sample 1 (280°C)	Sample 3 (250°C)	Sample 4 (340°C)
8	RuO	1.3 ± 0.9	6.1 ± 3.3	4.1 ± 1.2	97 ± 28	100.0 ± 7.8	99 ± 21	5.7 ± 0.7	3.5 ± 0.1	5.7 ± 0.3
7	Ru	58.5 ± 5.1	50.0 ± 6.7	52.3 ± 2.0	96.3 ± 1.9	95.0 ± 2.7	99.1 ± 1.2	3.1 ± 0.4	10.0 ± 1.8	3.5 ± 0.3
6	Ta	39.3 ± 5.1	43.5 ± 5.6	46.0 ± 2.0	98.0 ± 4.9	95.0 ± 5.5	96.5 ± 2.1	9.9 ± 4.2	10.0 ± 6.5	5.6 ± 1.7
5	Al_2O_3	21.6 ± 1.2	20.8 ± 0.8	21.7 ± 0.2	98 ± 16	100 ± 16	98.6 ± 7.4	4.9 ± 0.2	5.0 ± 0.2	4.6 ± 0.1
4	CoFeB	17.3 ± 1.4	17.6 ± 1.1	17.6 ± 0.9	98.9 ± 7.7	95.0 ± 6.2	97.1 ± 4.0	8.0 ± 1.7	5.8 ± 0.8	4.7 ± 0.2
3	IrMn	66.2 ± 1.2	65.3 ± 0.8	65.9 ± 0.9	99.8 ± 3.3	100.0 ± 2.8	99.2 ± 1.9	5.1 ± 1.0	4.9 ± 0.8	6.1 ± 0.8
2	Ru	277.4 ± 0.6	278.7 ± 0.5	278.3 ± 0.5	98.0 ± 1.4	97.4 ± 1.4	99.72 ± 0.9	4.8 ± 0.5	4.1 ± 0.4	3.9 ± 0.2
1	Ta	44.1 ± 0.2	43.9 ± 0.3	43.1 ± 0.4	97.47 ± 1.8	95.0 ± 1.8	95.1 ± 1.1	0.5 ± 1.3	0.5 ± 1.8	0.7 ± 1.5
Sub	SiO_2	∞	∞	∞	99 ± 13	100 ± 13	99.8 ± 8.1	2.5 ±0.1	2.5 ± 0.1	2.5 ± 0.1

Table 6-3: Fitted parameter for the fits shown in Figure 6-18 above.

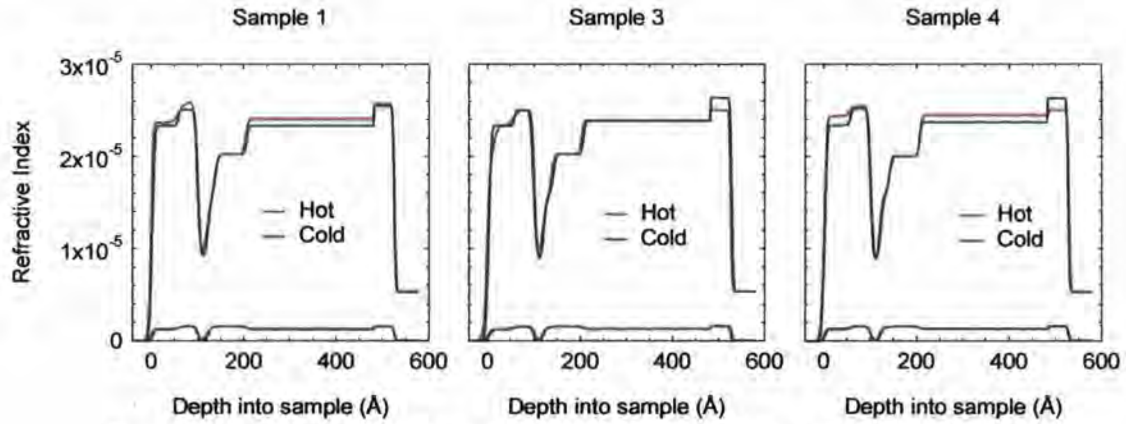

Figure 6-19: Comparison of the real and imaginary parts of the refractive index profile of the hot and cold models for the three samples

The fits are extremely good, although not as close as the room temperature measurements and simulations. The minima between Kiessig fringes appear very sharp when viewed on a log scale, and this is where the fit is poorest. The minimising 'cost' function uses the log of the intensity so that the fitting is not biased to the scatter around the critical angle, however, these sharp minima are difficult to fit because the scattered intensity is extremely sensitive to the incident angle. Any errors in this angle make fitting extremely tricky.

Fitting just the higher angle scatter has been attempted. However this approach, whilst giving a better fit to the experimental data in this region, repeatedly deviates at low angle from what is reasonable, and no consistency between models is found. The low angle scatter is important in determining the densities, both from the critical angle, and the refraction effects on the Kiessig fringes, and finding an acceptable solution without this is difficult. Attempts were also made to refine the simulation by splitting the CoFeB layer into two layers, to allow the model to respond to the possibilities of boron segregation, manganese diffusion, and oxygen re-distribution. However, whilst this enhanced the fit, the physical interpretation was difficult and lacked consistency. The enhancement may have arisen from simply increasing the number of free parameters available to the model; if there are enough free parameters then any profile can be fitted, although little is learned from the model. This line of attack was not pursued further.

Accompanying any long range material diffusion a change in the position of the interfaces is expected. No significant change in the interfaces has been observed and so long range diffusion is unlikely to be significant. The model is attempting to account for the changes in scatter by adjusting the buffer and capping layers more than the magnetically active region. Even with a structure based on the nominal form there are too many free parameters, and the precision on the interface widths is insufficient to determine exactly what is happening on the annealing, that may affect the TMR.

REFS is restricted in the number of constraints that can be put into the modelling. Whilst this is not a problem for finding an initial fit to the data at room temperature, when the sample is annealed there is the constraint that the number of atoms must be conserved., even if their distribution is changed. This can be achieved by requiring that the product of layer thickness and density is constant and matches with the room temperature model.

REFS is unable to do this, and therefore custom C++ code was written to simulate the scatter with this conservation constraint, within the Parratt formalism and with genetic fitting along the same methodology that REFS uses and with the same Goodness of Fit (GOF) function [36]. Corrections to the data for the instrument function were not included in the code and so the output from REFS was simulated with and without the instrument function so that the form of the correction could be found and applied to the experimental data before it was imported into the new program. The simulated scatter from the models was compared to that using REFS to verify that there were no differences, and no material differences were seen. Errors on the fitted parameters were calculated by taking the fitted model back into REFS and using its error calculating routines. They are therefore calculated using the same methodology as the other errors quoted in this work, but they do not reflect the constraints on thickness and density, nor the errors on the initial values from the 20°C model used to form the constraint. The results of fitting are presented in Figure 6-20, the model is shown in Table 6-4, and the refractive index profiles shown in Figure 6-21 below.

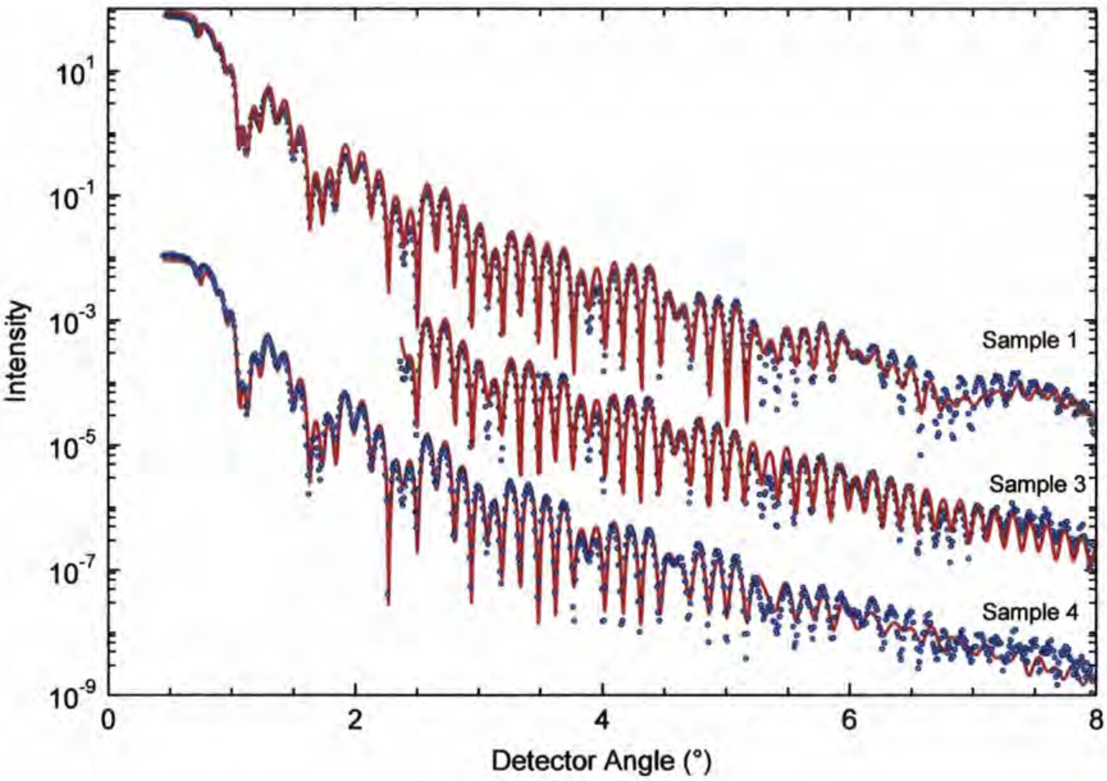

Figure 6-20: Graph of data and free fit at high temperatures with the constraint that atoms are conserved.

Layer	Material	Thickness (Å)			Density (% of bulk)			Interface Width (Å)		
		Sample 1	Sample 3	Sample 4	Sample 1	Sample 3	Sample 4	Sample 1	Sample 3	Sample 4
8	RuO	5.2 ± 0.5	6.1 ± 3.1	5.8 ± 0.5	99 ± 72	95 ± 10	99 ± 67	3.4 ± 1.0	3.4 ± 0.2	4.0 ± 0.8
7	Ru	53.1 ± 6.7	51.3 ± 7.0	53.0 ± 4.9	94.7 ± 1.8	98.0 ± 3.3	95.3 ± 1.9	2.8 ± 0.8	9.0 ± 1.6	3.4 ± 0.7
6	Ta	42.1 ± 6.3	41.7 ± 6.5	42.8 ± 4.3	95.2 ± 4.4	97.6 ± 6.6	95.1 ± 3.6	9.9 ± 5.3	8.9 ± 6.5	7.6 ± 2.8
5	Al_2O_3	22.0 ± 0.8	20.2 ± 0.9	21.0 ± 0.4	99 ± 13	97 ± 20	95 ± 12	4.5 ± 0.1	5.4 ± 0.2	4.7 ± 0.2
4	CoFeB	15.1 ± 3.1	19.9 ± 1.8	19.9 ± 3.6	99 ± 11	101.9 ± 7.3	99.5 ± 7.9	5.3 ± 0.7	6.0 ± 0.8	4.9 ± 0.4
3	IrMn	70.3 ± 3.5	64.7 ± 1.5	64.6 ± 3.6	97.9 ± 2.7	99.4 ± 3.6	99.2 ± 2.6	7.2 ± 3.5	5.1 ± 1.4	9.1 ± 4.0
2	Ru	275.3 ± 0.4	276.3 ± 7.0	274.7 ± 9.3	95.0 ± 1.3	96.9 ± 2.1	96.8 ± 1.5	3.5 ± 0.3	3.8 ± 0.4	3.3 ± 0.3
1	Ta	44.3 ± 0.2	45.8 ± 7.0	46.5 ± 9.4	97.3 ± 1.9	98.1 ± 7.1	96.6 ± 5.7	1.0 ± 0.6	8.4 ± 5.7	9.0 ± 6.4
Sub	SiO_2	∞	∞	∞	100 ± 14	99 ± 37	100 ± 29	2.5 ± 0.1	2.5 ± 0.1	2.6 ± 0.1

Table 6-4: Fitted parameter for the fit shown in Figure 6-20 above.

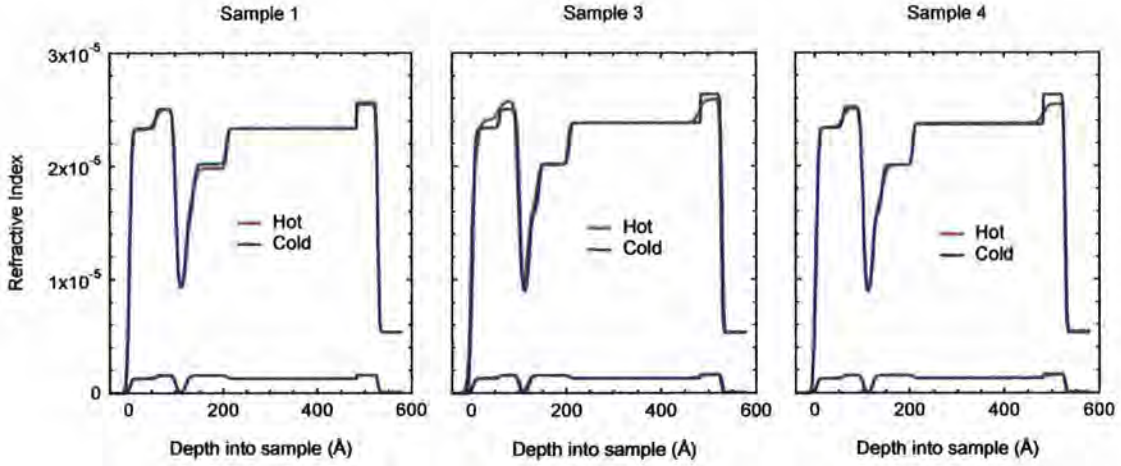

Figure 6-21: Comparison of the refractive index profile of the hot and cold models

From the data it can be seen that the fit is less good. There is the possibility that the initial model is inaccurate, and so the thickness-density products used as constraints are incorrect. These parameters themselves have their own error values which have not been taken into account. In reality there will be a range of allowed thickness and density values that conserve the number of atoms within the error bounds on those particular values. However the inclusion of error values to determine the possible values of thickness and density increases the complexity of the program significantly, particularly as the errors on each individual model tested have to be computed to check they are within the limits, which through the coupling of all the parameters is not trivial.

The next step employed was to look at the effect of changing only one parameter at a time. With the CoFeB/AlO$_x$ interface known to be thermally active, the effect of changing the interface width of the CoFeB/AlO$_x$ interface on the simulated scatter was investigated, and is shown in Figure 6-22 below. This gives the required peak intensity enhancements at higher angles with very little change at lower angles, which matches the experimentally observed data well. The changes in interface width, however, fail to account for the splitting of the peaks just below a detector angle of 4.6°.

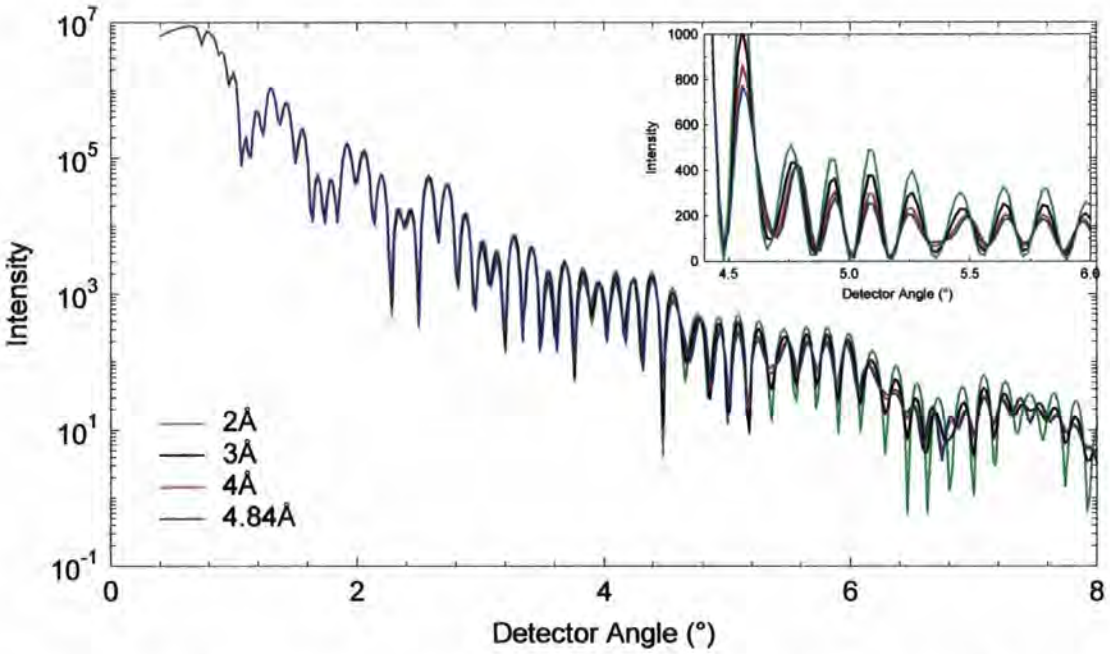

Figure 6-22: The specular reflectivity for different CoFeB/AlO$_x$ interface widths, based on the best fit model to the experimental data. The inset shows the higher angle scatter on a linear scale for comparison.

As a contrast, the effects of modification of the top surface are shown in figures 6-23 and 6-24 below. Any change in the thickness of the top oxide causes the profile to change over the whole angular range. As the sample grows in thickness, which could be as a result of surface oxidation, so the Kiessig fringes shift in position. If the top oxide smoothes, then the amplitude of the Kiessig fringes is also seen to increase, but with a much greater shift in position than was seen with just sharpening of the CoFeB/AlO$_x$ interface.

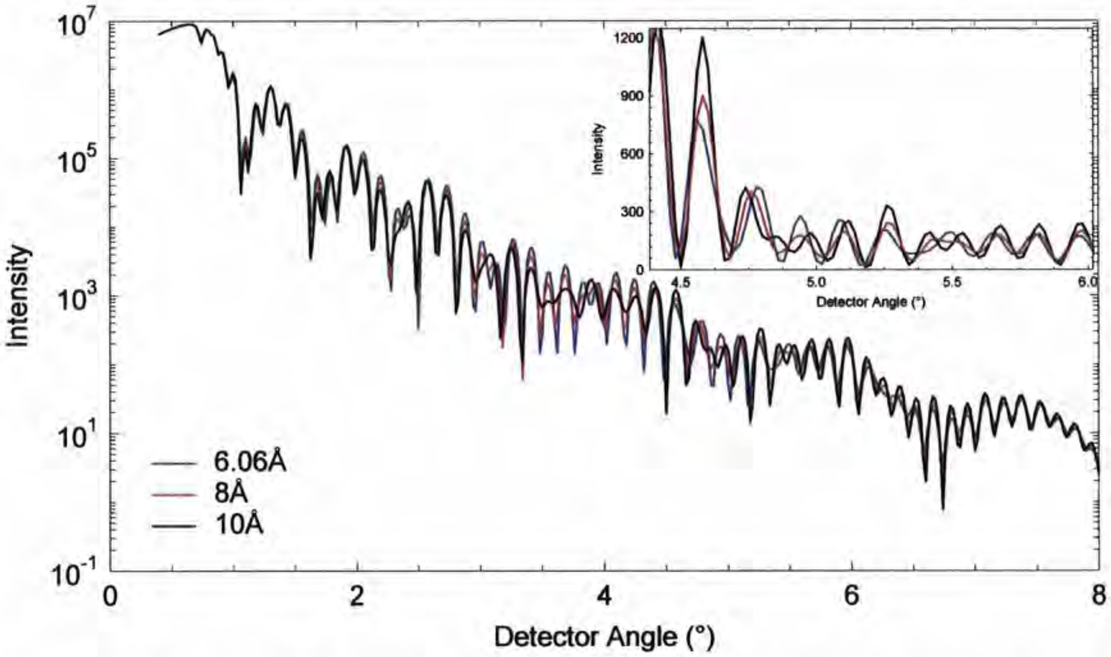

Figure 6-23: The specular reflectivity for different thickness of the top oxide, based on the best fit model to the experimental data. The inset shows the higher angle scatter on a linear scale for comparison.

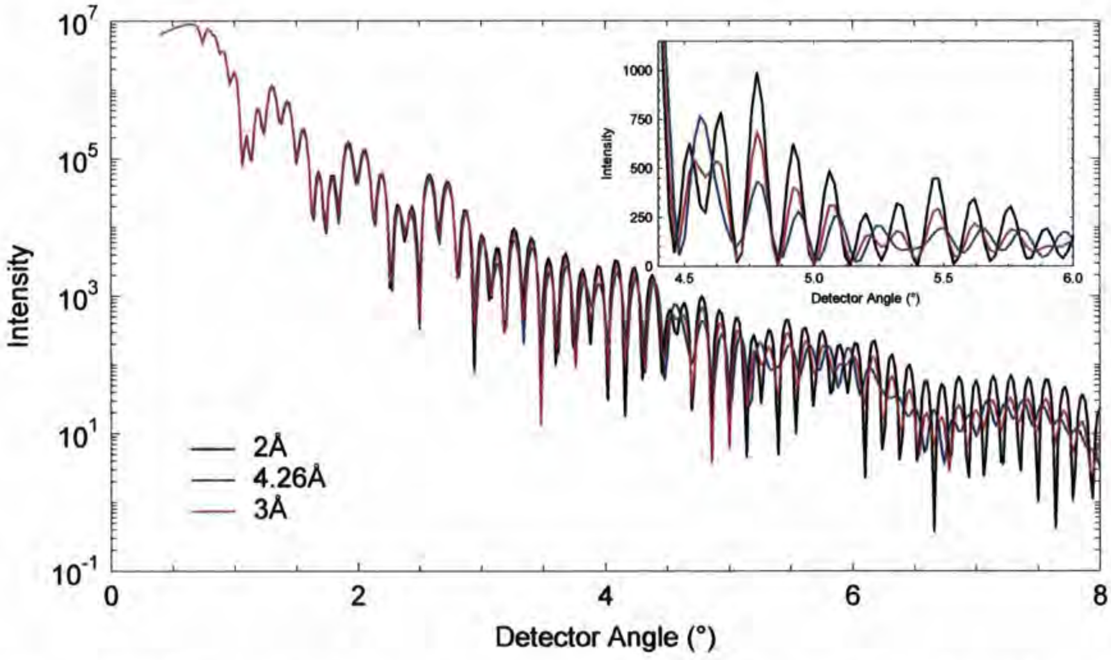

Figure 6-24: The specular reflectivity for smoothing of the top oxide, based on the best fit model to the experimental data. The inset shows the higher angle scatter on a linear scale for comparison.

There are very good reasons for believing that these changes at the top surface cannot occur. Experiments have been performed in both vacuum and argon at the SRS and later in higher vacuum at the ESRF. In all cases the same enhancement to the fringe amplitude was observed. Ruthenium at room temperature forms a passivating oxide preventing further oxidation. At elevated temperatures there will be little scope for the addition of extra oxygen. Even if a very small increase in the oxide layer thickness was permissible at higher temperatures in the vacuum, oxygen atoms will be very scarce and if the sample is oxidising then it would be expected that the process of oxide growth would be very slow and the scatter would evolve for a significant length of time after the temperature change. Finally, in the experiments in the previous chapter, conducted in the same vacuum chamber, no changes on annealing of CoFe/Ru ML's and CoFeB/Ru ML were seen. These both have ruthenium as a top capping layer. If Ru changes were responsible for the differences in the specular scatter in the MTJ structure then changes would be expected in the profile of these samples, which is not the case.

The previous chapter identified sharpening in the CoFeB/AlO$_x$ interface and cross-sectional TEM images of CoFe/AlO based junctions also show that at around 300°C sharpening of the electrode/barrier interface occurs [37]. Assuming that this is the only interface responsible for the changes, an estimate of the interface width can be made by comparing the fringe amplitude of the experimental scatter and that of the simulation where only the CoFeB/AlO interface sharpens. This does not take into account any refraction effects from changes in density with thermal expansion, and so it is not possible to fit the whole range of the scatter. However, the peak at a sample angle of 2.55° is invariant in its position. Fitting this peak with only the CoFeB/AlO width varying is possible and gives an indication of how the interface width may be changing. The results are shown in Figure 6-25 below.

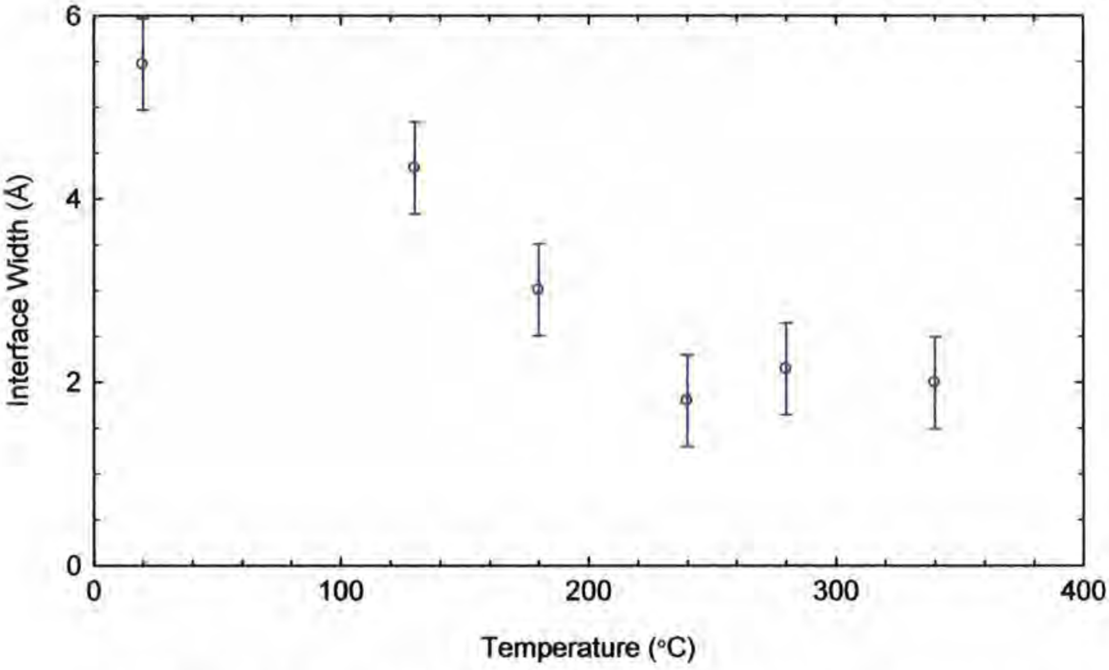

Figure 6-25: Interface width of the CoFeB/AlO interface as a function of temperature.

Here the interface widths are seen to fall steadily until around 250°C, precisely where the TMR reaches a maximum (see Figure 6-26 below). The range from 5.5Å down to 2Å is wider than the change in width seen in the previous chapter where CoFeB/AlO$_x$ was seen to sharpen from 4.9Å to 3.7Å over the same temperature range (Figure 5-33), but these were average values taken over a whole multilayer stack.

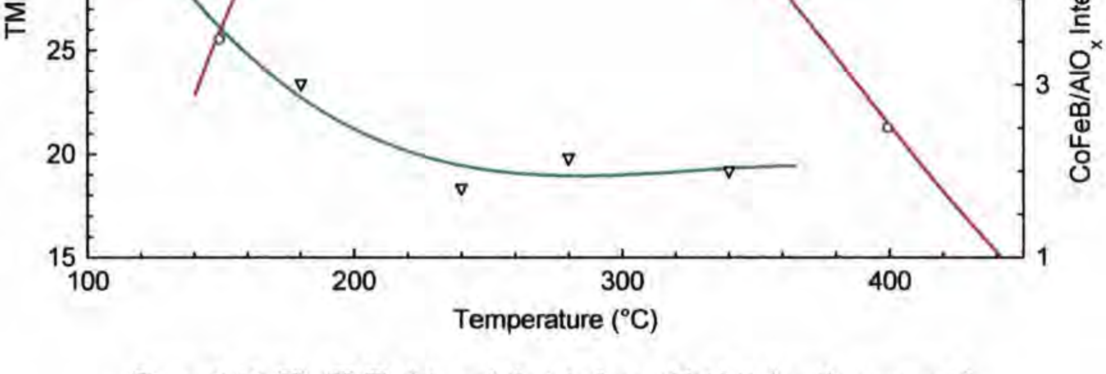

Figure 6-26: The TMR data and the interface width plotted on the same graph. TMR data taken from reference [6]

That the scatter was not able to be fitted over the whole angular range by letting only the CoFeB/AlO_x interface width change shows that the changes seen are not solely due to the CoFeB/AlO_x interface sharpening, although this is a significant contributing component. To identify the other components responsible for these changes more subtle techniques will be required.

6.4.8 Effect of changing energy

The cobalt, iron and manganese elements present in the magnetically active region have absorption edges in the range 6keV to 8keV, which are easily accessible on the hard x-ray beamlines used. These absorption edges have a large effect on the refractive index of the layers through variations in the anomalous dispersion corrections, f' and f'', as shown in Figure 6-27 below. The absorption edges have been listed in Table 6-5 below. The contrast between two materials can thus be changed, which is especially useful for separating cobalt, iron and manganese, where the differences in scattering factors are usually very small.

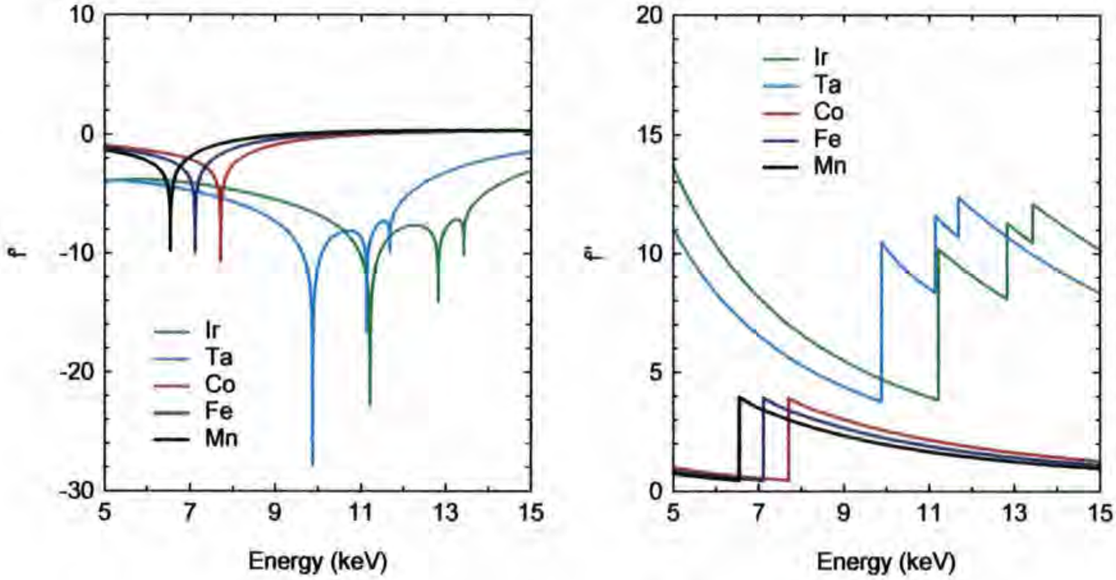

Figure 6-27: Real and imaginary parts of the anomalous dispersion corrections for the materials in the sample.

Element	Energy of Edge
Mn	6.54 keV (K)
Fe	7.11 keV (K)
Co	7.71 keV (K)
Ta	9.88 keV (L3), 11.14 keV (L2), 11.68 keV (L1)
Ir	11.22 keV (L3), 12.82 keV (L2), 13.42 keV (L1)

Table 6-5: Energies of the absorption edges of elements in the MTJ sample in the range 5keV to 15keV

The technique of reflectivity with varying energy goes by various different names, such as Reflectivity Anomalous Fine Structure (RAFS), Anomalous Scattering, and Variable Energy Reflectivity. The effects of changing the energy on scattering from Fe/Cr multilayers have been demonstrated by Bai *et al.* [38]. The Co/FeMn interface in particular has been studied by Luo *et al.* where, from the change in intensity of a Bragg peak with energy, the inter-diffusion of cobalt with the iron has been seen, with a mixing region expanding over 14Å [39]. Multilayers of $[Co_{90\%}Fe_{10\%}/Cu]_{x20}$ have been examined by An *et al.* [40] using these anomalous scattering techniques at the first Bragg peak, together with q_x diffuse scatter at that Bragg peak, to identify island growth during the sample deposition, asymmetries in the interfaces, and the widening of intermixing regions on annealing. The published data to date using this technique is, so far as the author is aware, solely measured at Bragg peaks which demonstrate enhanced sensitivity to the interfaces.

From now on the scattering data is presented in reciprocal space, so that the effect of energy on the angular positions can be removed and scans are directly comparable. Two different approaches can be used. Repeated q_z (specular) scans can be performed at different set energies, and the scatter compared to identify any changes occurring. Alternatively the scatter can be recorded as the energy changes, with the incident and detector angles changing to remain in the same position in reciprocal space, to measure the effect of passing through an absorption edge. The previously mentioned C++ code written to perform reflectivity was easily modified to calculate scattering at different energies, and to generate theoretical scatter in an energy scan at constant q. The program uses values of f' and f'' at different energies from look-up tables taken directly out of Bede REFS. This code is included in Appendix C.

The variation in the refractive index profiles for the MTJ sample, as a function of wavelength, are shown in Figure 6-28 below. The real part shows clear depressions in the layers associated with the edges, whereas the imaginary part shows clear steps when the absorption edge is passed and the incident x-ray has sufficient energy to eject a more tightly bound electron.

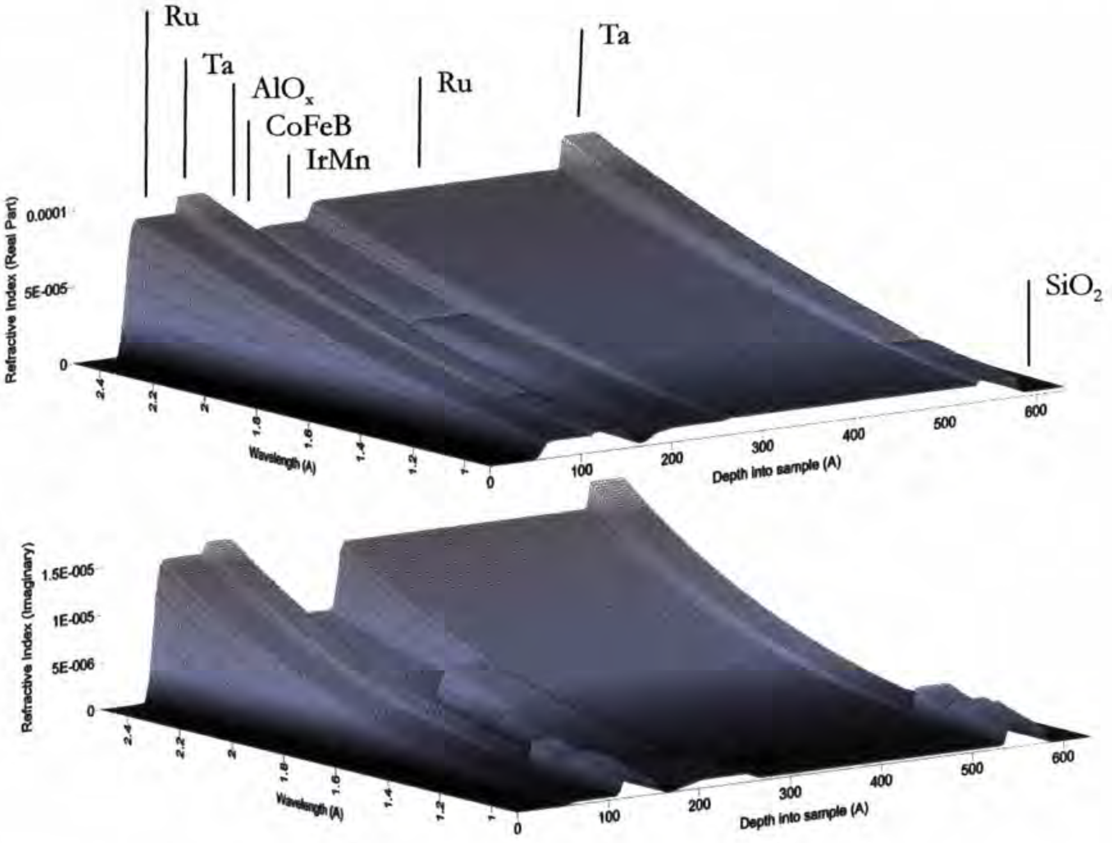

Figure 6-28: Refractive index profile as a function of wavelength of the MTJ structure for the real part, δ, (top) and the imaginary part, β, (bottom).

A closer look at the AlO$_x$/CoFeB/IrMn edge of the 'well' in the refractive index profile associated with the tunnel barrier interface, over the restricted range of energies corresponding to the K-edges of cobalt (7.71keV), iron (7.11keV) and manganese (6.54keV), is shown in Figure 6-29 below. The edges in the real part of the refractive index extend into the boundary regions and thus in principle can be used to determine the extent of the diffusion of one material. However the change in the refractive index is not markedly different away from the edges. This is less pronounced than the form of f' from Figure 6-27 because of the effect of alloying materials together and delta is proportional to $Z+f'$ (from equation (2-13)). The changes in beta are more marked where the change in absorption on moving through an edge are clearly seen and the contrast between layers is changed significantly.

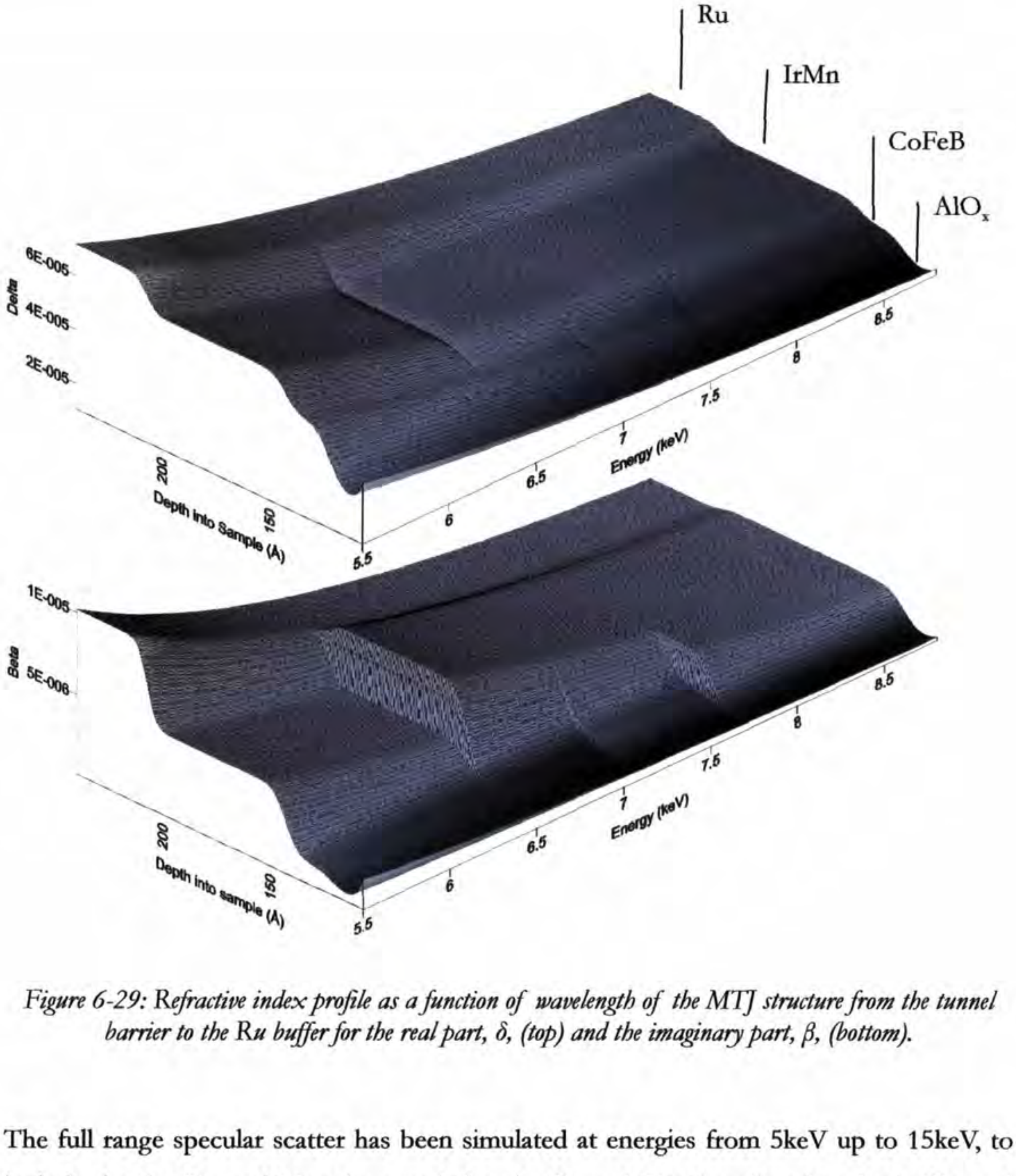

Figure 6-29: Refractive index profile as a function of wavelength of the MTJ structure from the tunnel barrier to the Ru buffer for the real part, δ, (top) and the imaginary part, β, (bottom).

The full range specular scatter has been simulated at energies from 5keV up to 15keV, to include the Co, Fe, and Mn edges, and also the Ru and Ta edges forming the buffer and cap. This has been based on the models for the room temperature scatter from the sample shown previously in Table 6-1 above and is shown in Figure 6-30 below. The largest changes are between 10keV and 12keV where the Ta L edges are located. The changes occurring at lower energies, associated with the Co, Fe and Mn edges, are much less pronounced but nevertheless still present. This figure shows both types of scan, and measurements can be made moving parallel to either the energy or q_z axis.

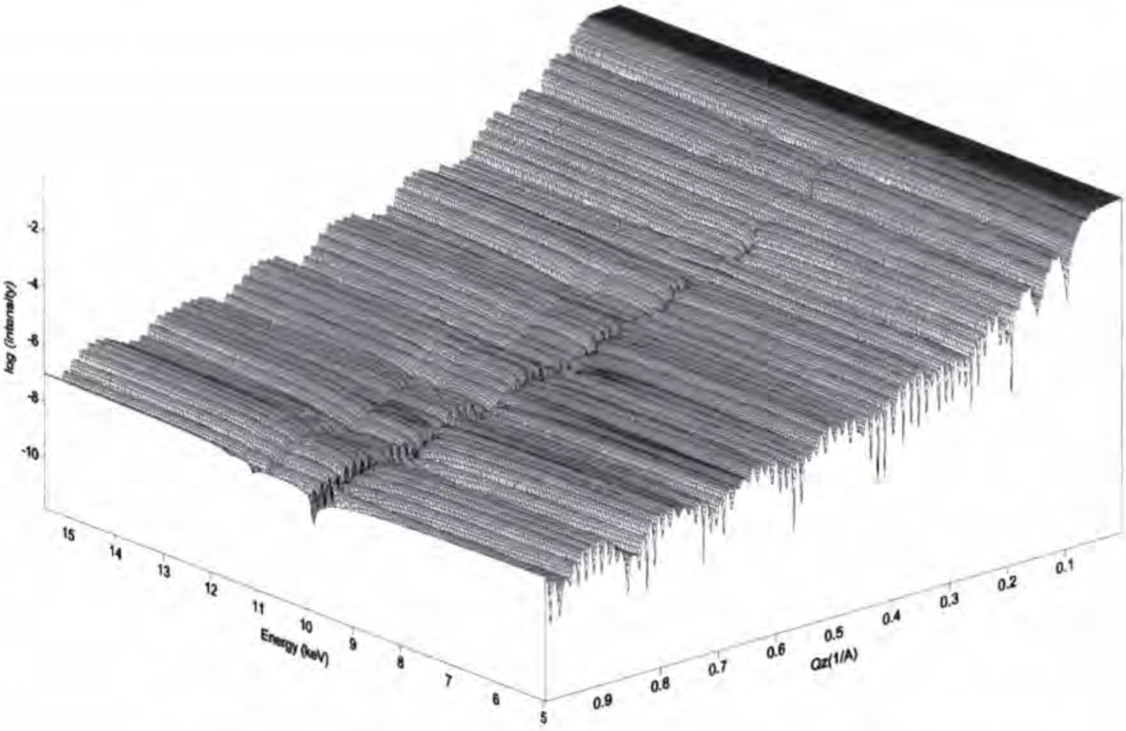

Figure 6-30: The full range specular scatter at different energies from 5keV to 15keV showing the absorption edges.

The specular scatter simulated at some selected energies is compared in Figure 6-31 below. The energies at which the simulations were done were chosen to match those in an experiment to record this scatter at different energies. This shows more clearly the difference between energies and that there are definitely areas where significant changes are occurring. Although the intensity at the critical angle follows a systematic decrease as the energy is increased the intensity at high angles does not follow the same order as a result of changing refraction and absorption in the sample.

By simulating the differences between the curves it should be possible to identify more closely the atomic distributions within the sample. In comparing experimentally recorded specular scatter from the same sample at different energies, all changes must occur from changes in the f' and f''. If these anomalous dispersion coefficients were constant then the specular scatter would be invariant when the energy is changed and when viewed in reciprocal space.

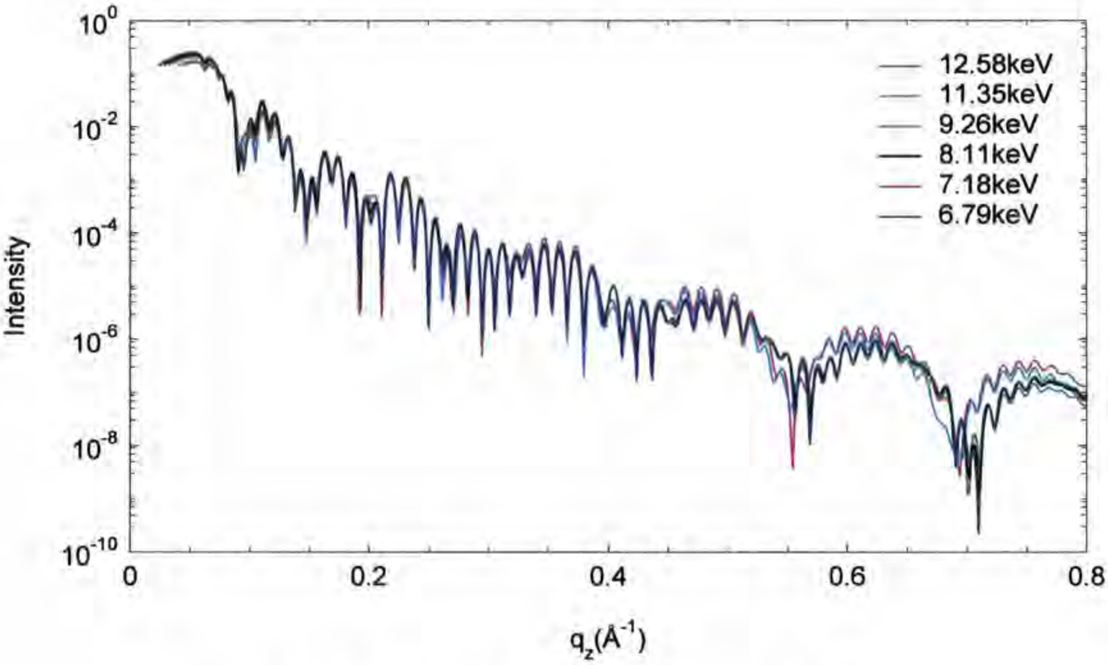

Figure 6-31: Simulated specular scatter at different energies using the best fit model to the room temperature specular scatter.

6.4.9 q_z scans at different fixed energies

Experiments were conducted to record the specular scatter at different energies at Daresbury station 2.3 to test these theoretical predictions on more samples cut from the MTJ wafer. The position of the monochromator was found to be slipping when the energy was changed, meaning that accurate selection of energy was not possible, and that energy scans at constant q_z could not be performed. Nevertheless, by noting that the position of the low angle Kiessig fringes was invariant when the energy is changed, it was possible to move to an approximate energy, measure the specular scatter, and from the position of the Kiessig fringes in angle, determine the energy at which the measurement had been performed.

The experimentally collected data is shown in Figure 6-32 below and close in views are provided in Figure 6-33 below. The regions where changes are seen on annealing are precisely where the scans at different energies are showing up differences. Fitting these parts accurately may be the key to better determination of the sample structure. However this is precisely where the fit in the starting model, and at higher temperatures, is poorest

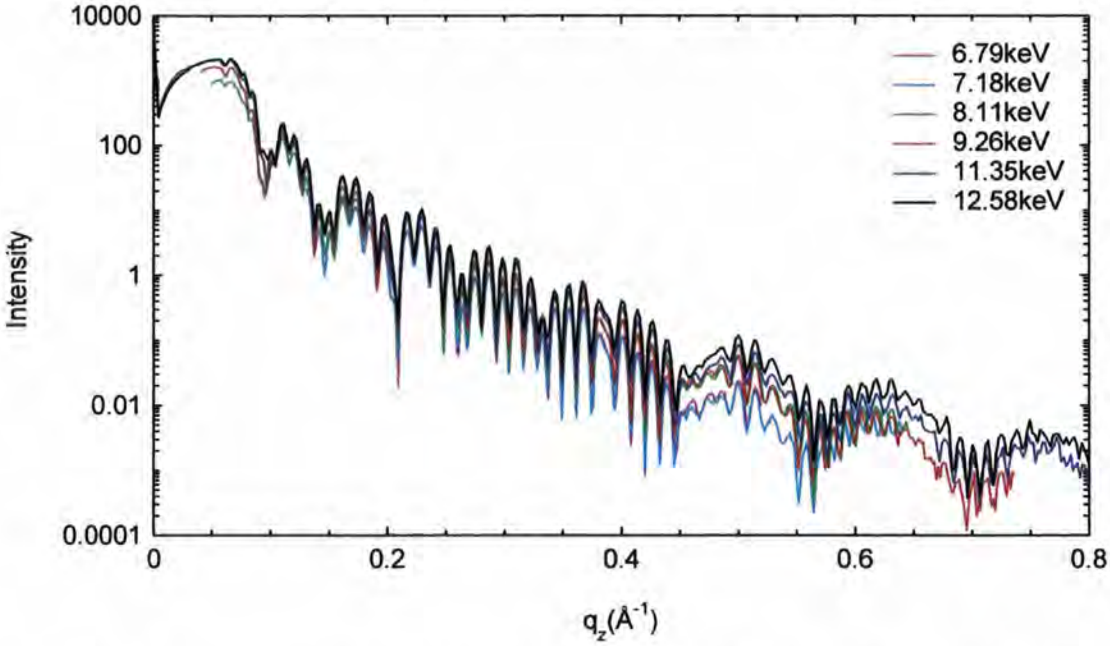

Figure 6-32: Specular scatter from the same sample recorded at 20°C and at different energies.

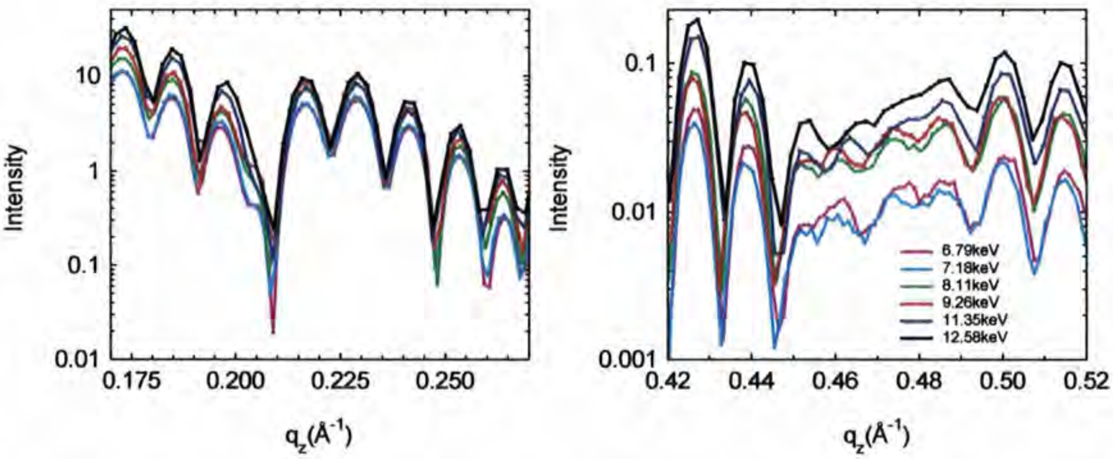

Figure 6-33: High angle close-in specular scatter from the same sample recorded at 20°C and at different energies.

To best use data recorded at different energies from the same sample it is necessary to perform a co-minimisation of the scatter at multiple energies to the identical sample structure. The C++ code was modified to perform this. Specular scans, at room temperature, taken either side of the iron K edge were recorded. The recorded data and simulated fit is shown in Figure 6-34 below.

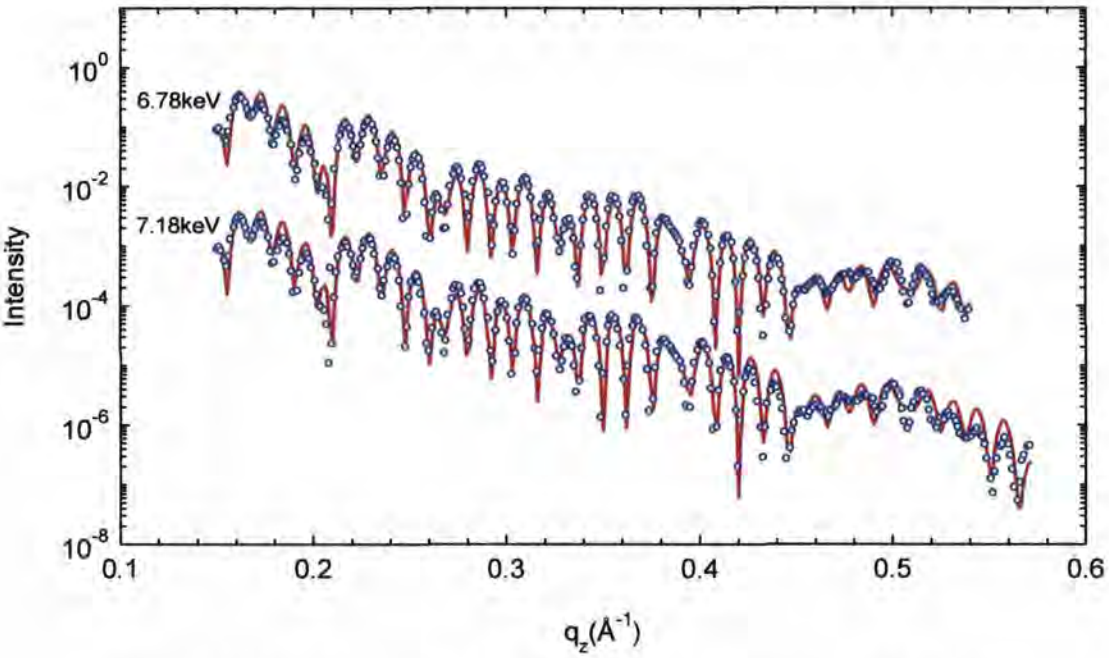

Figure 6-34: Simultaneous Fit of the scatter recorded at 6.78keV and 7.18keV. The curves have been offset by a factor of 100 for clarity.

Satisfactory fits to the data have been achieved. However, the very small and subtle differences between the actual data have not been fitted. This is where the differences between scans at different energy are seen. Very small differences in the scatter need to be simulated to a high degree of accuracy for this method to be of use. Computationally working out the errors on the fitted parameters is not trivial. In the previous results, errors were calculated in REFS. However, that will not take into account the parallel fitting at two energies. It was not considered worthwhile going through the detailed process of incorporating the non-trivial error calculating routines into the C++ code for simultaneous fitting because the results are unlikely to prove fruitful in solving the structure.

The scatter recorded at 300°C at different energies is shown in Figure 6-35 below. The same enhancement to fringe peak amplitude seen before is seen at all energies. The differences between energies are much less, the only differences are an intensity shift, whilst the profile shapes are broadly the same. Whatever it is in the sample structure that gives rise to the differences in the scatter with energy at room temperature, the effect of annealing is to remove it. Simulating the scatter at these higher temperatures will not add to the sensitivity of the technique as there are no appreciable differences to use to get a foothold.

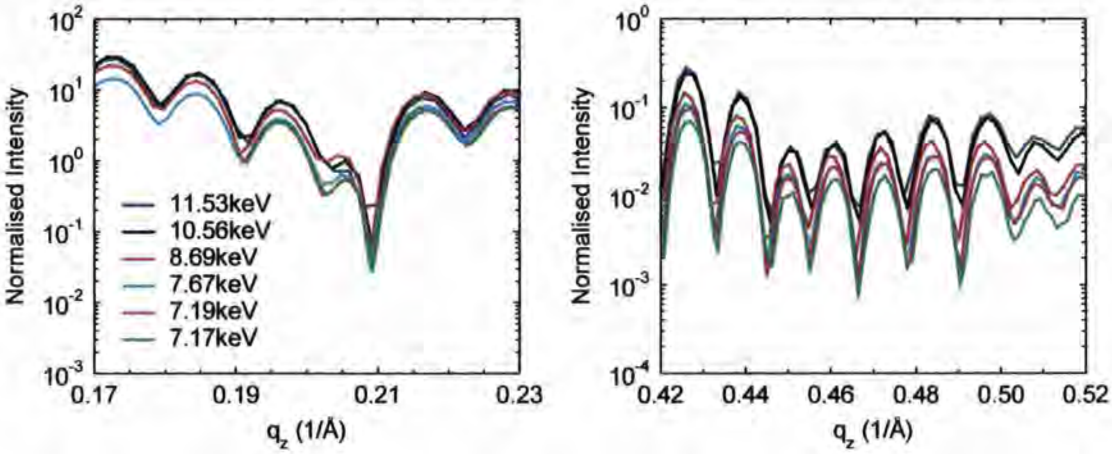

Figure 6-35: Recorded specular scatter at 300°C at different energies

It has to be concluded that the starting model lacks the subtleties to account for the features seen between energies at room temperature, and even by recording at multiple energies it not possible to refine the model further. It is not to say that the right parameter values to put into the model cannot be found, but that the model appears not to be using good enough parameters to describe the sample.

6.4.10 Energy scans at constant q_z

Where the layers in a sample are formed from alloys and compounds, and diffusion of individual elements is to be considered, the simplified layer structure, with a single roughness value applied to all constituents of a mixture, is no longer applicable. Dimopoulos identified a structural transition occurring in the CoFeB layers above 300°C, after which, at 400°C, manganese was detected, via Auger depth profiling, in the vicinity of the barrier [6]. It is postulated that the crystallisation of the CoFeB allows longer range manganese diffusion via the grain boundaries which is driven by the affinity Mn has for oxygen. Manganese could also be incorporated during growth into the amorphous CoFeB preferentially over iridium, which would lead to a more complex interface structure.

To investigate the effect of different elements diffusing, a more general approach has to be adopted to the simulation of the scatter. The sample structure in the simulation was divided into individual 1Å layers, which had their elemental composition calculated to reflect an interface width, but which were assumed to be perfectly sharp. More details relating to this approach are given in reference [41]. This then allows for the study of arbitrary profiles, but it is much more computationally intensive. Different manganese profiles within the sample were considered in order to identify the effect this has on the scatter. The iridium in the IrMn alloy was assumed to have a fixed erf(z) interface profile.

The Mn was assumed to have a differing erf(z) profile. The combination of the two profiles is no longer a simple erf(z) profile and so the CoFeB, with which the IrMn forms an interface, was distributed to fill the available space in the sample. The erf(z) profiles used for the iridium and manganese are symmetric and so by this method atoms are conserved between models. The different atomic profiles are shown in Figure 6-36 below for the different manganese interface widths. The profiles of the other atoms have been based on the fit to the 20°C data from sample 4.

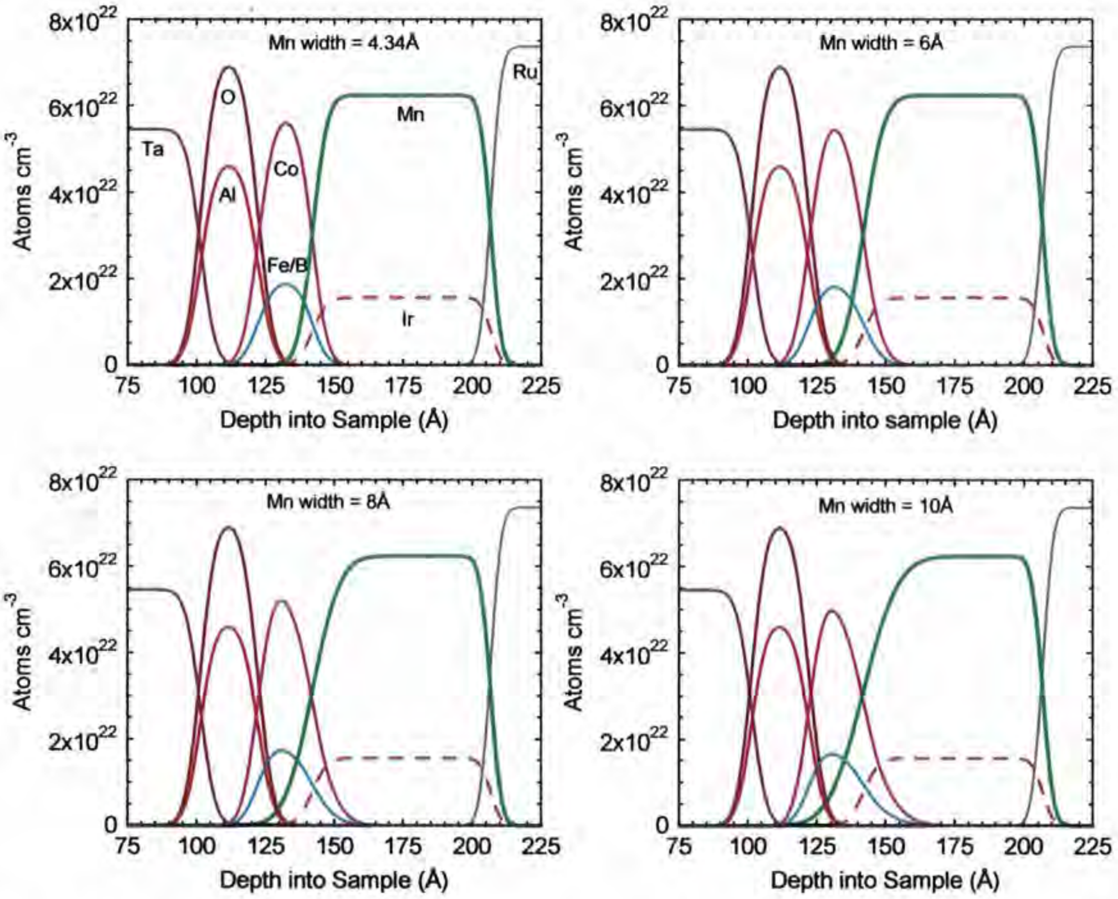

Figure 6-36:Atomic profiles of AlO/CoFeB/IrMn section of the samples with different widths for the manganese component, constant widths for the iridium component, and CoFeB used to compensate for the Mn widths.

The specular scatter simulated from these structures at 7.4keV is shown in Figure 6-37 below and shows the scatter is virtually indistinguishable for the different profiles on a log scale. However if variable energy scans are performed keeping the value of **q** constant then clear differences in the profiles can be seen, as shown in Figure 6-38 below. In these scans there are changes both in the overall shape of the scatter over the whole energy range, and also the behaviour close to the absorption edges. In some of the **q** positions, particularly the lower ones, these edges change from giving an enhancement to the scatter, to causing a reduction in the scatter. Changes are also seen over the whole range of **q**.

These scans have assumed an incident intensity of 10^6 cps which is realistic and shows that long counting times are not required for these measurements. The higher q_z scatter shows initially a big change in shape to a small change in the Mn width, but then further widening of the Mn interface does not change the scatter further.

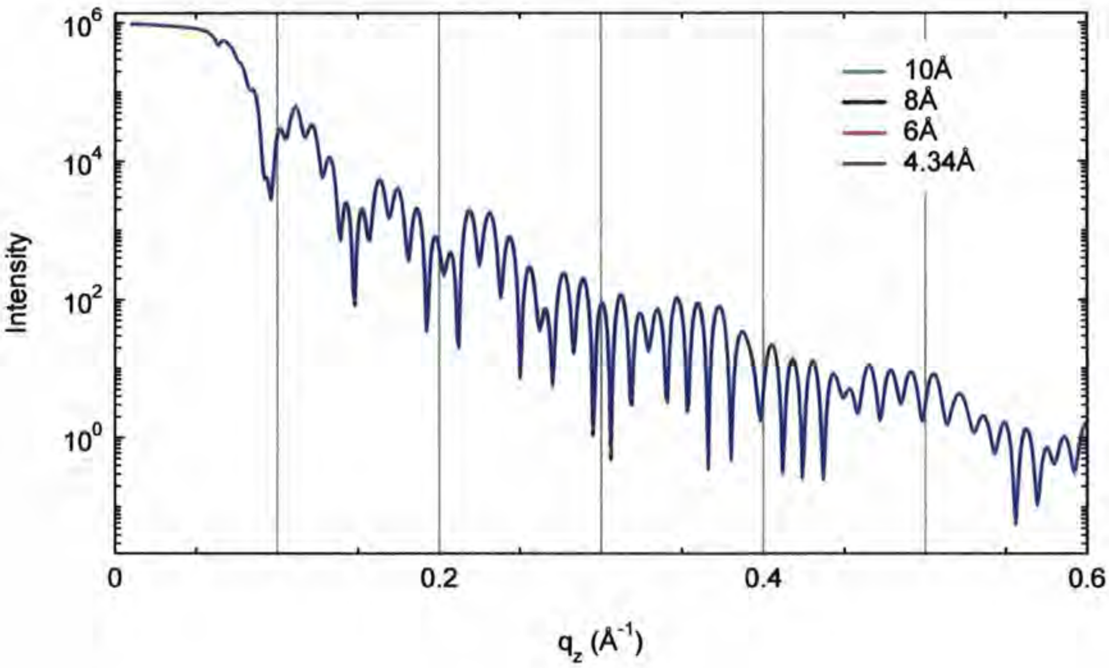

*Figure 6-37: Simulated specular scatter at 7.4keV from the different atomic profiles shown in Figure 6-36. The grey lines show the positions of simulated constant **q** energy scans in Figure 6-38.*

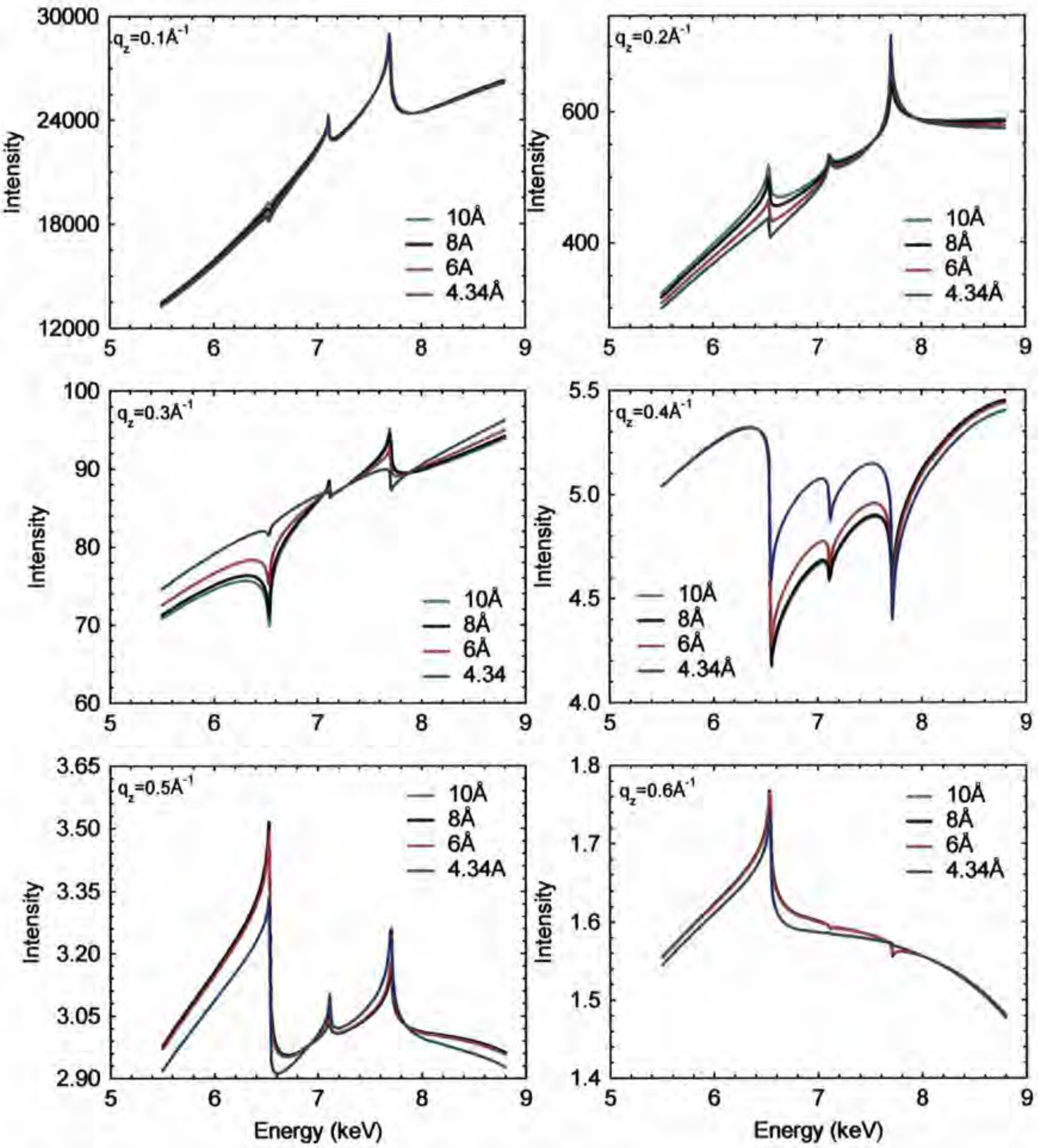

*Figure 6-38: Constant **q** energy scans for different manganese width. The incident intensity has been assumed to be 1×10^6 cps to approximate the intensity in a typical experiment.*

Measurements were performed on the XMaS beam line where the cryo-furnace stage was used. A beryllium shroud fits over the sample stage, making a seal with two O-rings, enabling the sample environment to be pumped down to a low pressure. More details are given in section 3.6. Typical pressures of 5 x 10^{-4}mbar were achieved. In the high temperature scans at the ESRF, the sample had to be physically attached to the sample stage in order to prevent noise from mechanical vibration being detected. Silver epoxy resin was used to 'glue' the sample onto the copper sample stage. However, at high temperatures the epoxy failed and the sample separated from stage and noise increased.

The variable energy scans recorded, without any normalisation or instrument function correction, are shown in Figure 6-39 below. They were recorded on the top of the Kiessig fringes so that any imperfections in the positioning of the diffractometer had a minimal effect on the scattered intensity. They have been plotted on a log scale so that changes in intensity over the whole range of energies become evident as a vertical translation of the profile, and they can be separated from any changes in shape. In all cases the peak amplitude increases seen in the q_z specular scan is shown by an increase in the scattered intensity with temperature. No dramatic change in shape is seen in the scans at the three lowest q_z values in contrast to what was expected from the simulations presented above. There is no change in the orientation of the scatter close to the edges. Changes were seen in the scans at q_z=0.460Å^{-1} at higher energies.

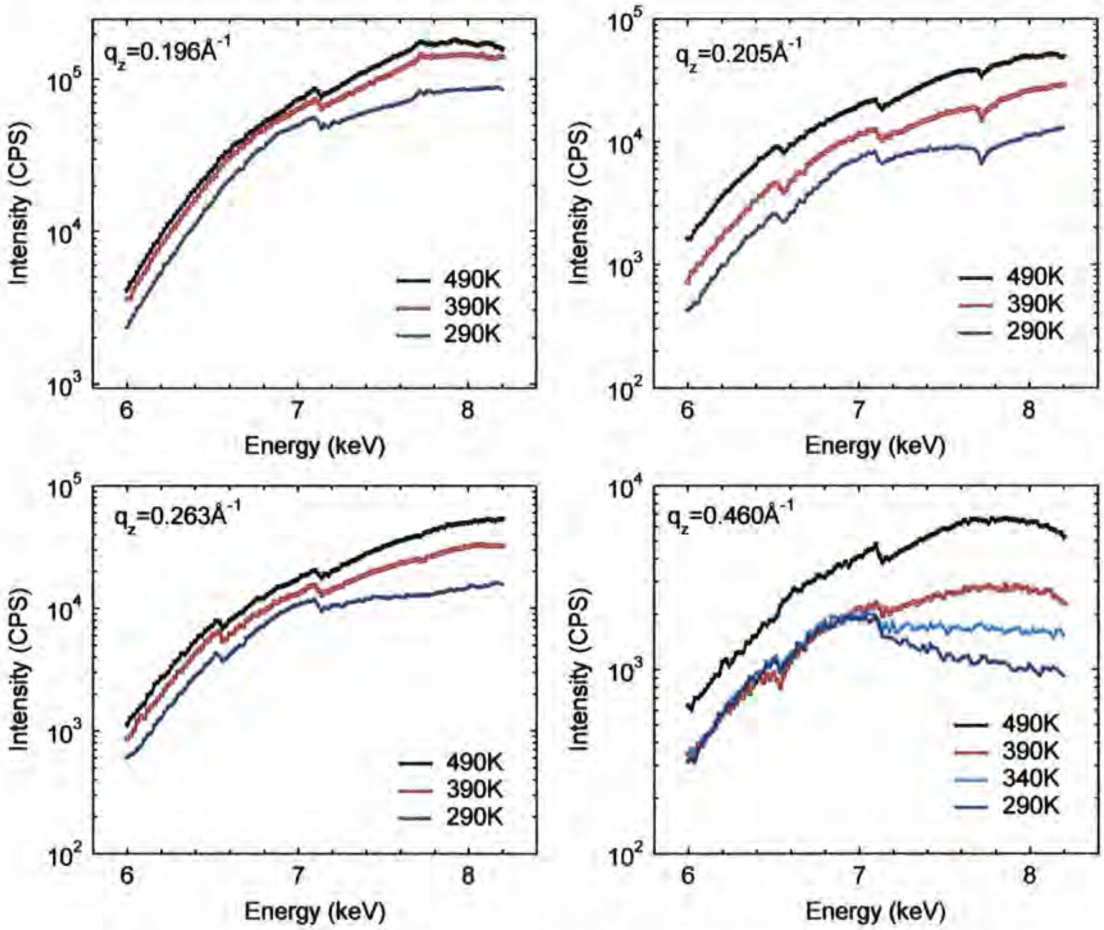

Figure 6-39: Variable energy scans recorded at different fixed positions in reciprocal space at different sample temperatures.

To use these scans quantitatively, by using fitting to infer the sample structure is very difficult. Close to an absorption edge the values of f' change very quickly; a good energy calibration and narrow energy bandwidth is necessary to be able to fit the scatter. Very close to an edge the values of f' and f" become less well known and more difficult to calculate. At the absorption edge the fluorescence cross section increases rapidly, before gradually falling as the energy is increased further. This either has to be factored into any simulation of the profiles, as a change in the background, or an 'off-specular' energy scan could be run to enable it to be subtracted. Difficulties also arise from the energy dependence of the instrument function, which arises from varying photon flux at different energies, detector response at different energies, and, at softer energies, absorption in air can be significant. The kapton foil of the monitor assembly also has an energy dependence making normalisation difficult. Practically, the data from q_z scans are easier to handle as the energy dependent parameters are constant during the scan.

Computationally each individual scan presents the problem at constant **q**, the **q** dependence of roughness is not probed, and so within the Parratt formalism it is impossible to separate interface width and density contrast. Complex co-minimisation is required on all the variable energy scans simultaneously, and at the same time on the full q_z specular scatter at fixed energies.

It is again reassuring that the sharpening was occurring. If the manganese was diffusing, or any other material, a change in the shape of the profiles would be expected.

6.4.11 Beam damage of samples

In performing the measurements in the chapter at the ESRF, an intense third generation synchrotron, beam damage was noted in these samples. Figure 6-40 below shows the scatter recorded at 500K from the same structure, after measuring at the same position at other lower temperatures (green line). A translation of the sample horizontally, so the beam hit a different and as yet untouched part of the surface was done, and the peak profile was seen to change. Moving again to another fresh area of the sample, but this time with an attenuator in the beam to reduce the intensity, the large fringe amplitude is seen to reappear. These fringes are measured at higher angles, where the beam footprint is larger, and yet they are still seen to be affected by the incident beam.

The full intensity x-ray beam appears to be interacting with and altering the sample. The possibility of localised heating by the beam cannot be discounted. It is commonly thought that only biological samples or complex organic molecules are susceptible to beam damage. An x-ray induced insulator to metal transition has been seen in a magnetoresistive manganite [42], but the effects are comparatively rare. This may become more prevalent as the intensity of synchrotron sources increases further in the future.

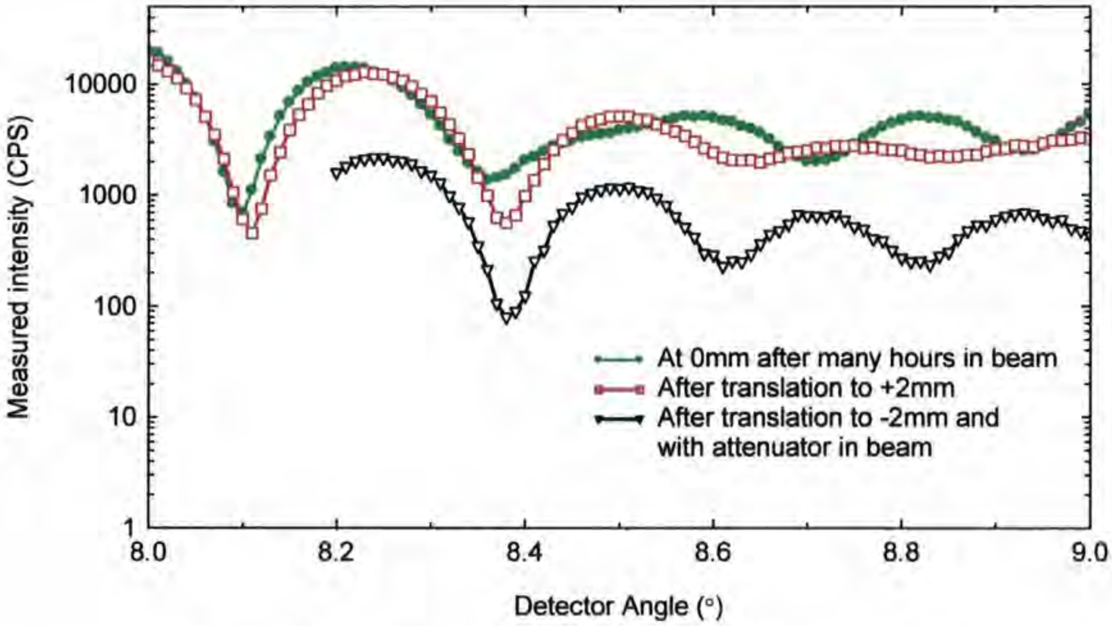

Figure 6-40: Specular scatter from sample no 10 at 6keV and 500K

The damage to samples can be seen optically on the surface. Figure 6-41 below shows an optical microscope image of the top surface of a different MTJ that was used to align the I16 beamline for the first ever user run at the Diamond Synchrotron Light Source, the new UK synchrotron radiation facility. There is an obvious spot where the beam was hitting, and also a tail. Closer inspection reveals this tail to be comprised of many small dots and the 'cloud' above the 'eye' is dendritic. Above the eye is a region where dendritic filaments are seen.

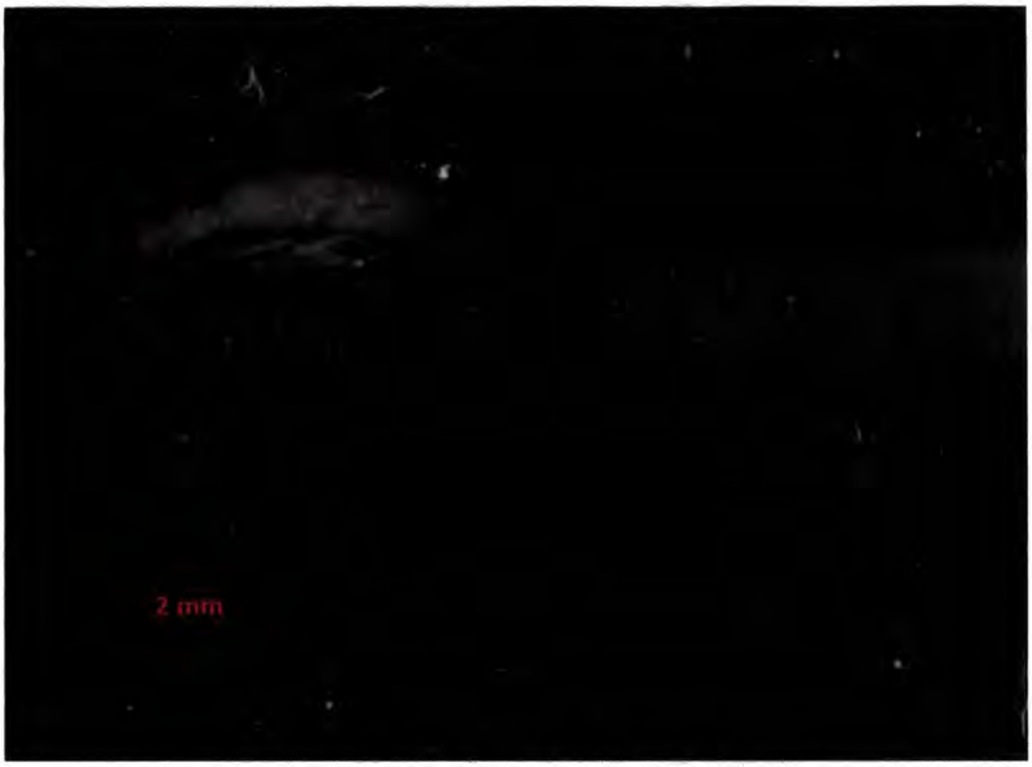

Figure 6-41: Beam damage at the Diamond synchrotron

Figure 6-42: Close up images of the 'tail', left, and above the 'eye', right.

6.5 Interpretation and discussion

From the rate of fall of the specular scatter and the very low intensity of the diffuse scatter the samples are seen to be extremely smooth with very narrow interface widths. The majority component of the interface widths is inter-diffusion although it has not been possible to determine the width components individually for each interface in the sample. Very good sample homogeneity has been achieved by Siemens, the sample growers, over the surface of the wafer.

With very smooth interfaces the correlation out-of-plane is expected to be very large; a stack of perfectly smooth interfaces would have an infinite out-of-plane correlation length of the roughness, despite there being no roughness present. The sample has an out-of-plane correlation length which is well in excess of the sample stack thickness. Therefore the barrier will be of very uniform thickness across the wafer. The very low degree of roughness also means that orange peel coupling across the barrier, which is detrimental to the performance of the MTJ, will be small. No change was seen in the diffuse scatter with annealing below 300°C, so, as in the previous chapter, no change in the topological roughness can be detected.

Reassuringly, from the expectations raised in the previous chapter on the temperature dependence of the CoFeB/AlO_x interface, the MTJ structures examined also demonstrate changes when annealed at relatively low temperatures. The changes in the specular scatter follow a similar profile to the TMR curve versus temperature measured by Siemens which is consistent with a link between the structure and the TMR. The sample quickly reaches a thermal equilibrium, where the structural transformations are complete and no further changes are observed until the temperature is increased again.

Fitting the scatter, to determine the structure and the relation between structure and TMR, at higher temperatures has proved difficult. Although a reasonable fit can be achieved, which in most circumstances would be considered satisfactory, here the changes occurring appear to be very subtle and the fitting is just not close enough to the measured scatter to determine exactly what is happening. There is a limitation in the precision of the fit of the initial starting model to which all models at higher temperatures are compared. The uncertainties on this model are such that it is impossible to say precisely what is changing.

In fitting specular scatter within the Parratt formalism (see section 2.4.2) a change in the density of one layer alters the contrast between that layer and its two neighbouring layers, thus altering two reflectivity coefficients in the system. A change in roughness only alters the reflectivity amplitudes for one interface. Thus when fitting a structure both density and roughness are inter-related; a lower density of one layer, causing a change in contrast between two layers, can be compensated by a change in the interface widths of both interfaces. A unique solution for the separation of roughness and density is only possible where the **q** dependence from the roughness is taken into account. Changes in the density not only affect the position of the critical angle, but also the wavevector transfer in the layer. This has the most pronounced effect at low angles where refraction is significant and changes in densities will alter the position of the interference fringes.

These measurements were recorded in either the relatively poor vacuum of the SRS, or an argon atmosphere, or the relatively good vacuum of the ESRF. These should protect the top surface from further oxidation during the experiment. The same fringe enhancement has been seen in all three environments, confirming that internal sharpening is occurring, and the modifications are not surface related. The simulations show that an increase in the top surface density could cause the fringe amplitude to increase through the amplitude reflectivity coefficients of the top oxide increasing. However, this is discounted and the most likely cause of the changes observed is the sharpening of an internal interface, such as the CoFeB/AlO$_x$ interface, which is consistent with the results in the previous chapter on the CoFeB/AlO$_x$ multilayers.

In the literature a temperature induced enhancement of TMR is seen not just in CoFeB/AlO$_x$ MTJs but also in CoFe/AlO$_x$ MTJs [5,6,10]. The importance of the amorphous nature of the CoFeB layer is that it is believed to act as a barrier to manganese diffusion. In the variable energy studies performed, no evidence was seen for manganese diffusion being thermally activated, although an initial asymmetry in the manganese diffusion may be incorporated into the sample at room temperature. This leads to the conclusion that the changes in TMR are a result of oxygen redistribution in the CoFeB/AlO$_x$ interface, as has been discussed in detail in the previous chapter.

The crystallisation of the sample has been observed by a sudden change in profile of the scatter in both the specular and diffuse scans. This is very similar to the behaviour in the CoFeB/Ru multilayer of the previous chapter, except that the thickness of CoFeB in the MTJ sample is only 30Å thick. Despite being only 30Å thick, this crystallisation is sufficient to disrupt the larger structure significantly. This crystallisation puts an upper limit on the temperatures at which the devices can be operated. At 300°C it is too low for integration with CMOS technology. Different amorphous alloy composition may be the answer to this. Degradation in performance may not be solely caused by a phase change in the CoFeB. Pinhole formation in MTJs, where a conductive channel through the insulating barrier linking the two electrodes is established, is a well established failure mechanism [43, 44].

In variable energy reflectivity, the measurements have been restricted to the energy range 5keV to 15keV which allows the cobalt, iron, manganese, tantalum and ruthenium edges to be accessed. However, to look at the distribution of lighter elements at the CoFeB/AlO$_x$

interface such as oxygen or boron much softer energies must be used. The only Boron edge is at 188eV and oxygen is at 543.1eV which are impossible to probe at the hard x-ray beamlines used to do the measurements in this work.

The observation that certain regions in reciprocal space show a dramatic change on heating is interesting because it shows that the observed changes are only associated with certain real space length scales in the structure. In much the same way that in chapter four the diffuse scatter allowed the correlation length to be examined for different spatial frequency components, so the specular scatter in q_z also has the same relation to the real space structure of the sample. Interpreting the scatter as being closely related to the Fourier transform of the layer structure, it is seen from the wide spacing of locations where differences with heating occur, that these changes must originate from very small length scale features.

The use of electron microscopy techniques is limited by the field of view and the sample area that can be imaged, made worse by the fact that these are very thin layers, typically only 1nm to 3nm. To be able to resolve these vertically the lateral field of view is correspondingly restricted. There is also the significant problem of preparing a sample, and the fact that only a single cross section can be examined at a time. A critical review of electron microscopy and x-ray techniques applied to MTJs can be found at [45]. One study has confirmed sharpening at the interface between AlO and CoFe [37].

Recently Mizuguchi *et al.* published some scanning tunnelling microscopy measurements of MgO barrier layers, grown by molecular beam epitaxy (MBE). They observed that the top surface of the MgO layer exhibits terracing and, when annealed, the terraces are seen to flatten over the 2500Å x 600Å field of view. The initial as-deposited roughness was 1.49Å which fell to 1.36Å on annealing [46]. This was measured *in-situ* in the MBE chamber before a top Fe electrode was deposited and so it is a surface and not an interface that was observed to smooth. It is interesting nevertheless that the oxide demonstrates this surface smoothing re-organisation when annealed.

6.6 Conclusions

Detailed changes have been seen at higher angles in the specular scatter when the MTJ structure is annealed. In particular peak amplitudes of the Kiessig fringes increase with temperature, which is interpreted, as it was in the last chapter, as being from the sharpening of an internal interface. The amplitude of these fringes match closely with the TMR vs. temperature curve and demonstrate that the structural changes affecting the TMR are detectable with x-ray reflectivity.

The system is very complex and a change to the AlO_x/CoFeB interface width is not sufficient in itself to model all the changes that are occurring. The modelling of the structure has proved very difficult and a structural model that accounts for the room temperature scatter and the scatter from the hot sample with as few parameters changing as possible has proved elusive. Extra constraints have been added into the modelling but have not helped establish the parameter values required to fit the data.

The problem may be that the parameter set used to describe the sample does not reflect its structure to a close enough degree. A more general approach, breaking the system down into thin perfectly sharp interfaces, which can model longer range diffusion, was investigated. Techniques involving changing the incident energy have been investigated, and the shape of the energy scan at constant **q** has been shown to be very sensitive to elemental distributions that deviate from an erf(z) function. Experimentally measuring this is not difficult, however computational simulation is particularly challenging because the energy dependent instrument function needs to be known. From fitting scans recorded at a single **q** vector a unique solution cannot be found as the **q** dependence of the roughness is not probed preventing it from being isolated from a density contrast. Detailed co-minimisation of multiple scans, coupled with a specular scan at constant energy may make it possible to find a unique solution, but at the cost of being computationally intensive.

References for Chapter 6:

[1] Djayaprawira, D. D., *et al.*, App. Phys. Lett., **86** (2005) 092502

[2] Yuasa, S., *et.al.*, App. Phys. Lett., **89** (2006) 042505

[3] Freescale Semiconductor Inc., News Release, 10th July 2006.

[4] http://www.freescale.com/files/memory/doc/white_paper/MRAMWP.pdf
(date accessed: 17th July 2006)

[5] Sousa, R. C., *et al.*, App. Phys. Lett., **73** (1998) 3288

[6] Dimopoulos, T., *et al.*, J. App. Phys., **96** (2004) 6382

[7] Sousa, R. C., *et al.*, J. App. Phys., **85** (1999) 5258

[8] Sato, M., *et al.*, J. App. Phys., **83** (1998) 6691

[9] Parkin, S. S. P., *et al.*, App. Phys. Lett., **75** (1999) 543

[10] Cardoso, S., *et al.*, App. Phys. Lett., **76** (2000) 610

[11] Telling, N. D., *et al.*, App. Phys. Lett., **85** (2004) 3803

[12] Tsymbal, E. Y., *et al.*, App. Phys., **87** (2005) 10C910

[13] Miller, C. W., *et al.*, App. Phys. Lett., **90** (2007) 043513

[14] Seve, L., *et al.*, Europhys. Lett., **55** (2001) 439

[15] Schrag, B. D., *et al.*, App. Phys. Lett., **77** (2000) 2373

[16] Egelhoff, W. F., *et al.*, IEEE Trans. Magn. **42** (2006) 2664

[17] Egelhoff, W. F., iet al., App. Phys. lett, **88** (2006) 162508

[18] Peng X., *et al.*, J. Vac. Sci. Technol. A, **24(4)** (2006) 1652

[19] Cardoso, S., *et al.*, App. Phys. Lett., **76** (2000) 3792

[20] Li, F. F., *et al.*, J. App. Phys., **98** (2005) 113710

[21] Mellor, J. W., "A Comprehensive Treatise on Inorganic and Theoretical Chemistry", Volume XV, First Edition (1936), Longmans Green & Co Ltd, London.

[22] Rard, J. A., Chem. Rev., **85** (1985) 1

[23] Sharma, S. P., *et. al*, IEEE T. Compon. Hybr. & Man. Tech., **6** (1983) 89

[24] Campbell, P.F., *et al.*, Anal. Chem., **30** (1961) 58

[25] Böttcher, A., *et al.*, Phys. Rev. B., **60** (1999) 14396

[26] Blume, R., *et al.*, J. Chem. Phys., **120** (2004) 3871

[27] Buchanan, J. D., *et al.*, App. Phys. Lett., **81** (2002) 751

[28] Lee, J. H., *et al.*, J. App. Phys., **91** (2002) 1431

[29] Yoon, C. S., *et al.*, App. Phys. Lett., **80** (2002) 3976

[30] Boeve, H., *et al.*, IEE Trans. Magn., **40** (2004) 2278

[31] Cardoso, S., *et al.*, App. Phys Lett., **76** (2000) 610

[32] Boeve, B., *et al.*, IEEE Trans. Magn., **40** (2004) 2278

[33] Cardoso, S., *et al.*, J. App. Phys., **87** (2000) 6058

[34] Jeong, H. D., *et al. App. Sur. Sci.*, **199** (2002) 6

[35] Lee, J. H., *et al.*, Mat. Res. Soc. Symp. Proc., **690** (2002) F3.9.1

[36] Wormington, M., *et al.*, Phil. Trans. R. Soc. Lond. A, **358** (1999) 2827

[37] Lee, J. H., *et al.*, J. App. Phys., **91** (2002) 217

[38] Bai, J., *et al.*, Physica B, **221** (1996) 411

[39] Luo, G. M., *et al.*, J. App. Phys., **91** (2002) 150

[40] An, Y. K., *et al.*, Thin Solid Films, **496** (2006) 571

[41] Tolan, M., "X-ray Scattering from Soft-Matter Thin Films", Springer Tracts in Modern Physics, Vol 148, 1st Edition, 1999, Berlin.

[42] Kiryukhin, V., *et al.*, Nature, **386** (1997) 813

[43] Åkerman, J. J., *et al.*, App. Phys Lett, **79** (2001) 3104

[44] Rabson, D. A., *et al.*, J. App. Phys., **89** (2001) 2786

[45] Song, S.A., *et al.*, Microsc. Microanal., **11** (2005) 431

[46] Mizuguchi, M., *et al.*, J. Nanosci. Nanotecnol, **7** (2007) 255

7 Summary, conclusions and further work

7.1 Summary

7.1.1 Co/Pd and Co/Ru samples

The diffuse scatter from repeated bi-layers of Co/Pd and Co/Ru was examined in detail over the Brillouin zones. From measurements of the Bragg sheet full-width-at-half-maximum the out-of-plane correlation length of the roughness at different spatial frequencies was examined, and found to fall as the spatial frequency increased. This shows that the short wavelength features propagate less well than the longer wavelength features in the roughness. This was the case for both the Co/Pd and Co/Ru samples. There was no observable change in the correlation lengths with the number of layers deposited. The technique is restricted to the correlated features between the interfaces, and so is not able to probe the non-conformal features.

The Hurst parameter from the in-plane correlation function can be directly extracted from the scaling behaviour of the intensity integrated over an entire Brillouin zone. As more layers were deposited the layers were seen to become more two-dimensional in nature. The Co/Pd system was observed to smooth after less material had been deposited than the Co/Ru system. From the shape of the intensity distribution, and the change in position of the q_y value at which scaling ceases, the behaviour was seen to be in good agreement with the expected form when a self-affine fractal form of the correlation function is used to model the roughness. The values of the fractal parameter show that initially a KPZ model is appropriate, and later the TAB model. This change in predominant mechanism does not appear to affect the out-of-plane correlation length.

7.1.2 CoFe/Ru and CoFeB/Ru samples

From the structural analysis of the specular scatter CoFe/Ru multilayers, it was identified that the RMS interface widths become progressively larger as more and more layers are deposited. Through the asymmetries in the CoFe/Ru and Ru/CoFe interfaces it was observed that the roughening originated during the deposition of the CoFe material, and that during the ruthenium deposition smoothing occurred. The smoothing effect of the ruthenium was not sufficient to prevent the interface width increasing as successive layers were deposited.

The effect of including boron within a CoFeB layer was to increase the interface widths. Although the widths are increased, the out-of-plane correlation length was measured to be much larger in the CoFeB/Ru material than the CoFe/Ru material.

The effects on the interfaces of annealing the multilayer structures were investigated. The CoFe/Ru structure was seen to be stable to annealing up to 300°C, with no changes occurring in either the specular or the diffuse scatter. Some subtle changes were identified in the amorphous-CoFeB/Ru layers on annealing up to 270°C and are attributed to the substrate interface. At higher temperatures more dramatic changes occurred when the CoFeB layers underwent crystallisation and the sample structure was substantially disrupted. There was no change in the diffuse scatter below crystallisation, showing there was no change in the roughness. Therefore, where exchange coupled structures are included in an MTJ, they are unlikely to be affected by annealing treatments.

7.1.3 CoFeB/AlO samples

The interfaces between CoFeB and AlO_x were examined. An asymmetry in the AlO_x on CoFeB verses CoFeB on AlO_x interfaces was identified with the latter interface being systematically 0.5Å smoother, in a similar way to the CoFe/Ru samples examined before. They demonstrated progressively more changes in the specular scatter as the annealing temperature was increased below the crystallisation temperature of the CoFeB layer. On crystallisation again a dramatic change in the specular scatter was observed. Although the specular scatter was seen to change dramatically no changes were seen in the diffuse scatter. This is attributed to a change in the compositional grading occurring, rather than a change in the hard topological roughness. From the invariance of the transverse diffuse scatter no changes are seen in the fractal parameter or the in-plane correlation length.

The growth of the AlO_x layers involves sputter etching an aluminium layer with oxygen. The observed results were discussed in the light of evidence of changes in oxidation state at the interfaces, and mechanisms postulated for the sharpening.

7.1.4 CoFeB/AlO in an MTJ

When only a single CoFeB/AlO interface was examined on a realistic MTJ sub-structure, again the specular scatter was seen to change progressively as the annealing temperature was increased. This was repeatable, both with different samples on the same equipment, and also at different synchrotron beamlines. Again dramatic changes in the scatter was seen when the CoFeB layer crystallised. The changes in the specular scatter were interpreted as a sharpening of the interface, and more precisely a reduction in the inter-diffusion. The diffuse scatter showed very little change, indicating that the hard topological roughness was not being altered by annealing. The matching of the high angle fringe intensity to the variation in the TMR performance of the MTJ shows a very similar form, which is consistent with a link between the two. From the observation previously that the CoFeB/AlO$_x$ interfaces are actively modified on annealing the sharpening was attributed to this interface, although the specular scatter and modelling were not sensitive enough to identify this directly. Nor was the scatter sufficiently sensitive to be able to identify any possible manganese diffusion.

7.1.5 Variable energy reflectivity

To attempt to pinpoint the interfaces which sharpen, and to investigate any changes in the distribution of manganese within the system, refinements to the x-ray scattering analysis were attempted. Further constraints on the models were included in moving between room temperature and higher temperatures, but this did not enable a structure to be deduced with any more certainty. It was identified that theoretically any diffusion of manganese within the system should cause a dramatic change in the variable energy reflectivity profiles at constant **q**. The use of reflectivity at different energies was attempted, although it was not possible without a very detailed knowledge of the energy dependent instrument function to identify with clarity what was occurring. The experimental requirements for variable energy reflectivity are stringent, and a detailed list of the requirements has been identified.

7.2 Conclusions

The evolution of the interfaces has been seen with the diffuse scatter analysis. This required a very intense synchrotron source and whether it could be performed in a standard laboratory diffractometer is questionable because of the limited incident intensity available. The analysis has proved an excellent way of extracting the fractal parameter from the correlation function of the interface roughness. Asymmetries in the interfaces depending on the order of the materials have been observed. In the case of magnetic tunnel junctions this raises important questions about the tunnel barrier where an insulating barrier is sandwiched between two identical electrodes. The interface states here are very important for the electron tunnelling and any asymmetry could have a large effect on the tunnelling current and operation of the device. It will also affect the performance of top-pinned verses bottom-pinned magnetic tunnel junctions where the stacks are grown in the opposite order.

A naïve expectation of annealing a multilayer would be that increasing the temperature increases the kinetic energy of the atoms and thus diffusion is enhanced, leading to wider interfaces. This has been shown not to be the case and that annealing can lead to a beneficial re-ordering of the interface. This has only occurred where AlO_x in included. The reduction in interface width does not change the topological roughness and so there is a limit, even if the CoFeB remained amorphous at high temperatures, to the enhancement that can be obtained by annealing. It also is unlikely that devices could be specifically designed with the incorporation of CoFeB/AlO to specifically achieve a sharper interface after anneal than is possible without the boron.

The enhancement in the TMR observed in the MTJs with moderate annealing has been associated here with a sharpening of the interfaces. This has been studied in detail and found to be a reduction in the interface width rather than a smoothing of the topological roughness. Following from the AlO_x/CoFeB multilayers there are assurances that it is this interface that is undergoing the same sharpening in the MTJs. For the TMR to change the most likely area for any changes is the tunnel barrier region, again confirming that the sharpening is consistent with the TMR variation. The closeness in the form of the peak intensity, and therefore the interface width, with temperature, and the variation in the TMR with temperature is beyond doubt.

The changes in the interfaces as successive layers are deposited has been seen both in the diffuse scatter work on Co/Pd and Co/Ru, where the differences were predominantly in the Hurst parameter describing the dimensionality of the interfaces. Evolution of the interfaces was also seen in the CoFe/Ru and CoFeB/AlO_x where the interface widths successively increased as more layers were deposited. These raise important considerations for the design of devices and as structures become more complex, such as double tunnel junctions, the opportunities within the devices for adding in buffer layers to achieve the desired foundations for a particular layer diminish. Careful deposition of the necessary layers for the device will need to be done with a view to what is to be deposited above, possibly even several layers away. The dispersion in the interface widths in the CoFe/Ru and CoFeB/AlO was seen to occur throughout the whole sample.

Boron has of late become an extremely common electrode material in thin film devices. The performance enhancing benefits are without doubt. It does however have the significant disadvantage that where it is used in amorphous layers the crystallisation of those layers is below the temperature necessary for integrating devices with CMOS technology. On crystallisation a significant disruption to the layer structure has been observed which will be detrimental to the performance of any device. This has recently been overcome in MgO based MTJs where the action of the crystalline tunnel barrier, in contrast to the amorphous AlO_x barriers, is to persuade the CoFeB into a bcc structure on crystallisation without impairment of the TMR [1-3].

Once the CoFeB has crystallised the benefit of the amorphous diffusion barrier against manganese from the pinning layer is lost and gain boundary diffusion pathways become available. The recently reported room temperature TMR values in excess of 450% have used a 'pseudo-spin-valve magnetic tunnel junction' where the IrMn pinning layer is omitted [1,3]. This enables the TMR to be studied without any complications from manganese, but it is not a realistic MTJ. If the degradation in TMR observed can be attributed to manganese diffusion in the AlO_x system as some authors suggest, then it is likely the same mechanism exists in the MgO system. Although this will not prevent the integration of MTJs with CMOS technology it will limit the performance until the manganese can be constrained.

In the optimisation of magnetic tunnel junctions there is still much work to be done both in improving the interfaces, and eliminating the diffusion of manganese with temperature. Variable energy reflectivity represents a potentially very sensitive tool for doing this. However, there is considerable practical difficulty in performing the measurements.

7.3 Further work

The detrimental effects of manganese diffusion within the structures remain a concern. Similar reflectivity measurements with *in-situ* annealing on repeated bi-layers of IrMn/CoFeB and IrMn/CoFe would enable the inter-diffusion to be studied as a function of annealing temperature, and the degree to which amorphous CoFeB is a good barrier to manganese diffusion assessed. To assist CoFeB in blocking the manganese diffusion thin diffusion-barrier layers could be investigated. They would have to be located between the pinned electrode and the pinning layer and must not affect the pinning itself. CoFeB electrodes with a composition gradient might be possible so that the interface with the IrMn remains amorphous even if the interface with the tunnel barrier, be it MgO or AlO_x, crystallises.

For completeness it would also be interesting to examine samples of CoFe/AlO_x to identify the rôle of boron and the amorphous under-layer in establishing an interface which sharpens with annealing. If the distribution of oxygen is important in driving the sharpening a different distribution would be expected when the AlO_x is grown on a different material which would lead to differences in the sharpening.

The sharpening observed was not reversible when the samples were cooled and so atomic profiling techniques can be used *ex-situ* to study the interfaces. High resolution electron microscopy of cross sections from samples annealed to a variety of temperatures would be useful to compare with the existing measurements. Similarly, a structural determination using techniques such as three-dimensional atom probe analysis on the structures would further elucidate the mechanisms in force.

References for Chapter 7:

[1] Lee, Y. M., *et al.*, App. Phys. Lett., **90** (2007) 212507
[2] Yuasa, S., *et al.*, App. Phys. Lett., **87** (2005) 242503
[3] Lee, Y. M., *et al.*, App. Phys. Lett., **89** (2007) 042506

Appendix A:
Instrument height alignment errors

The diffractometer's centre of rotation should be placed in the centre of the beam and the centre of the sample's top surface placed at the point so that on rotation the sample remains in the beam and the detector is always aligned with the centre of scattering. If the beam and sample are not positioned correctly then two errors are introduced into the experiment. Firstly there is a change in position of the scattering centre which changes the angle at which the scattered beam intersects the detector arc. Secondly the beam footprint on the sample is altered giving a change in intensity of the reflected beam.

Assuming the incident beam profile to be a symmetric peak the scattering centre will be where the sample surface intersects the beam. Let the beam pass a distance b above the centre of rotation and the sample, of length l, mounted a distance s above the centre of rotation. The situation is shown in Figure A-1 below.

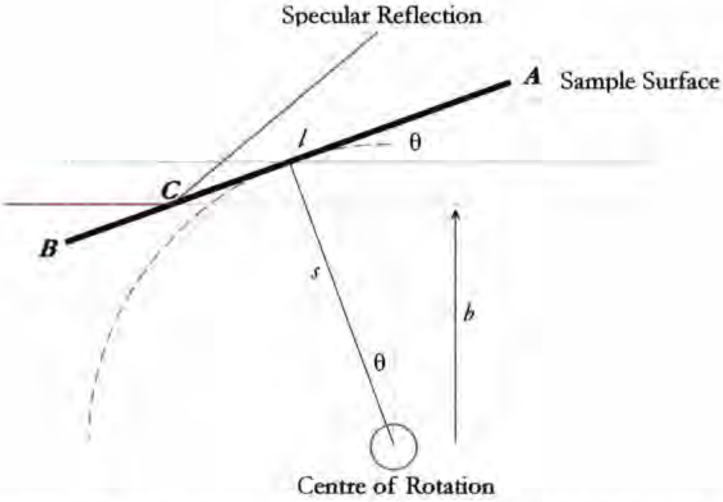

Figure A-1: The sample surface runs from A to B. As the sample is rotated its midpoint traces a circle around the centre of rotation. The position of the scattering centre, C, moves horizontally.

The coordinates of the two end points **A** and **B** of the sample are given by:

$$A_x = \frac{l}{2}\cos\theta - s\sin\theta \qquad B_x = -\frac{l}{2}\sin\theta - s\sin\theta \tag{A-1}$$

$$A_y = \frac{l}{2}\sin\theta + s\cos\theta \qquad B_y = -\frac{l}{2}\sin\theta + s\cos\theta$$

Using these to write the equation of the line describing the sample surface, and working through the algebra, gives:

$$y_{\text{sample surface}} = \frac{x\sin\theta + s}{\cos\theta} \tag{A-2}$$

The intersection of this line describing the sample surface with the beam occurs when $y=b$, giving the x-coordinate of the scattering centre to be:

$$C_x = \frac{b\cos\theta - s}{\sin\theta} \qquad \text{valid for } B_y < b \tag{A-3}$$

As the sample is rotated the scattering centre moves along the sample surface. This horizontal shift along the direction of the beam results in a perpendicular shift in the reflected beam when compared to the ideal case, as shown below:

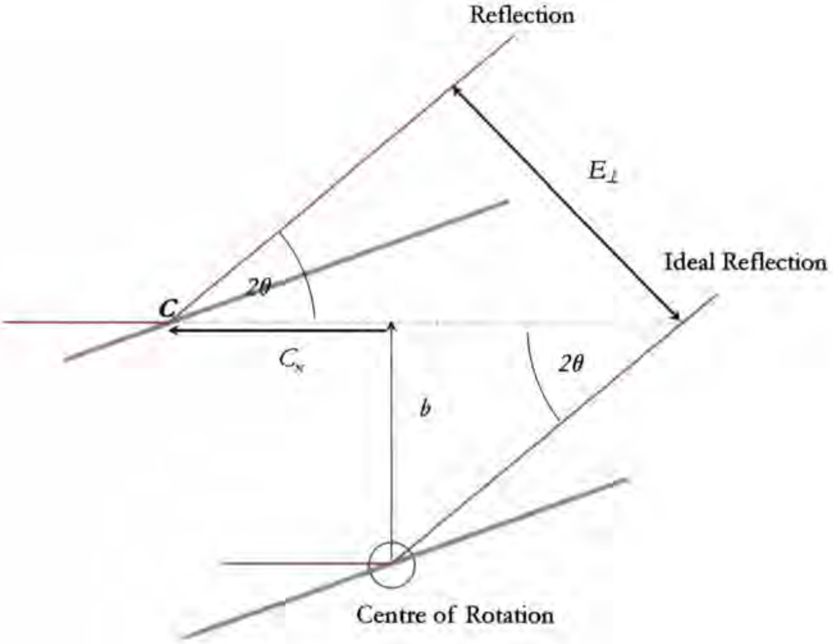

Figure A 2: The movement of the scattering centre, C, away from the centre of rotation causes the reflected beam to be parallel to the ideal reflection but off-set by a perpendicular distance E⊥

From trigonometry on the two triangles above the perpendicular separation, $E_\perp$, of the reflected beam to a parallel beam passing through the centre of rotation is:

$$E_\perp = \left(\frac{b}{\tan(2\theta)} - C_x\right)\sin(2\theta) \tag{A-4}$$

Substituting the value for C_x gives:

$$E_{\perp} = \left(\left(\frac{b}{\tan(2\theta)} \right) - \left(\frac{b\cos\theta - s}{\sin\theta} \right) \right) \sin(2\theta) \qquad \text{(A-5)}$$

Where the beam has been properly aligned over the centre of rotation and only the sample is misaligned in the beam this reduces to the more simple form:

$$E_{\perp} = \frac{s}{\sin\theta} \sin(2\theta) \qquad \text{(A-6)}$$

In reflectivity all the angles are small and the small angle approximations can be applied. The perpendicular offset will be approximately constant and twice the displacement of the sample from the centre of rotation. The constant offset means that in reflectivity this can be calibrated out of the data by recalibrating the detector angle. Then, in scanning the sample, assuming no sample curvature, it is possible to remain on the specular ridge without a perfect alignment. The reflected beam intersects with the detector arc, a distance *d* from the centre of rotation, at a different angle giving an apparent shift in detector angle from the ideal case. This angular shift is given by:

$$E_{2\theta} = \arcsin\left(\frac{E_{\perp}}{d} \right) \qquad \text{(A-7)}$$

Again in the reflectivity regime small angle approximations can be applied and then for a perfectly aligned beam the angular error (in radians) on the specular reflection is 2s/d. If the sample was 100μm off alignment, and the detector 80cm from the sample the angular error is 0.014°. This error is small in comparison to the beam footprint effects discussed in section 3.4.2.

Appendix B:

C++ code for analysis of MAR CCD image files

The full code for this program included a menu system to ease operation and also on screen graphing, using the DISLIN library. For simplicity these have been omitted here and only the analysis stages of the program are included. All the coding was done in C++, using the GSL scientific library, and compiled in DEV C++ 4.9.9.2.

The Program header file, specifying the libraries to include and defining all the variables used globally by the program and its functions, was:

```
///////////////////////////////
/// Analysis of MCCD Data Files
///////////////////////////////

#include <cstdlib>
#include <iostream>
#include <fstream>
#include <cmath>
#include <iomanip>
#include <dislin.h>
#include <windows.h>
#include <gsl/gsl_multimin.h>

using std::cout;
using std::cin;
using std::string;
using std::endl;
using std::ios;
using std::ofstream;
using std::setw;
using std::ifstream;

char file[40];                    //Filename to analyse
int column;                       //Column number held in column_y;
int row;                          //Row index
float column_x[2048];             //Qz values of column
float column_y[2048];             //Particular column being fitted
float column_xsim[2048];          //Simulated data qz-values
float column_ysim[2048];          //Simulated data y-values
int image[2048][2048];            //Column held in memory
float contour[2048][2048];
int loaded_column_low = 4000;     //Lower limit of columns held in memory
int loaded_column_high = 4001;    //Upper limit of columns held in memory
double integrated_intensity = 0 ; //Value of integrated intensity

int i,x,y;                         //Loop indexing variables
int y_min=1;                       //Limits of array
int y_max=2047;                    //Limits of array
int col_min=900;                   //Column limits for sequential fitting
int col_max=1100;                  //Column limits for sequential fitting

double intensity;                  //The measured intensity
int dummy;
double pi=3.1415927;

double theta,tth,htth,qx,qy,qz;  //Variables holding angles and q components
```

```
double k=5.0675;                //The wavevector in the experiment
int x_spec=1072;                //x-coordinate of the specular point
int y_spec=1050;                //y-coordinate of the specular point
double x_size=0.0051;           //angular size of each pixel
double y_size=0.0051;           //angular size of each pixel


//Set initial parameters for fit (linear background and PearsonVII parameters)
//And initialisation of the GSL minimisation vectors

double *parametersPtr=NULL;
size_t number_of_variables=6;

double gradient=0;
double gradient_start=0;
double constant=10;
double constant_start=0;
double amplitude=40;
double amplitude_start=0;
double max_amplitude=0;
double peak_center=0.27;
double peak_center_start=0;
double width=0.02;
double width_start=0;
double shape=1;
double shape_start=0;

gsl_vector *variablesPtr=gsl_vector_alloc(number_of_variables);
gsl_vector *minimised_variablesPtr=gsl_vector_alloc(number_of_variables);
```

The global functions used are defined as follows:

```
//Define global functions

void load_image(int column);      //To load image from file to memory
double load_column(int column);   //To load a column from memory
double gof(const gsl_vector *variablesPtr, void *params);
                                  //To Calculate goodness of fit
void minimize(void);              //To optimise the fit

void plot_axes(double max_intensity);   //Show axes on screen
void plot_sim(void);                    //Show data on screen
void clear_graph(void);                 //Clear data on screen
void menu(void);                        //Show the menu on screen
```

The Program began by asking for the file name, and the sample angle and coordinates of the specular point which were used to calculate the scattering position in reciprocal space.

```
int main()
{
    cout<<"CCD Image Analysis"<<endl;

    cout<<"Enter file to read: ";
    cin>>file;
    cout<<endl;


    cout<<"IMAGE SETTINGS:"<<endl;
    cout<<"Enter sample angle (degrees):";
    cin>>theta;
    cout<<"Enter coordinates of specular point: "<<endl;
    cout<<"x: ";
    cin>>x_spec;
    cout<<"y: ";
```

```
    cin>>y_spec;
    cout<<endl;
```

The image, specified above in the variable 'file' was loaded into memory by the following function:

```
void load_image (int column){

    int x;
    int y;
    int n;
    float intensity;

    cout<<"reading from file"<<endl;
    ifstream readFileA;
    readFileA.open( file , ios::in);

    int i=0;
    while (readFileA >> intensity ) {

        x=i%2048;
        y=i/2048;
        i++;

            image[x-loaded_column_low][y]=static_cast<int>(intensity);

        if(i%10000==0){cout<<"loaded: "<<((100*i/(2048*2048)))<<"%\r";}
    }
}
```

Each column (a cut in q_z at fixed q_y) of the data was analysed in turn and converted to reciprocal space with the following function:

```
double load_column(int column){

    max_amplitude=0;

    htth=(column-x_spec)*x_size;

    for(y=0; y<2048;y++){
        tth =(y-y_spec)*y_size+2*theta;
        column_x[y]=k*(sin((tth-theta)*pi/180)+sin(theta*pi/180));
        column_y[y]=image[column-loaded_column_low][y];
        if (column_y[y]>max_amplitude){max_amplitude=column_y[y];}
    }

    qy=k*(cos((tth-theta)*pi/180)*sin(htth*pi/180));

    cout<<"qy = "<<qy<<endl;

    return(qy);
}
```

Output text files were set up for the analysed data:

```
    // Initialise Graph Plotting and output files

    ofstream writeFile1;
    writeFile1.open( "widths(+ve fit).txt", ios::out);
    ofstream writeFile2;
    writeFile2.open( "widths(-ve fit).txt", ios::out);
```

```
    ofstream writeFile3;
    writeFile3.open( "intensity.txt", ios::out);
    ofstream writeFile4;
    writeFile4.open( "Fitted XYZ.txt", ios::out);
```

Sequential fitting was run from col_min to col_max with the following procedure. A similar procedure was included to fit the data from col_max backwards to col_min so that fitting could be performed in either direction.

```
        gradient_start=gradient;
        constant_start=constant;
        amplitude_start=amplitude;
        peak_center_start=peak_center;
        width_start=width;
        shape_start=shape;

        for(column=col_min;column<col_max;column++){

            cout<<endl<<endl<<"COLUMN "<<column<<endl;
            cout<<"Gradient_start: "<<gradient_start<<endl;
            cout<<"Constant_start: "<<constant_start<<endl;
            cout<<"Amplitude_start: "<<amplitude_start<<endl;
            cout<<"Peak_centre_start: "<<peak_center_start<<endl;
            cout<<"width_start: "<<width_start<<endl;
            cout<<"shape_start: "<<shape_start<<endl<<endl;

            gsl_vector_set(variablesPtr, 0 , gradient_start);
            gsl_vector_set(variablesPtr, 1 , constant_start);
            gsl_vector_set(variablesPtr, 2 , amplitude_start);
            gsl_vector_set(variablesPtr, 3 , peak_center_start);
            gsl_vector_set(variablesPtr, 4 , width_start);
            gsl_vector_set(variablesPtr, 5 , shape_start);

            writeFile1<<setw(15)<<load_column(column);
            minimize();
            writeFile1<<setw(15)<<width;
            writeFile1<<setw(15)<<peak_center;
            writeFile1<<setw(15)<<shape;
            writeFile1<<setw(15)<<amplitude<<endl;

            cout<<"minimised gradient: "<<gradient<<endl;
            cout<<"minimised constant: "<<constant<<endl;
            cout<<"minimised amplitude: "<<amplitude<<endl;
            cout<<"minimised center: "<<peak_center<<endl;
            cout<<"minimised width: "<<width<<endl;
            cout<<"minimised shape: "<<shape<<endl<<endl;

            for(y=0; y<(y_max-y_min);y++){
                writeFile4<<setw(15)<<qy;
                writeFile4<<setw(15)<<column_xsim[y];
                writeFile4<<setw(15)<<column_ysim[y];
                writeFile4<<setw(15)<<column_y[y+y_min]<<endl;
            }
        }
```

The minimise( ) function is used to find the best peak fit. This is done within the procedures included in the GSL reference library:

```
void minimize(void){
```

```
// Initialise file output

double size;                         //Size of minimizer
size_t iter = 0, i;                  //Variable to count number of
                                     //iterations
size_t max_num_iter=10000;           //Maximum number of iterations
double target_minimizer_size=0.0001; //Target size to exit iterating

int status;

cout<<"Goodness of fit: "<<gof(variablesPtr, parametersPtr)<<endl;

// DEFINE MINIMISING ALGORITHM

const gsl_multimin_fminimizer_type *minimizer_typePtr;
minimizer_typePtr=gsl_multimin_fminimizer_nmsimplex;

// SET STEPSIZE FOR SEARCHING

gsl_vector *stepsizePtr=gsl_vector_alloc(number_of_variables);

gsl_vector_set(stepsizePtr, 0, 1);                            //grad
gsl_vector_set(stepsizePtr, 1, 1);                            //const
gsl_vector_set(stepsizePtr, 2, 1);                            //amp
gsl_vector_set(stepsizePtr, 3, 0.005);                        //cent
gsl_vector_set(stepsizePtr, 4, 0.005);                        //width
gsl_vector_set(stepsizePtr, 5, 0.1);                            //shape


// ALLOCTE FUNCTION TO MINIMISE

gsl_multimin_function function_to_minimize;
function_to_minimize.f=&gof;
function_to_minimize.n=number_of_variables;
function_to_minimize.params=parametersPtr;

// INITIALISE MINIMISER STATE

gsl_multimin_fminimizer *minimizer_statePtr=NULL;

minimizer_statePtr=gsl_multimin_fminimizer_alloc(minimizer_typePtr,
number_of_variables);

gsl_multimin_fminimizer_set(minimizer_statePtr, &function_to_minimize,
variablesPtr,stepsizePtr);

// ITERATE MINIMISING ROUTINE

do{
    iter++;
    status = gsl_multimin_fminimizer_iterate(minimizer_statePtr);
    if (status!=0) {break;}
    size=gsl_multimin_fminimizer_size (minimizer_statePtr);
    minimised_variablesPtr=gsl_multimin_fminimizer_x(minimizer_statePtr);
    status=gsl_multimin_test_size (size, target_minimizer_size);
}

while (status==GSL_CONTINUE && iter < max_num_iter);

// Extract values to return

gradient=gsl_vector_get(minimised_variablesPtr,0);
constant=gsl_vector_get(minimised_variablesPtr,1);
amplitude=gsl_vector_get(minimised_variablesPtr,2);
peak_center=gsl_vector_get(minimised_variablesPtr,3);
width=gsl_vector_get(minimised_variablesPtr,4);
shape=gsl_vector_get(minimised_variablesPtr,5);
```

```
    // COPY MINIMISED VARIABLES TO STARTING VARIABLES FOR NEXT TIME

    gradient_start=gradient;
    constant_start=gsl_vector_get(minimised_variablesPtr,1);

    if (amplitude>0){amplitude_start=amplitude;}

    if(fabs(peak_center_start-peak_center)<0.005){
        peak_center_start=peak_center;
        }

    if(width>0.01 && width<0.2){width_start=width;}

    if(shape>1 && shape<10){shape_start=shape;}

    // CLEAR THE MINIMISER

    gsl_vector_free(stepsizePtr);
    gsl_multimin_fminimizer_free (minimizer_statePtr);

}
```

Where needed the goodness of fit of the peak to the experimental data was calculated using this routine:

```
double gof(const gsl_vector *variablesPtr, void *params){

     double goodness=0;
     double gradient=gsl_vector_get(variablesPtr,0);
     double constant=gsl_vector_get(variablesPtr,1);
     double amplitude=gsl_vector_get(variablesPtr,2);
     double peak_center=gsl_vector_get(variablesPtr,3);
     double width=gsl_vector_get(variablesPtr,4);
     double shape=gsl_vector_get(variablesPtr,5);

     int y;

     for(y=0; y<(y_max-y_min);y++){
        column_xsim[y]=column_x[y+y_min];
        column_ysim[y]=gradient*column_xsim[y]+constant +
        (amplitude/
        pow((1+4*(pow(((column_xsim[y]-peak_center)/width),2)*
        (pow(2,(1/shape))-1))),shape));

        goodness+=pow(column_ysim[y]-column_y[y+y_min],2);
     }
     return goodness;
}
```

Finally, integration over a Brillouin zone was performed using this routine, the Brillouin zone boundary being specified by y_min and y_max.

```
         for(column=col_min;column<col_max;column++){
             writeFile3<<setw(15)<<load_column(column);
             integrated_intensity=0;
             for(row=y_min;row<y_max;row++){
                   integrated_intensity+=column_y[row];
             }
             cout<<"integrated intensity= "<<integrated_intensity<<endl;
             writeFile3<<setw(15)<<integrated_intensity<<endl;
         }
```

Appendix C:

C++ code for simulation of variable energy reflectivity

This program calculates the specular scatter for a particular q_z value for a range of energies. It breaks the structure down into a series of thin perfectly sharp layers of varying composition to model the interfaces. By this method the scatter from arbitrary interface profiles can be modelled.

The full code for this program included a menu system to ease operation and also on screen graphing, using the DISLIN library. For simplicity these have been omitted here and only the analysis stages of the program are included. All the coding was done in C++, using the GSL scientific library, and compiled in DEV C++ 4.9.9.2.

The Program header file, specifying the libraries to include and defining all the variables used globally by the program and its functions, was:

```
///////////////////////////////
//////////////////////////////////////////////////
/// VARIABLE ENERGY REFLECTIVITY v2.4
/// Form of variable energy code in functions
//////////////////////////////////////////////////

#include <cstdlib>
#include <iostream>
#include <complex>
#include <cmath>
#include <fstream>
#include <iomanip>

using std::complex;
using std::cout;
using std::endl;
using std::ios;
using std::setw;
using std::setiosflags;
using std::setprecision;
using std::ifstream;
using std::ofstream;

//GLOBAL CONSTNTS AND VARIABLES:
const double r0=2.81794092e-13;        //Thomson scattering length(cm)
const double pi=3.14159265359;         //pi
const double Na=6.02213670e23;         //Avagadro's Number
const double h=6.6260755e-34;          //Plank's Constant
const double c=2.99792458e8;           //Speed of light
const double e=1.60217733e-19;         //Charge of Electron
double energy;                         //Selected Energy
double sample_structure[7][100];       //Sample Structre
double atomic_profile[15][1000];       //Atomic Profile
complex<double> layer_n[1000];         //Refractive Index Profile of sample
double f_array[11][3][1001];           //Anomalous dispersion corrections
double layer_total;                    //Total number of layers in sample
```

```
double interfaces[100];                //Interface positions
int material_number;                   //Material Reference Number
double total_thickness;                //Total Thickness of stack
int row_count;                         //Total number of rows in matrix
double output_array[3][1000];          //Output Specular
double zstep;                          //Stepsize in Z
double mass_density [18] = { 0, 2.46 , 2.7 , 2.328 , 7.3 , 7.87 , 8.86 , 12.37
,
         16.4 , 22.65 , 8.4 , 3.97 , 0 , 0 , 0 , 0 , 7.05, 2.533 };//Mass
densities
double A[11] = { 0, 10.811, 26.981538 , 28.0855 , 54.938049 , 55.845 ,
58.9332,
                     101.07 , 180.9479 , 192.217 , 15.9994  };  //Atomic
Weights
int Z[11] = { 0, 5 , 13 , 14 , 25 , 26, 27 , 44 , 73 , 77 , 8}; //Atomic
Numbers
double Q;                              //Qz-vector for scattering
double beam_intensity=1e6;             //Intensity of incident beam

//FUNCTION PROTOTYPES:
void   LoadSampleStructure(void);
void   LoadAnomolousDispersion(void);
void   LoadReferenceData(void);
void   CalcInterfacePositions(void);
void   CalcAtomicDensityProfile(void);
void   CalcRefractiveIndexProfile(double energy);
double CalcSpecularReflectivity(double energy, double Q);
void   WriteAtomicDensityProfile(void);
void   WriteRefractiveIndexProfile(void);
void   WriteSampleStructure(void);
double AtomicVolume(int);
double MassFractionCompound (int material_number, double mixture[2][4]);
double VolumeFractionAlloy  (int material_number, double mixture[2][4]);
double TotalThickness(void);
```

The main program had the very simple structure of first loading the sample structure from a columnar text file specifying the parameters for each layer of material, thickness, density, interface width. From this an atomic density profile was calculated. Then at each energy, using the anomalous dispersion corrections, the refractive index profile could be calculated, and from this the specular scatter at a particular position in **q** calculated. The energy was then incremented in a 'for loop' to calculate the variable energy reflectivity.

```
////////////////
//MAIN PROGRAM:
////////////////

int main()
{

    LoadSampleStructure();
    LoadAnomolousDispersion();

    CalcInterfacePositions();
    cout<<"Total Stack Thickness: "<<TotalThickness()<<endl;

    CalcAtomicDensityProfile();
    WriteAtomicDensityProfile();

    ofstream WriteFile( "Specular.ep", ios::out );
```

```
    for(energy=5.5;energy<8.8;energy+=0.01){

        CalcRefractiveIndexProfile(energy);

        for(Q=0.435;Q<0.5;Q+=0.1){

           WriteFile << setw(15) << energy
                     << setw(15) << Q
                     << setw(15) << CalcSpecularReflectivity(energy,Q)
                     << endl ;
        }
    }

    system("PAUSE");
    return EXIT_SUCCESS;
}
```

The sample structure was read from the file sample.txt and stored in the sample_structure array:

```
void LoadSampleStructure(void){

     int layer_number;
     int material;
     double thickness;
     double roughness;
     double density;

     layer_total=0;

     ifstream readSampleFile( "sample.txt", ios::in);

     cout << "Sample structure read from file: " << endl <<endl ;
     cout << setw(11) << "layer"
          << setw(11) << "material"
          << setw(11) << "thickness"
          << setw(11) << "roughness"
          << setw(11) << "density"
          << endl << endl;

     while (readSampleFile >> layer_number >> material >> thickness
                           >> roughness >> density){

          sample_structure[0][layer_number]=layer_number;
          sample_structure[1][layer_number]=material;
          sample_structure[2][layer_number]=thickness;
          sample_structure[3][layer_number]=roughness;
          sample_structure[4][layer_number]=density;
          layer_total+=1;
    }
}
```

The anomalous dispersion corrections were loaded from text files and held in the f_array array. This was repeated for all the different elements in the sample.

```
void LoadAnomolousDispersion(void){

    int a;
    double energy;
    double fprime;
    double fprimeprime;

    ifstream readElement1Fs( "Element1_fs.txt", ios::in);
    a=0;
    while (readElement1Fs >> energy >> fprime >> fprimeprime){
```

```
          f_array[1][0][a]=energy;
          f_array[1][1][a]=fprime;
          f_array[1][2][a]=fprimeprime;
          a++;
    }
```

From the layer thicknesses the positions of the interfaces within the sample was calculated and stored in the interfaces array.

```
void CalcInterfacePositions(void){

    double total_thickness = 0;
    int layer_number=0;

    cout<<"Total Number of layers in CalcInterfacePositions:"
        <<layer_total<<endl;

    cout<<"Interface Depths from Surface (A):"<<endl;

    for (layer_number=1;layer_number<layer_total+1;layer_number++){

        interfaces[layer_number]=total_thickness;
        total_thickness+=sample_structure[2][layer_number];

        cout << layer_number << "    " << interfaces[layer_number]<<endl;

    }

    interfaces[layer_number]=10000000;
    cout << layer_number << "    " << interfaces[layer_number]<<endl<<endl;

}
```

The atomic density profile was calculated for each individual layer by the following function, which uses erf(z) functions to spread the atoms over the interface regions. Layers of single elements, layers of compounds and layers containing mixtures were all handled differently on account of the way in which atomic density is calculated. This routine also broke the structure down into thin sharp layers of thickness zstep.

```
void CalcAtomicDensityProfile(void){

     int n=0;                       //layer number variable
     int a=0;                       //indexing variable
     double z=0;                    //depth into sample
     zstep=1;                       //stepsize when analysing z
     int material_number=0;         //material number

     for (n=1;n<layer_total+1;n++){

        material_number=static_cast<int>(sample_structure[1][n]);
        cout<<material_number<<endl;

        switch (material_number) {

            case 1 :   //B
            case 2 :   //Al
            case 3 :   //Si
            case 4 :   //Mn
```

```
case 5 :   //Co
case 6 :   //Fe
case 7 :   //Ru
case 8 :   //Ta
case 9 :   //Ir



    a=0;
    for (z=-50;z<total_thickness+50;z+=zstep){
        atomic_profile[0][a]=z;
        atomic_profile[material_number][a]+=
            mass_density[material_number]*Na/A[material_number]*
            sample_structure[4][n]*0.25*
            ( erf((z-interfaces[n])/
            (pow(2,0.5 )*sample_structure[3][n]))+1)*
            ( erf((interfaces[n+1]-z)/
            (pow(2,0.5)*sample_structure[3][n+1]))+1);

    a++;
    }

    break ;

case 11:    //Al2O3 Compound

    a=0;
    double AlO[2][4];

    AlO[0][0]=2;
    AlO[0][1]=10;
    AlO[0][2]=0;
    AlO[0][3]=0;
    AlO[1][0]=0.4;
    AlO[1][1]=0.6;
    AlO[1][2]=0;
    AlO[1][3]=0;

    for (z=-50;z<total_thickness+50;z+=zstep){

        atomic_profile[2][a] += MassFractionCompound(0,AlO)*
                                mass_density[11]*
                                sample_structure[4][n]*
                                Na/A[2]*0.25*
                                ( erf((z-interfaces[n])/
                                (pow(2,0.5)*
                                 sample_structure[3][n]))+1)*
                                ( erf((interfaces[n+1]-z)/
                                ( pow(2,0.5)*
                                  sample_structure[3][n+1]))+1);

        atomic_profile[10][a] += MassFractionCompound(1,AlO)*
                                 mass_density[11]*
                                 sample_structure[4][n]
                                 *Na/A[10]*0.25*
                                ( erf((z-interfaces[n])/
                                  (pow(2,0.5)*
                                 sample_structure[3][n]))+1)*
                                ( erf((interfaces[n+1]-z)/
                                ( pow(2,0.5)*
                                  sample_structure[3][n+1]))+1);


        a++;
    }
    break;

case 12:    // CoFeB Mixture
```

```
    a=0;
    double CoFeB[2][4];

        CoFeB[0][0]=6;
        CoFeB[0][1]=5;
        CoFeB[0][2]=1;
        CoFeB[0][3]=0;
        CoFeB[1][0]=0.6;
        CoFeB[1][1]=0.2;
        CoFeB[1][2]=0.2;
        CoFeB[1][3]=0;

    for (z=-50;z<total_thickness+50;z+=zstep){

        atomic_profile[6][a]+= VolumeFractionAlloy(0,CoFeB) *
                                 mass_density[6]*Na/A[6]*
                                 sample_structure[4][n]*0.25*
                               ( erf((z-interfaces[n])/
                                (pow(2,0.5)*
                                 sample_structure[3][n]))+1)*
                               ( erf((interfaces[n+1]-z)/
                               ( pow(2,0.5)*
                                 sample_structure[3][n+1]))+1);

        atomic_profile[5][a]+= VolumeFractionAlloy(1,CoFeB) *
                                 mass_density[5]*Na/A[5]*
                                 sample_structure[4][n]*0.25*
                               ( erf((z-interfaces[n])/
                                (pow(2,0.5)*
                                 sample_structure[3][n]))+1)*
                               ( erf((interfaces[n+1]-z)/
                               ( pow(2,0.5)*
                                 sample_structure[3][n+1]))+1);

        atomic_profile[1][a]+= VolumeFractionAlloy(2,CoFeB) *
                                 mass_density[1]*Na/A[1]*
                                 sample_structure[4][n]*0.25*
                               ( erf((z-interfaces[n])/
                                (pow(2,0.5)*
                                 sample_structure[3][n]))+1)*
                               ( erf((interfaces[n+1]-z)/
                               ( pow(2,0.5)*
                                 sample_structure[3][n+1]))+1);
        a++;
    }
    break ;

case 13:        //IrMn mixture

    a=0;

    double IrMn[2][4];

    IrMn[0][0]=9;
    IrMn[0][1]=4;
    IrMn[0][2]=0;
    IrMn[0][3]=0;
    IrMn[1][0]=0.2;
    IrMn[1][1]=0.8;
    IrMn[1][2]=0;
    IrMn[1][3]=0;

    for (z=-50;z<total_thickness+50;z+=zstep){

        atomic_profile[9][a]+= VolumeFractionAlloy(0,IrMn) *
                                 mass_density[9]*Na/A[9]*
                                 sample_structure[4][n]*0.25*
                               ( erf((z-interfaces[n])/
                                (pow(2,0.5)*
```

```
                                 sample_structure[3][n]))+1)*
                               ( erf((interfaces[n+1]-z)/
                               ( pow(2,0.5)*
                                 sample_structure[3][n+1]))+1);

        atomic_profile[4][a]+= VolumeFractionAlloy(1,IrMn) *
                                 mass_density[4]*Na/A[4]*
                                 sample_structure[4][n]*0.25*
                               ( erf((z-interfaces[n])/
                                (pow(2,0.5)*
                                 sample_structure[3][n]))+1)*
                               ( erf((interfaces[n+1]-z)/
                               ( pow(2,0.5)*
                                 sample_structure[3][n+1]))+1);

        a++;
    }
    break ;

case 16:  //RuO2 compound

    a=0;

    double RuO2[2][4];

    RuO2[0][0]=7;
    RuO2[0][1]=10;
    RuO2[0][2]=0;
    RuO2[0][3]=0;
    RuO2[1][0]=0.33333;
    RuO2[1][1]=0.66666;
    RuO2[1][2]=0;
    RuO2[1][3]=0;

    for (z=-50;z<total_thickness+50;z+=zstep){

        atomic_profile[7][a]  += MassFractionCompound(0,RuO2)*
                                mass_density[16]*
                                sample_structure[4][n]
                                 *Na/A[7]*0.25*
                                ( erf((z-interfaces[n])/
                                ( pow(2,0.5)*
                                  sample_structure[3][n]))+1)*
                                ( erf((interfaces[n+1]-z)/
                                ( pow(2,0.5)*
                                  sample_structure[3][n+1]))+1);

        atomic_profile[10][a]  += MassFractionCompound(1,RuO2)*
                                 mass_density[16]*
                                 sample_structure[4][n]
                                 *Na/A[10]*0.25*
                                ( erf((z-interfaces[n])/
                                ( pow(2,0.5)*
                                  sample_structure[3][n]))+1)*
                                ( erf((interfaces[n+1]-z)/
                                ( pow(2,0.5)*
                                  sample_structure[3][n+1]))+1);
                a++;
    }
    break;

case 17:        //SiO2 Compound

    a=0;

    double SiO2[2][4];

    SiO2[0][0]=3;
    SiO2[0][1]=10;
```

```
                SiO2[0][2]=0;
                SiO2[0][3]=0;
                SiO2[1][0]=0.33333;
                SiO2[1][1]=0.66666;
                SiO2[1][2]=0;
                SiO2[1][3]=0;

                for (z=-50;z<total_thickness+50;z+=zstep){

                    atomic_profile[3][a] += MassFractionCompound(0,SiO2)*
                                            mass_density[17]*
                                             sample_structure[4][n]
                                             *Na/A[3]*0.25*
                                            ( erf((z-interfaces[n])/
                                            ( pow(2,0.5)*
                                              sample_structure[3][n]))+1)*
                                            ( erf((interfaces[n+1]-z)/
                                            ( pow(2,0.5)*
                                              sample_structure[3][n+1]))+1);

                    atomic_profile[10][a] += MassFractionCompound(1,SiO2)*
                                             mass_density[17]*
                                             sample_structure[4][n]
                                             *Na/A[10]*0.25*
                                            ( erf((z-interfaces[n])/
                                            ( pow(2,0.5)*
                                              sample_structure[3][n]))+1)*
                                            ( erf((interfaces[n+1]-z)/
                                            ( pow(2,0.5)*
                                              sample_structure[3][n+1]))+1);

                    a++;
                }

                break;

            default:
                    cout<<"ERROR - MATERIAL "<<material_number
                        <<" NOT RECOGNISED!"<<endl;

        }
    }

    row_count=a;
    cout << "Number of 1A rows: " <<row_count << endl ;

}
```

Where a compound, such as SiO_2, was calculated the fraction of each atom in the material making up the layer was modelled using this function:

```
double MassFractionCompound (int component, double mixture[2][4]){

    double mass_fraction ;

    int a;
    int b;
    int c;
    int d;

    a=static_cast<int>(mixture[0][0]);
    b=static_cast<int>(mixture[0][1]);
    c=static_cast<int>(mixture[0][2]);
    d=static_cast<int>(mixture[0][3]);

    int component_material;
    component_material=static_cast<int>(mixture[0][component]);
```

```
     mass_fraction    = A[component_material] * mixture[1][component] /
                            ( A[a] * mixture[1][0] +
                              A[b] * mixture[1][1] +
                              A[c] * mixture[1][2] +
                              A[d] * mixture[1][3]   ) ;

     return mass_fraction;

}
```

Where a mixture was included, the fraction of atoms making up the layers was calculated using this function:

```
double VolumeFractionAlloy (int component, double mixture[2][4]){

     double volume_fraction ;

     int a;
     int b;
     int c;
     int d;

     a=static_cast<int>(mixture[0][0]);
     b=static_cast<int>(mixture[0][1]);
     c=static_cast<int>(mixture[0][2]);
     d=static_cast<int>(mixture[0][3]);

     int component_material;
     component_material=static_cast<int>(mixture[0][component]);

     volume_fraction    = AtomicVolume(component_material)*
                          mixture[1][component]/
                        ( AtomicVolume(a) * mixture[1][0] +
                          AtomicVolume(b) * mixture[1][1] +
                          AtomicVolume(c) * mixture[1][2] +
                          AtomicVolume(d) * mixture[1][3]   ) ;


     return volume_fraction;

}
```

The atomic volume was based on a calculation from the density and the number of atoms per unit volume:

```
double AtomicVolume (int MaterialNumber){

    double volume;

    if (MaterialNumber==0) volume=0;
    else volume=A[MaterialNumber]/(mass_density[MaterialNumber]*Na);

    return volume;

}
```

The refractive index profile was calculated using this function:

```
void CalcRefractiveIndexProfile(double energy){

     double delta = 0;
     double beta = 0;
     int m=0;
```

```
     int a=0;
     int b=static_cast<int>((energy-4.999999)/0.01);
     double lambda = (h*c)/(e*1e-7*energy);

     for (a=0;a<row_count+1;a++){

        delta=0;
        beta=0;

        for (m=1;m<11;m++){

             delta += atomic_profile[m][a]*(Z[m]+f_array[m][1][b]);
             beta  += atomic_profile[m][a]*f_array[m][2][b];
        }

        atomic_profile[11][a] = delta*r0*pow(lambda*1e-8,2)
                                          /(2*pi);
        atomic_profile[12][a] = beta*r0*pow(lambda*1e-8,2)
                                          /(2*pi);

        real(layer_n[a])=1-atomic_profile[11][a];
        imag(layer_n[a])=atomic_profile[12][a];
     }

}
```

Finally, this is the function which used the Parratt formalism to calculate the reflectivity from the whole stack:

```
double CalcSpecularReflectivity(double energy, double Qz){
     complex<double> Q;
     real(Q)=Qz;
     complex<double> k;
     complex<double> lambda;
     complex<double> num1(1,0);
     complex<double> num2(2,0);
     complex<double> num8(8,0);
     complex<double> pi(3.14159265359,0);
     complex<double> i(0,1);
     complex<double> layer_Qj[1000];
     complex<double> layer_r[1000];
     complex<double> layer_R[1000];
     complex<double> intensity;
     int a;

     real(lambda)= (h*c)/(e*1e-7*energy);
     k=num2*pi/lambda;

// Wavevector Transfer Calculation in all layers (inc substrate):

     for(a=0;a<row_count+1;a++){
         layer_Qj[a]=sqrt(pow(Q,2)-num8*pow(k,2)*(num1-real(layer_n[a]))+
         i*num8*pow(k,2)*imag(layer_n[a]));
     }


// reflection coefficients at all interfaces:

     for (a=1;a<row_count;a++){
         layer_r[a]=(layer_Qj[a-1]-layer_Qj[a])/
        (layer_Qj[a-1]+layer_Qj[a]);

     }

// reflectivity from interfaces:
```

```
     layer_R[row_count]=layer_r[row_count];

     for(a=1;a<=row_count;a++){
         layer_R[row_count-a]=(layer_r[row_count-a]+
                              layer_R[row_count-a+1]
                              *exp(i*layer_Qj[row_count-a]*zstep))/
                              (num1+layer_r[row_count-a]*
                              layer_R[row_count-a+1]
                              *exp(i*layer_Qj[row_count-a]*zstep));
    }

// reflected intensity from top layer

      intensity = layer_R[1]*conj(layer_R[1]);

      return (real(intensity)*beam_intensity);

}
```